THESE

En vue de l'obtention du

DOCTORAT DE L'UNIVERSITÉ DE TOULOUSE

Délivré par Institut National Polytechnique de Toulouse
Discipline ou spécialité : Dynamique des fluides

Présentée et soutenue par Jean-Mathieu Senoner
Le 9 juin 2010

Simulation aux Grandes Échelles de l'écoulement diphasique dans un brûleur aéronautique par une approche Euler-Lagrange

---

JURY

F.X. DEMOULIN	Maître de conférences à l'Université de Rouen/CORIA	Rapporteur
P. BRUEL	Chargé de recherche à l'UPPA	Rapporteur
G. LAVERGNE	Professeur à l'ISAE / Onera Toulouse	Examinateur
M. LANCE	Professeur à l'Université Claude Bernard de Lyon	Examinateur
B. OESTERLE	Professeur à l'ESSTIN	Examinateur
B. CUENOT	Chercheur senior au CERFACS	Directrice de thèse
T. LEDERLIN	Ingénieur à Turbomeca	Membre Invité
C. HABCHI	Ingénieur de recherche à l'IFP	Membre Invité

Ecole doctorale : *Mécanique, Energétique, Génie civil, Procédés*
Unité de recherche : *CERFACS*
Directeur de Thèse : *Bénédicte Cuenot*
Co-Directeur de Thèse : *Rémi Abgrall*

Contents

PART I THE INDUSTRIAL CONTEXT

Chapter 1: General introduction

1.1 Combustion of fossil fuels. **3**
  1.1.1 Environmental context *3*
  1.1.2 Towards lean combustion in aeronautic engines. *5*
1.2 Numerical simulation of realistic combustion systems **6**
  1.2.1 Modeling of the gaseous phase *6*
  1.2.2 Modeling of the dispersed phase *7*
1.3 Objectives of the present work **12**
  1.3.1 Previous developments *12*
  1.3.2 Plan of the thesis *12*

PART II GOVERNING EQUATIONS AND NUMERICS

Chapter 2: Equations for the gaseous phase

2.1 Conservation equations **15**
  2.1.1 Stress tensor *16*
  2.1.2 Equation of state *16*
  2.1.3 Specific energy and thermodynamic relations *16*
  2.1.4 Diffusive species flux *17*
  2.1.5 Heat flux *17*
  2.1.6 Chemical source terms *17*
  2.1.7 Transport properties *18*

2.2 Large-Eddy Simulation . . . 19
2.2.1 Basic aspects of turbulence . . . 19
2.2.2 Resolution levels in turbulence simulations . . . 20
2.2.3 Filtered equations . . . 21
2.2.4 Subgrid closures . . . 22
2.2.5 Subgrid scale models . . . 23

Chapter 3: Equations for the particle phase

3.1 Lagrangian equations of motion for an isolated particle . . . 25
3.1.1 Generalized Basset-Boussinesq-Oseen equations . . . 25
3.1.2 Generalized drag force . . . 27
3.1.3 Momentum equation implemented in AVBP . . . 27
3.2 Evaporation of an isolated particle . . . 28
3.2.1 Mass transfer . . . 29
3.2.2 Heat transfer . . . 29
3.2.3 Determination of thermodynamic quantities over the integration path . . . 30
3.3 Interaction between fluid and particle phase . . . 31
3.3.1 Interphase exchange terms . . . 31
3.3.2 Interaction with turbulence . . . 33
3.4 Lagrangian Monte-Carlo approach . . . 34
3.5 Mesoscopic Eulerian approach . . . 37
3.6 Characteristic diameters of a spray . . . 40

Chapter 4: Numerics

4.1 The LES solver AVBP . . . 42
4.2 The finite volume approach . . . 42
4.2.1 Domain discretization . . . 42
4.2.2 Cell-vertex approach . . . 44
4.3 Convective schemes in AVBP . . . 45
4.3.1 The Lax-Wendroff scheme . . . 45
4.3.2 Taylor-Galerkin schemes . . . 46
4.4 Viscous and artificial diffusion operators . . . 49
4.4.1 2∆ diffusion operator (vertex-centered) . . . 49
4.4.2 Artificial viscosity . . . 50
4.5 Source terms . . . 50
4.5.1 Vertex-centered source term . . . 51

- *4.5.2 Finite-element source term* . . . *51*
- **4.6 Time advancement** . . . **51**
- **4.7 Numerics in the Lagrangian solver** . . . **52**
  - *4.7.1 Time advancement* . . . *52*
  - *4.7.2 Interpolation methods* . . . *52*
  - *4.7.3 Coupling between phases* . . . *54*
  - *4.7.4 Particle-wall interaction* . . . *54*

PART III SPRAY MODELING

Chapter 5: Liquid injection

- **5.1 Liquid disintegration mechanisms** . . . **57**
  - *5.1.1 Primary atomization* . . . *57*
  - *5.1.2 Secondary breakup* . . . *63*
  - *5.1.3 Numerical tools for the simulation of primary atomization* . . . *65*
  - *5.1.4 Reynolds Averaged Navier Stokes methods.* . . . *68*
- **5.2 The FIMUR approach** . . . **70**
  - *5.2.1 Methodolgy* . . . *71*
  - *5.2.2 Flow field inside pressure swirl atomizers* . . . *72*
  - *5.2.3 FIMUR in the Euler-Euler approach* . . . *74*
- **5.3 Particle injection in the Lagrangian solver** . . . **75**
  - *5.3.1 Numerical injection procedure in the Lagrangian solver* . . . *76*
  - *5.3.2 Reconstruction of particle size distributions* . . . *76*
  - *5.3.3 Test of the FIMUR injection procedure* . . . *77*
- **5.4 Secondary breakup model.** . . . **82**
  - *5.4.1 Bibliography* . . . *82*
  - *5.4.2 Formulation of the FAST secondary breakup model* . . . *85*
  - *5.4.3 Conclusions* . . . *89*

Chapter 6: Validation of the secondary breakup model

- **6.1 Diesel injection experiment** . . . **91**
  - *6.1.1 Experimental conditions* . . . *91*
  - *6.1.2 Numerical parameters* . . . *92*
  - *6.1.3 Results* . . . *93*
  - *6.1.4 Mesh dependency of results* . . . *102*

6.2 Simulation of a liquid jet in a turbulent gaseous crossflow 107
6.2.1 Physical mechanisms 107
6.2.2 Column model 108
6.2.3 Geometry 111
6.2.4 Computational details 112
6.2.5 Results 114
6.2.6 Conclusions 121

PART IV APPLICATION TO A COMPLEX GEOMETRY

Chapter 7: Two-phase flow simulations of the MERCATO test rig

7.1 Configuration 124
7.2 Computational mesh 125
7.3 Numerical parameters 127
7.3.1 Time scales of the gaseous flow field 129
7.4 Results for the purely gaseous flow simulations 131
7.4.1 Flow dynamics 132
7.4.2 Quality of the LES 134
7.4.3 Mean velocity profiles 140
7.4.4 Conclusion 145
7.5 Results for the two-phase flow simulations 146
7.5.1 Spray dynamics 146
7.5.2 Comparison of mean profiles 149
7.5.3 Effects of poydispersity 158
7.5.4 Impact of injection modeling 164
7.6 Comparison with the Euler-Euler approach 177
7.6.1 Numerical parameters in the Euler-Euler simulation 177
7.6.2 Comparison of flow dynamics 177
7.6.3 Comparison of statistics 178
7.6.4 Qualitative comparison of spray dynamics 180
7.6.5 Compuational cost 185
7.7 Conclusions 186

PART V TOWARDS REACTIVE LAGRANGIAN SIMULATIONS

Chapter 8: Simulations of one-dimensional saturated spray flames

8.1 Saturated two-phase flames **189**

8.1.1 Two-phase flame classifications *189*

8.1.2 Previous studies *191*

8.1.3 Preliminaries to the simulation of saturated two-phase flames. *192*

8.1.4 Verification of the two-step scheme for kerosene with preexponential constant adjustement *192*

8.1.5 Obtention of a saturated mixture *193*

8.1.6 Paramters of the study *195*

8.1.7 Numerical parameters *195*

8.2 Results **195**

8.2.1 Characteristics of two-phase flames *196*

8.2.2 Characteristic time and length scales of two-phase flames *196*

8.2.3 Discussion *198*

8.2.4 Flame thickening *215*

8.3 Conclusions **218**

General conclusions

Appendix A: Study of rounding error effects in Large-Eddy Simulations **240**

Appendix B: Implementation of a balance tool in the Lagrangian solver **243**

B.1 Implementation of basic balance tools **243**

B.1.1 Injection in a periodic cylindrical channel without evaporation *245*

B.1.2 Injection with evaporation in a gaseous crossflow. *246*

Remerciements

J'aimerais tout d'abord chaleureusement remercier les membres de mon jury de soutenance, François-Xavier Demoulin, Pascal Bruel, Gérard Lavergne, Michel Lance, Benoît Oesterlé, Thomas Lederlin et Chawki Habchi pour l'intérêt qu'ils ont manifesté pour mes travaux de thèse.

J'aimerais aussi remercier Thierry Poinsot ainsi que ma directrice de thèse, Bénédicte Cuenot, de m'avoir accueilli au sein de l'équipe CFD du Cerfacs et laissé une grande liberté de choix dans mes travaux de thèse. Je leur suis également reconnaissant pour les nombreuses discussions au cours desquelles ils m'ont fait partager leurs vastes connaissances dans le domaine de la mécanique des fluides (numérique).

À un niveau plus personnel, je suis redevable à un certain nombre de personnes qui m'ont initié à la mécanique des fluides au cours de mes études, en particulier les professeurs Wolfgang Polifke et Rainer Friedrich. Un grand merci aussi à mes divers encadrants de stage que sont Ludovic Durand, Andreas Huber et Bruno Schuermans, que j'ai la chance de pouvoir considérer comme des amis.

Côté technique, mes remerciements vont à l'ensemble de l'équipe CSG, en particulier Gérard Déjean pour son amabilité, disponibilité et efficacité dans la résolution de petits tracas informatiques. Côté administratif, j'aimerais saluer la remarquable Michèle Campassens, qui règle le moindre souci bureaucratique avec le sourire et dans les plus brefs délais. Je ne peux aussi manquer de mentionner Chantal Nasri, qui forme avec Michèle un irrésistible duo de la bonne humeur au Cerfacs. Finalement, un grand merci également à Marie Labadens pour son sa gestion des tâches administratives relatives à l'équipe CFD.

Le moment est maintenant venu de saluer tous les thésards du Cerfacs qui m'ont filé de sacrés coups de main au cours de ma thèse et permis de lâcher du lest au cours de délires variés, j'ai nommé Félix, compagnon de cyclisme, Thomas, compagnon de déprime, l'irremplaçable et inépuisable Benni, l'encyclopédie ambulante de football (et surtout d'AVBP !) Olivier Vermorel, Olivier Cabrit, constamment en vadrouille, Élé, toujours souriante et en Converse, Mr. Igor Cheval, (Yannick) Hallez le balèze, Benoît le Mac, Marta la bête de travail, Marlène la persévérante, mon conseiller en méthodes numériques atitré Nico Lamarque, Anthony Roux, interprète officiel des sagesses de Chuck Norris (facile la division par zéro...), Jean-Claude Van Damme et Steven Seagal, Matthieu Boileau et Matthieu Leyko, les deux forces tranquilles incarnées, Guilhem l'athlète à la belle crinière, Björn der Spanier im Geiste, Jorge et Camilo, l'équipe des danseurs colombiens, Matthias le numéricien serviable qui chausse du 56 1/2, Basti der entspannte Taschendieb, Papy Benoît, Simon, chroniqueur satyrique de l'actualité... un grand merci à vous tous !

Gros clin d'oeil aussi à ceux avec qui j'ai partagé le même toit durant cette thèse, notamment Thomas (les p'tits dejs' du samedi matin, les parties de PES et les délires devant les « films d'auteurs »), Benni (« E se rimassimo tutti a letto oggi ? »), Giacomo (e i suoi famosi discorsi sul sviluppo della Calabria, ma anche le partite di calcio di domenica pomeriggio) et Maite, notre fan inconditionelle du Real de Madrid ;).

Tambien aprovecho esas lineas para saludar a mis familias adoptivas mexicanas Wimber y Torres, espero que tengan el exito que se han prometido en la fabrica y que nos veamos muy pronto para echarnos un tequila. J'en profite également pour saluer l'ensemble de ma famille lannionaise, parisienne, oudonaise, rennaise, etc... Biei saluc ënghe a la familia de Gherdëina y Val Badia, a s'udëi !

Pour conclure, un gros baiser à ma petite chérie Selime, pourvu que notre belle histoire tienne la distance... Et last but not least, des remerciements tout particuliers à mes parents et à ma soeur pour leur soutien à distance ô combien crucial. C'est à eux que je dédie cette thèse.

Nomenclature

Roman letters

Symbol	Description	Units	Reference
a_p	Radius of parent particle (breakup)	m	sec. 5.97
A_a	Area of the air core	$[\mathrm{m}^2]$	sec. 5.2.2
A_p	Area of the tangential inlet ports	$[\mathrm{m}^2]$	sec. 5.2.2
$\overline{\overline{\mathcal{A}}}$	Jacobian tensor of inviscid fluxes	$[\mathrm{kg}/(\mathrm{m}^2\mathrm{s}^2)]$	eq. 4.18
B_1	Breakup constant time scale at high Weber numbers	[-]	eq. 5.122
B_2	Breakup constant time scale at low Weber numbers	[-]	eq. 5.123
c	Reaction progress variable	[-]	eq. 8.14
c_p	Specific heat capacity at constant pressure of the fluid	$[\mathrm{J}/(\mathrm{kgK})]$	sec. 2.1.3
c_v	Specific heat capacity at constant volume of the fluid	$[\mathrm{J}/(\mathrm{kgK})]$	sec. 2.1.3
C_d	Drag coefficient	[-]	sec. 3.1.2
C_D	Nozzle discharge coefficient	[-]	sec. 5.2.2
C_S	Constant of the standard Smagorinsky model	[-]	eq. 2.57
C_w	Constant of the Wale model	[-]	eq. 2.63
d_{32}	Sauter mean diameter (also abreviated SMD)	[m]	eq. 3.97
D_k	Molecular diffusivity of the species k	$[\mathrm{m}^2/\mathrm{s}]$	eq. 2.27
$\overline{\overline{D}}_{j,e}$	Residual distribution matrix of the element K_e to the node j	[-]	eq. 4.14
e_s	Specific sensible energy of the fluid phase	$[\mathrm{J}/\mathrm{kg}]$	eq. 2.10
E	Total non-chemical energy	$[\mathrm{J}/\mathrm{kg}]$	eq. 2.4
E_a	Chemical activation energy	[J]	eq. 2.1.6
f_i	Component (i) of the volumetric force vector	$[\mathrm{kg}/(\mathrm{ms}^2)]$	eq. 2.1
F	Flame thickening factor	[-]	eq. 8.31
$F_{p,i}$	Component (i) of the vector of forces acting upon a particle	$[\mathrm{kg}/(\mathrm{ms}^2)]$	eq. 3.2
$\overline{\overline{\mathcal{F}}}$	Flux tensor of conservative variables	$[\mathrm{kg}/(\mathrm{m}^2\mathrm{s}^2)]$	eq. 4.4
$\overline{\overline{\mathcal{F}^i}}$	Inviscid flux tensor of conservative variables	$[\mathrm{kg}/(\mathrm{m}^2\mathrm{s}^2)]$	eq. 4.5
$\overline{\overline{\mathcal{F}^v}}$	Viscous flux tensor of conservative variables	$[\mathrm{kg}/(\mathrm{m}^2\mathrm{s}^2)]$	eq. 4.6
g_i	Component (i) of the gravity vector	$[\mathrm{kg}/(\mathrm{ms}^2)]$	eq. 3.14
g_{ij}	Component (i,j) of the velocity gradient tensor	$[\mathrm{m}/\mathrm{s}^2]$	eq. 2.65
$G_{\bar{\Delta}}$	Filter kernel	[-]	eq. 2.35
h_s	Sensible enthalpy of the fluid/ gas phase	$[\mathrm{J}/(\mathrm{kg})]$	eq. 2.12
$h_{s,l}$	Sensible enthalpy of the liquid/ particle	$[\mathrm{J}/(\mathrm{kg})]$	eq. 3.2.2
$J_{k,i}$	Component (i) of the diffusive flux vector of the species k	$[\mathrm{kg}/(\mathrm{ms}^2)]$	eq. 2.14
k	Turbulent kinetic energy	$[\mathrm{m}^2/\mathrm{s}^2]$	eq. 2.2.2
k_1, k_2	Constants of the FAST secondary breakup model	[-]	eq. 5.122
K_{eq}	Equilibrium constant for a chemical reaction	[-]	eq. 2.20
K_f	Constant of the forward chemical reaction	[-]	eq. 2.21
K_r	Constant of the reverse chemical reaction	[-]	eq. 2.19

L_{ev}	Latent heat of evaporation	[J/(kg)]	eq. 3.26
n_d	Number of spatial dimensions	[-]	eq. 4.2.2
n_v^f	Number of vertices at the face f	[-]	eq. 4.2.2
p	Pressure	[N/m^2]	eq. 2.7
q	Momentum flux ratio (jet in crossflow)	[-]	eq. 6.3
q_i	Component (i) of the heat flux vector	[J/(m^{2}s)]	eq. 2.16
$r_p(d_p)$	Particle radius (diameter)	[m]	
R	Gas constant of a mixture (mass)	[J/(kg K)]	eq. 2.8
$\mathcal{R}$	Universal gas constant (molar)	[J/(mol K)]	sec. 2.1.2
R_0	Radius of the atomizer orifice	[m]	sec. 5.2.2
R_a	Air core radius	[m]	sec. 5.2.2
R_s	Swirl chamber radius	[m]	sec. 5.2.2
R_s^x	Main radial spray position at the axial position x	[m]	sec. 5.2.3
s	Specific entropy of the fluid phase	[J/kg]	sec. 2.1.6
$\overrightarrow{s}, s_i$	Surface normal vector/ component (i)	[m^2]	eq. 4.10
s_i^{f-p}	Component (i) of the coupling term between phases	[kg/(ms^2)]	eq. 3.3.1.b)
s_{ij}	Component (i, j) of the velocity deformation tensor	[m/s^2]	eq. 2.6
S_l	Laminar gaseous flame speed	[m/s]	eq. 8.31
t_{bu}	Characteristic breakup time scale	[s]	eq. 5.25
T	Temperature of the fluid/ gas	[K]	
$\overrightarrow{u}, u_i$	Fluid velocity vector/ component (i)	[m/s]	
$u_{p,i}$	Component (i) of the particle velocity vector	[m/s]	eq. 3.2
$V^{c,i}$	Component (i) of the correction diffusion velocity	[m/s]	eq. 2.15
$V^{k,i}$	Component (i) of the diffusion velocity of the species k	[m/s]	eq. 2.13
V_e	Volume of the primary cell of the element e	[m^3]	eq. 4.13
V_j	Volume of the dual cell of the node j	[m^3]	sec. 4.2.2
W	Molecular weight	[kg/m^3]	eq. 2.9
$x_{p,i}$	Component (i) of the particle position vector	[m]	eq. 3.1
X	Area ratio of the air core to the atomizer orifice	[-]	eq. 5.51
Y_k	Mass fraction of the species k	[-]	sec. 2.1.2
z	Mixture fraction	[-]	eq. 8.25

Greek letters

Symbol	Description	Units	Reference
α_l	Liquid volume fraction	[-]	eq. 3.70
$\delta(\cdot)$	Dirac delta function	[-]	eq. 3.58
δ_{ij}	Component (i, j) of the Kronecker delta	[-]	eq. 3.76
$\delta\breve{R}_{ij}$	Component (i, j) of the uncorrelated motion tensor	[m^2/s^2]	eq. 3.74
$\delta\theta_l$	Decorrelated energy	[m^2/s^2]	eq. 3.75
$\bar{\Delta}$	Characteristic filter width	[m]	eq. 2.35

$\Delta h^0_{f,k}$	Formation enthalpy of the species k	[J/kg]	sec. 2.1.6
η_k	Kolmogorov length scale	[m]	sec. 2.2.1
λ	Thermal conductivity of the fluid/ gas	[J/(mKs)]	eq. 2.28
μ	Dynamic viscosity	[kg/(ms)]	eq. 2.26
ν	Kinematic viscosity	[m^2/s]	eq.
ν_{bu}	Breakup frequency	[1/s]	eq. 5.116
ν'_{kj}	Stoechimoetric coefficient of the reactants for the species k in reaction j	[-]	sec. 2.1.6
ν''_{kj}	Stoechimoetric coefficient of the products for the species k in reaction j	[-]	sec. 2.1.6
ν_t	Turbulent kinematic viscosity	[m^2/s]	sec. 2.2.5
$\omega^k_{j,e}$	Distribution weight from the particle p to the node k	[-]	eq. 4.54
Ω	Computational domain	[-]	eq. 4.7
ϕ_g	Gaseous equivalence ratio	[-]	eq. 8.23
ϕ_l	Liquid equivalence ratio	[-]	eq. 8.10
ϕ_t	Total equivalence ratio	[-]	eq. 8.11
Φ^c	Particle conductive heat flux	[J/s]	eq. 3.2.2
Φ^{cv}	Particle convective heat flux	[J/s]	eq. 3.2.2
ρ	Fluid/ gas density	[kg/m^3]	sec. 2.1
ρ_k	Partial density of the species k	[kg/m^3]	sec. 2.1.2
ρ_l, ρ_p	Particle/ liquid density	[kg/m^3]	sec. 3.1.1
σ_l, σ_p	Particle/ liquid surface tension	[N/m]	sec. 5.23
τ_c	Characteristic chemical time scale	[s]	sec. 8.2.2
τ_{cv}	Characteristic convective time scale	[s]	eq. 7.3
τ_{ev}	Droplet evaporation time scale	[s]	sec. 8.2.2
τ_{ij}	Component (i, j) of the stress tensor	[N/m^2]	eq. 2.5
τ_p	Particle relaxation time scale	[s]	eq. 3.15
θ_S	Spray angle	[°]	sec. 5.2
ζ	Artificial viscosity sensor	[-]	sec. 4.4.2
$\dot{\omega}_{kj}$	Reaction rate of the species k in the reaction j	[kg/(m^{3}s)]	sec. 2.1.6
$\dot{\omega}_T$	Heat release	[J/(m^{3}s)]	sec. 2.1.6

Non-dimensional numbers

Symbol	Description	Reference
B_M	Spalding number for mass transfer	eq. 3.21
B_T	Spalding number for heat transfer	eq. 3.33
Da	Damköhler number	sec. 8.2.2
Le	Lewis number	sec. 3.2.2
Nu	Nusselt number	eq. 3.32
Oh	Ohnesorge number	eq. 5.3

Re	Reynolds number	eq. 2.29
Re_p	particle Reynolds number	eq. 3.7
St	Stokes number	eq. 3.16
Sc	Schmidt number	eq. 2.27
Sh	Sherwood number	sec. 3.2.1
We	Weber number	eq. 5.23

Subscripts

Symbol	Description
0	Plane of the atomizer orifice
0	Thermodynamic reference state
1	State in the fresh gases
2	State in the burnt gases
∞	State in the far-field
ζ	Interface between particle and fluid
cc	Interface on the saturation curve
f	Index of the fuel species
i	Translated injection plane
k	General index of the species
l	Index of the liquid phase
lam	Laminar component
p	Index of the particle phase
t	Turbulent component
v	Index of the vapor species

Superscripts

Symbol	Description
$\bar{f}$	Filtered quantity
$\tilde{f}$	Density weighted filtered quantity
$\breve{f}$	Fluid quantity undisturbed by the particle
$\breve{f}$	Mesoscopic liquid quantity in the Eulerian framework
f'	Fluctuation in the sense of filtering
f''	Fluctuation in the sense of averaging
f^i	Invscid component
f^{sgs}	Subgrid-scale contribution
f^v	Viscous component

Abreviations

Acronym	Description
DNS	Direct Numerical Simulation
EE	Euler-Euler
EL	Euler-Lagrange
LES	Large-Eddy Simulation
MERCATO	Moyen d’Étude et de Recherche en Combustion Aérobie par Techniques Optiques
NSCBC	Navier-Stokes Characteristic Boundary Condition
RANS	Reynolds Averaged Navier-Stokes
RMS	Root Mean Square
TIMECOP	Towards Innovative Methods for Combustion Prediction in aeroengines

Partie en français

Contexte de l'étude

La disponibilité de resources énergétiques peu coûteuses et en quantités abondantes a été une condition préalable de la révolution industrielle. De nos jours, la combustion de carburants fossiles fournit toujours la majeure partie de l'énergie mondiale. L'utilisation de ces resources est problématique à plusieurs titres. Tout d'abord, ces resources sont finies. Certaines estimations basées sur les resources connues et le rythme de consommation actuel prevoient un épuisement des resources petrolières dans les quarante prochaines années alors que les resources en gaz naturel semblent suffisantes pour encore au moins 60 ans [155]. De ce fait, des alternatives aux énergies fossiles sont requises sur le moyen à long terme. Par ailleurs, les énergies fossiles ont un impact majeur sur l'environnement par le réchauffement climatique et la pollution atmosphérique.

Le réchauffement climatique est lié à l'émission de gaz à effet de serre qui absorbent et émettent du rayonnement infrarouge dans l'atmosphère, contribuant à une augmentation générale du niveau de température sur la planète. Le rôle prédominant de l'activité humaine dans ce processus a été largement reconnu dans la communauté scientifique. À titre d'exemple, le comité intergouvernemental sur le réchauffement climatique constate dans son quatrième rapport [151] que « la majeure partie de l'augmentation moyenne de la température terrestre de ces cinquante dernières années est très probablement liée à l'augmentation de l'émission de gaz à effet de serre anthropogéniques ». Le dioxyde de carbone (CO_2) est le constituant majeur des gaz à effet de serre (70 %), le méthane (CH_4) et les oxydes d'azote (NO_x) représentant deux autres sources importantes avec respectivement 18 % et 8 % des émissions totales (source : Emission Database for Global Atmospheric Research). Les conséquences possibles du réchauffement sont sujettes à discussion dans la communauté scientifique. Alors que l'augmentation du niveau des océans due à la fonte des calottes polaires a été largement démontrée [27], l'augmentation de la fréquence d'évènements climatiques extrêmes (ouragans, sécheresses, etc...) ou l'extinction d'écosystèmes fragiles (la grande barrière de corail) comme conséquences possibles du réchauffement climatique sont plus controversées.

La pollution atmosphérique est liée à l'émission de substances nocives et toxiques lors de la combustion de carburants fossiles. Parmi ces polluants se trouvent :

- le monoxyde de carbone (CO), qui se lie avec l'hémoglobine du sang et réduit sa capacité de transport d'oxygène.
- les oxydes d'azote et l'ozone (NO_x, O_3), qui affectent les fonctions pulmonaires et entrainent des difficultés respiratoires.
- de fines particules telles que les suies qui se déposent dans les bronches et endommagent les poumons. Elles sont aussi à l'origine de maladies cardiovasculaires et divers cancers.

Combattre le réchauffement climatique requiert une réduction signficative des émissions de gaz à effet de serre. Bien que des alternatives potentiellement moins polluantes soient apparues pour le transport automobile (voitures électriques, piles à combustible) et la production d'électricité, (énergies renouvelables) aucune alternative aux carburants fossiles ne semble actuellement envisageable pour le transport aérien à moyen terme. Ceci est lié à deux raisons principales :

- les contraintes sur le poids des appareils requièrent l'utilisation de carburants à forte densité énergétique, ce qui exclut l'utilisation de batteries électriques ou de piles à combustible.

- des considérations de sûreté dans le maniement de la source d'énergie, sa fiabilité et des dangers potentiels lors d'accidents. Ceci exclut l'utilisation des énergies solaires ou nucléaires pour la propulsion aéronautique.

Pour ces raisons, la recherche et le développement dans le secteur aéronautique se focalisent essentiellement sur une augmentation de l'efficacité du processus de conversion énergétique. Une telle augmentation peut être obtenue par des modifications dans la conception globale de l'appareil. Par exemple, un engin aéronautique moderne repose sur un réacteur à double flux (une partie de l'air contourne le compresseur et se mélange avec les gaz d'échappement en sortie) et double corps (deux arbres de transmission séparés qui permettent une vitesse de rotation optimale des différents composants de l'appareil) pour augmenter son rendement global. D'un point de vue thermodynamique, le fonctionnement d'un engin de propulsion aéronautique peut être représenté par un cycle de Joule-Brayton idéalisé. L'efficacité thermodynamique η du cycle de Joule Brayton dépend directement du taux de compression $\beta = p_2/p_1$ atteint dans le compresseur et du rapport entre plus haute et plus basse température $\tau = T_3/T_1$ dans le cycle. La température maximale T_3 dépend directement du processus de combustion, mais son augmentation requiert la conception d'alliages métalliques capables de résister à ces hautes température sans compromettre le fonctionnement ou la durée de vie de la turbine. Toutefois, l'amélioration des propriétés thermiques de ces alliages a été relativement limitée lors des dernières décennies (2-3 K par an [49]). Refroidir les parties les plus exposées de l'engin résoud ce problème mais réduit aussi le travail fourni par l'expansion des gaz brûlés dans la turbine par une déviation par rapport à une expansion adiabatique. De manière plus générale, il apparait que la combustion est seulement un facteur parmi d'autres pour améliorer le rendement global d'une turbine. Par contre, la réduction d'émissions polluantes dépend seulement de la conception et de la meilleure compréhension du phénomène de combustion.

Vers la combustion en régime pauvre

Dans les applications aéronautiques, la réduction d'émissions polluantes porte essentiellement sur les oxydes d'azote et le monoxyde de carbone. D'une manière générale, les émissions d'oxydes d'azote (NO_{x}) augmentent avec la température [198] alors que le contraire est vrai pour le monoxyde de carbone (CO). De cette double contrainte émerge une plage de température intermédiare pour limiter l'émission de ces deux polluants. Les brûleurs pauvres prévaporisés (LPP) apparaissent comme une solution prometteuse pour faire fonctionner les turbines dans la plage de température ciblée. Cependant, ces brûleurs sont susceptibles d'engendrer des instabilités de combustion, qui résultent d'un couplage entre fluctuations du dégagement de chaleur et ondes acoustiques dans une boucle fermée. Ces instabilités peuvent entrainer des dommages importants allant jusqu'à la destruction totale de l'appareil et représentent donc des risques de sécurité considérables. De plus, le prémelange entraine des risques de retour de flamme dans le système de mélange, pouvant fortement endommager ce dernier à cause de contraintes thermiques importantes. Ces difficultés peuvent être partiellement résolues par un mélange et une évaporation incomplète du carburant et de l'oxydant en amont de la flamme, comme cela est réalisé dans les systèmes « Lean Premixed »(LP). Par ailleurs, des systèmes d'injection multipoint (MI) sont aussi examinés à titre d'alternative aux systèmes LPP. Dans les systèmes MI, une série de jets liquides est injectée perpendiculairement à l'écoulement gazeux pénétrant dans la chambre de combustion, permettant un mélange rapide et une distribution homogène de vapeur en amont du front de flamme. Dans les systèmes LP et MI, le mélange du spray liquide avec l'écoulement fluide, son évaporation et son interaction avec le front de flamme ont un impact majeur sur la dynamique de la combustion et doivent être bien compris. Cependant, les études expérimentales dans les chambres de combustion industrielles sont difficiles à cause des conditions de pression et température qui y règnent. Les méthodes non intrusives telles que les lasers permettent de s'affranchir de ces difficultés, mais leur coût reste élevé. Dans ce contexte, les études numériques représentent une alternative moins coûteuse que les études expérimentales. De plus, elles permettent l'accès à des variables qui ne sont pas mesurables expérimentalement et permettent la visualisation de champs tridimensionels complets. Pour ces raisons et de par leurs progrès constants, les outils de simulation numérique sont de plus en plus fréquemment utilisés pour la conception de chambres de combustion.

Simulation de configurations réactives complexes

La simulation numérique de foyers aéronautiques industriels présente une série de difficultés qui sont brièvement décrites ci-dessous. La modélisation de la phase gazeuse sera évoquée dans un premier temps, suivie de la modélisation de la phase particulaire.

Modélisation de la phase fluide

Turbulence

La plupart des systèmes réactifs industriels reposent sur la combustion turbulente. En effet, celle-ci permet une atomisation plus efficace du liquide injecté et favorise le mélange du spray avec le fluide. De plus, elle augmente les dégagements de chaleur spécifiques par l'interaction entre le front de flamme et la turbulence. Ainsi, la compréhension de la combustion turbulente requiert des connaissances approfondies de la turbulence. La turbulence est caracterisée par la présence de structures tourbillonaires cohérentes sur une large gamme d'échelles de longueur et de temps. La résolution de toutes ces échelles dans la simulation numérique directe (SND) d'une configuration industrielle impliquerait un coût informatique trop important et des approches simplificatrices sont nécessaires. Les méthode de type « Reynolds-Averaged Navier-Stokes » (RANS) appliquent un opérateur de moyenne statistique aux équations de conservation et modellisent les effets de toutes les échelles de la turbulence, ce qui les rend peu coûteuses en terme de resources de calcul. De plus, les effets de la turbulence non résolue sont généralement incorporés dans le terme diffusif, favorisant la stabilité numérique. Cependant, les informations sur l'évolution instationaire de l'écoulement sont perdues par le processus de moyenne et ces méthodes ne permettent pas de capturer les instabilités de combustion. De plus, les constantes des modèles sont sensibles à l'écoulement simulé et peuvent ainsi nécessiter un ajustement *ad hoc*. La simulation aux grandes échelles (SGE) est apparue comme une solution intermédiare prometteuse entre les approches RANS et SND. En SGE, les équations de conservation sont filtrées de manière à ne résoudre explicitement que les plus grandes échelles de l'écoulement alors que les effets des plus petites échelles sont modellisés. Cette approche de filtrage préserve l'information sur l'instationarité de l'écoulement et les instabilités de combustion peuvent de ce fait être simulées en SGE. Avec le développement d'architectures massivement parallèles, le coût de la SGE devient accessible à des simulations de configurations complexes [20] et même des SND de démonstration semblent envisageables [140] pour de telles configurations. Ces simulations permettront peut-être de mieux comprendre la combustion turbulente dans les géométries complexes.

Chimie et combustion

La combustion est un processus chimique complexe impliquant des centaines d'espèces intermédiaires et des milliers de réactions pour des hydrocarbures complexes. Prendre en compte toutes ces espèces et réactions dans une simulation numérique n'est pas envisageable à cause de l'énorme coût calcul engendré et des approches de modélisation moins coûteuses sont requises. Une première approche consiste à dériver des mécanismes basés sur un nombre d'espèces et de réactions réduits. Idéalement, ces mécanismes devraient être capapbles de reproduire la vitesse de propagation du front de flamme, la température adiabatique de fin de combustion, les niveaux de polluants sur une large plage de richesse et éventuellement le délai d'allumage. Une seconde approche consiste à construire une table des taux de réaction chimiques par la simulation de configurations simplifiées telles que des flammes mono-dimensionelles laminaires prémélangées ou à contre-courant avec des codes numériques reposant sur une description détaillée de la cinétique chimique et des mécanismes de tranport. Les taux de réaction des simulations simplifiées sont alors tabulés en fonction de variables caractéristiques de la combustion, typiquement la variable d'avancement de la réaction c et la fraction de mélange z. Dans de telles méthodes, la principale difficulté réside dans la réduction de la taille des tables tout en maintenant une bonne précision dans la description de la cinétique chimique.

Dans les applications de la combustion turbulente, le front de flamme interagit fortement avec les structures tourbillonaires de l'écoulement qui plissent la flamme ou entrainent des extinctions localisées. Puisque le front de flamme est trop mince pour être explicitement résolu dans les simulations numériques, la majorité de l'interaction flamme-turbulence doit être modellisée. Dans l'approche G-equation, le front de flamme est vu comme une surface infiniment mince résolue par une approche numérique de suivi d'interface de type Level Set. Le front de flamme est identifié par une iso-surface d'un champ scalaire et son évolution décrite par une équation de convection scalaire avec un terme supplémentaire prenant en compte la propagation du front de flamme turbulent [154, 158]. Dans les approches de type densité de surface de flamme, les équations de conservation d'une variable de progrès (une variable avec une variation monotone à travers le front de flamme) est filtrée. La propagation du front de flamme est alors représentée par l'évolution de la surface du front de flamme filtré et la vitesse de flamme laminaire [83]. En supposant une interface nette entre gaz frais et gaz brûlés, les approches G-equation et densité de surface de flamme ne sont *a priori* applicables que dans un contexte de combustion parfaitement prémélangée.

Cependant, des flammes de diffusion peuvent également être rencontrées dans les application industrielles. Les flammes de diffusion turbulentes sont contrôlées par les temps caractéristiques du mélange moléculaire et turbulent car ceux-ci sont généralement bien plus importants que ceux de la chimie. Pour cette raison, la plupart des modèles de combustion turbulente non prémélangée utilisent une description statistique du mélange local basée sur un scalaire passif z (un scalaire sans terme source dans son équation de transport) et une fonction de densité de probabilité. Les différents modèles se distinguent par le degré de simplification concernant le terme source chimique (chimie infiniment rapide ou non) et l'évaluation de la fonction de densité de probabilité, en supposant sa forme ou en résolvant des équations supplémentaires pour ses premiers moments [98, 35]. Finalement, le modèle de flamme épaissie prend un point de vue opposé à l'approche G-equation puisqu'il épaissit artificiellement le front de flamme afin de permettre sa résolution explicite sur la grille de calcul. L'incovénient de ce modèle est qu'il entraine une modification de l'interaction flamme turbulence qui doit être prise en compte par un terme correctif [33].

Acoustique

Pour prédire le développement d'instabilités thermo-acoustiques, la propagation des ondes acoustiques doit être explicitement prise en compte dans les simulations numériques. Puisque ces ondes ont un contenu énergétique faible par rapport à l'écoulement hydrodynamique moyen, elles doivent être résolues à l'aide d'un schéma numérique précis afin de limiter les effets de dissipation numérique. De plus, le schéma numérique employé devrait idéalement préserver la phase des ondes acoustiques puisque les instabilités de combustion ne peuvent se développer que si fluctuations de dégagement de chaleur et de pression sont en phase (critère de Rayleigh [171]). La conception de tels schémas numériques sur des maillages non structurés est assez difficile, mais l'utilisation de tels maillages s'avère nécessaire pour permettre la discrétisation de géométries complexes en des temps humains raisonnables. De plus, des conditions numériques adéquates doivent être imposées sur les bords du domaine de calcul tronqué. Ces conditions numériques doivent être conçues pour imposer les quantités physiques souhaitées de manière consistante sans altérer la simulation numérique par des oscillations ou des réflexions purement numériques [70, 159]. La reproduction précise des réflexions acoustiques est primordiale car l'augmentation de l'énergie acoustique du système peut être compensée ou annihilée par les flux acoustiques aux limites du domaine.

Dynamique de la phase dispersée

En dépit des difficultés de modélisation de la combustion turbulente en géométrie complexe décrits ci-dessus, des études menées au Cerfacs ont démontré la capacité de son outil numérique AVBP à prédire des niveaux de polluants [198] ainsi que l'apparition d'instabilités thermo-acoustiques [201, 185]. Cependant, ces études supposaient un carburant à l'état gazeux, négligeant ainsi tous les aspects liés à l'atomisation du liquide en un spray dilué, le mélange de ce spray avec l'écoulement gazeux, son évaporation ainsi que son interaction avec le front de flamme. Inclure ces effets dans les simulations engendre de nouvelles difficultés de modélisation qui sont brièvement décrites ci-dessous.

Atomisation

Dans les chambres de combustion aéronautiques, le carburant est généralement injecté par des atomiseurs pressurisés swirlés sous forme d'une fine nappe liquide. Après injection, des instabilités se développent à l'interface gaz-liquide et engendrent l'apparition d'ondes longitudinales et transverses à la surface de la nappe. L'amplitude de ces ondes augmente rapidement, conduisant à la pulvérisation de la nappe. Les étapes entre la déformation initiale du liquide et l'apparition des premiers fragments liquides sont regroupées sous la désignation d'atomisation primaire. Différents régimes d'atomisation primaire peuvent être distingués selon le type d'instabilité régissant la pulvérisation de la nappe liquide.

La simulation numérique de l'atomisation primaire requiert la résolution explicite des équations de Navier-Stokes pour les deux phases. De plus, celles-ci doivent être couplées par des conditions de saut à l'interface pour prendre en compte les échanges de masse, de quantité de mouvement et d'énergie. De plus, la position et l'évolution de l'interface doivent être décrits avec précision pour permettre l'évaluation fidèle des forces capillaires. Ceci peut être réalisé avec des méthodes de type « Volume of Fluid » (VOF) ou « Level Set » [74]. De manière analogue à la turbulence, l'atomisation primaire est régie par une large gamme d'échelles spatiales et temporelles. Leur résolution dans une simulation numérique directe demande des resources de calcul très importantes et des approches simplificatrices sont requises. Ceci a conduit au développement d'approches RANS pour la modélisation de l'atomisation primaire [14].

Les ligaments liquides issus de l'atomisation primaire se désintègrent en fragments/ particules plus petites sous l'action de forces aérodynamiques exercées sur ces dernières ou par des mécanismes d'instabilités individuels. Ce processus est nommé atomisation secondaire. Il existe divers régimes d'atomisation secondaire caractérisés par le nombre de Weber, qui représente un rapport entre les forces aérodynamiques déstabilisatrices et la tension de surface stabilisatrice s'exerçant sur la goutte.

En plus de la prise en compte de la désintegration des ligaments liquides, d'autres difficultés de modélisation apparaissent dans la zone d'atomisation secondaire. La première est liée à la forte déformation des particules avant leur rupture. Ces déformations modifient fortement les propriétés de trainée de ces particules et les lois de trainées usuelles décrivant le mouvement de particules sphériques isolées ne sont plus valables. Par ailleurs, la probabilité de collision/ coalescence est importante de par la nature dense du spray. En termes numériques, cette zone est généralement traitée avec les mêmes outils que ceux utlisés pour la modélisation de sprays dilués, avec des modifications appropriées de la loi de trainée et une prise en compte de l'atomisation secondaire ainsi que des phénomènes de collision/ coalescence [148, 174].

Régime dilué

Une fois que les mécanismes d'atomisation primaire et secondaire sont achevés, le spray atteint un état dilué. Ceci implique que le volume occupé localement par les particules est faible par rapport à celui du fluide compte tenu de la différence de densité entre les phases fluide et particulaire. Si la taille des particules est petite devant les échelles caractéristiques de l'écoulement fluide, elles peuvent être traitées comme des inclusions ponctuelles sans une résolution explicite de l'écoulement à leur surface. Puisque l'interface entre particules et fluide n'est plus explicitement résolue, des lois décrivant leur interaction sont nécessaires. Deux cadres de modélisation majeurs sont à distinguer pour la description des sprays dilués dispersés.

Les méthodes Eulériennes traitent les deux phases comme des milieux continus et ne considèrent que des quantités moyennées de la phase particulaire. L'information sur les trajectoires individuelles des particules n'est pas prise en compte et les propriétés du spray sont moyennées au sens volumique ou d'ensemble [232]. Les propriétés caractéristiques du spray sont décrites par une fonction de densité de probabilité (pdf) et obtenues par la résolution d'une équation issue de la cinétique des gaz [229]. À ce stade, il peut être choisi de résoudre des équations de transport pour les premiers moments de la pdf, comme cela est fait pour le formalisme Eulérien implémenté dans AVBP [97, 180]. Les méthodes de quadrature de moments proposent un approche différente puisqu'elles discrétisent la pdf par une somme de fonctions Dirac et résolvent une équation de transport pour chaque Dirac [40]. La polydispersion peut être reproduite en discrétisant l'espace du diamètre des particules par sections [79, 109]. Dans ce cas, le système d'équation de transport Eulérien doit ensuite être résolu pour chaque section caractérisant une classe de diamètre différente.

Contrairement à l'approche Eulérienne, l'approche Lagrangienne suit l'évolution de particles individuelles dans leur propre référentiel. Les particules sont traitées comme des inclusions locales et leurs trajectoires sont évaluées par un bilan de force sur chaque inclusion. Comme les positions des particules ne coincident pas nécessairement avec le maillage, une interpolation précise des propriétés fluides à la position de la particule est requise. Cette interpolation ne pose aucune difficulté théorique si toutes les échelles de l'écoulement fluide sont explicitement résolues. Toutefois, ceci n'est pas le cas dans le cadre d'approches RANS ou SGE qui ne résolvent respectivement que l'écoulement fluide moyen ou filtré alors que l'évaluation des forces agissant sur la particule requiert une connaissance du champ fluide instantané total. De ce fait, les effets du champ fluide non résolu sont reconstruits par des considérations statistiques. Ceci conduit à des approches Lagrangiennes statistiques/ Monte Carlo [44]. Dans les applications pratiques de SGE Lagrangiennes, les effets des échelles non résolues sont souvent négligés [3, 180].

Il n'y a certainement pas de jugement arrêté à donner quant à la superiorité de l'approche Lagrangienne ou Eulérienne en général, chacune d'elles disposant d'avantages spécifiques pouvant être déterminants pour une application considérée. Le coût des méthodes Eulériennes est indépendant du nombre de particules simulé. Par ailleurs, le traitement des deux phases d'un point de vue Eulérien est également avantageux dans les zones denses ou liquides. De plus, le traitement du couplage entre phases est simple puisque toutes deux sont résolues sur le même maillage. Par contre, le coût d'une méthode Eulérienne peut devenir important lors de la prise en compte de la polydispersion puisque les équations de transport doivent être résolues pour chaque classe de taille séparément. Par ailleurs, le système d'équation caractérisant la phase particulaire ressemble à celui d'un fluide fortement compressible et doit être résolu avec des schémas numériques appropriés. D'un autre côté, l'approche Lagrangienne semble moins coûteuse dans les zones diluées [180, 202]. Cet avantage en terme de coût peut cependant être perdu pour des simulations massivement parallèles si un équilibrage dynamique de la charge n'est pas garanti pour chaque processeur. Ceci est lié au fait que la phase particulaire est généralement présente sur quelques processeurs seulement. Par ailleurs, la localisation des particules sur un maillage non-structuré est un point numérique délicat qui doit être implémenté de manière efficace.
En terme de phénomènes physiques, l'interaction particule paroi et l'atomisation secondaire sont plus faciles à modéliser dans un contexte Lagrangien et contrairement à une approche Eulérienne, la polydispersion est directement prise en compte puisque l'on procède à un suivi individuel des particules. La prédiction de croisement de trajectoires dans le contexte Eulérien nécessite un traitement spécifique puisque deux vitesses distinctes doivent être définies à une même position de l'espace (méthodes multi-fluides). Les limitations physiques de l'approche Lagrangienne concernent principalement le couplage entre phases. La supposition sous-jacente de l'approximation point force [133] est que les particules sont petites devant la taille caractéristique de maille. De ce fait, les erreurs associées au couplage entre phase peuvent croître avec le raffinement du maillage et une grille plus grossière peut éventuellement fournir une meilleure description de la phase particulaire [168]. Finalement, la convergence statistique de l'approche Lagrangienne est lente, ce qui peut engendrer des coûts de calcul important. Plus précisément, il peut être démontré par le théorème central limite que pour un nombre de particules N_p suffisamment grand, la convergence de l'errreur statistique sur la variance d'une propriété particulaire est proportionelle à $N_p^{-1/2}$ [163]. La table 1 donne un aperçu de certains avantanges et inconvénients avérés des deux approches.

Combustion diphasique

La combustion dans les écoulements diphasiques se distingue fortement de la combustion purement monophasique. Ceci est dû au fait que les caractéristiques du front de flamme dépendent fortement de la quantité de

Euler-Lagrange	Euler-Euler
Avantages	
Prise en compte directe de la polydispersion Implémentation simple de mécanismes physiques (interaction particule paroi) Bonne robustesse numérique	Adapté pour la description de zones denses Coût numérique indépendant de la densité de particules Couplage simple avec la phase fluide Parallélisation identique au solveur fluide
Inconvénients	
Dépendance en maillage du couplage entre phases Répartition de charge inefficace en calcul parallèle Localisation des particules sur le maillage non structuré	Schémas numériques spécifiques requis (forts gradients) Description de croisement de trajectoires Prise en compte de la polydispersion coûteuse

Table 1 : *Énumération d'avantages et d'inconvénients identifiés des approches Eulériennes et Lagrangiennes pour la description de la phase particulaire*

carburant évaporé en amont du front de flamme. Même si l'évaporation est complètement achevée en amont du front de flamme, le caractère ponctuel des particules peut conduire à des inhomogénéités spatiales de vapeur de carburant et des fluctuations du front de flamme. Si l'évaporation des particules et la zone de réaction se chevauchent, différents modes de combustion peuvent apparaître. Réveillon et Vervisch [176] donnent une description synthétique de ces modes en enrichissant des résultats préalables de la littérature [28] par des données issues de leurs simulations numériques directes. Les auteurs classent la structure des flammes diphasiques par le nombre caractéristique sans dimension G. G représente le ratio du taux d'évaporation de la particule au taux de diffusion de chaleur à l'intérieur du nuage de particules. Quand les effets convectifs sont larges comparés aux effets de diffusion (nombre de Péclet élevé), G peut être approximé par :

$$G \approx \frac{5N_p^{2/3}}{S} \tag{1}$$

N_p représente le nombre de particules dans le nuage et S le paramètre de séparation moyen defini par :

$$S = \frac{\delta_s}{\delta_{r_f}} \tag{2}$$

avec δ_s la distance moyenne inter-particules et δ_{r_f} un rayon caractéristique de flamme de diffusion. Pour de grandes valeurs de G, le spray est trop dense pour permettre une diffusion de chaleur significative en son intérieur. Ainsi, le front de flamme englobe le nuage de particules et brûle en régime de diffusion. Cette structure de flamme est dénommée combustion en eveloppe externe. Pour un spray très dilué, la distance entre particules est grande, ce qui entraine une évaporation importante des particules par diffusion de gaz brûlés. Dans ce cas, un front de flamme enveloppe chaque particule et ce régime de combustion est appelé combustion individuelle de particules. Des régimes de combustion diphasique intermédiaires existent entre ces deux extrêmes.

La combustion diphasique se déroule généralement en régime partiellement prémélangé ou de diffusion. Les théories utilisées pour les flammes non prémélangées gazeuses ne peuvent pas être directement transposées à la combustion de sprays car l'évaporation des particules rend impossible la définition d'une équation de transport de scalaire passif.

Objectifs des travaux et plan de la thèse

Développements antérieurs et contexte

Le solveur non structuré hybride AVBP a été développé conjointement entre le CERFACS et l'IFP (Institut Français du Pétrole) au cours des 15 dernières années. Le code AVBP a été conçu pour des applications massivement parallèles et il a demontré son excellente scalablité sur un grand nombre de processeurs à de maintes reprises [211]. Pour la composante diphasique, un module Eulérien basé sur l'approche théorique de Février et al. [54] a été implémenté par Kaufmann [97]. Pascaud a démontré la capacité du solveur Euler-Euler à simuler la combustion diphasique dans des applications indutrielles. Riber [179] a étendu le formalisme de Février et al. [54] à la SGE dans AVBP. Boileau [20] a présenté la SGE de la séquence d'allumage d'une chambre de combustion complète basée sur une approche Euler-Euler. Plus récemment, García [63] a développé un module Lagrangien dans AVBP et démontré sa compétitivité en termes de coût informatique et de précision par rapport à une approche Euler-Euler sur des configurations académiques telles qu'une turbulence homogène isotrope chargée en particules ou un écoulement avec obstacle chargé en particules. Jaegle [93] a implémenté un modèle d'évaporation dans le solveur Lagrangien identique à celui disponible dans le solveur Eulérien. De plus, il a réalisé la SGE d'un écoulement diphasique évaporant dans un brûleur aéronautique complexe avec étagement de carburant en utilisant les approches Euler-Euler et Euler-Lagrange. Ses résultats ont révélé une précision similaire des deux méthodes, avec un avantage non négligeable en terme de coût calcul pour la méthode Lagrangienne.

Objectifs et plan de thèse

L'objectif de la présente thèse est de développer des outils numériques qui permettront la simulation future d'écoulements réactifs diphasiques complexes avec une approche Euler-Lagrange. Cette thèse a été financée par l'Union Européenne dans le cadre du projet ECCOMET (« Efficient and Clean COmbustion Experts Training ») dans un effort de meilleure compréhension de la combustion diphasique. La simulation de systèmes réactifs requiert une représentation adéquate de la dynamique du spray en amont du front de flamme. Cependant, une représentation précise du mécanisme de désintégration du spray semble hors de portée des présents travaux. De ce fait, des modèles d'injection simplifiés sont développés et appliqués à la simulation d'une géométrie plus complexe représentative de configurations industrielles. La motivation de la présente étude est double en terme de modélisation de l'injection. Premièrement, le développement d'un modèle d'injection simplifié reproduisant de conditions d'injection similaires pour les approches Euler-Euler et Euler-Lagrange est entrepris. Ensuite, une part de complexité physique est ajoutée à la partie Lagrangienne du modèle d'injection en la combinant à un modèle d'atomisation secondaire. Les développements entrepris en terme de modélisation de l'injection sont ensuite appliqués à la simulation d'un brûleur aéronautique expérimental utilisant un système d'injection représentatif d'une configuration indutrielle. L'impact de conditions d'injection simplifiées sur la dynamique du spray est étudiée. Dans ce cadre, les effets de la poydispersion du spray sont également examinés. Par ailleurs, une comparaison entre les méthodes Euler-Euler et Euler-Lagrange pour cette configuration est effectuée. Pour conclure, la simulation de flammes mondimensionelles diphasiques avec le solveur Euler-Lagrange, première étape vers la simulation d'écoulements réactifs plus complexes, est étudiée.

Le manuscrit est organisé comme suit :

- La seconde partie décrit les équations pour les phases fluide et particulaire ainsi que les méthodes numériques du solveur employé. Dans le chapitre 2, les équations décrivant l'évolution d'un fluide compressible réactif interagissant avec une phase particulaire dispersée sont présentées. Puis, le concept de Simulation aux Grandes Échelles (SGE) est décrit et les équations de Navier-Stokes filtrées sont dérivées. Dans le chapitre 3, les équations de la phase particulaire sont présentées dans un contexte Lagrangien. Dans un premier temps, les forces agissant sur une particule isolée sont traitées. Ensuite, les équations décrivant l'évaporation d'une particule isolée seront présentées. Les termes de couplage entre phases sont abordés avec une insistance particulière sur l'approximation point-force. Pour conclure, les approches

Lagrangiennes stochastiques et méscoscopiques Eulériennes sont brièvement décrites. Dans le chapitre 4, les méthodes numériques du code de Simulation aux Grandes Échelles AVBP utilisé dans la présente étude sont brièvement passées en revue.

- La troisième partie est dédiée à la description de la modélisation de l'injection liquide. Le chapitre 5 débute avec une présentation d'aspects théoriques sur l'atomisation primaire de jets liquides de nappes liquides. Ensuite, les régimes fondamentaux d'atomisation secondaire sont décrits. Finalement, les outils numériques permettant la simulation de l'atomisation primaire sont présentés. De par la complextié de ces outils, leur implémentation n'a pas été considérée dans la présente étude. Au lieu de cela, un modèle d'injection simplifié pour des atomiseurs de type pressurisés swirlés est décrit dans un premier temps. Ce modèle néglige les effets de l'atomisation sur la dynamique du spray et injecte directement le spray développé à l'orifice de l'atomiseur. La caractéristique principale de ce modèle est la reproduction de conditions d'injection similaires pour des approches Eulériennes et Largangiennes. Pour partiellement prendre en compte les phénomènes de pulvérisation liquide dans le solveur Lagrangien, un modèle d'atomisation secondaire de la litérature est implémenté dans un second temps. Dans le chapitre 6, deux cas d'application du modèle d'atomisation secondaire sont présentés. Le premier cas reproduit l'injection d'un jet liquide dans un cylindre fermé à différentes pressions gazeuses. Le second cas reproduit l'injection d'un jet liquide perpendiculairement à un écoulement gazeux. Les simulations s'appuient sur les travaux antérieurs de Jaegle [93] sur cette configuration, qui a développé un modèle prenant en compte la présence d'une colonne liquide mais négligeant les effets de l'atomisation secondaire. L'impact de la prise en compte de l'atomisation secondaire dans cette configuration est ainsi directement étudié par comparaison avec des résultats expérimentaux et ceux de Jaegle [93].
- Dans la quatrième partie, le modèle d'injection développé est appliqué à la simulation d'une géométrie plus complexe. La configuration cible est un brûleur aéronautique swirlé installé sur le banc expérimental MERCATO (Moyen d'Étude et de Recherche en Combustion Aérobie par Techniques Optiques) de l'ONERA (Office national d'études et de recherches aérospatiales). Dans un premier temps, l'écoulement purement gazeux de cette géometrie est validé par comparaison avec l'expérience. La qualité de la SGE de cette configuration est caractérisée par comparaison de simulations à deux résolutions de maillage différentes. Dans un second temps, trois simulations diphasiques Euler-Lagrange de la géométrie MERCATO sont comparées : des simulations monophasique et polydisperse reposant sur un modèle d'injection simplifié ainsi qu'une simulation polydisperse utilisant le modèle d'atomisation secondaire implémenté. De plus, une comparaison des présents résultats avec ceux obtenus par Sanjosé [191] dans des simulations Euler-Euler utilisant des conditions d'injection similaires est effectuée.
- Dans une cinquième partie, les simulations de flammes saturées laminaires mono-dimensionelles sont présentées. Ces simulations représentent une première étape vers la simulation de systèmes réactifs diphasiques avec le solveur Euler-Lagrange. Une étude paramétrique permet de caractériser les effets de variation de richesse et de diamètre de particules sur des flammes saturées diphasiques. L'interaction entre dégagement de chaleur, évaporation de particules et combustion est examinée plus en détail. De plus, des comparaisons qualitatives avec des résultats de la littérature sont données. La simulation de ces flammes mono-dimensionelles permet aussi de valider l'extension du modèle de flamme épaissie à la combustion diphasique avec une approche Euler-Lagrange.
- Le premier appendice se présente sous forme d'un article rédigé durant cette thèse mais dont le sujet n'est pas en rapport direct avec les objectifs de la thèse. L'article s'intéresse à une question d'intérêt pratique pour la Simulation aux Grandes Échelles : est-il raisonnable d'obtenir des champs instantanés différents pour des Simulation aux Grandes Échelles avec paramètres physiques et informatiques identiques ? Le second appendice décrit les outils de bilans de masse pour les particules et l'espèce évaporante implémentés dans le solveur Euler-Lagrange. Ces outils sont utilisés pour vérifier le couplage correct entre phases dans les simulations diphasiques Euler-Lagrange.

Conclusions générales

La présente étude s'est consacrée à la simulation d'écoulements diphasiques dans une géometrie réprésentative d'une configuration industrielle avec une méthode Euler-Lagrange. Après une présentation du contexte général de l'étude, les équations des phases fluide et particulaire ont été présentées. Les méthodes numériques du code de Simulation aux Grandes Échelles AVBP, qui a servi aux calculs de cette étude, ont ensuite été résumées.

Dans une seconde partie, des développements concernant la modélisation de l'injection liquide ont été décrits. L'implémentation d'une méthode de suivi d'interface pour une reproduction fidèle du processus de pulvérisation liquide était hors de portée des présents travaux et a donc été écartée. Ainsi, un modèle d'injection simplifié pour des atomiseurs de type pressurisés swirlés, développé conjointement avec Sanjosé [191], a été dérivé. Ce modèle néglige le processus d'atomisation et injecte directement le spray développé à l'orifice de l'atomiseur. La granulométrie du spray est un paramètre d'entrée du modèle alors que les profils de vitesse liquides sont obtenus par des considérations sur l'écoulement à l'intérieur de l'atomiseur. Les paramètres manquants du modèle sont obtenus à partir de corrélations empiriques de la litérature. Puisqu'un des objectifs de l'étude portait sur une comparaison entre approches Eulériennes et Lagrangiennes pour la simulation de la phase dispersée dans une géométrie complexe, une attention particulière a été apportée au développement d'un modèle d'injection unifié pour les deux approches. Alors que l'injection du spray développé à la position de l'orifice de l'atomiseur ne pose aucune difficulté numérique dans le cadre d'une approche Euler-Lagrange, l'approche Eulérienne doit artificiellement décaler sa condition d'injection vers des zones suffisamment diluées du spray pour mailler la surface d'injection avec un coût numérique raisonnable. Cette translation a nécessité la dérivation de méthodes analytiques pour caractériser l'évolution du spray entre la position de l'orifice de l'atomiseur et la condition d'injection translatée. La résolution analytique des équations d'évolution du spray impose des contraintes supplémentaires sur les profils d'injection à la position de l'orifice de l'atomiseur. Cependant, la validation de l'injection numérique dans le solveur Euler-Lagrange a démontré que ces modifications avaient un impact limité sur les profils de vitesse du spray en aval. Des comparaisons directes entre les approches Eulériennes et Lagrangiennes sur des cas simplifiés (atmosphère au repos) n'ont maheureusement pas pu être menés à cause de la raideur numérique des profils engendrés, mais des validations supplémentaires sont actuellement en cours.

Dans un second temps, cette méthode d'injection a été combinée à une description simplifiée du processus de désintegration liquide par l'implémentation d'un modèle d'atomisation secondaire. Le choix s'est porté sur le modèle d'atomisation secondaire « Fast Atomization STochastic »(FAST) [73], qui tend naturellement vers de larges distributions de taille particulaires, comparé à d'autres modèles prédisant une taille de particule unique pour chaque atomisation. Le modèle repose sur l'hypothèse fondamentale que le nombre de particules générées par le processus d'atomisation secondaire ne dépend pas de la taille de la particule mère. Sous cette hypothèse, l'évolution de la distribution de taille du spray est décrite par une fonction lognormale. Pour fermer ce modèle, la moyenne et l'écart type de la distribution de taille après atomisation doivent être déterminés. Le modèle contient une constante pour chacune de ces quantités.

Pour valider l'implémentation du modèle d'atomisation secondaire FAST, deux cas tests différents ont été simulés. Le premier cas test reproduisait l'atomisation d'un spray dans un cylindre fermé à différentes pressions gazeuses représentatives de moteurs Diesel. Les résultats obtenus ont mis en évidence une forte dépendance en maillage de la longueur de pénétration et de l'angle du spray. Cette forte sensibilité au maillage semble résulter d'une différente distribution spatiale des termes de couplage entre phases et de différentes erreurs d'interpolation des propriétés gazeuses à la position de la particule. Ces effets conduisent à une plus forte accélération de la phase gazeuse et en conséquence des longueurs de pénétration plus importantes avec des angles de spray réduits. En dépit de ces limitations, un accord raisonnable avec l'expérience et des simulations antérieures utilisant le modèle FAST sur une grille de calcul de résolution identique [6] a été observé.

Le second cas test reproduisait l'injection d'un jet liquide perpendiculairement à un écoulement gazeux turbulent. Un modèle numérique prenant en compte la présence de la colonne liquide avait été développé au préalable par Jaegle [93] et a été couplé au modèle d'atomisation secondaire FAST dans les présents travaux.

Les résultats obtenus ont ensuite été comparés à des données expérimentales et des résultats obtenus par Jaegle [93], qui a négligé les effets de l'atomisation secondaire. Alors qu'aucune amélioration significative n'a été observée pour les profils de flux volumique, les profils spatiaux de diamètres moyens de Sauter étaient en bien meilleur accord avec l'expérience avec prise en compte de l'atomisation secondaire, en particulier pour des débits liquides réduits. La cause de cette amélioration réside probablement dans la description plus adéquate des propriétés du spray dans la zone d'atomisation secondaire, notamment en terme de trainée par la prise en compte de la désintegration sucessive de grandes particules inertielles. Pour cette configuration, une distribution de taille particulaire de type lognormale permettait une reproduction satisfaisante de la distribution particulaire expérimentale. Cependant, ces résultats n'ont pu être obtenus qu'après un réajustement des constantes du modèle d'atomisation, dont les valeurs variaient sensiblement entre les deux cas de validation.

Deux conclusions majeures sont à tirer de ces résultats. Premièrement, la prise en compte de l'atomisation secondaire peut conduire à une nette amélioration des distributions spatiales de diamètre du spray, comme cela a été observé dans le cas du jet liquide injecté perpendiculairement à un écoulement gazeux. Ce cas a également montré que ces améliorations n'étaient pas forcément restreintes à la zone proche injection. Deuxièmement, le modèle d'atomisation secondaire n'est pas prédictif en terme de distribution de taille du spray dilué. De ce fait, les relations définissant la moyenne et la variance de la distribution de taille particulaire après atomisation doivent être modifiées. Ceci peut nécessiter une distinction entre différents régimes d'atomisation, notamment les distributions de taille bimodales résultant de l'atomisation secondaire à nombre de Weber élevé, composées de quelques grands et nombreux petits fragments liquides. Dans le présent modèle, une telle distribution peut seulement être obtenue en supposant le diamètre moyen de la distribution de taille après atomisation proche du diamètre de la particule mère. Ceci est lié au fait qu'aucune limitation sur le nombre de particules filles n'est faite dans le modèle actuel. La limitation du nombre de particules filles constituerait une modification aisée du modèle et permettrait de reproduire une distribution de taille à caractère bimodal par conservation de la masse. Cependant, cette modification ajouterait un paramètre supplémentaire dans le modèle et une justification physique pour fixer ce dernier semble difficile. Par ailleurs, une telle limitation du nombre de particules filles pourrait fortement influencer la distribution de taille finale, conduisant à une éventuelle déviation d'une distribution lognormale. La non prise en compte de phenomènes de coalescence et d'effets de déformation de gouttes avant l'atomisation secondaire constituent d'autres limitations importantes de la présente modélisation. Ces deux mécanismes pourraient conduire à une augmentation globale de la taille des particules du spray développé : la coalescence par la fusion de particules et les effets de déformation par une vitesse relative entre phases réduite. Cependant, la prise en compte de la coalescence pourrait s'avérer numériquement coûteuse alors que la prise en compte d'effets de déformation reposerait sur des corrélations empiriques sujettes à des incertitudes importantes. Finalement, une autre limitation d'un modèle d'atomisation secondaire réside dans la détermination de l'échelle de temps caractérique d'atomisation. Bien qu'il existe un large consensus sur sa définition, celle-ci contient une constante dont les valeurs varient sensiblement entre les différents modèles [148, 29, 174]. De par ces nombreuses incertitudes et la grande sensibilité de simulations Lagrangiennes à la résolution en maillage pour des sprays denses, il n'est pas certain qu'un modèle d'atomisation secondaire puisse être prédictif en terme de distribution de taille du spray développé.

Dans la troisème partie, les développements entrepris en terme d'injection liquide ont été appliqués à la simulation d'un brûleur aéronautique swirlé, installé sur le banc expérimental MERCATO.

Dans un premier temps, l'écoulement purement gazeux dans cette configuration a été validé. Deux résolutions de maillage différentes ont été étudiées et un très bon accord des profils de vitesse moyens et fluctuants avec l'expérience a été observé pour les deux résolutions. L'amélioration des profils fluctuants de vitesse avec la résolution était modérée compte tenu de l'importante augmentation du coût de calcul. Ces résultats indiquent que les méthodes numériques implémentées dans le code de calcul AVBP sont bien adaptées à la simulation de l'écoulement gazeux dans ce type de configuration.

Dans un second temps, trois simulations Euler-Lagrange de l'écoulement diphasique évaporant dans la chambre MERCATO ont été considérées : une simulation monodisperse, une simulation polydisperse avec injection simplifiée et une simulation utilisant le modèle d'atomisation secondaire présenté dans le chapitre précédent. Les effets de polydispersion étaient limités sur les profils moyens et fluctuants de vitesses de particules. Cette observation a été confirmée par des profils moyens de vitesse particulaire conditionnés par la taille, qui ne montraient qu'un faible impact du diamètre de particule sur les amplitudes de vitesse, excepté en region proche injecteur. Dans cette zone, l'injection directe du spray polydisperse conduisait à une surestimation importante de l'accélération des petites particules alors que la prise en compte de l'atomisation secondaire améliorait considérablement l'accord avec l'expérience. Cependant, cette amélioration proche injecteur n'entrainait pas de différences significatives entre les deux simulations plus en aval, notamment dans les second et troisième plans de mesure expérimentaux. Cet effet est probablement lié à une mise à l'équilibre de la phase particulaire, hypothèse qui semble confirmée par des histogrammes taille-vitesse relativement plats plus en aval de l'injection. Cependant, les histogrammes de taille de particules montraient des distributions locales fortement polydisperses. De plus, la comparaison d'histogrammes de taille des simulations polydisperses et avec atomisation avec l'expérience indiquaient une nette amélioration de résultats pour la simulation avec atomisation en zone proche injection. Cependant, un réajustement des constantes du modèle d'atomisation secondaire s'est avéré nécessaire pour reproduire fidèlement la distribution de taille particulaire expérimentale, confirmant que des développements supplémentaires de ce modèle étaient requis.

Pour conclure, une brève comparaison de simulations monodisperses Euler-Euler et Euler-Lagrange a été effectuée. Celle-ci a révélé un bon accord entre les approches Eulériennes et Lagrangiennes pour des profils de vitesses particulaires moyennes et fluctuantes. Une comparaison qualitative basée sur des trajectoires Lagrangiennes et des lignes de courant instantanées Eulériennes a mis en évidence un comportement global similaire des deux approches en terme de dynamique et d'évaporation. De plus, des taux d'évaporation globaux des deux approches pris aux mêmes instants étaient très proches, confirmant le comportement similaire de leur modèle d'évaporation commun. La configuration MERCATO s'est montrée particulièrement adaptée à une approche Lagrangienne puisque son coût de calcul était sensiblement plus faible que celui d'une approche Eulérienne. La conclusion principale à tirer de cette comparaison est que les deux méthodes donnent des résultats de précision comparable pour l'écoulement diphasique évaporant dans la configuration MERCATO. De par la forte accélération des particules en zone proche injecteur, l'impact du modèle d'injection sur les profils de vitesse proche injecteur demeure incertain. En particulier, le bon accord des simulations Euler-Euler et Euler-Lagrange avec l'expérience en proximité de l'atomiseur ne peut pas être considéré comme une validation de l'approche FIMUR. Concernant les perspectives des comparaisons entre approches Eulériennes et Lagrangiennes, l'extension du solveur Euler-Euler pour permettre le traitement d'écoulements polydisperses par une approche de classes est actuellement en cours [226]. Ces développements permettront une comparaison future entre des simulations Lagrangiennes et Eulériennes polydisperses.

Concernant le modèle d'injection, sa surestimation de l'accélération de petites particules en zone proche injection requiert son amélioration. Une voie de développement possible consisterait dans la prise en compte explicite de la présence d'une nappe liquide à l'orifice de l'atomiseur par une loi de trainée modifié, comme cela a été fait pour le jet liquide injecté dans un écoulement gazeux transverse. Dans sa formulation la plus simple, cette modification nécessiterait seulement un coefficient de trainée modifiée pour la nappe et un temps caractéristique de rupture. Cette modification n'impliquerait aucun changement pour l'approche Lagrangienne puisque le coefficient de trainée serait directement appliqué dans le code. Pour l'approche Eulérienne, la prise en compte de la nappe liquide nécessiterait une modification de la dérivation des profils de vitesse liquides dans le plan d'injection translaté. Plus précisement, les lois de conservation intégrales devraient être décomposées en deux contributions : une pour la nappe et une autre pour le spray développé. Cependant, il ne semble pas qu'une telle modification entraine des changements significatifs de la méthode. En particulier, aucune des hypothèses du présent modèle ne sera invalidée par une telle extension. Cependant, une limitation de l'approche FIMUR réside dans la translation de la condition limite d'injection dans l'approche Eulérienne, ce qui entraine une modification de la géométrie. Ceci pourrait éventuellement conduire à une perturbation de l'écoulement gazeux dans la zone proche injecteur, rendant une comparison entre approches Eulérienne et Lagrangienne délicate.

Les différents niveaux de simplification de l'injection ont conduit à un changement significatif de la distribution spatiale du spray en zone proche injecteur. Cet effet résultait de la forte interaction du spray avec le « precessing vortex core » (PVC). En conséquence, un fort impact de particules sur les parois du diffuseur était observé pour les simulations injectant directement le spray développé au niveau de l'orifice d'atomisation. Au contraire, l'impact de spray sur les parois était mineur pour la simulation avec atomisation du fait de la présence de particules plus inertielles dans la zone proche injecteur. Ceci a conduit à des distributions spatiales du spray qui différaient considérablement entre les simulations avec injection simplifiée et avec atomisation. Malheureusement, aucune donnée expérimentale permettant de caractériser la distribution spatiale du spray n'était disponible et aucune conclusion claire n'a ainsi pu être tirée sur les prédictions de cette distribution par les différents modèles d'injection. Si l'impact de liquide sur les parois du diffuseur se révèle confirmée par l'expérience, une amélioration de la modélisation de l'interaction particules paroi sera requise. Au contraire, la reconstruction de contributions de sous-maille pour l'évaluation des équations particulaires ne semble pas être critique pour le présent type d'application qui considère surtout la reproduction d'effets de grande échelle tels l'interaction du spray avec le PVC, les effets de tri balistique des particules selon leur taille et la distribution spatiale du spray. Il est à noter cependant que cette affirmation pourrait ne plus être valable dans un cas réactif.

En terme de méthodes numériques, la mauvaise scalabilité du solveur Lagrangien liée à l'absence d'une répartition dynamique de charge est actuellement une limitation importante qui devra être considérée dans le futur. De plus, les operateurs d'interpolation des propriétés gazeuses à la position de la particule ne sont que du premier ordre. Cet aspect constitue actuellement la plus grande limitation de l'approche Lagrangienne en terme de précision. Les erreurs induites par l'avancement en temps à l'ordre un semblent moins critiques de par les faibles pas de temps du solveur gazeux, limité par une condition de type CFL acoustique. Finalement, il est à noter que l'utilisation d'outils de bilans particulaires dans la configuration MERCATO a révélé des pertes de particules. Ces pertes étaient seulement mineures en nombre et n'ont pas influencé les résultats. Ces pertes semblent résulter d'une mauvaise définition de vecteurs normaux de paroi pour certaines cellules de paroi, mais ce point reste à clarifier.

Dans une quatrième partie, des simulations numériques de flammes saturées mono-dimensionelles ont été effectuées en tant que première étape vers la simulation de systèmes diphasiques réactifs plus complexes. Les flammes ont été simulées pour trois diamètres particulaires différents et sur une large plage de richesses. La chimie a été modellisée par un schéma cinétique à deux étapes pour le kérosène combiné à un ajustement de constante préexponentielle [57], permettant une reproduction fidèle de la vitesse de flamme laminaire en régime riche. Pour de faibles diamètres particulaires, le carburant liquide était totalement évaporé en amont du front de flamme, ce qui a conduit à une structure et une vitesse de flamme semblables à ceux d'une flamme purement gazeuse. La quantité de vapeur de carburant évaporée en amont du front de flamme décroissait avec le diamètre et les flammes diphasiques résultantes brûlaient à des richesses gazeuses bien inférieures à la richesse totale du spray. En conséquence, la propagation de fronts de flamme diphasiques a pu être observée pour des richesses totales supérieures à la limite d'extinction riche d'une flamme gazeuse. Concernant la structure de flamme, une évolution d'une combustion prémélangée vers une combustion partiellement prémélangée/ en diffusion a été observée. Par ailleurs, une forte influence de la présence de particules a été observée sur l'équilibre des fractions massique CO-CO_2 pour des mélanges riches. De ce fait, la température adiabatique de flamme variait considérablement avec le diamètre particulaire à richesse totale constante.

Même si les simulations de flammes saturées monodimensionelles réalisées ont permis de retrouver des comportements qualitatifs de la litérature, une validation quantitative est nécessaire pour étudier l'impact des simplifications faites sur la cinétique chimique et les propriétés de transport simplifiées. Des Simulations Numériques Directes de flammes de spray à contre-courant [106] ou de flammes de spray swirlées [228] étudiées expérimentalement semblent de bons candidats pour une telle analyse. Une autre étude consisterait dans la comparaison de flammes monodimensionelles saturées entre le code de calcul AVBP et un code dédié reposant sur une description détaillée de la chimie et des propriétés de transport complexes. Une telle comparaison permettrait de quantifier plus précisément les erreurs résultant d'une telle approche simplificatrice (cinétique chimique réduite, nombre de Schmidt égaux, description simplifiée des coefficients de diffusion) sur les propriétés globales de la flamme telles que sa vitesse, température adiabatique et équilibre CO-CO_2.

Dans un second temps, le modèle de flamme épaissie a été étendu à la simulation de flammes diphasiques épaissies dans le cadre d'une approche Euler-Lagrange. Les résultats obtenus ont permis de valider l'extension de ce modèle et montré que la façon juste de procéder consistait à diviser les termes de trainée et d'évaporation des particules par le facteur d'épaissement. Cependant une division du terme de trainée semble problématique puisqu'elle implique une modification de la dynamique du spray. Pour cette raison, l'impact de la division du terme de trainée par l'épaississement a brièvement été évalué. Des erreurs sur la vitesse de flamme augmentant avec le facteur d'épaississement ont été observées. Ces erreurs n'étaient pas beaucoup plus faibles que celles résultant d'une absence totale de traitement sur la phase particulaire (pas de division du terme de trainée ni de celui de l'évaporation). Ainsi, une simple non prise en compte de la division du terme de trainée par le facteur d'épaississement dans l'extension du modèle de flamme épaissie aux flammes diphasiques ne semble pas représenter une solution satisfaisante. De ce fait, l'impact de la division du terme de trainée par le facteur d'épaississement sur la dynamique du spray doit être examinée plus en détail. La simulation numérique directe d'une flamme diphasique saturée dans une turbulence homogène isotrope semble être une bonne configuration cible pour effecter une telle analyse.

Si l'on considère l'application du modèle de flamme épaissie à la simulation aux grandes échelles de flammes diphasiques turbulentes, des points supplémentaires sont à clarifier. Premièrement, l'impact du plissement de flamme non résolu sur le taux d'évaporation doit être quantifié. De plus, il n'est pas certain que des modes de combustion de groupe, où le front de flamme englobe un nuage de particules, ne soient pas présents aux échelles de sous-maille. Si c'était le cas, ces régimes de combustion devraient être pris en compte dans le modèle de combustion. Par ailleurs, les effets de concentration préférentielle aux échelles de sous-maille pourraient nécessiter une prise en compte de leur impact sur les taux d'évaporation locaux et des inhomogénéités de vapeur de carburant [175]. Ces questions pourraient également être étudiées par des Simulations Numériques Directes d'une flamme diphasique saturée dans une turbulence homogène isotrope, qui apparait comme une configuration préliminaire importante avant le passage à des configurations plus complexes.

Part I

The industrial context

Chapter 1

General introduction

1.1 Combustion of fossil fuels

1.1.1 Environmental context

The availability of abundant and inexpensive energy from fossil fuels, especially coal, was one prerogative for the industrial revolution. Still today, combustion of fossil fuels provides the major part of the world's energy, be it for transportation, power generation or heating. As an illustrative example, fig. 1.1 displays the world shares in primary energy consumption in 2007. The use of these energy sources is problematic for several reasons. First, these resources are finite. From the world's proved oil resources and at the present consumption rate, the depletion of oil resources may occur in the next 40 years while gas resources seem sufficient for another 60 years [155]. Thus, alternatives to fossil fuels are required on the mid- to long-term. More importantly, fossil fuels have a major environmental impact through global warming and air pollution.

Global warming is linked to the emission of greenhouse gases which absorb and emit infrared light in the atmosphere, leading to a general increase in earth's temperature. The predominant role of human activity in global warming over the last decades has been largely recognized. For instance, the Intergovernmental Panel on Climate Change (IPCC) states in its fourth report [151] that "most of the observed increase in globally averaged temperatures since the mid-20th century is very likely due to the observed increase in anthropogenic greenhouse gas concentrations". Carbon dioxide (CO_2) constitutes more than 70 % of the world's total greenhouse gas emissions, methane (CH_4) and nitric oxides (NO_x) being the two other major sources with respectively 18 % and 8 % of total emissions (source: Emission Database for Global Atmospheric Research). The possible consequences of global warming are subject to discussion in the scientific community. While the rise of sea-levels due to melting ice caps has been largely admitted [27], the increase in the frequency of extreme wheather events (hurricanes, droughts, etc...) or the complete extinction of fragile ecosystems (the great coral reef) as possible consequences of global warming are more controversed [47, 100].

Another environmental impact of fossil fuel combustion is air pollution, related to the emission of nocive and toxic substances. Found among these air pollutants are [194]:

- carbon monoxide (CO), which binds with hemoglobin in the human blood and reduces the oxygen carrying capacity of the blood.
- nitrogen oxides and ozone (NO_x, O_3), which affect the lung functions and lead to respiratory difficulties.
- fine particles such as soot which deposit in the bronchies and damage the lungs. They are also at the origin of cardiovascular diseases and several sorts of cancer.

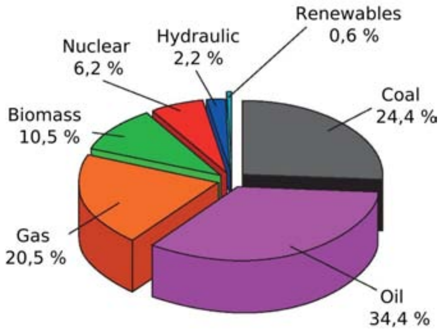

Figure 1.1 : *Shares in world primary energy consumption in 2007 (Source: Keyworld Energy Statistics)*

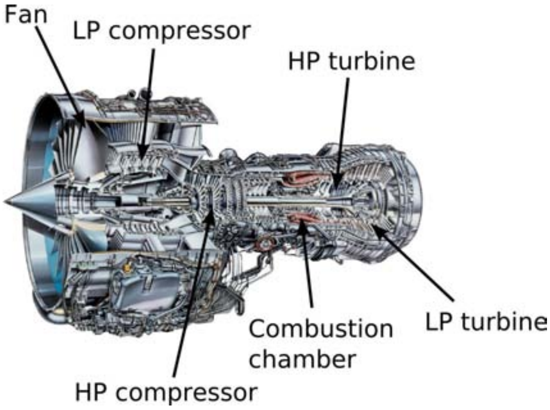

Figure 1.2 : *Midplane cut through a modern aircraft engine (V 2500). The air enters through the ducted fan. Part of the air then enters into the engine core through the LP compressor while the remaining air bypasses the engine core and mixes with the exhaust gases from the nozzle (high bypass turbofan engine). The LP compressor / LP turbine and the HP compressor / HP turbine are mounted on different shafts to allow a rotation at their optimal speeds (twin-spool concept)*

Fighting global warming requires a significant reduction in greenhouse gas emissions. While potentially less emissive alternatives to fossil fuels have recently emerged in the autombile industry (electric cars, fuel cells) and for power generation (renewable energy sources), no viable alternatives have appeared for aircraft transportation at this day and will probably not appear in the mid-term. This has two main reasons:

- the constraints on system weights require the use of media with high volumetric energy densities. This excludes the use of electric batteries or fuel cells.
- security considerations in the handling of the energy source, its reliability and security hazards in the aftermaths of crashes. This excludes the use of solar or nuclear energy for aircraft propulsion.

Thus, the reduction of greenhouse gas emissions focuses on the efficiency increase of the energy conversion process in aeronautic gas turbines. This increase may be achieved by changes in the overall design of the system. For instance, fig. 1.2 displays the layout of a modern aircraft engine, which uses a high bypass turbofan engine (part of the air bypasses the compressor and mixes with exhaust gases from the nozzle) and a twin-spool concept (two separate mechanical shafts to allow for the rotation of the engine parts at their optimal speeds) to improve its efficiency. From a thermodynamic point of view, the operation of aircraft propulsion systems may be represented by the idealized Joule-Brayton process, which is sketched in fig. 1.3.

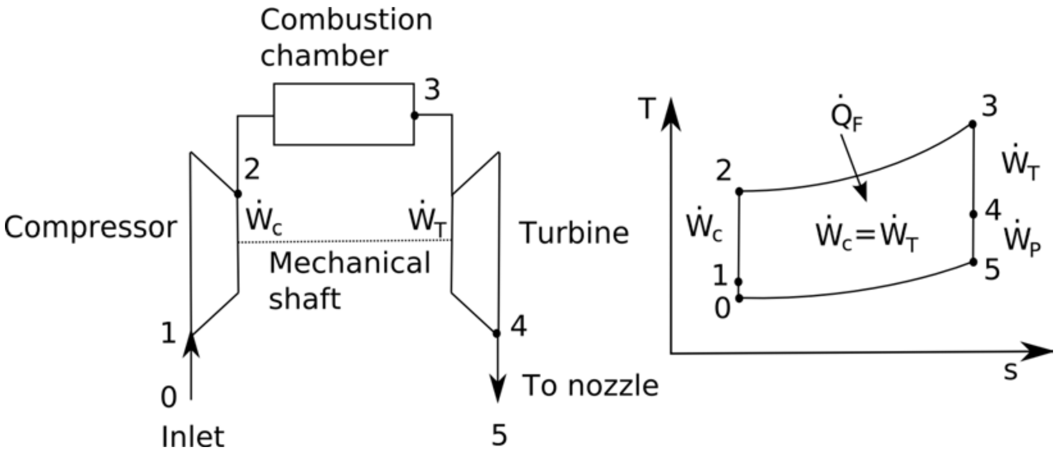

Figure 1.3 : *Schematic of a simplified jet engine operation (left) and the associated idealized Joule-Brayton cycle (right).* $\dot{Q}_F$ *is the heat generated by combustion,* $\dot{W}_C$ *the work applied in the compressor,* $\dot{W}_T$ *the work generated in the turbine to run the compressor. The excess work* $\dot{W}_P$ *is available for engine thrust*

The thermodynamic efficiency η of the Joule-Brayton cycle is directly dependent on the compression ratio $\beta = p_2/p_1$ achieved in the compressor and on the ratio between highest and lowest temperatures $\tau = T_3/T_1$ resulting in the thermodynamical cycle. The maximum temperature T_3 is dictated by the combustion process, but its increase requires the design of specific metallic alloys capable of withstanding high temperatures without affecting the operation of the engine or its lifetime. However, improvements in the thermal properties of such alloys have been relatively limited over the last decades (2-3 K per year [49]). Cooling the hottest engine parts solves this problem but also reduces the work generated by the expansion of hot gases in the turbine because due to the departure from an adiabatic expansion. More generally, it appears that combustion is only one factor among many to help increase the global engine efficiency. On the contrary, the reduction of pollutant emissions depends only on the design and the deeper understanding of the combustion process.

1.1.2 Towards lean combustion in aeronautic engines

In aeronautic applications, the reduction of pollutant emissions mainly focuses on nitric oxides and carbon monoxides. Globally, it can be said that the emissions of nitric oxides (NO_x) increase with temperature [198]. The contrary is true for carbon monoxide (CO), whose concentration decreases at lower temperatures. From both constraints, an optimal mid-temperature range for the combustion process emerges which allows to limit the emissions of both pollutants. Lean Premixed Prevaporized (LPP) combustors appear as a promising technology to run engines in this temperature range. In LPP systems, the fuel is injected far upstream the flame front to allow for a complete evaporation and mixing of the fuel with the air flow upstream the flame. However, it turns out that such designs are very prone to combustion instabilities, which arise from the unstable coupling between unsteady heat release and acoustic waves in a closed loop. They may cause severe mechanical damage or even destruction of the engine and therefore represent very high safety risks. Furthermore, premixing increases the risk of flame flashback into the premixing system, with a risk of failure of parts of the combustor due to severe thermal stresses. These problems may be partly solved by achieving only incomplete evaporation upstream the flame front, as done in Lean Premixed (LP) systems. Multipoint injection (MI) systems are also investigated as an alternative to LPP systems. In MI systems, a series of liquid jets is injected perpendicularly to the airflow entering the combustion chamber, resulting in a quick mixing and a homogeneous vapor distribution upstream the flame front. In LP and MI systems, the mixing of the liquid spray with the air flow, the spray evaporation and its interaction with the flame front have an important impact on combustion dynamics and must be well understood.

In realistic reacting systems, experimental studies are rather difficult to obtain because of the severe pressure and temperature conditions in combustion chambers. Non intrusive measurement techniques such as lasers avoid these difficulties but remain expensive. Numerical studies offer a less costly alternative. Furthermore, they allow access to variables which are not measurable in experiments and provide visualizations of complete three-dimensional flow fields. For these reasons and because of their continuous improvement, numerical simulation tools are increasingly used in the design of modern combustion chambers.

1.2 Numerical simulation of realistic combustion systems

The numerical simulation of realistic combustion systems poses several challenges, which are briefly enumerated in the following. Modeling aspects for the gaseous phase are described in a first part, followed by the modeling aspects of the dispersed phase.

1.2.1 Modeling of the gaseous phase

1.2.1.a) Turbulence

Most industrial combustion devices rely on turbulent combustion as the latter favors the atomization process of the injected liquid fuel, enhances mixing between liquid and gas, promotes evaporation and greatly increases the specific heat releases. Therefore, a detailed knowledge of turbulence is a preliminary to the understanding of turbulent combustion. Turbulence is characterized by the presence of coherent vortical structures in a large spectrum of length and time scales [165]. Explicitly resolving all these scales in a Direct Numerical Simulation (DNS) of an industrial scale configuration involves huge computational costs and simplifying approaches need to be found. Reynolds-averaged Navier-Stokes methods (RANS) perform a statistical average of the governing equation system and model the effects of all turbulence scales, which makes them computationally cheap. Furthermore, the effects of turbulence on flow field dynamics are incorporated through a diffusive term which favors numerical stability. However, information on the unsteady evolution of the flow field is lost through the averaging process and RANS methods do for instance not allow to capture combustion instabilities. In addition, the model constants of RANS models display high sensitivity to the simulated geometry and may require *ad-hoc* adjustment. Large-Eddy Simulation (LES) appears as a promising intermediate approach between DNS and RANS. In LES, the flow field equations are filtered so that the smallest scales of turbulence are modelled while the largest and most energy containing scales are explicitly resolved. This filtering procedure preserves information on the unsteadiness of the flow field and combustion instabilities may be simulated in LES. With the constant increase in computational power through the development of massively parallel architectures, the cost of LES becomes affordable for realistic geometries [20] and even DNS demonstration simulations appear feasible [140]. Such demonstration simulations will possibly help to better understand turbulent combustion phenomena in realistic geometries.

1.2.1.b) Chemistry and combustion

Combustion is a chemical process involving hundreds of intermediate species and thousands of chemical reactions for complex hydrocarbons. Accounting for all these species in a numerical simulation through a detailed chemistry is not viable because of the high computational expense and less costly methods are necessary. A first approach consists in deriving chemical mechanisms based on a reduced number of species and reactions [52, 57]. Ideally, the simplified mechanisms should reproduce the flame propagation speed, the adiabatic flame temperature, pollutant levels over a large range of equivalence ratios and possibly the ignition delay. A second approach consists in the building of chemistry tables from the numerical simulation of simplified configurations such as laminar one-dimensional flames using detailed chemistry and transport descriptions [130, 68]. The reaction rates of the simplified simulation are then tabulated over the characteristic variables transported in the full simulation. In such methods, the main challenges lie in the reduction of table sizes while keeping an accurate description of the flame characteristics.

In turbulent combustion applications, the flame front strongly interacts with the vortical structures of the flow field which wrinkle the flame front or trigger local extinctions. Since the flame front is too thin to be explicitly resolved in numerical simulations, most of the interaction between the flame front and turbulence needs to be modeled. In the G-equation approach, the flame front is viewed as an infinitely thin propagating surface. The evolution of the flame front is then described by a convection equation with an additional term accounting for the turbulent flame front propagation [154, 158]. In flame surface density approaches, the conservation equations of a progress variable, i.e. a variable displaying a monotonic variation across the flame front, is filtered. The propagation of the flame front is then modelled through the evaluation of the filtered flame surface and the laminar flame speed [83]. Both G-equation and flame surface density approaches are only suited for premixed combustion. Turbulent diffusion flames are controlled by the molecular and turbulent mixing timescales as these are much larger than the chemical timescale. Therefore, most nonpremixed combustion models use a statistical description of the local mixture based on a passive scalar (a scalar without source terms in its transport equation) and a probability density function approach. The different models are distinguished by the degree of simplification on the chemical source term (infinitely fast chemistry or finite rate chemistry) and the evaluation of the probability density function, by either assuming its shape or solving additional transport equations for its first moments [98, 35]. Finally, the thickened flame model [161] takes an opposite point of view to the G-equation formalism as it artificially thickens the flame front to allow its explicit resolution on the numerical grid. The drawbacks of this method are a modification of the flame turbulence interaction which needs to be corrected through a modeling term [33].

1.2.1.c) Acoustics

In order to predict the occurence of thermo-acoustic instabilities, acoustic waves need to be explicitly resolved in numerical simulations. Acoustic waves have a very low energy content compared to the mean hydrodynamic flow field. Therefore, their simulation requires high-order accurate numerical schemes in order to limit numerical dissipation effects. Furthermore, the employed numerical scheme should also preserve the correct phase of the acoustic waves as combustion instabilities only arise if heat release and pressure fluctuations are in phase (so called Rayleigh-criterion [171]). The design of such high-order schemes is especially difficult on unstructured compuational meshes, which are however necessary for the numerical discretization of realistic combustor geometries. Furthermore, adequate conditions need to be specified at the boundaries of the truncated computational domain. These numerical boundary conditions must be designed so as to impose the desired physical quantities in a consistent manner while not altering the numerical simulation through noise or spurious reflections [70, 159]. Correctly handling acoustic reflections at these boundaries is particularly important as the increase in the acoustic energy of the system may be compensated or annihilated by fluxes over the boundaries.

1.2.2 Modeling of the dispersed phase

Despite the mentioned difficulties in the modeling of turbulent combustion, numerical studies performed at CERFACS have demonstrated the ability of its LES solver AVBP to reproduce pollutant levels [198] and the occurence of combustion instabilities in realistic configurations [201, 185]. However, these studies assumed the fuel to be in gaseous form and neglected all aspects related to the atomization of the liquid into a dilute spray, the mixing of the spray with the gaseous flow field as well as its evaporation and interaction with the flame front. Including these aspects in numerical simulations rises additional modeling difficulties which are summarized in the following.

1.2.2.a) Atomization

In aircarft engines, the fuel is generally injected by means of pressure swirl atomizers. In the latter, the liquid leaves the atomizer orifice as a thin conical sheet. Following injection, instabilities are triggered on the liquid-gas interface and cause the formation of waves on the liquid sheet's surface [45]. The amplitude of these waves quickly grows, resulting in the sheet disintegration. The steps covering the deformation of the liquid until the formation of the first isolated liquid fragments are called primary atomization or primary breakup. Different primary atomization regimes may be distinguished depending on the predominance of the instability mechanism dictating liquid disintegration. Fig. 1.4 from Lozano et al. [127] provides an illustration of two different disintegration regimes of liquid sheets. The numerical resolution of primary atomization requires the explicit resolution of the Navier-Stokes equations for both phases and the coupling between them through jump relations at the interface in order to account for the exchanges of mass, momentum and energy. In addition, the motion and the location of the phase interface need to be described with high accuracy for the evaluation of capillary forces. This may be done with Volume of Fluid (VOF) or Level-Set approaches [74]. Similarly to turbulence, primary atomization is composed of a large range of time and length scales. Their resolution in a Direct Numerical Simulation is computationally intensive and simplifying approaches need to be found. This has led to the development of RANS approaches for the modeling of primary atomization [14].

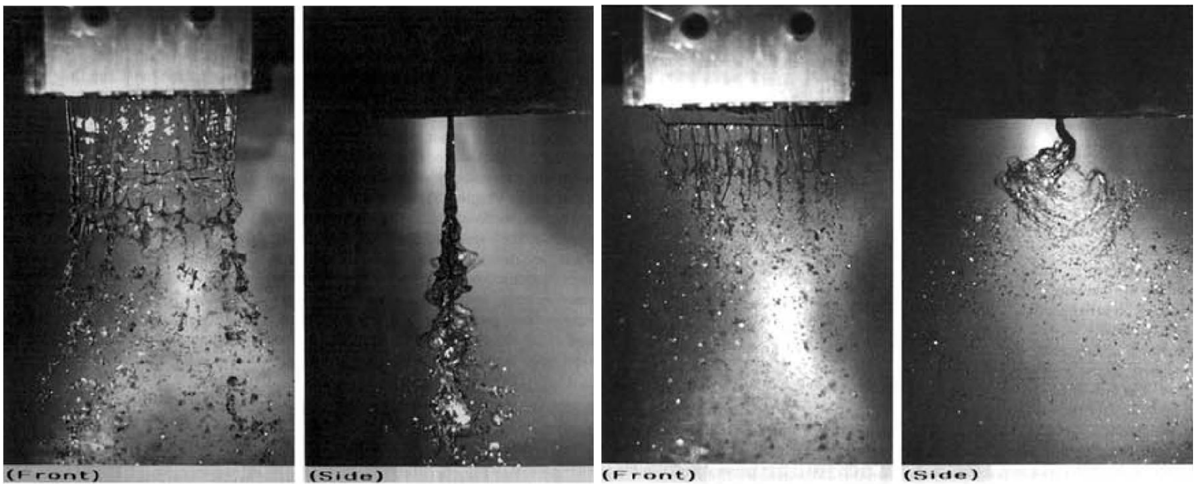

Figure 1.4 : *Different regimes of the disintegration of an air assisted liquid sheet. Left: cellular breakup regime. Right: streamwise ligament breakup regime. Images from Lozano et al. [127]*

The liquid ligaments issued from primary breakup undergo further desintegration into droplets due to aerodynamic forces exerted upon them or individual droplet/ ligament instability mechanisms. This process is called secondary breakup or secondary atomization. There exist several secondary breakup regimes; their classification is based on the Weber number, which is defined as the ratio between aerodynamic forces destabilizing the droplet and surface tension forces stabilizing the latter. Fig. 1.5 from Chou et al. [29] displays three different instants in the breakup of a glycerol droplet.

In addition to the explicit account for droplet desintegration, other modeling difficulties arise in the secondary breakup zone. First, the particles undergo strong deformations prior to breakup, which modifies their drag properties. Therefore, standard drag laws describing the motion of isolated spherical droplets become invalid in the secondary breakup zone. Second, the probability for collision/ coalescence phenomena to occur is also significant given the high spray density. In terms of numerics, the secondary breakup zone is generally modeled with the same tools that are used for the dilute spray, with appropriate modifications for drag, explicit account for secondary breakup and possibly collisions/ coalescence [148, 174].

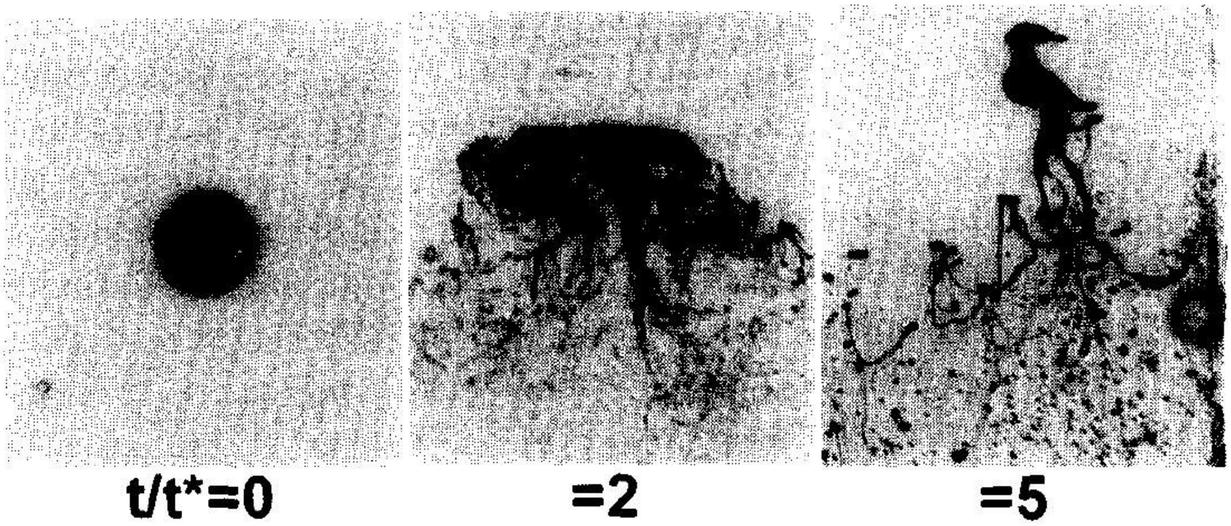

Figure 1.5 : *Flash shadowgraphs of the secondary breakup of a glycerol droplet as a function of an adimensional time* t/t^* *(*$d_p = 1000\mu m$*,* $We = 250$*). Images from Chou et al. [29]*

1.2.2.b) Dilute regime

Once the primary and secondary atomization processes are completed, the spray reaches a dilute state. This implies that the volume occupied by the droplets is small compared to the fluid phase so that they may be treated as local inclusions through the point source approximation [126]. The interpolation of the punctual forces induced by the particles on the Eulerian grid is achieved by resorting to the Particle Source in Cell (PSIC) approximation [38]. Since the interface between the droplets and the fluid is not explicitly resolved, laws for the fluid-droplet interaction such as drag and evaporation must be derived. Two main modeling frameworks exist for dilute two-phase flows.

Eulerian methods consider both phases as continuums and capture only averaged quantities of the dispersed phase. The information on the individual droplet paths is lost as spray properties are averaged in a volumetric or an ensemble sense [232]. The characteristic properties of the spray are obtained through the evolution equation of a probability density function (pdf) which fully characterizes the spray [229]. At this point, different numerical strategies may be found for the resolution of the pdf. Transport equations may be solved for the first moments of the pdf, which is done for the Eulerian formalism implemented in AVBP [97, 180]. Quadrature momentum methods discretize the probability density function by a sum of Dirac delta functions and solve a transport equation for each Dirac delta [40]. Polydispersity may be reproduced by discretizing the droplet diameter space in the Eulerian approach, leading to so called sectional methods [79, 109]. The Eulerian set of transport equations for the dispersed phase must then be solved for each section characterizing a different droplet diameter class.

Contrary to Eulerian approaches, Lagrangian approaches track the evolution of indivual droplets in their own frame of reference. Droplets are treated as local inclusions and their trajectories are evaluated from the force balance on each inclusion. As the droplet locations do not necessarily coincide with the computational mesh, properties of the fluid need to be interpolated at the droplet location with an accurate numerical algorithm. This interpolation does not pose any theoretical difficulties if all flow scales of the carrier phase are explicitly resolved, for instance in a DNS. Such Lagrangian simulations are referred to as deterministic. When the carrier phase is simulated by the means of LES or RANS approaches, only filtered or averaged properties are available for the carrier phase. However, the evaluation of the forces exerted upon the droplets requires knowledge of the total instantaneous fields of the carrier phase. Thus, the effects of the unresolved flow field scales need to be reconstructed at the droplet location through statistical considerations. This leads to stochastic / Monte-Carlo Lagrangian simulations [44]. However, the effect of the unresolved scales on droplet dynamics is neglected in many practical LES's of two-phase flows [3, 180].

There is certainly no clear judgement to be made on the superiority of Eulerian or Lagrangian methods in general as each of them has certain advantages which may become determining for a considered application.

The cost of Eulerian methods is independent of the droplet number. Furthermore, the treatment of both phases from an Eulerian point of view is advantageous in dense spray zones. However, the cost of Eulerian approaches may become substantial when accounting for polydispersity as the set of transport equations for the dispersed phase needs to be solved for each diameter class separately. Furthermore, the Eulerian equations for the dispersed phase resemble those of a strongly compressible fluid and must be solved with specific numerical schemes capable of handling strong gradients.

The Lagrangian approach seems computationally cheaper in dilute zones [180, 202]. However, the lower computational cost of the Lagrangian approach may be mitigated in parallel simulations if no particular effort on load balancing is made since the spray is generally only present on a few processors. In addition, the localization of droplets on unstructured meshes (which are mandatory for the discretization of complex geometries) is a bottleneck in terms of computational performance and must be implemented efficiently. In terms of physical models, droplet-wall interactions and secondary breakup are more straightforward to handle in the Lagrangian framework and contrary to the Eulerian approach, polydispersity is directly accounted for as individual droplets are tracked. The prediction of crossing trajectories in the Eulerian context requires specific treatment as two distinct spray velocities need to be defined at the same location (multi-velocity methods). Physical limitations of the Lagrangian approach concern the coupling between phases. The underlying assumption of the point source approximation is that the droplets are small compared to the computational grid. Therefore, errors associated with the coupling between phases increase for finer grid resolutions and a larger grid may actually yield more accurate results [168]. Finally, the convergence of statistics in the Lagrangian framework is relatively slow, which may result in large computational expenses. In particular, it may be shown from central limit theorem that for a sufficiently large particle sample number N_p, the root mean square statistical error of a particular quantity tends to zero as $N_p^{-1/2}$ [163]. Table 1.1 provides an overview of certain respective advantages of both numerical approaches.

Euler-Lagrange	Euler-Euler
Advantages	
Inherent description of polydispersity	Well suited for description of dense zones
Easier implementation of physical mechanisms	Numerical cost independent of droplet number
(droplet-wall interaction, secondary breakup)	Straightforward coupling between phases
Good numerical robustness	Parallelization identical to gas solver
Disadvantages	
Grid dependent coupling terms	Specific numerical schemes required
Unefficient load balancing	(strong gradients)
Particle localization on unstructured grids	Description of crossing trajectories
Statistical convergence	Representation of polydispersity numerically costly

Table 1.1 : *Summary of identified advantages and drawbacks of Euler-Lagrange and Euler-Euler approaches*

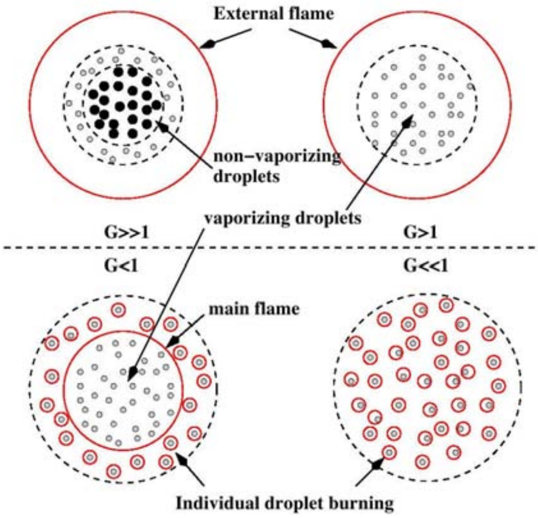

Figure 1.6 : *Classification of different spray combustion regimes from Réveillon and Vervisch [176] based on former previous studies of Chiu et al. [28]*

1.2.2.c) Two-phase combustion

Combustion in two-phase flows presents marked differences to its single phase counterpart. This is because the flame characteristics are strongly influenced by the quantity of fuel evaporated by the droplets before reaching the flame front. Even if droplets are completely evaporated before reaching the flame front, their pointwise nature may induce inhomogeneities of the fuel vapor field and induce flame front fluctuations. If the droplet evaporation and combustion zones overlap, different combustion modes appear. Réveillon and Vervisch [176] give a synthetic description of spray flame structures based on both previous studies [28] and results from their own Direct Numerical Simulations. They classify the different flame structures with the characteristic dimensionless number G. G represents the ratio of the droplet evaporation rate and the diffusion rate of hot gases within the droplet cloud. When convective effects are large compared to diffusive effects (large Péclet number), G may be approximated as:

$$G \approx \frac{5N_p^{2/3}}{S} \tag{1.1}$$

N_p represents the number of droplets in the cloud and S a mean droplet spacing parameter:

$$S = \frac{\delta_f}{\delta_{r_f}} \tag{1.2}$$

with δ_f and δ_{r_f} respectively the average distance between droplets and a characteristic diffusion flame radius. For large values of G, the spray is too dense to allow for notable heat diffusion inside the cloud. Thus, the flame front is located around the droplet cloud and burns in a diffusion regime. This flame structure is referred to as external sheath combustion. For very dilute sprays, the distance between droplets is large and leads to high evaporation rates of the droplets through diffusion of hot gases. In that case, a flame front is located around each single droplet and this combustion regime is called single droplet combustion. Additional intermediate regimes are found between these extrema. Fig. 1.6 from Réveillon and Vervisch [176] provides an illustration of the different spray combustion regimes.

Two-phase combustion generally occurs in partially premixed or diffusion regimes. Theories used for non-premixed gaseous flames may not directly be applied to spray combustion since a transport equation for a passive scalar (a quantity without source term in its evolution equation) may no longer be defined due to droplet evaporation.

1.3 Objectives of the present work

1.3.1 Previous developments

The unstructured hybrid LES solver AVBP has been jointly developped by CERFACS and IFP (Institut Français du Pétrole) over the last 15 years. From the very beginnings, the AVBP code was designed for massively parallel applications and it has repeatedly demonstrated excellent scalability up to a very large number of processors [211]. Kaufmann [97] implemented an Eulerian module for the dispersed phase in AVBP based on the theoretical approach proposed by Février et al. [54]. Pascaud [152] demonstrated the ability of the Euler-Euler solver to reproduce two-phase combustion in a realistic configuration. Riber [179] extended the formulation of Février et al. [54] to handle LES's of the dispersed phase. Boileau [20] presented the LES of an ignition sequence of a full helicotper combustion chamber based on the Euler-Euler approach. More recently, García [63] implemented a Lagrangian module in the AVBP solver. García demonstrated the competitiveness of the Euler-Lagrange solver compared to the Euler-Euler solver in both accuracy and computational cost on canonic test cases such as the DNS of a homogeneous isotropic turbulence (HIT) and for the LES of a bluff-body configuration both laden with particles. Jaegle [93] extended the Lagrangian solver to handle evaporation and implemented the same evaporation model as in the Eulerian solver. Furthermore, he performed the LES of the evaporating two-phase flow in a complex combustor with fuel staging. Both Euler-Euler and Euler-Lagrange simulations of the configuration were performed and results revealed similar accuracies for both methods, with an advantage in terms of computational cost for the Lagrangian solver.

1.3.2 Plan of the thesis

The aim of the present thesis is to develop numerical tools that will allow for future simulations of reactive flows using the Euler-Lagrange approach. It was financed by the European Union in the framework of the ECCOMET project ('Efficient and Clean COMbustion Experts Training') in an effort to increase the understanding of two-phase combustion. The simulation of reacting two-phase flows requires a good representation of the spray dynamics upstream the flame front. However, the numerical simulation of the spray disintegration mechanisms leading to the formation of the dilute spray were considered out of reach for the present work. Therefore, the aim of the present work is to develop simplified injection models which allow to correctly reproduce spray dynamics in realistic configurations such as aeronautical combustors. The motivation of the present study is twofold in terms of injection modeling. First, it is attempted to develop an injection model which reproduces similar injection conditions for Euler-Euler and Euler-Lagrange approaches. Then, complexity is added to the injection model in order to assess the impact of the simplifications on spray dynamics in a more realistic configuration. The developments in terms of injection modeling are then applied to the simulation of an aeronautical combustor. Besides examining the impact of injection modeling on spray dynamics, effects of polydispersity are also investigated. Furthermore, a comparison between Euler-Euler and Euler-Lagrange simulations of such configurations is made.

The manuscript is organized as follows:

- The second part describes the governing equations for the carrier and dispersed phases as well as the numerical methods of the AVBP solver used in the present study. In chapter 2, the governing equations for a compressible fluid laden with particles and with chemical reactions are presented. Then, the concept of Large-Eddy Simulation is presented and the filtered governing equations are derived. The modeling of unclosed terms is discussed. In chapter 3, the description of the dispersed phase in a Lagrangian framework is discussed. First, the forces acting upon an isolated particle are derived. Then, the mass and temperature evolution equations characterizing the evaporation of a single isolated droplet are presented. Coupling terms describing the interactions of both phases are derived, with a particular emphasis on the point source approximation. To conclude the chapter, stochastic Lagrangian and mesoscopic Eulerian approaches are briefly presented. In chapter 4, the numerical methods of the Large-Eddy Simulation solver AVBP used in the present work are briefly reviewed.

- The third part is dedicated to the description of injection modeling. In chapter 5, theoretical aspects on the disintegration of liquid streams are presented. First, primary atomization mechanisms of liquid jets and liquid sheets are briefly discussed. Second, secondary breakup regimes are characterized. Then, numerical tools for the simulation of primary atomization are described. Due to the numerical complexity of these tools, they were not considered in the present work. Instead, a simplified injection model for pressure-swirl atomizers is presented in a first step. This model neglects the liquid atomization process and directly injects a developed spray at the atomizer orifice. The essential feature of this model is that it aims to reproduce similar injection conditions for both Eulerian and Lagrangian representations of the dispersed phase. To partially account for the liquid disintegration process in the Lagrangian solver, a secondary breakup model available in literature is implemented in a second step. In chapter 6, the secondary breakup model is applied to different test cases. The first case consists in the injection of liquid through a single hole nozzle into a closed cylinder at various gas pressures. The second case reproduces the injection of a liquid jet perpendicularly to a gaseous crossflow. It is based on prior work of Jaegle [93] on this configuration, who derived a model for the liquid column but neglected secondary breakup. The impact of the inclusion of secondary breakup in this configuration is directly assessed through comparison with experimental data and results of Jaegle [93].

- In the fourth part, the developed injection models are applied to the simulation of a more complex geometry. The chosen target configuration is a swirled aernoautical combustor, installed on the experimental test-rig MERCATO of ONERA (Office national d'études et de recherches aérospatiales). In a first step, the purely gaseous flow inside the geometry is validated. The quality of the present LES is evidenced by comparison of simulation results obtained for two different grid resolutions. In a second step, three Euler-Lagrange simulations of the evaporating two-phase flow inside the MERCATO geometry are compared. This comparison allows to assess the impacts of polydispersity and different levels of injection modeling on simulation results. Furthermore, a comparison of the present Euler-Lagrange simulations with the Euler-Euler simulations of Sanjosé relying on the common simplified injection model is performed.

- In a fifth part, simulations of laminar one-dimensional saturated two-phase flames are presented. These simulations represent a first step towards Euler-Lagrange simulations of two-phase combustion. A parametric study is performed to assess effects of equivalence ratio variations and droplet diameter on saturated two-phase flames. The interaction of heat transfer, droplet evaporation and combustion is analyzed in detail. Furthermore, qualitative comparisons are made between the present results and studies reported in the literature. The simulation of these flames also allows to validate the extension of the thickened flame model to two-phase combustion.

- The first appendix presents an article published during this thesis but whose subject is not directly related to the thesis objectives. It attempts to answer a question of practical interest for LES solvers: is it reasonable that parallel LES's with identical physical and computational parameters yield different instantaneous flow fields after a given simulation time? The second appendix describes the implementation of numerical balance tools in the Euler-Lagrange solver. These tools are used to monitor the conservation of the evaporating particle species in the two-phase flow simulations.

Part II

Governing equations and Numerics

Chapter 2

Equations for the gaseous phase

The present chapter considers the mathematical description of a reacting fluid phase laden with particles. The evolution of the fluid phase is governed by the compressible Navier-Stokes equations with coupling terms between phases and chemical reactions. These equations are recalled and the different modeling assumptions are briefly discussed. Then, the concept of filtering in the framework of Large-Eddy Simulation (LES) and the closures of the unresolved terms are described.

2.1 Conservation equations

The system of conservation laws describing the evolution of a compressible particle-laden fluid with chemical reactions and coupling between phases writes:

$$\frac{\partial \rho u_i}{\partial t} + \frac{\partial}{\partial x_j}\rho u_i u_j = -\frac{\partial p}{\partial x_i} + \frac{\partial \tau_{ij}}{\partial x_j} + \rho f_i + s_{m,i}^{p-f} \tag{2.1}$$

$$\frac{\partial \rho E}{\partial t} + \frac{\partial}{\partial x_j}\rho E u_j = \frac{\partial}{\partial x_j}(-p u_j + u_i \tau_{ij} - q_j) + \dot{\omega}_T + \rho f_i u_i + s_e^{p-f} \tag{2.2}$$

$$\frac{\partial \rho_k}{\partial t} + \frac{\partial}{\partial x_j}\rho_k u_j = -\frac{\partial}{\partial x_j}J_{j,k} + \dot{\omega}_k + s_{v,k}^{p-f} \qquad \text{for k = 1, N} \tag{2.3}$$

Index notation has been adopted and Einstein's summation rule holds over repeated indices except for the index k which denotes species of the mixture. The above equations respectively state the conservation of momentum, total non-chemical energy and partial density over N species. The total non-chemical energy is defined as:

$$E = e_s + \frac{1}{2}u_i u_i \tag{2.4}$$

where e_s denotes the specific energy, which is defined in section 2.1.3. f_i denotes a volumetric force, s^{p-f} the fluid source terms arising through coupling with the particle phase. The latter are derived in section 3.3.1. In order to close the above equation system, material laws for the the stress tensor τ_{ij}, the pressure p, the specific energy e_s, the diffusive species flux $J_{j,k}$, the diffusive heat flux q_j and the chemical source terms $\dot{\omega}$ are required.

2.1.1 Stress tensor

For Newtonian fluids, the stress tensor τ_{ij} may be derived from kinetical gas theory as [89]:

$$\tau_{ij} = 2\mu s_{ij} + \left(\mu_b - \frac{2}{3}\mu\right) s_{ll}\delta_{ij} \tag{2.5}$$

with μ and μ_b respectively the dynamic and bulk viscosities. s_{ij} denotes the symmetric part of the velocity gradient tensor:

$$s_{ij} = \left(\frac{\partial u_i}{\partial x_j} + \frac{\partial u_j}{\partial x_i}\right) \tag{2.6}$$

The bulk viscosity accounts for internal friction effects of molecules at strong fluid expansions. Since such expansions are not expected in the present applications, the bulk viscosity is neglected.

2.1.2 Equation of state

The equation of state for an ideal gas writes:

$$p = \rho R T \tag{2.7}$$

R represents the gas constant of the mixture given by:

$$R = \frac{\mathcal{R}}{W} \tag{2.8}$$

$\mathcal{R}$ is the universal gas constant and W the molar mass of the mixture:

$$W = \left(\sum_k \frac{Y_k}{W_k}\right)^{-1} \tag{2.9}$$

with Y_k the mass of the species k to the total mass.

2.1.3 Specific energy and thermodynamic relations

Assuming a thermically ideal gas, the caloric relation reduces to [161]:

$$e_{s,k} = \int_{T_0}^{T} c_{v,k}(\theta)d\theta - \frac{RT_0}{W} \tag{2.10}$$

with $c_{v,k}$ the specific heat capacity at constant volume of the species k. The subscript 0 denotes a thermodynamical reference state. In AVBP, the pressure and temperature at the reference state are respectively $p_0 = 1\,\text{bar}$ and $T_0 = 0\,\text{K}$. The sensible energy of the mixture is given as:

$$\rho e_s = \sum_k Y_k e_{s,k} \tag{2.11}$$

The sensible enthalpy writes:

$$h_{s,k} = \int_{T_0}^{T} c_{p,k}(\theta)d\theta \tag{2.12}$$

with $c_{p,k}$ the calorific capacity at constant pressure of the species k.

2.1.4 Diffusive species flux

The species diffusion velocity $V_{k,i}$ is approximated by the Hirschfelder-Curtis relation [89]:

$$Y_k V_{k,i} = -D_k \frac{W_k}{W} \frac{\partial X_k}{\partial x_i} \tag{2.13}$$

Effects of temperature or pressure gradients on the species diffusion velocity [71] are neglected. Mass conservation states that the sum of all species diffusions be zero. This is not guaranteed by eq. 2.13 for mixtures of more than two species. Thus, a correction velocity V_i^c ensuring mass conservation is added [161]:

$$J_{i,k} = -\rho \left(D_k \frac{W_k}{W} \frac{\partial X_k}{\partial x_i} - Y_k V_{k,i}^c \right) \tag{2.14}$$

with:

$$V_{i,k}^c = \sum_k D_k \frac{W_k}{W} \frac{\partial X_k}{\partial x_i} \tag{2.15}$$

The diffusion coefficients for species D_k are specified in section 2.1.7.

2.1.5 Heat flux

The heat flux vector is composed of two distinct contributions:

$$q_i = -\lambda \frac{\partial T}{\partial x_i} + \sum_k J_{i,k} h_{s,k} \tag{2.16}$$

with $J_{i,k}$ defined by eq. 2.14. The first term on the right-hand side of eq. 2.16 denotes heat conduction (modeled by Fourier's law) while the second term represents the heat flux through species diffusion. The Dufour effect, which accounts for the heat flux induced by a chemical potential gradient [71], is neglected in eq. 2.16.

2.1.6 Chemical source terms

A system of M chemical reactions involving N species may be summarized as follows:

$$\sum_{k=1}^{N} \nu'_{kj} \mathcal{M}_{kj} \rightleftharpoons \sum_{k=1}^{N} \nu''_{kj} \mathcal{M}_{kj} \qquad \text{for j = 1, M} \tag{2.17}$$

$\mathcal{M}_{kj}$ denotes the reacting species k in the reaction j. ν'_{kj} and ν''_{kj} are the stoichiometric coefficients of the products and reactants respectively. The progression rate $\mathcal{Q}_j$ is composed of a forward and a backward contribution:

$$\mathcal{Q}_j = K_{f,i} \prod_{k=1}^{N} \left(\frac{\rho Y_k}{W_k} \right)^{\nu'_{kj}} - K_{r,i} \prod_{k=1}^{N} \left(\frac{\rho Y_k}{W_k} \right)^{\nu''_{kj}} \tag{2.18}$$

The forward reaction constant $K_{f,j}$ is modelled by an Arrhenius-law:

$$K_{f,j} = A_{f,j} \exp \left(-\frac{E_{a,j}}{\mathcal{R}T} \right) \tag{2.19}$$

The backward reaction constant $K_{r,j}$ is obtained from the assumption of a thermodynamic equilibrium:

$$K_{r,j} = \frac{K_{f,j}}{K_{eq}} \tag{2.20}$$

The equilibrium constant K_{eq} is derived from the minimization of the Gibbs free energy combined with the equation of state for ideal gases [92]:

$$K_{eq} = \left(\frac{p_0}{\mathcal{R}T}\right) \exp\left(\frac{\Delta S_j^0}{\mathcal{R}}\right) - \left(\frac{\Delta H_j^0}{\mathcal{R}T}\right) \tag{2.21}$$

ΔS_j^0 and ΔH_j^0 respectively denote the entropy and enthalpy variations:

$$\Delta S_j^0 = \sum_{k=1}^{N} \nu_{kj} s_k(T) \tag{2.22}$$

$$\Delta H_j^0 = \sum_{k=1}^{N} (\nu''_{kj} - \nu'_{kj}) \int_{T_0}^{T} c_{p,k}(\theta) d\theta + \Delta h^0_{f,k} \tag{2.23}$$

From eqs. 2.18-2.23, the species reaction rates may be determined:

$$\dot{\omega}_k = \sum_{j=1}^{M} \dot{\omega}_{k,j} = W_k \sum_{j=1}^{M} \nu_{kj} \mathcal{Q}_j \tag{2.24}$$

The heat release is directly deduced from eq. 2.24 as:

$$\dot{\omega}_T = - \sum_{k=1}^{N} \dot{\omega}_k \Delta h^0_{f,k} \tag{2.25}$$

$\Delta h^0_{f,k}$ is the formation enthalpy of the species k at the thermodynamical reference state.

2.1.7 Transport properties

For ideal gases, the dynamic viscosity μ is relatively independent of the species composition. A standard power law is used to account for its temperature dependence [215]:

$$\mu = \mu_0 \left(\frac{T}{T_0}\right)^b \tag{2.26}$$

The exponent b depends on the gaseous mixture and ranges between 0.6 and 1.0.

The species diffusion coefficients D_k should ideally be derived from kinetic gas theory as a collision integral between molecules [89]. However, this level of modeling is not required for the present applications and a simpler evaluation which assumes constant Schmidt numbers Sc_k for all species is made:

$$D_k = \frac{\mu}{\rho Sc_k} \tag{2.27}$$

The heat conduction coefficient λ is computed from the viscosity μ as:

$$\lambda = \frac{\mu c_p}{Pr} \tag{2.28}$$

Pr is the Prandtl number which is assumed constant.

2.2 Large-Eddy Simulation

This section presents the derivation of the filtered governing equations in the framework of Large-Eddy Simulation. First, a few concepts related to turbulent flows are introduced. Then, the different resolution levels in numerical simulations of turbulent flows are presented. Finally, the filtered Navier-Stokes equations are derived and the approximations related to the closure of subgrid terms are described.

2.2.1 Basic aspects of turbulence

The transition from a laminar flow, for which the trajectories of single fluid elements are parallel, to a turbulent flow is characterized by the Reynolds number:

$$Re = \frac{ul}{\nu} \tag{2.29}$$

u and l are respectively characteristic velocity and length scales of the flow field. The Reynolds number represents a ratio of inertial to viscous forces and may be interpreted as an ability of the flowfield to damp the development of instabilities.

Turbulent flows are characterized by significant and irregular variations of fluid velocity in both space and time. An additional essential feature of turbulent flows is the presence of a continuous spectrum of vortical structures, the so called eddies. These eddies strongly interact with each other through a cascade process. The largest eddies display characteristic length and velocity scales which are comparable to the Reynolds number of the flow field and are thus very little affected by viscous effects. The large eddies tend to become unstable and break down into smaller eddies. These smaller eddies become in turn unstable, they are also stretched and distorted through shear forces and interactions with larger eddies. These complex interaction processes are intrinsically three dimensional. The cascade process is repeated down to scales where viscous effects become predominant so that the eddy motion is stable and viscosity is effective in dissipating the eddy's energy. Therefore, turbulence is also intrinsically a dissipative phenomenon which converts kinetic energy into heat. In terms of length scales, the largest turbulent structures are related to the integral length scale l_t whereas the smallest dissipative structures define the Kolmogorov scale η_k. The energetic density spectrum $E(k)$ of the turbulent eddies may be displayed in a diagram over the wave number k, which is proportional to the inverse of the eddy lengthscale. For isotropic steady turbulence, an inertial range characterized by a constant $k \sim -5/3$ slope is observed in the energetic density spectrum, which is displayed in fig. 2.1.

Given the stochastic nature of turbulence, statistical averaging appears as an adequate tool to describe turbulent flows. If the existence of a statistical mean is assumed, a deviation from this mean immediately follows, yielding the splitting:

$$u_i = \langle u_i \rangle + u_i'' \tag{2.30}$$

$\langle \cdot \rangle$ denotes an ensemble averaging operator. This decomposition was first introduced by Osborne Reynolds [177]. The most general averaging operator $\langle \cdot \rangle$ corresponds to an arithmetic average over a large number of realizations N of the same experiment at the same location:

$$\langle u_i \rangle (x_i, t) = \frac{1}{N} \sum_{k=1}^{N} u_i(x_i, t) \tag{2.31}$$

If the flowfield is statistically steady or homogeneous in certain directions, statistical averaging may be performed in time or in space over the homogeneous directions. Instead of eq. 2.31, short-time averages are often defined:

$$\langle u_i \rangle (x_i, t) = \frac{1}{T} \int_{-T/2}^{T/2} u_i(x_i, t+\tau) d\tau \tag{2.32}$$

T represents the averaging time interval, which must be small compared to the timescales of the statistically unsteady turbulence and large compared to the integral scales of the fluctuations.

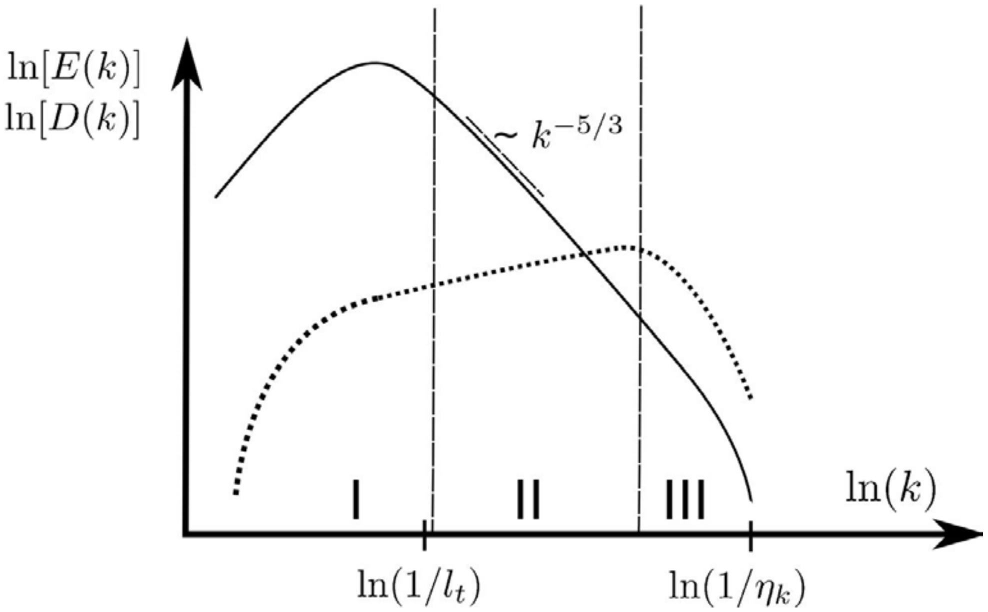

Figure 2.1 : *Sketch of energy spectrum E(k) (solid lines) and dissipation spectrum D(k) (dashed lines). Distinction between energy containing (I), inertial (II) and dissipation ranges (III). The abscissa of the integral (l_t) and Kolmogorov (η_k) length scales are indicated*

2.2.2 Resolution levels in turbulence simulations

A first possibility when performing numerical simulations of turbulent flows is to average the Navier-Stokes equations according to eq. 2.30. This yields the Reynolds-averaged Navier-Stokes (RANS) equations. Due to the nonlinearity of the Navier-Stokes equations, unclosed higher order terms appear. These terms can either be modelled or explicitly resolved through additional transport equations, but unclosed terms will necessarily appear in the additional transport equations (closure problem of turbulence). The unclosed terms represent the effect of the entire turbulence spectrum on the mean flow field. It appears that the largest scales of turbulent motion mainly depend on the simulated configuration and RANS closure models are thus expected to lack universality.

The opposite approach to RANS consists in performing resolved turbulence simulations without any averaging procedure. This approach is referred to as Direct Numerical Simulation (DNS). It requires the explicit resolution of all turbulent structures down to the Kolmogorov scale η_k on the numerical grid. From dimensional analysis, it appears that the number of mesh points required for the simulation of a three dimensional cubic domain of side lengths $L = 5l_t$ is a pure function of the turbulent Reynolds number Re_t:

$$N^3 = \left(\frac{L}{\eta_k}\right)^3 \approx 27 Re_t^{9/4} \tag{2.33}$$

with:

$$Re_t = \frac{(2k)^{1/2} l_t}{\nu} \tag{2.34}$$

where $k = 1/2\langle u_i'' u_i'' \rangle$ denotes the turbulent kinetic energy. From eq. 2.33, it follows that the Direct Numerical Simulation of realistic configurations is computationally very intensive.

An intermediate approach between RANS and DNS consists in filtering the Navier-Stokes equations so as to remove the smallest scales of motion while explicitly resolving the largest scales. This approach is called

Large-Eddy Simulation (LES). Explicitly resolving geometry dependent large structures, LES also appears advantageous in that smaller turbulent scales are assumed to exhibit more universal behavior (loss of history effects through the turbulent cascade process). LES filtered quantities are defined as the convolution product of the non-filtered scalar quantity f with a filter kernel $G_{\overline{\Delta}}$ of characterstic width $\overline{\Delta}$:

$$\overline{f}(x_i, t) = \int f(x_i, t) G_{\overline{\Delta}}(x_i - x_i') dx_i \tag{2.35}$$

$\overline{f}(x_i, t)$ is now a spatially and temporally fluctuating value in opposition to the the statistical average in eq. 2.31. The unresolved or subgrid scale contribution is denoted as:

$$f'(x_i, t) = f(x_i, t) - \overline{f}(x_i, t) \tag{2.36}$$

For variable density flows it appears advantageous to weigh filtered quantities by the volumetric mass in order to avoid the appearance of additional terms when filtering the Navier-Stokes equations. Favre filtering is defined as:

$$\overline{\rho}\widetilde{f} = \overline{\rho f} \tag{2.37}$$

2.2.3 Filtered equations

Applying Favre filtering to the compressible Navier-Stokes equations with chemical source terms and coupling between phases yields:

$$\frac{\partial \overline{\rho}\widetilde{u}_i}{\partial t} + \frac{\partial \overline{\rho}\widetilde{u}_i\widetilde{u}_j}{\partial x_j} = -\frac{\partial}{\partial x_i}\overline{p} + \frac{\partial}{\partial x_j}[\overline{\tau}_{ij} + \overline{\tau}_{ij}^{sgs})] + \overline{s}_{m,i}^{p-f} + \overline{\rho}\widetilde{f}_i \tag{2.38}$$

$$\frac{\partial \overline{\rho} E}{\partial t} + \frac{\partial \overline{\rho}\widetilde{E}\widetilde{u}_j}{\partial x_j} = -\frac{\partial}{\partial x_j}[\overline{pu_j} - \overline{\tau_{ij}u_i} + \overline{q}_j + \overline{q}_j^{sgs}] + \overline{\rho}\widetilde{f_i u_i} + \overline{\dot{\omega}}_T + \overline{s}_e^{p-f} \tag{2.39}$$

$$\frac{\partial \overline{\rho_k}}{\partial t} + \frac{\partial \overline{\rho_k}\widetilde{u}_i}{\partial x_i} = \frac{\partial}{\partial x_i}[\overline{J_{i,k}} - \overline{J}_{i,k}^{sgs}] + \overline{\dot{\omega}}_k + \overline{s}_{v,k}^{p-f} \qquad \text{for k = 1, N} \tag{2.40}$$

The superscript sgs (for subgrid-scale) denotes unclosed terms appearing through the filtering operation due to the nonlinearity of the Navier-Stokes equations, they are explicited in section 2.2.4. The filtered source terms arising from the coupling with the particle phase are presented in section 3.3.1. In the derivation of eqs. 2.38-2.40, it has been tacitly assumed that the order of filtering and differenciation operations may be exchanged. However, Ghosal and Moin [67] show that this permutation is only valid for constant filter widths. The error associated with the permutation for varying filter widths is of second order in the filter width and thus only tolerable for numerical schemes with at most second order spatial accuracy. The permutation error may be included in the subgrid closure terms, but this seems rarely done in practice.

The filtered viscous stress tensor is approximated as follows:

$$\overline{\tau}_{ij} = \overline{2\mu s_{ij} - \frac{2}{3}\mu s_{ll}\delta_{ij}} \tag{2.41}$$

$$\overline{\tau}_{ij} \approx 2\overline{\mu}\widetilde{s_{ij}} - \frac{2}{3}\overline{\mu}\widetilde{s}_{ll}\delta_{ij} \tag{2.42}$$

This assumes that dynamic viscosity is constant across the filter width and that it may be extracted from the filtering operator. For the dynamic viscosity as for all other material properties, it is assumed that:

$$\overline{\mu} \approx \mu(\widetilde{T}) \tag{2.43}$$

This approximation may induce large errors for strongly nonlinear behaviors of the given material property, but such behaviors are not expected in the present applications.

Similar simplifications to the derivation of the viscous stress tensor are made for the species diffusive fluxes:

$$\overline{J_{i,k}} = \overline{-\rho \left(D_k \frac{W_k}{W} \frac{\partial X_k}{\partial x_i} - Y_k V^c_{k,i} \right)} \tag{2.44}$$

$$\overline{J_{i,k}} \approx -\overline{\rho} \left(\overline{D_k} \frac{W_k}{W} \frac{\partial \widetilde{X_k}}{\partial x_i} - \widetilde{Y_k} \widetilde{V_{k,i}}^c \right) \tag{2.45}$$

For the heat flux, one obtains:

$$\overline{q}_i = \overline{-\lambda \frac{\partial T}{\partial x_i} + \sum_k J_{j,k} h_{s,k}} \tag{2.46}$$

$$\overline{q}_i \approx -\overline{\lambda} \frac{\partial \widetilde{T}}{\partial x_i} + \sum_k \overline{J_{i,k}} \widetilde{h_{s,k}} \tag{2.47}$$

with:

$$\overline{\lambda} \approx \frac{\overline{\mu}\, \overline{c_p}}{Pr} \tag{2.48}$$

2.2.4 Subgrid closures

Many closure models rely on the observation that turbulent flows mix fluid much more effectively than laminar flows. A basic modeling idea then consists in representing the unclosed terms as diffusive contributions with an associated turbulent viscosity μ_t (eddy-viscosity models). Under this assumption, the subgrid stress tensor may be rewritten as:

$$\overline{\tau}^{sgs}_{ij} = -\overline{\rho}(\widetilde{u_i u_j} - \widetilde{u_i}\widetilde{u_j}) = 2\overline{\mu}_t \widetilde{s_{ij}} - \frac{2}{3} \overline{\mu}_t \widetilde{s_{ll}} \delta_{ij} \tag{2.49}$$

This supposes that the principal axes of the strain rate tensor are aligned with those of the subgrid stress tensor which is not fulfilled in general [192]. The turbulent viscosity may be derived from algebraic relations or through the resolution of additional transport equations. A few models to determine the turbulent viscosity are detailed in subsection 2.2.5.

The subgrid species flux is modelled in an analogous manner to the subgrid stress tensor:

$$\overline{J}^{sgs}_{i,k} = \overline{\rho} \left(\widetilde{u_i Y_k} - \widetilde{u_i} \widetilde{Y_k} \right) \tag{2.50}$$

$$\overline{J}^{sgs}_{i,k} = -\overline{\rho} \left(D^t_k \frac{W_k}{W} \frac{\partial \widetilde{X_k}}{\partial x_i} - \widetilde{Y_k} \widetilde{V_{k,i}}^{c,t} \right) \tag{2.51}$$

with:

$$\widetilde{V_{k,i}}^{c,t} \approx \sum_k D^t_k \frac{W_k}{W} \frac{\partial \widetilde{X_k}}{\partial x_i} \tag{2.52}$$

The turbulent species diffusions are deduced from a turbulent Schmidt number Sc^t_k:

$$D^t_k = \frac{\mu_t}{\rho Sc^t_k} \tag{2.53}$$

The constant value $Sc_k^t = 0.7$ is chosen for all species.

For the subgrid heat flux, one obtains:

$$\overline{q}_i^{sgs} = \overline{\rho}\left(\widetilde{u_i E} - \widetilde{u}_i \widetilde{E}\right) \tag{2.54}$$

$$\overline{q}_i^{sgs} = -\overline{\lambda_t}\frac{\partial \widetilde{T}}{\partial x_i} + \sum_k \overline{J}_{i,k}^{sgs}\widetilde{h_{s,k}} \tag{2.55}$$

with:

$$\lambda_t = \frac{\nu_t \overline{c_p}}{Pr_t} \tag{2.56}$$

The turbulent Prandtl number $Pr_t = 0.6$ is also assumed constant [138].

2.2.5 Subgrid scale models

The main task of the subgrid scale model is to correctly reproduce the energy fluxes between resolved and unresolved turbulent scales. This involves interactions among the whole turbulence spectrum and the subgrid scale model must ideally account for interactions between turbulent structures of different sizes ("non-local interactions") as well as between structures of comparable sizes ("local interactions") [60]. Due to the difficulty of this task, one may only expect subgrid scale models to be correct in the statistical sense.

Eddy-viscosity subgrid scale models require the determination of a turbulent viscosity. Viscosities are the product of characteristic length and velocity scales. As the most energetic unresolved scales are found at the cut-off frequency k_c of the LES filter, the filter width $\overline{\Delta}$ is a natural choice for the length scale of the turbulent viscosity. The characteristic velocity scale is determined from the subgrid scale energy. The models based on an eddy viscosity assumption make different levels of simplification to obtain an estimate for this energy.

2.2.5.a) The Smagorinsky model

The Smagorinsky model is among the most popular subgrid scale models due to its simplicity. It assumes equilibrium between production and dissipation of turbulent kinetic energy at the subgrid scales. This assumption is justified in regions of isotropic turbulence for which the Smagorinsky model reproduces correct dissipation levels. In regions of anisotropy however, the model shows to be overdissipative as it cannot predict the occurrence of backscatter, i.e. the instantaneous and localized backflow of turbulent energy from smaller to larger scales. Piomelli et al. [157] showed that the failure to reproduce this phenomenon may result in wrong prediction of perturbation growth in transitional flows. Furthermore, it appears that the Smagorinsky model does not accurately distinguish between zones of pure shear and turbulence. It writes:

$$\nu_t = \left(C_S \overline{\Delta}\right)^2 \sqrt{2\widetilde{s_{ij}}\widetilde{s_{ij}}} \tag{2.57}$$

Smagorinsky determined an analytical value of 0.18 for the constant C_S. However, C_S is often adjusted to the given application case and values ranging between 0.1 and 0.18 may be found in the literature.

2.2.5.b) Dynamic Smagorinsky model

The dynamic Smagorinsky model [66] relies on the same expression as eq.2.57 with the notable difference that the Smagorinsky constant is now evaluated from a dynamic procedure:

$$\nu_t = \left(C_S^{dyn} \overline{\Delta}\right)^2 \sqrt{2\widetilde{s_{ij}}\widetilde{s_{ij}}} \tag{2.58}$$

An additional high-pass filter of characteristic width $\widehat{\Delta}$ is introduced, yielding two distinct filter scales which are parametrized in a similar manner:

$$\overline{\tau}_{ij}^{d} = -2C_S^{dyn}\overline{\Delta}^2\sqrt{2\widetilde{s_{ij}}\widetilde{s_{ij}}} = -2C_S^{dyn}\alpha_{ij} \tag{2.59}$$

$$\widehat{\overline{\tau}}_{ij}^{d} = -2C_S^{dyn}\widehat{\Delta}^2\sqrt{2\widehat{\widetilde{s_{ij}}}\widehat{\widetilde{s_{ij}}}} = -2C_S^{dyn}\beta_{ij} \tag{2.60}$$

A scale-similarity assumption is made for both filter scales, which implies that C_S^{dyn} takes the same value in eqs. 2.59 and 2.60. τ_{ij}^d denotes the anisotropic part of the stress tensor:

$$\tau_{ij}^d = \tau_{ij} - \frac{1}{3}\delta_{ij}\tau_{kk} \tag{2.61}$$

The dynamic constant C_S^{dyn} may be determined from eqs. 2.59 and 2.60 using the Germano identity [65]:

$$L_{ij} = \widehat{\overline{u}_i\overline{u}_i} - \widehat{\overline{u}}_i\widehat{\overline{u}}_i = -2C_S^{dyn}\beta_{ij} + 2\widehat{C_S^{dyn}\alpha_{ij}} \tag{2.62}$$

Eq. 2.62 presents two major difficulties. First, C_S^{dyn} is under the filter operator in the second term on the right-hand side of eq. 2.62, which implies that it must be determined with specific numerical methods. A first approach uses the Germano identity in an integral manner and minimizes an associated error function. A second approach considers eq. 2.62 as implicit in C_S^{dyn} and solves it through an iterative process. A second difficulty of eq. 2.62 arises from the fact that it provides 5 independent equations for a single unknown. Germano [65] proposes to multiply eq. 2.62 with $\widetilde{s_{ij}}$, which reduces the relation to a single equation for C_S^{dyn}. Lilly [122] proposes to minimize eq. 2.62 in a least squares sense in order to obtain C_S^{dyn}. The dynamic Smagorinsky model is capable of predicting backscatter which manifests itself through locally negative values of the turbulent viscosity. The latter favor numerical oscillations and make the dynamic Smagorinsky model difficult to handle in practice. For this reason, the dynamic Smagorinsky model is not used as a subgrid scale model in the present work.

2.2.5.c) The Wale model

The Wale model was designed by Ducros and Nicoud [43] to recover the correct y^3 scaling of turbulent viscosity close to walls for wall resolved simulations. The turbulent viscosity ν_t is defined as:

$$\nu_t = (C_w\overline{\Delta})^2\frac{(\widetilde{s}_{ij}^d\widetilde{s}_{ij}^d)^{3/2}}{(\widetilde{s}_{ij}\widetilde{s}_{ij})^{5/2} + (\widetilde{s}_{ij}^d\widetilde{s}_{ij}^d)^{5/4})} \tag{2.63}$$

$C_w = 0.4929$ is a model constant. $\widetilde{s}_{ij}^d$ is the traceless symmetric part of the square of the velocity gradient tensor:

$$\widetilde{s}_{ij}^d = \frac{1}{2}(\widetilde{g}_{ij}^2 + \widetilde{g}_{ji}^2) - \frac{1}{3}\widetilde{g}_{kk}^2\delta_{ij} \tag{2.64}$$

$\widetilde{g}_{ij}$ represents the resolved velocity gradient:

$$\widetilde{g}_{ij} = \frac{\partial\widetilde{u}_i}{\partial x_j} \tag{2.65}$$

An advantage of the Wale model is its improved behavior in zones of pure shear compared to the Smagorinsky model. For this reason, the Wale model is prefered to the Smagorinsky model in the present work.

Chapter 3

Equations for the particle phase

This chapter provides a general overview of spray modeling, for which two main frameworks may be evidenced. The Lagrangian approach tracks individual particles in their own frame of reference. In deterministic Lagrangian approaches, each numerical particle represents a physical particle [21, 132, 224] while in stochastic/ Monte-Carlo Lagrangian approaches, the numerical particles represent samples of the physical spray [147, 17, 209, 51]. The Eulerian formalism describes the spray as a continuum of point particles for which the exchanges of mass, momentum and heat are described from a statistical point of view, in analogy to gas kinetics. The present chapter focuses on the deterministic Lagrangian approach. First, the forces acting upon an isolated rigid spherical particle are derived. Then, the evaporation model employed in the present work is presented. Interphase exchange terms are derived and a few notions on secondary atomization are provided. The chapter also gives brief summaries of the Lagrangian Monte-Carlo and the Eulerian modeling approaches for the particle phase. It concludes with a description of characteristic diameters of a spray.

Note : in the present work, the spray is either designated by the expressions “particle phase" or “liquid phase". In the Lagrangian approach, evaporating droplets are also named particles for simplicity.

3.1 Lagrangian equations of motion for an isolated particle

3.1.1 Generalized Basset-Boussinesq-Oseen equations

Basset [11], Boussinesq [23] and Oseen [150] examined the flow of a settling particle under gravity in a quiescent fluid flow and derived an analytical expression for the forces acting upon a particle in such flow. Tchen [219] extended their work to the motion of a rigid sphere in a nonuniform flow. More recently, Maxey and Riley [134] corrected certain inconsistencies in Tchen’s derivations. The following derivations follow those of Maxey and Riley [134].

The tracking of an isolated rigid spherical particle in its own frame of reference is considered. Particle rotation is excluded and only the translatory motion of the particle is taken into account. The kinematic equation writes:

$$\frac{dx_{p,i}}{dt} = u_{p,i} \tag{3.1}$$

The momentum balance is obtained as:

$$m_p \frac{du_{p,i}}{dt} = \int_{S_p} (-p\delta_{ij} + \tau_{ij}) n_j dS = F_{p,i} \tag{3.2}$$

The subscript p denotes particle properties. The force $F_{p,i}$ exerted upon the particle is obtained by integrating the fluid pressure and the fluid viscous stresses over the particle surface S_p. This force may be decomposed in two distinct contributions:

$$F_{p,i} = F^u_{p,i} + F^d_{p,i} \tag{3.3}$$

$F^u_{p,i}$ denotes the force acting upon a fluid element coinciding with the particle. $F^d_{p,i}$ represents the force exerted upon the particle resulting from the perturbation of the fluid flow field by the particle. In order to derive both contributions, Maxey and Riley [134] split the fluid flow field into an undisturbed component $\breve{u}_i$ and a disturbed component set by the particle. The authors assume that the particle diameter is small compared to the smallest flow field length scale, for example the Kolmogorov scale in a turbulent flow:

$$d_p \ll \eta_k \tag{3.4}$$

With these simplifications, the force contribution resulting from the undisturbed flow component writes:

$$F^u_{p,i} = \frac{\pi d_p^3}{6}\left[\rho \frac{D\breve{u}_i}{Dt}\bigg|_{x_i = x_{p,i}} - (\rho_p - \rho) g_i\right] \tag{3.5}$$

where g_i is the gravity vector. $\breve{u}_i$ denotes the undisturbed fluid velocity at the particle location and D/Dt represents the total derivative along the undisturbed fluid trajectory:

$$\frac{D}{Dt} = \frac{\partial}{\partial t} + \breve{u}_j \frac{\partial}{\partial x_j} \tag{3.6}$$

Through the total derivative of the undisturbed fluid velocity, eq. 3.5 accounts for the pressure and viscous forces acting upon a fluid element coinciding with the particle. In order to analytically derive the unsteady disturbance flow set by the particle, a low particle Reynolds number is assumed in addition to the previous hypotheses:

$$Re_p = \frac{d_p \|\overrightarrow{\breve{u}} - \overrightarrow{u_p}\|}{\nu} \ll 1 \tag{3.7}$$

The forces arising from the unsteady disturbance flow set by the particle may be obtained from a temporal Laplace transform of the disturbed flow field momentum equation (see Maxey and Riley [134]) for more details. One obtains:

$$\begin{aligned} F^d_{p,i} = \frac{\pi d_p^3}{6}\Bigg[& \frac{18\rho\nu}{d_p^2}(\breve{u}_i - u_{p,i}) + \frac{\rho}{2}\frac{d}{dt}(\breve{u}_i - u_{p,i}) + \\ & \frac{9\rho}{d_p}\sqrt{\frac{\nu}{\pi}}\int_{-\infty}^{t} \frac{d}{d\tau}(\breve{u}_i - u_{p,i})\frac{d\tau}{\sqrt{t-\tau}}\Bigg] \end{aligned} \tag{3.8}$$

The first term on the right-hand side of eq. 3.8 represents the Stokes drag force. The second term denotes the added mass force, which accounts for the acceleration/ deceleration of fluid by the particle. The third term is the Basset history force and originates from the lagging development of the boundary layer on the surface of an accelerated particle [37]. Gatignol [64] generalizes the previous derivations to a particle diameter comparable to the smallest flow field lengthscale, partly relaxing the assumption expressed in eq. 3.4. The expressions obtained for the forces $F^u_{p,i}$ and $F^d_{p,i}$ remain unchanged in eqs. 3.5 and 3.8, except that the undisturbed fluid velocity $\breve{u}_i$ at the particle location is replaced by an undisturbed fluid velocity averaged either over the particle surface $\breve{u}^s_i$ or the particle volume $\breve{u}^v_i$, depending on the considered force.

3.1.2 Generalized drag force

The drag term in eq. 3.8 corresponds to the force originally derived by Stokes in a steady viscous fluid flow for small particle Reynolds numbers. Introducing the drag coefficient C_d, this force may be rewritten as:

$$F_{p,i}^{drag} = \frac{1}{8}\rho\pi d_p^2 C_d \left\| \overrightarrow{u_p} - \overrightarrow{\breve{u}} \right\| (u_{p,i} - \breve{u}_i) \tag{3.9}$$

with:

$$C_d = \frac{24}{Re_p} \tag{3.10}$$

This assumption of a small particle Reynolds number allows to neglect inertial effects of the fluid flow in the derivation of the drag force. Oseen [150] accounted for a linearized inertial term and obtained the following correction to the Stokes drag coefficient:

$$C_d = \frac{24}{Re_p}\left(1 + \frac{3}{16}Re_p\right) \tag{3.11}$$

Eq. 3.11 is valid for particle Reynolds numbers up to 5. More general analytical solutions for the evolution of the drag coefficient have not been derived to this date. Instead, empirical correlations are used to cover the large range of particle Reynolds numbers encountered in practical applications. In this study, the correlation proposed by Schiller and Naumann [197] is used:

$$C_d(Re_p) = \frac{24}{Re_p}\left(1 + 0.15 Re_p^{0.687}\right) \qquad \text{for} \qquad Re_p \leq 1000 \tag{3.12}$$

The validity of eq. 3.12 ranges up to particle Reynolds numbers of approximately 1000 with a maximum deviation of 5% from experimental data. In some of the presented applications, the values of the particle Reynolds number may exceed 1000. In this case, the drag coefficient is evaluated according to Clift et al. [30]:

$$C_d = 0.44 \qquad \text{for} \qquad Re_p > 1000 \tag{3.13}$$

Note that similar empirical corrections need to be applied to all previously enumerated forces when the assumption of small particle Reynolds number no longer holds.

3.1.3 Momentum equation implemented in AVBP

In order to simplify the momentum equations for the isolated particle, the following assumptions are made:

- H1: particle diameters are small compared to unity ($d_p \ll 1$).
- H2: dense particles are considered and the density ratio between particles and fluid is large compared to unity ($\rho_p/\rho \sim \mathcal{O}(10^3)$).
- H3: the perturbation of the fluid flow field induced by a single particle is negligible compared to the perturbations arising from the remaining particles in the fluid flow.

The first assumption allows to neglect all forces but drag from a dimensional analysis since it is the only force scaling with the square of the inverse particle diameter. Under the second assumption, the expression for the gravity force may be simplified. Finally, the third assumption allows to approximate the unperturbed fluid velocity $\breve{u}_i$ at the particle location by the fluid velocity perturbed by the particle u_i. Therefore, the momentum equation simplifies to:

$$\frac{du_{p,i}}{dt} = \frac{1}{\tau_p}(u_i - u_{p,i}) + g_i \tag{3.14}$$

τ_p is the particle relaxation time, which is defined as:

$$\tau_p = \frac{4}{3}\frac{\rho_p}{\rho}\frac{d_p}{C_d(Re_p)\|\overrightarrow{u_p} - \overrightarrow{u}\|} \tag{3.15}$$

with $C_d(Re_p)$ given by eqs. 3.12 and 3.13. The relaxation time scale τ_p defines a characteristic time scale of particle acceleration. The behavior of the particle in a fluid flow field is therefore dictated by the ratio of the particle relaxation time scale τ_p to a characteristic convective fluid flow time scale τ_{cv}. This ratio defines the Stokes number St:

$$St = \frac{\tau_p}{\tau_{cv}} \tag{3.16}$$

For large Stokes numbers ($St \gg 1$), the particle is insensitive to fluid flow perturbations and follows the trajectory dictated by its inertia. On the contrary, a particle with small Stokes number ($St \ll 1$) follows the fluid flow like a tracer. In a turbulent flow field, effects of preferential concentration (see section 3.3.2) are most pronounced for a unitary Stokes number ($St \approx 1$).

3.2 Evaporation of an isolated particle

A Spalding type evaporation model based [208] on an equilibrium law was implemented in the Lagrangian solver by Jaegle [93] and is briefly described in the following. This evaporation model is identical to the evaporation model previously implemented in the Eulerian module by Boileau [19]. The equations for particle evaporation are derived from the conservation equations of mass, vapor and energy of a single particle. The following assumptions are made:

- H1: the particle is isolated and effects of particle interactions on evaporation are neglected.
- H2: the atmosphere around the particle is at rest and the problem is quasi-steady, which implies that equations are independent of time
- H3: the particle is at equilibrium with the surrounding gas.
- H4: the thermal conductivity inside the particle is considered infinite, which leads to a uniform particle temperature.

The problem is treated in spherical coordinates and due to spherical symmetry, only the radial coordinate is considered. The gaseous conservation laws between the particle's surface (denoted by the subscript ζ) and the far-field (denoted by the subscript ∞) write:

$$\rho u r^2 = \text{constant} = \frac{\dot{m}_v}{4\pi} \tag{3.17}$$

$$\rho u r^2 \frac{dY_v}{dr} = \frac{d}{dr}\left(r^2[\rho D_v]\frac{dY_v}{dr}\right) \tag{3.18}$$

$$\rho u r^2 \frac{dh}{dr} = \frac{d}{dr}\left(r^2 \frac{\lambda}{c_p}\frac{dh}{dr}\right) \tag{3.19}$$

where the vapor species is denoted by the subscript v. Note that since the equations are written in spherical coordinates, a flux directed away from the particle is positive.

3.2.1 Mass transfer

Integrating eq. 3.18 twice between the particle surface and the far-field, an expression for the vapor mass flux as a function of the vapor mass fractions may be derived:

$$\dot{m}_p = 4\pi r_\zeta [\rho D_v] \ln(B_M + 1) \tag{3.20}$$

B_M denotes the Spalding mass number:

$$B_M = \frac{Y_{v,\zeta} - Y_{v,\infty}}{1 - Y_{v,\zeta}} \tag{3.21}$$

Considering the evolution of the particle mass over time, eq. 3.20 may be rewritten as:

$$\dot{m}_p = \pi d_p Sh [\rho D_v] \ln(B_M + 1) \tag{3.22}$$

The Sherwood number Sh represents a ratio of convective to conductive mass transfer and takes the value 2 in a quiescent atmosphere. However, the flow field around the particle is generally not quiescent in practical applications and the Sherwood number is modified using empirical correlations to account for the relative velocity between the particle and the surrounding gas. Ranz and Marshall [170] propose the following correction:

$$Sh = 2 + 0.55 Re_p^{1/2} Sc_v^{1/3} \tag{3.23}$$

Sc_v denotes the Schmidt number of the vapor species. Finally, the vapor mass fraction at the particle surface is deduced from the Clausius-Clapeyron law:

$$p_{v,\zeta} = p_{cc} \exp\left(\frac{W_v L_{ev}(T_{ref})}{\mathcal{R}} \left(\frac{1}{T_{cc}} - \frac{1}{T_\zeta}\right)\right) \tag{3.24}$$

with the subscript cc designating an arbitrary reference point on the saturation curve. $\mathcal{R}$ is the universal gas constant and $L_{ev}(T_{ref})$ the latent heat of vaporization at the reference temperature T_{ref}. The vapor partial pressure $p_{v,\zeta}$ directly yields the molar fraction $X_{F,\zeta}$ and in turn allows to obtain the vapor mass fraction at the particle's surface $Y_{v,\zeta}$. The Clausius-Clapeyron law assumes a thermodynamic equilibrium at the particle's surface during the evaporation process, which is consistent with assumption H3.

3.2.2 Heat transfer

The evolution of the particle's temperature is derived from eq. 3.19. Since no enthalpy can be stored at the interface between the particle and the surrounding gas ζ, an equilibrium can be stated for the conductive and convective heat fluxes, respectively Φ^c and Φ^{cv}, on both sides of the interface:

$$\Phi_l^{cv} + \Phi_l^c + \Phi_g^{cv} + \Phi_g^c = 0 \tag{3.25}$$

The liquid and gaseous convective fluxes may be equated to the latent heat of vaporization L_{ev}:

$$\Phi_l^{cv} + \Phi_g^{cv} = -\dot{m}_v h_{s,p}(T_\zeta) + \dot{m}_p h_{s,v}(T_\zeta) = \dot{m}_v L_{ev}(T_\zeta) \tag{3.26}$$

The liquid conductive contribution writes:

$$\Phi_l^c = \left(4\pi r_p^2 \lambda \frac{dT_p}{dr}\right)_{\zeta^-} \tag{3.27}$$

with the supersript ζ^{-} denoting quantities measured on the "particle side" of the interface. The gaseous conductive flux is written in an analogous manner:

$$\Phi_g^c = \left(4\pi r_p^2 \lambda \frac{dT_p}{dr}\right)_{\zeta^+} \tag{3.28}$$

with the subscript ζ^{+} denoting quantities measured on the "gaseous side" of the interface.

Considering the temporal evolution of the particle enthalpy [1], one may write:

$$\frac{d}{dt}(m_p h_{s,l}(T_p)) = \Phi_l^c + \Phi_l^{cv} \tag{3.29}$$

Splitting the right hand-side of eq. 3.29 through partial differentiation, using the relation $dh_{s,l}(T_p) = c_{p,l} dT_p$ together with eqs. 3.25 and 3.26, an equation for the evolution of the particle temperature is obtained:

$$\frac{dT_p}{dt} = \frac{1}{m_p c_{p,l}}(-\Phi_g^c + \dot{m}_v L_{ev}(T_\zeta)) \tag{3.30}$$

Finally, the conductive flux on the gaseous side needs to be determined. More specifically, an expression for the temperature gradient on the gaseous side of the particle's surface must be derived. This is done by integrating the enthalpy conservation equation (eq. 3.19) twice between the particle's surface and infinity. This yields:

$$\Phi_g^c = \lambda d_p Nu (T_\zeta - T_\infty) \frac{\ln(B_T + 1)}{B_T} \tag{3.31}$$

The Nusselt number Nu represents a ratio of convective to conductive heat transfer at the particle's surface and assumes a value of 2 in a quiescent gaseous environment. It is expressed in an analogous manner to the Sherwood number in order to account for the relative velocity between the particle and the surrounding gas:

$$Nu = 2 + 0.55 Re_p^{1/2} Pr_v^{1/3} \tag{3.32}$$

B_T is the Spalding number for the temperature:

$$B_T = \frac{(T_\infty - T_\zeta)\dot{m}_p c_{p,l}}{T_\zeta - T_\infty} \tag{3.33}$$

A relation between the Spalding number for mass B_M and temperature B_T may be derived by equating the mass flow rates in eqs. 3.20 and 3.33:

$$B_T = (1 + B_M)^{Sh/(Nu Le_v)} - 1 \tag{3.34}$$

with Le_v the Lewis number of the vapor species, which represents a ratio of thermal to mass diffusivities.

3.2.3 Determination of thermodynamic quantities over the integration path

Integrating eqs. 3.18 and 3.19 from the particle surface to the far-field requires the knowledge of averaged thermodynamic quantities over the integration path, for instance the dynamic viscosity $\bar{\mu}$ and the heat capacity $\bar{c}_p$ of the gaseous mixture. These average quantities are evaluated by interpolating the temperature and the mixture fractions between the droplet surface and the far-field with the so called "$1/3^{rd}$" rule [91]:

$$T_{int} = T_\zeta + \frac{1}{3}(T_\infty - T_\zeta) \tag{3.35}$$

$$Y_{v,int} = Y_{v,\zeta} + \frac{1}{3}(Y_{v,\infty} - Y_{v,\zeta}) \tag{3.36}$$

---

[1] in order to avoid confusion, the particle enthalpy and particle constant heat capacity are denoted with the subscript 'l' for liquid

3.3 Interaction between fluid and particle phase

The interaction of particles with the fluid phase is twofold. First, direct coupling occurs through the perturbation of the fluid phase induced by the presence of the particles, it is accounted for through interphase exchange terms. Second, the direct coupling leads to an alteration of turbulence dynamics in the fluid phase, which has been the focus of numerous experimental and numerical studies.

3.3.1 Interphase exchange terms

The exact evaluation of the coupling terms between a particle and the surrounding gas would require the explicit numerical resolution of the interface between them and lead to excessive computational costs. Instead, the point-force approximation of Saffman [187] is used. It allows to represent the interphase exchange terms by punctual source terms coinciding with the particle location. The derivation of the point-force approximation is given in the following.

3.3.1.a) Point source approximation

The motion of N_p rigid spherical particles in a steady viscous flow is considered. The volumetric concentration of particles is low and the fluid density constant. Under these assumptions, the mass and momentum conservation equations for the fluid write:

$$\frac{\partial u_i}{\partial x_i} = 0 \tag{3.37}$$

$$\mu \frac{\partial^2 u_i}{\partial x_j^2} - \frac{\partial p}{\partial x_i} = -F^n_{p,i} \tag{3.38}$$

The coupling between both phases is accounted for through the no-slip conditions on the particle surfaces S_p:

$$u_i = u^n_{p,i} \qquad \text{for} \qquad x \in S^n_p, \qquad n = 1, N_p \tag{3.39}$$

The force acting upon the particle n writes:

$$F^n_{p,i} = \int_{S_p} (-p\delta_{ij} + \tau_{ij}) n_j dS \tag{3.40}$$

According to the *actio* = *reactio* principle, the particle exerts the opposite force upon the flow field:

$$- F^n_{p,i} = \int_{S_p} (p\delta_{ij} - \tau_{ij}) n_j dS \tag{3.41}$$

Therefore, the derivation of the coupling force between phases requires knowledge of the flow field on the particle's surface. In order to avoid this tedious evaluation, Saffman [187] introduced the point-force approximation which specifies a distribution of force singularities centered on each particle and allows to roughly fulfill the boundary conditions of eq. 3.39 [133]. The forces acting upon the particles are rewritten as multipole expansions:

$$\mu \frac{\partial^2 u_i}{\partial x_j^2} - \frac{\partial p}{\partial x_i} = \\ \sum_{n=1}^{N_p} \left[F^n_i \delta(\overrightarrow{x} - \overrightarrow{x_p}) + F^n_{ij} \frac{\partial}{\partial x_j} \delta(\overrightarrow{x} - \overrightarrow{x_p}) + F^n_{ijk} \frac{\partial^2}{\partial x_j \partial x_k} \delta(\overrightarrow{x} - \overrightarrow{x_p}) \right] \tag{3.42}$$

The coefficients F_i^n, F_{ij}^n and F_{ijk}^n respectively denote the force monopole, dipole and quadripole. They are related to the fluid force and torque on the n-th particle. Due to the linearity of the Stokes flow, the local fluid velocity may be obtained by a linear superposition of the flows induced by each multipole force term. This allows to use the fundamental solution for the perturbation velocity induced by the motion of an isolated particle in a fluid at rest:

$$u_i = T_{ij} F_j \tag{3.43}$$

T_{ij} denotes the Oseen tensor:

$$T_{ij} = \frac{1}{8\pi\mu}\left(\frac{\delta_{ij}}{r} + \frac{r_i r_j}{r^3}\right) \tag{3.44}$$

The perturbation velocity induced by a force dipole may be obtained from the derivative of the Oseen tensor, the perturbation velocity induced by a force quadrupole from the second-order derivative and so forth. The forces acting upon an isolated spherical particle of diameter d_p in a fluid at rest are drag and a degenerate force quadrupole [133]:

$$F_i = F_{p,i} = 3\pi d_p \mu (u_i - u_{p,i}) \tag{3.45}$$

$$F_{ijk} = \frac{d_p^2}{24} F_{p,i} \delta_{jk} \tag{3.46}$$

The perturbed fluid velocity due to an isolated particle in a Stokes flow is then obtained as:

$$u_i = \breve{u}_i + \frac{1}{8\mu\pi} F_{p,j}\left(\frac{\delta_{ij}}{r} + \frac{r_i r_j}{r^3}\right) + \frac{d_p^2}{96\mu\pi} F_{p,j}\left(\frac{\delta_{ij}}{r^3} + 3\frac{r_i r_j}{r^5}\right) \tag{3.47}$$

The perturbation of the velocity field by the particle is composed of a long range contribution induced by the force monopole, proportional to the inverse of the particle radius. The second contribution is a short range contribution induced by the force quadripole, proportional to the inverse of the cube of the particle radius. For particles which are small compared to all flow field length scales, only the long range contribution needs to be taken into account as the perturbation induced by the particle is rapidly dissipated by viscous fluid effects. This allows to truncate the multipole expansion after the first term. Thus, the perturbation of the flow field by N_p particles in a steady viscous fluid flow may be represented by the sum of punctual forces centered on the particles:

$$\mu \frac{\partial^2 u_i}{\partial x_j^2} - \frac{\partial p}{\partial x_i} = -\sum_{n=1}^{N_p} F_{p,i} \delta(\overrightarrow{x} - \overrightarrow{x_p}) \tag{3.48}$$

This result is strictly speaking only valid for a steady viscous fluid flow but extended to more general flow fields in practice.

3.3.1.b) Expressions for the source terms

This section derives the interphase exchange terms of mass, momentum and energy between fluid and particle phase. According to the point source approximation, all interphase exchange terms are treated as the sums of source terms centered on the particles. The evaporated mass of the particles appears as a positive source term in the conservation equation of the evaporating species:

$$s_{ev,k}^{p-f}(x_i) = -\sum_{p=1}^{N} \dot{m}_p \delta(\overrightarrow{x} - \overrightarrow{x_p}) \delta_{kv} \tag{3.49}$$

The subscript v denotes the index of the evaporating species. When considering an evaporating particle, the momentum exchange term between phases writes:

$$s_{m,i}^{p-f}(x_i) = -\sum_{p=1}^{N}\left[\frac{dm_p}{dt}u_{p,i} + F_{p,i}\right]\delta(\overrightarrow{x} - \overrightarrow{x_p}) \tag{3.50}$$

The energy exchange term gathers the contributions of the work done by the particles and the enthaply fluxes due to evaporation.The work done by the particles is the product between the forces acting upon the particles and the gaseous velocity at the particle surface. Since a no-slip condition must be fulfilled at the particles' surfaces, the gaseous velocity at the particle location is equal to the particle velocity. The exchanged enthalpy fluxes are retrieved from the particle temperature evolution equation, see eqs. 3.30 and 3.31. This yields:

$$s_{e}^{p-f}(x_{p,i}) = \sum_{p=1}^{N}\left[-F_{p,i}u_{p,i} - \dot{m}_p(L_{ev} + \frac{1}{2}u_{p,i}^2) - \Phi_g^c\right]\delta(\overrightarrow{x} - \overrightarrow{x_p}) \tag{3.51}$$

In the context of Large-Eddy Simulation, these source terms are filtered, which involves replacing all the fluid quantities by their filtered counterparts:

$$\begin{aligned}
\overline{s}_{v,k}^{p-f}(x_i) &= -\sum_{p=1}^{N}\overline{\dot{m}}_p\delta(\overrightarrow{x} - \overrightarrow{x_p})\delta_{kv} \\
&= \pi d_p Sh[\overline{\rho}\overline{D}_v]\ln\left[\left(\frac{\widetilde{Y}_{v,\zeta} - \widetilde{Y}_{v,\infty}}{1 - \widetilde{Y}_{v,\zeta}}\right) + 1\right]\delta(\overrightarrow{x} - \overrightarrow{x_p})\delta_{kv} \qquad (3.52) \\
\overline{s}_{m,i}^{p-f}(x_i) &= -\sum_{p=1}^{N}\left[\frac{dm_p}{dt}u_{p,i} + F_{p,i}\right]\delta(\overrightarrow{x} - \overrightarrow{x_p}) \\
&= \sum_{p=1}^{N}\left[-\overline{\dot{m}}_p u_{p,i} - \frac{m_p}{\tau_p}\left(\widetilde{u}_i - u_{p,i}\right)\right]\delta(\overrightarrow{x} - \overrightarrow{x_p}) \qquad (3.53) \\
\overline{s}_{e}^{p-f}(x_{p,i}) &= \sum_{p=1}^{N}\left[-F_{p,i}u_{p,i} - \dot{m}_p(L_{ev} + \frac{1}{2}u_{p,i}^2) - \Phi_g^c\right]\delta(\overrightarrow{x} - \overrightarrow{x_p}) \\
&= \sum_{p=1}^{N}\left[-F_{p,i}u_{p,i} - \overline{\dot{m}}_p(L_{ev} + \frac{1}{2}u_{p,i}^2) - \lambda d_p Nu(\widetilde{T}_\zeta - \widetilde{T}_\infty)\frac{\ln(\overline{B}_T + 1)}{\overline{B}_T}\right] \\
&\quad \delta(\overrightarrow{x} - \overrightarrow{x_p}) \qquad (3.54)
\end{aligned}$$

3.3.2 Interaction with turbulence

Hinze [85] provided an early description of the modulation of a turbulent fluid flow laden with particles and evidenced the following fundamental mechanisms:

- local increase of shear due to the presence of particles which alters the spectrum of turbulent energy of the fluid phase in the range of interparticle distances
- turbulence generated in the wake of particles which locally alters the dynamics of turbulence
- modulation of turbulence due to the volume occupied by particles.

Longmire and Eaton [125] experimentally examined the behavior of a jet dominated by vortex ring structures laden with glass particles and reported that particles tended to accumulate in the low vorticity region between separate vortex rings. However, the authors did not observe any significant attenuation of turbulence or the development of instabilities within the gaseous jet due to the presence of particles. Kulick et al. [105] experimentally investigated a turbulent channel flow laden with particles and reported that the turbulence of the fluid phase was attenuated by the presence of particles, the attenuation being more pronounced at larger particle mass loadings and at larger particle relaxation time scales. Sato et al. [193] performed experimental studies of a vertical jet and demonstrated that the presence of particles in such a configuration led to a decrease of the Reynolds stresses, resulting in a lower production of turbulent kinetic energy. Fessler and Eaton [53] investigated the interaction between fluid turbulence and particles in a backward facing step flow. The authors found that the modulation of gas phase turbulence increased with the particle Reynolds number and the particle relaxation time. The authors also noted negligible attenuation of turbulence after the reattachment point of the fluid flow, where dynamics were mainly dictated by lingering effects from the shear layer at the separation point.

Squires and Eaton [210] performed Direct Numerical Simulations (DNS) of a statistically stationary turbulent flow laden with particles and found that the overall dissipation of turbulent kinetic energy increased with mass loading but that it was almost insensitive to the particle relaxation time. The authors related the different modulation of turbulence through particles of different sizes to the accumulation of small particles in zones of low vorticity or high strain. They called this phenomenon preferential concentration. Elgobashi and Truesdell [46] performed DNS's of decaying isotropic turbulence laden with particles and observed that the increased dissipation of turbulent kinetic energy by particles was the result of an accumulation of fluid energy at the small scales. The modulation of the turbulence spectrum at the small scales by the presence of particles was found to depend on particle size. Furthermore, the authors noted that the increased dissipation at the small scales increased the spectral energy transfer from the large to the small scales. Boivin et al. [21] performed DNS's of a statistically stationary turbulent flow laden with particles. The authors reported that while particles could add energy to the small scales of turbulence (particles "drag" the small eddies), resulting in an increased viscous dissipation, they could also remove energy from the larger scales of turbulence (large eddies "drag" the particles).

These considerations raise the question of a modification of the subgrid scale model when performing Large-Eddy Simulations of particle laden fluid flows. Boivin et al. [22] conducted Large-Eddy Simulations of a statistically stationary turbulent flow laden with particles accounting for two-way coupling and examined the behavior of various subgrid scale models. Their *a priori* and *a posteriori* analysis revealed that more complex subgrid scale models such as mixed models or the dynamic Smagorinsky model were able to correctly reproduce local energy fluxes and dissipation spectra in a statistically stationary turbulent flow without further modifications for particle relaxation times larger than the characteristic subgrid time scale. On the contrary, O'Kongo and Bellan [145] conducted DNS's of temporal mixing layers laden with evaporating particles and reported a strong impact of spray evaporation source terms on subgrid dissipation from an *a priori* analysis. In an *a posteriori* analysis, Leboissetier et al. [112] found the constant and dynamic coefficient Smagorinsky models to be overly dissipative for temporal mixing layers laden with particles. Scale similarity and dynamic gradient based models were more accurate in predicting overall dissipation and turbulent dispersion at the subgrid scales. However, it must be noted that these conclusions are restricted to this particular configuration where the flow must undergo transition from a laminar state to turbulence. In the present work, no modifications are applied to the subgrid scale model to account for the presence of particles.

3.4 Lagrangian Monte-Carlo approach

The previous derivations considered the interaction between particles and the flow field from a deterministic point of view. Such an approach assumes that all flow field scales are explicitly resolved, which is not the case when using RANS or LES methods for the simulation of the fluid phase. In the latter, only the averaged or the filtered flow field is known at a given instant. Thus, the interaction between particles and the flow field may not be entirely evaluated in a deterministic manner and the effect of the unresolved flow field scales on the particles must be reconstructed through a stochastic procedure. For this reason, a statistical point of view is adopted and the particles are viewed as samples of the physical spray. These methods are called stochastic / Monte Carlo Lagrangian approaches. In such methods, a set of M independent variables which allows to fully describe a particle j is chosen:

$$\Phi_j(t) = \phi^+_{j,1}(x^0_i, t), \dots, \phi^+_{j,M}(x^0_i, t) \tag{3.55}$$

with:

$$\phi^+_{j,1}(x^0_i, t) = \phi_{j,1}(x^+(x^0_i, t), t) \tag{3.56}$$

where $x^+(x^0_i, t)$ represents the location (at the time t) of the particle initially located at $x_i = x^0_i$. This allows to define the fine-grained density function $\mathcal{F}$ as:

$$\mathcal{F}(\Psi, x_i; t|x^0_i) = \sum_{j=1}^{N} \prod_{i=1}^{M} \delta[\phi^+_{j,i}(x^0_i, t) - \psi_i] \tag{3.57}$$

where ψ_i represents the phase composition space of the quantity $\phi_i(t)$ and δ denotes the Dirac delta function. Note that the fine-grained density function is conditional upon the initial particle location x^0_i but not its initial properties [162]. If convergence to a limiting value is ensured for a large number of realizations N, $\mathcal{F}$ becomes the Lagrangian fine-grained probability density function $\mathcal{P}$ [17]:

$$\mathcal{P}(\Psi, x_i; t|x^0_i) = \sum_{j=1}^{N} \prod_{i=1}^{M} \delta[\phi^+_{j,i}(x^0_i, t) - \psi_i] \tag{3.58}$$

In the following, the functional dependencies of $\phi^+_{j,i}(x^0_i, t)$ are omitted for convenience. The partial differentiation of eq. 3.58 yields:

$$\begin{aligned}
\frac{\partial \mathcal{P}(\Psi, x_i; t|x^0_i)}{\partial t} &= \frac{\partial}{\partial t} \sum_{j=1}^{N} \prod_{i=1}^{M} \delta[\phi^+_{j,i} - \psi_i] \\
&= \sum_{j=1}^{N} \prod_{i=1}^{M} \frac{\partial \phi^+_{j,i}}{\partial t} \frac{\partial \delta[\phi^+_{j,i} - \psi_i]}{\partial \phi^+_{j,i}} \\
&= -\sum_{j=1}^{N} \prod_{i=1}^{M} \frac{\partial \phi^+_{j,i}}{\partial t} \frac{\partial \delta[\phi^+_{j,i} - \psi_i]}{\partial \psi_i} \\
&= -\sum_{j=1}^{N} \prod_{i=1}^{M} \frac{\partial}{\partial \psi_i} \left[\frac{\partial \phi^+_{j,i}}{\partial t} \delta[\phi^+_{j,i} - \psi_i] \right] \\
&= -\sum_{j=1}^{N} \frac{\partial}{\partial \psi_i} \left\langle \frac{d\psi_i}{dt} |_{\Psi=\Phi} \right\rangle \mathcal{P}(\Psi, x_i; t|x^0_i)
\end{aligned} \tag{3.59}$$

with $\langle d\psi_i/dt|_{\Psi=\Phi} \rangle$ the temporal rate of change of the state space coordinate ϕ_i conditioned upon the particles found at state $\Psi = \Phi$. For example, chosing a state space $\Phi = \{c_{p,i}(x^0_i, t), \mu_p(x^0_i, t), \zeta_p(x^0_i, t)\}$, respectively composed of the particle's velocities $u_{p,i}$, mass m_p and temperature T_p, the evolution of the joint probability density function $\mathcal{P}(u_{p,i}, T_p, m_p, x_i; t, x^0_i)$ may be written as:

$$\frac{\partial \mathcal{P}}{\partial t} + \frac{\partial}{\partial c_{p,i}} \left\langle \frac{du_{p,i}}{dt} \bigg|_{\Psi=\Phi} \right\rangle \mathcal{P} + \frac{\partial}{d\mu_p} \left\langle \frac{dm_p}{dt} \bigg|_{\Psi=\Phi} \right\rangle \mathcal{P} + \frac{\partial}{\partial \zeta_p} \left\langle \frac{dT_p}{dt} \bigg|_{\Psi=\Phi} \right\rangle \mathcal{P} = 0 \tag{3.60}$$

where functional dependencies have been omitted for better lisibility. Moreover, the absence of coalescence and breakup phenomena has been assumed for simplicity. In the context of LES, this equation is filtered:

$$\frac{\partial \overline{\mathcal{P}}}{\partial t} + \frac{\partial}{\partial c_{p,i}} \left\langle \left. \frac{du_{p,i}}{dt} \right|_{\Psi=\Phi} \right\rangle \overline{\mathcal{P}} + \frac{\partial}{d\mu_p} \left\langle \left. \frac{dm_p}{dt} \right|_{\Psi=\Phi} \right\rangle \overline{\mathcal{P}} + \frac{\partial}{\partial \zeta_p} \left\langle \left. \frac{dT_p}{dt} \right|_{\Psi=\Phi} \right\rangle \overline{\mathcal{P}} = 0 \tag{3.61}$$

In order to close eq. 3.61, the conditional rates of change of each state coordinate must be evaluated. Making the same assumptions than in section 3.1.3 for the particle momentum equation (all forces except drag and gravity are neglected), one obtains:

$$\frac{du_{p,i}}{dt} = \frac{1}{\tau_p}(\widetilde{u}_i - u_{p,i}) + \frac{1}{\tau_p} u_i' + g_i \tag{3.62}$$

The first term on the right-hand side of eq. 3.62 corresponds to the contribution from the filtered velocity field while the second term represents contributions from the unresolved scales, which must be reconstructed in a stochastic manner. For LES, different modeling approaches to evaluate the subgrid-scale fluid velocity u_i' may be found in the literature.

The first method is based on the resolution of a simplified Langevin equation [164, 16] to reconstruct the fluid fluctuation velocity along the particle trajectory. Written as a stochastic differential equation, the simplified Langevin equation is:

$$du_i'(t) = -u_i'(t)\frac{dt}{T} + \sqrt{\frac{4k}{T}} dW_i(t) \tag{3.63}$$

where k, T respectively denote the subgrid-scale kinetic energy and the Lagrangian integral time scale. $W(t)$ is a vector-valued Wiener process with zero mean and variance dt:

$$\langle dW_i \rangle = 0 \tag{3.64}$$

$$\langle dW_i dW_j \rangle = dt\, \delta_{ij} \tag{3.65}$$

Eq. 3.63 is consistent with the fundamental properties of homogeneous isotropic turbulence at high Reynolds numbers [164]. However, experimental findings [227] have shown that the probability density functions of particle acceleration in homogeneous istrotropic turbulence are far from Gaussianity, heavy-tailed and that they display intermittent character. These behaviors may not be reproduced by eq. 3.63 and a more general formulation of the Langevin equations have recently been proposed, for instance by Bini and Jones [16]. Bini and Jones [17] reported a substantial improvement of particle properties and dispersion at the subgrid scale for the LES of a particle laden mixing layer using this model.

Other methods reconstruct the subgrid scale velocity through an inverse filtering operation referred to as deconvolution [213]. This method is based on the approximation of the inverse LES filter kernel $G_{\bar{\Delta}}$ by a truncated Van Cittert expansion [213]:

$$G_{\bar{\Delta}}^{-1} = \sum_{\alpha=1}^{N} (I - G_{\bar{\Delta}})^{\alpha} \tag{3.66}$$

where I denotes the identity operator. Shotorban and Mashayek [204] used this approach and investigated the impact of the fluctuating fluid velocity on turbulent dispersion in a particle-laden homogeneous shear flow by *a priori* and *a posteriori* comparisons between DNS and LES data. The authors reported a significant improvement in particle statistics when reconstructing the subgrid-scale fluid velocity. However, Kuerten [104] reported that the gains obtained with such procedure in the predicition of near wall particle accumulation could be lost when using inaccurate interpolation operators to reconstruct fluid properties at the particle locations. To evaluate subgrid scale fluctations at the particle location, Patel and Menon [153] used the Liner-Eddy Model (LEM) approach for the two-phase flow LES of lean direct injection in a combustor. In the LEM framework, subgrid processes are described on a one-dimensional domain embedded inside each computational cell. Evolution equations for the subgrid scale quantities are then derived on this embedded grid.

More generally, the effect of subgrid scale fluctuations on particle drag must not necessarily be included in LES as the latter only becomes significant when the particle Stokes number based on the Kolmogorov time scale τ_η approaches unity [137, 50]. Furthermore, Apte et al. [3] observed that the direct effect of the unresolved scales on particle statistics were small for swirling separated flows with subgrid scale energy contents much smaller than those of the resolved scales. This assumption is also made in the present work and the fluid subgrid contributions at the particle location are neglected for both drag and evaporation.

3.5 Mesoscopic Eulerian approach

In the Euler-Euler approach, the description of the history of each particle is replaced by the description of the spray's mean properties, regarding it as a continuous fluid. The averaging procedure to obtain the mean may be carried out in a volumetric or statistical sense, leading to two different formulations for the dispersed phase, whose systems of equations are however very similar [97]. In the following, only the main steps leading to the derivation of the Eulerian set of equations for the dispersed phase are summarized. For more detailed descriptions, the reader is referred to Kaufmann [97] and Boileau [19].

The equations for the Eulerian treatment of the dispersed phase are derived within the same framework as the Lagrangian Monte-Carlo approach, starting from eq. 3.58. However, the probability density function (pdf) is now conditioned by a particular realization of the fluid phase denoted $\mathcal{H}_f$:

$$f_p(c_{p,i}, \zeta_p, \mu_p, x_i, t, \mathcal{H}_f) = \langle \mathcal{P}(c_{p,i}, \zeta_p, \mu_p, x_i, t) | \mathcal{H}_f \rangle \rangle \tag{3.67}$$

The Eulerian probability density function also verifies a Boltzmann-type equation for the chosen state space variables:

$$\frac{\partial}{\partial t} f_p + \frac{\partial}{\partial x_j} u_{p,j} f_p + \frac{\partial}{\partial c_{p,i}} \left\langle \frac{\partial u_{p,i}}{\partial t} \middle| c_{p,i}, \zeta_p, \mu_p \right\rangle f_p + \frac{\partial}{\partial \mu_p} \left\langle \frac{\partial m_p}{\partial t} \middle| c_{p,i}, \zeta_p, \mu_p \right\rangle f_p + \frac{\partial}{\partial \zeta_p} \left\langle \frac{\partial T_p}{\partial t} \middle| c_{p,i}, \zeta_p, \mu_p \right\rangle f_p = \left(\frac{\partial}{\partial t} f_p \right)_{coll} \tag{3.68}$$

The phase average of any particle function $\psi(c_{p,i}, \zeta_p, \mu_p)$ is defined as its integration over the entire phase space, i.e. the entire possible realizations of this given function. The phase average is weighted by the particle mass, which allows to simplify the resulting set of equations. One obtains:

$$\breve{\psi} = \langle \psi \rangle_l = \frac{1}{\rho_l \breve{\alpha}_l} \int \psi(c_{p,i}, \zeta_p, \mu_p) f_p(c_{p,i}, \zeta_p, \mu_p, x_i, t, \mathcal{H}_f) dc_{p,i} d\zeta_p d\mu_p \tag{3.69}$$

α_l denotes the liquid volume fraction:

$$\alpha_l = \frac{\pi}{6} n_l d_l^3 \tag{3.70}$$

and:

$$\rho_l \breve{\alpha}_l = \int \mu_p f_p(c_{p,i}, \zeta_p, \mu_p, x_i, t, \mathcal{H}_f) dc_{p,i} d\zeta_p d\mu_p \tag{3.71}$$

Eq. 3.69 yields the instantaneous local mean value of a given particle quantity conditioned by the given fluid phase realization, referred to as the mesoscopic quantity. The deviation from this mean, denoted by the superscript $(\cdot)''$, is the random uncorrelated part:

$$\psi_l = \langle \psi \rangle_l + \psi_l'' \qquad \text{with} \qquad \langle \psi_l'' \rangle_l = 0 \tag{3.72}$$

similarly to the Reynolds-averaged Navier-Stokes equations. Replacing $\breve{\psi}_l$ with the particle velocity $u_{p,i}$ gives the local instantaneous mean velocity of the liquid spray, conditioned on the gaseous flow realization $\mathcal{H}_f$:

$$\breve{u}_{l,i}(x_i, t | \mathcal{H}_f) = \langle u_{p,i} \rangle_l \tag{3.73}$$

In the spray, a set of particles share the the same mesoscopic motion $\breve{u}_{l,i}$ while each particle has its own motion at the uncorrelated velocity $u''_{p,i}$. The modeling of the uncorrelated motion introduces a number of additional quantities. Among these are the uncorrelated velocity tensor $\delta\breve{R}_l$:

$$\delta\breve{R}_{l,ij}(x_i, t|\mathcal{H}_f) = \langle u''_{p,i} u''_{p,j} \rangle_l \tag{3.74}$$

and the uncorrelated energy $\delta\breve{\theta}_l$:

$$\delta\breve{\theta}_l = \frac{1}{2} \langle u''_{p,i} u''_{p,i} \rangle_l \tag{3.75}$$

From eqs. 3.74 and 3.75, it appears that $\delta\breve{\theta}_l$ if the half-trace of the uncorrelated velocity tensor and that it obeys a transport equation. The deviatoric part of the uncorrelated velocity tensor is noted $\delta\breve{R}^*_{l,ij}$:

$$\delta\breve{R}^*_{l,ij} = \delta\breve{R}_{l,ij} - \frac{2}{3}\delta\breve{\theta}_l \delta_{ij} \tag{3.76}$$

with δ_{ij} the Kronecker symbol, which is unity for equal indices and zero for distinct indices.

Multiplying eq. 3.68 with any particle function ψ and integrating over the state space yields the evolution equation for this quantity, called *the general form of the Enskog equation* of the function ψ:

$$\begin{aligned} \frac{\partial}{\partial t}\rho_l \breve{\alpha}_l \langle \breve{\psi} \rangle_l + \frac{\partial}{\partial x_j}\rho_l \breve{\alpha}_l \langle \breve{u}_{l,i} \breve{\psi} \rangle_l = -\frac{\partial}{\partial x_j}\rho_l \breve{\alpha}_l \langle u''_{l,i} \psi \rangle_l + \rho_l \breve{\alpha}_l \left\langle \frac{\partial u_{p,i}}{\partial t} \frac{\partial \psi}{\partial u_{p,i}} \right\rangle_l + \\ \rho_l \breve{\alpha}_l \left\langle \frac{\partial T_p}{\partial t} \frac{\partial \psi}{\partial T_p} \right\rangle_l + \rho_l \breve{\alpha}_l \left\langle \frac{\partial m_p}{\partial t} \frac{\partial \psi}{\partial m_p} \right\rangle_l \end{aligned} \tag{3.77}$$

The first term on the right-hand side of eq. 3.77 is called uncorrelated flux operator, it is also abreviated by $\mathbf{T}(\psi)$. Similarly to the Reynolds-averaged Navier-Stokes equations, this term is unclosed and requires modeling. When the function ψ varies both in time and space, for instance the uncorrelated energy defined in eq. 3.75, additional terms appear in the right-hand side of eq. 3.77:

$$\rho_l \breve{\alpha}_l \left\langle \frac{\partial}{\partial t}\psi \right\rangle_l + \rho_l \breve{\alpha}_l \left\langle u_{p,i} \frac{\partial}{\partial x_j}\psi \right\rangle_l \tag{3.78}$$

The set of Eulerian conservation equations characterizing the spray may now be derived. To simplifiy the description, the following main assumptions are made:

- H1: all particles have locally the same diameter: the spray is monodisperse.
- H2: all particles have locally the same temperature.
- H3: the particles remain spherical.
- H4: the particle diameters are small compared to unity.
- H5: the density ratio between particle and fluid phases is large compared to unity, typically $\rho_p/\rho \sim \mathcal{O}(10^3)$.
- H6: the liquid volume fraction remains small so that all particle interactions are negligible and that the fluid phase is undisturbed by the presence of the dispersed phase. This justifies the conditioning of the probability density function by one realization of the fluid phase (eq. 3.67).

The hypotheses H4 and H5 are also made in the Lagrangian approach to neglect all forces but drag and to simplify the expression of the gravity force. However, H1-H3 are additional restrictions to the spray characteristics compared to the Lagangian framework. Finally, H6 prohibits the simulation of dense spray zones with the Eulerian approach. Note that this assumption may also become questionable in reactive simulations where coupling effects between phases are pronounced.

The evolution equation of number density is obtained by taking $\psi = 1/m_p$:

$$\frac{\partial \breve{n}_l}{\partial t} + \frac{\partial \breve{n}_l \breve{u}_{l,j}}{\partial x_j} = \mathbf{T}(\frac{1}{m_p}) + \mathbf{C}(1) \tag{3.79}$$

Since the spray is locally monodisperse, all particles locally have the same mass and $\mathbf{T}(\frac{1}{m_p}) = -\frac{\partial}{\partial x_j}\rho_l \breve{\alpha}_l \langle u''_{l,i}\frac{1}{m_p}\rangle_l = 0$. Furthermore, collisions, denoted by the operator $\mathbf{C}(1)$ are neglected according to H5.

The evolution equation of liquid volumetric mass fraction is obtained by taking $\psi = 1$:

$$\frac{\partial \rho_l \breve{\alpha}_l}{\partial t} + \frac{\partial \rho_l \breve{\alpha}_l \breve{u}_{l,j}}{\partial x_j} = \mathbf{T}(1) + \mathbf{C}(m_p) + \Gamma_l \tag{3.80}$$

$\mathbf{T}(1)$ vanishes according to eq. 3.72 and collisions are neglected. $\Gamma_l = \rho_l \breve{\alpha}_l \left\langle \frac{1}{m_p}\frac{dm_p}{dt} \right\rangle$ denotes the mass exchange with the gaseous phase through evaporation.

The evolution equation of liquid momentum is obtained by taking $\psi = u_{p,i}$:

$$\frac{\partial \rho_l \breve{\alpha}_l \breve{u}_{l,i}}{\partial t} + \frac{\partial \rho_l \breve{\alpha}_l \breve{u}_{l,i}\breve{u}_{l,j}}{\partial x_j} = \mathbf{T}(u''_{p,i}) + \mathbf{C}(u''_{p,i}) + \Gamma_{u,i} + F_{d,i} + \mathbf{T}(u''_{p,i}) \tag{3.81}$$

$\mathbf{T}(u''_{p,i})$ represents the transport of momentum by the uncorrelated motion. $\mathbf{C}(u''_{p,i})$ describes the exchange of momentum through particle-particle interactions and is neglected. $F_{d,i} = \rho_l \breve{\alpha}_l \left\langle \frac{F_{p,i}}{m_p} \right\rangle$ denotes the exchange of momentum with the gaseous phase via the drag force $F_{p,i}$ exerted upon each particle. $\Gamma_{u,i} = \rho_l \breve{\alpha}_l \left\langle \frac{u_{p,i}}{m_p}\frac{dm_p}{dt} \right\rangle$ represents the exchange of momentum through evaporation. Since all particles have the same temperature and diameter, it reduces to $\Gamma_{u,i} = \Gamma \breve{u}_l$.

The evolution equation of uncorrelated energy is obtained by taking $\psi = \frac{1}{2}\langle u''_{p,i}u''_{p,i}\rangle$:

$$\frac{\partial \rho_l \breve{\alpha}_l \breve{\theta}_l}{\partial t} + \frac{\partial \rho_l \breve{\alpha}_l \breve{\theta}_l}{\partial x_j} = \mathbf{T}(\frac{1}{2}u''_{p,i}u''_{p,i}) + \mathbf{C}(m_p u_{p,i}) + \mathbf{U}_\theta + W_\theta + \Gamma_\theta \tag{3.82}$$

$\mathbf{T}(\frac{1}{2}u''_{p,i}u''_{p,i})$ represents the transport of uncorrelated energy by the uncorrelated motion. $\mathbf{C}(m_p u_{p,i})$ is the exchange of uncorrelated energy between particles, it is neglected. $W_\theta = \rho_l \breve{\alpha}_l \left\langle u''_{p,i}\frac{F_{p,i}}{m_p} \right\rangle$ denotes the variation of uncorrelated energy through the drag force. Similarly, Γ_θ is the variation of uncorrelated energy through evaporation, it simplifies to $\Gamma_\theta = \Gamma \breve{\theta}_l$

Finally, the evolution of liquid enthalpy is obtained by taking $\psi = h_{s,p}$:

$$\frac{\partial \rho_l \breve{\alpha}_l \breve{h}_{s,l}}{\partial t} + \frac{\partial \rho_l \breve{\alpha}_l \breve{h}_{s,l}}{\partial x_j} = \Pi_l + \mathbf{T}(h''_{s,p}) + \mathbf{C}(m_p h''_{s,p}) \tag{3.83}$$

$\mathbf{T}(h''_{s,p})$ represents the transport of liquid enthalpy through the random uncorrelated motion. $\mathbf{C}(m_p h''_{s,p})$ is the exchange of enthaply through particle-particle interactions, it is neglected. Π_l is the sensible enthalpy change rate through evaporation.

In the context of LES, the Eulerian set of equations describing the particle phase needs to be filtered. The filtering procedure for the particle phase is identical to that for the fluid phase. By analogy with mass-weighted filtering of the fluid phase, a Favre average for the dispersed phase is introduced by using the mesoscopic liquid volume fraction $\breve{\alpha}_l$:

$$\overline{\breve{\alpha}_l}\widehat{f_l} = \overline{\breve{\alpha}_l \breve{f}_l} \tag{3.84}$$

In order to obtain an equivalence between the Favre average based on the liquid volume fraction and the droplet number density, the assumption of a monodisperse spray at the filter size is made ($\overline{d} = d$):

$$\overline{\breve{n}_l \breve{f}_l} = \overline{\frac{6\breve{\alpha}_l}{\pi d^3}\breve{f}_l} = \frac{6}{\pi d^3}\overline{\alpha_l}\breve{f}_l = \overline{n}_l \breve{f}_l \tag{3.85}$$

Applying the filter operator to eqs. 3.80-3.83 yields the following governing set of equations for the particle phase:

$$\begin{array}{rcrcrcrcrr}
\dfrac{\partial \overline{n}_l}{\partial t} & + & \dfrac{\partial \overline{n}_l \widehat{u}_{l,j}}{\partial x_j} & = & 0 & + & 0 & + & 0 & (3.86) \\
\dfrac{\partial \rho_l \overline{\alpha}_l}{\partial t} & + & \dfrac{\partial \rho_l \overline{\alpha}_l \widehat{u}_{l,j}}{\partial x_j} & = & 0 & + & 0 & + & \overline{s}_{\alpha}^{p-f} & (3.87) \\
\dfrac{\partial \rho_l \overline{\alpha}_l \widehat{u}_{l,i}}{\partial t} & + & \dfrac{\partial \rho_l \overline{\alpha}_l \widehat{u}_{l,j}\widehat{u}_{l,i}}{\partial x_j} & = & \dfrac{\partial \tau_{l,ij}^{sgs}}{\partial x_j} & + & \mathbf{T}(u''_{p,i}) & + & \overline{s}_{m}^{p-f} & (3.88) \\
\dfrac{\partial \rho_l \overline{\alpha}_l \widehat{\theta}_l}{\partial t} & + & \dfrac{\partial \rho_l \overline{\alpha}_l \widehat{u}_{l,i}\widehat{u}_{l,j}}{\partial x_j} & = & \dfrac{\partial q_{\theta,i}^{sgs}}{\partial x_i} & + & \mathbf{T}(\dfrac{1}{2}u''_{p,i}u''_{p,i}) & + & \overline{s}_{\theta,i}^{p-f} & (3.89) \\
\dfrac{\partial \rho_l \overline{\alpha}_l \widehat{h}_{s,l}}{\partial t} & + & \dfrac{\partial \rho_l \overline{\alpha}_l \widehat{h}_{s,l}\widehat{u}_{l,j}}{\partial x_j} & = & \dfrac{\partial q_{h_l,i}^{sgs}}{\partial x_i} & + & & + & \overline{s}_{hl,i}^{p-f} & (3.90) \\
\text{temporal} & & \text{mesoscopic} & & \text{subgrid-scale} & & \text{uncorrelated} & & \text{source} & \\
\text{evolution} & & \text{movement} & & \text{fluxes} & & \text{movement} & & \text{terms} &
\end{array}$$

The subgrid-scale fluxes are written as follows:

$$\tau_{l,ij}^{sgs} = \rho_l \overline{\alpha}_l (\widehat{u_{l,j} u_{l,i}} - \widehat{u}_{l,j}\widehat{u}_{l,i}) \tag{3.91}$$

$$q_{\theta,i}^{sgs} = \rho_l \overline{\alpha}_l (\widehat{u_{l,j}\delta\theta} - \widehat{u}_{l,j}\widehat{\delta\theta}) \tag{3.92}$$

$$q_{h_l,i}^{sgs} = \rho_l \overline{\alpha}_l (\widehat{u_{l,j} h_{l,i}} - \widehat{u}_{l,j}\widehat{h}_{l,i}) \tag{3.93}$$

The modeling of the subgrid scale fluxes and the source terms is not discussed and the reader is referred to Riber [178] and Boileau [19] for details on these aspects. However, note that the drag and evaporation models implemented in the Euler-Lagrange and Euler-Euler approaches are strictly identical in order to allow for direct comparisons between them.

3.6 Characteristic diameters of a spray

To characterize droplet sprays, different representative diameters are defined in the literature [8]. The most common is the mean particle diameter, which is denoted $d_{p,m}$ or d_{10} in the present work. It is defined as the arithmetic diameter average within a group of N particles:

$$d_{p,m} = d_{10} = \frac{1}{N}\sum_{i=1}^{N} d_{p,i} \tag{3.94}$$

Alternatively, for a sample divided into k diameter classes, eq. 3.95 may be rewritten as:

$$d_{p,m} = d_{10} = \frac{1}{N} \sum_{i=1}^{k} N_i d_{p,i} \tag{3.95}$$

More generally, all representative spray diameters may be calulated from the following formula:

$$d_{mn} = \frac{\sum_{i=1}^{N} d_{p,i}^{m}}{\sum_{i=1}^{N} d_{p,i}^{n}} = \frac{\sum_{i=1}^{k} N_i d_{p,i}^{m}}{\sum_{i=1}^{k} N_i d_{p,i}^{n}} \tag{3.96}$$

The Sauter mean diameter d_{32} is also often used in practice:

$$d_{32} = \frac{\sum_{i=1}^{N} d_{p,i}^{3}}{\sum_{i=1}^{N} d_{p,i}^{2}} \tag{3.97}$$

The Sauter mean diameter (SMD) describes the average ratio of volume to surface of the spray and represents an important quantity for evaporating flows. Finally, note that for a continuous size distribution described by a function f, eq. 3.96 writes:

$$d_{mn} = \frac{\int_0^\infty f(d_p) d_p^m dd_p}{\int_0^\infty f(d_p) d_p^n dd_p} \tag{3.98}$$

Chapter 4

Numerics

4.1 The LES solver AVBP

The LES code AVBP solves the compressible Navier-Stokes equations on unstructured hybrid meshes. It relies on a cell-vertex discretization, i.e. variables are stored at nodes while conservation laws are integrated inside the elements. AVBP was designed for parallel simulations and contains a very efficient parallel library named MPL. The basic numerical tools of AVBP were implemented by Rudgyard and Schönfeld [200] in collaboration with the University of Oxford. Lartigue [108] added characteristic decomposition according to the Navier-Stokes Characteristic Boundary Condition (NSCBC) formalism [160] and extended the code to handle multi-component flows [141]. Colin [34] implemented an efficient low dissipative two step Taylor-Galerkin scheme called TTGC which showed to be very well suited for accurate LES's. Moureau [141] implemented mesh deformation into AVBP using an Arbitrary Lagrangian Eulerian (ALE) technique. Two-phase flow modules were added by Kaufmann [97] for the Eulerian treatment of the dispersed phase and by García [63] for the Lagrangian particle tracking technique. Recently, the residual distribution scheme PSI [214] was implemented by Lamarque and Roux [184] to numerically handle the strong discontinuities present in the Eulerian representation of the dispersed phase. Finally, generalized thermodynamic laws accounting for real gas behavior in the vicinity of the critical point were included by Schmitt [199].

4.2 The finite volume approach

The finite difference method relies on a concurrence between geometrical and computational data. Hence, there is no need to store connectivities and neighbouring elements may be directly identified, allowing a more straightforward implementation and in particular an easy design of high-order numerical schemes. However, making the geometrical and computational data coincide imposes severe constraints on the topology of the computational mesh and one must resort to finite volume or finite element approaches for the simulation of realistic geometries.

4.2.1 Domain discretization

A compact formulation of the compressible Navier-Stokes equations (eqs. 2.1-2.3) is considered. Source terms are omitted in a first step for simplicity. Proper initial and boundary conditions are assumed, yielding:

$$\frac{\partial \vec{w}}{\partial t} + \nabla \cdot \overline{\overline{\mathcal{F}}} = 0 \qquad \text{in} \qquad \Omega_T \subset \mathbb{R}^d \times \mathbb{R}^+ \tag{4.1}$$

$$\overrightarrow{w}(\overrightarrow{x}, t=0) = \overrightarrow{w}_0 \qquad \text{in} \qquad \mathbb{R}^+ \tag{4.2}$$

with:

$$\overrightarrow{w} = (\rho\overrightarrow{u}, \rho E, \rho_k)^T \tag{4.3}$$

The flux tensor of conservative variables $\overline{\overline{\mathcal{F}}}$ is decomposed into its inviscid (superscript "i") and viscous components (superscript "v") as their numerical treatment is different:

$$\overline{\overline{\mathcal{F}}} = \overline{\overline{\mathcal{F}^i}}(\overrightarrow{w}) + \overline{\overline{\mathcal{F}^v}}(\overrightarrow{w}, \nabla\overrightarrow{w}) \tag{4.4}$$

with:

$$\overline{\overline{\mathcal{F}^{\mathbf{i}}}}(\overrightarrow{w}) = \begin{pmatrix} \rho u^2 + p & \rho uv & \rho uw \\ \rho vu & \rho v^2 + p & \rho vw \\ \rho wu & \rho wv & \rho w^2 + p \\ (\rho E + p)u & (\rho E + p)v & (\rho E + p)w \\ \rho_k u & \rho_k v & \rho_k w \end{pmatrix} \tag{4.5}$$

and:

$$\overline{\overline{\mathcal{F}^{\mathbf{v}}}}(\overrightarrow{w}) = \begin{pmatrix} -\tau_{xx} & -\tau_{xy} & -\tau_{xz} \\ -\tau_{yx} & -\tau_{yy} & -\tau_{yz} \\ -\tau_{zx} & -\tau_{zy} & -\tau_{zz} \\ u_i\tau_{xi} + q_x & u_i\tau_{yi} + q_y & u_i\tau_{zi} + q_z \\ J_{x,k} & J_{y,k} & J_{z,k} \end{pmatrix} \tag{4.6}$$

The first step in the numerical solution of systems of conservation laws consists in the tesselation of the spatial domain into a set of non-overlapping geometrical control volumes that completely cover the domain:

$$\Omega = \bigcup_{K_e \in T_h} K_e \tag{4.7}$$

In the following, only conformal tesselations will be considered, which means that faces of adjacent elements always coincide. In each control volume, a conservation law is imposed. Spatial integration of eq. 4.1 and the use of the Green-Gauss theorem lead to:

$$\frac{\partial}{\partial t}\int_{\Omega} \overrightarrow{w}\, d\nu + \oint_{\partial\Omega} \overline{\overline{\mathcal{F}}} \cdot \overrightarrow{n}\, ds = 0 \tag{4.8}$$

In the finite volume context, the choice of the control volumes on which the conservation laws are integrated is flexible. Furthermore, variables need not necessarily be stored at the mesh nodes. Three major approaches may be distinguished:

- cell-centered methods, where variables are stored at the cell centers and conservation laws are integrated over the geometric control volumes of the mesh. These control volumes are referred to as primary cells (see fig. 4.1).
- vertex-centered methods, where variables are also stored at the cell centers. However, the computational control volumes are now formed by joining median segments or centroid segments of the primary cells. These control volumes are called dual cells (see fig. 4.1).
- cell-vertex methods, where variables are stored at the element nodes and the computational control volumes are taken as the primary cells.

The cell-vertex method is the discretization method of the AVBP solver and is discussed in more detail in the following.

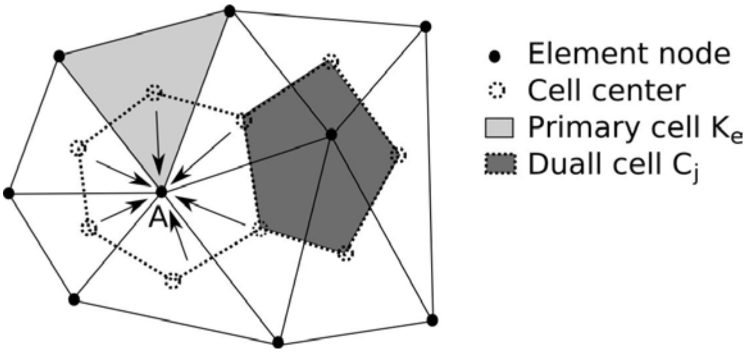

Figure 4.1 : *Illustration of the cell-vertex method. The plain lines and circles represent the nodes and the computational control volumes of the mesh (primary cell K_e). In the cell-vertex method, the variables are stored at the nodes and the integration volume is the primary cell. In order to obtain the temporal update of the node A, contributions from all its direct neighbours are summed (scatter operation). The dual cell C_j (dashed lines) is defined by joining the cell centers or the median segments of the primary cells.*

4.2.2 Cell-vertex approach

In the cell-vertex approach, the variables are stored at the element nodes. The computational control volumes used for the evaluation of the residual are the primary cells. An illustration of the cell-vertex approach is given in fig. 4.1.

The residual $\overrightarrow{r}_e$ inside each element K_e is defined as:

$$\overrightarrow{r}_e := \frac{1}{V_e}\int_{K_e} \nabla\cdot\overline{\overline{\mathcal{F}}}d\nu = \frac{1}{V_e}\int_{\partial K_e}\overline{\overline{\mathcal{F}}}\cdot\overrightarrow{n}ds \tag{4.9}$$

with V_e the volume of the element K_e. The computation of this residual requires the definition of normal vectors and a numerical approximation of the fluxes. In AVBP, normal vectors are defined at the vertices of an element as the sum of the normal vectors of the adjacent faces:

$$\overrightarrow{s}_k = \sum_{k\in f} -\frac{n_d}{n_v^f}\overrightarrow{s}_f \tag{4.10}$$

with n_d and n_v^f respectively the number of dimensions and the number of vertices of the face f. The face normals are weighted by the face area and the normals at the vertices point inwards, leading to an opposite sign in the following derivations. Directly evaluating the fluxes at the element nodes is equivalent to a linear average of the fluxes over the element faces:

$$\sum_{f\in K_e}\left(\sum_{k\in f}\frac{1}{n_v^f}\overline{\overline{\mathcal{F}}}_k\right)\overrightarrow{s}_f = -\frac{1}{n_d}\sum_{k\in K_e}\overline{\overline{\mathcal{F}}}_k\cdot\overrightarrow{s}_k \tag{4.11}$$

From eqs. 4.9 and 4.11, the numerical approximation of the residual is obtained as:

$$\overrightarrow{r}_e = -\frac{1}{n_d V_e}\sum_{k\in K_e}\overline{\overline{\mathcal{F}}}_k\cdot\overrightarrow{s}_k \tag{4.12}$$

The volume V_e is evaluated using the relation $\nabla\cdot\overrightarrow{x} = n_d$:

$$V_e = \frac{1}{n_d^2}\sum_{k\in K_e}\overrightarrow{x}_k\cdot\overrightarrow{s}_k \tag{4.13}$$

In order to obtain the temporal update of the node j, an average of the residuals in the cells sharing this node is performed. This average is called scatter operation and leads to the following spatial discretization:

$$\mathcal{L}_j = \frac{1}{V_j} \sum_{e \in D_j} \overline{\overline{D}}_{j,e} \overrightarrow{r}_e V_e \tag{4.14}$$

V_j and $\overline{\overline{D}}_{j,e}$ respectively represent the volume of the dual cell and the residual distribution matrix of the node j. In the semi-discrete form (omitting temporal discretization), one obtains:

$$\frac{d\overrightarrow{w}_j}{dt} = -\mathcal{L}_j \tag{4.15}$$

The derivation of the residual distribution matrix and details of the temporal discretization are provided in the following.

4.3 Convective schemes in AVBP

The present section describes the discretization of convective fluxes for the numerical schemes which are used in the present applications, namely the Lax-Wendroff scheme [110] and the TTG schemes. A much more detailed review of the numerical tools implemented in AVBP may be found in the thesis of Lamarque [107].

4.3.1 The Lax-Wendroff scheme

The Lax-Wendroff scheme [110] combines temporal and spatial discretizations. A Taylor expansion of the time solution vector based on the previous iteration is performed:

$$\overrightarrow{w}^{n+1} = \overrightarrow{w}^{n} + \left.\frac{\partial \overrightarrow{w}}{\partial t}\right|^{n} \Delta t + \frac{1}{2} \left.\frac{\partial^2 \overrightarrow{w}}{\partial t^2}\right|^{n} \Delta t^2 + \mathcal{O}(\Delta t^3) \tag{4.16}$$

The first-order time derivative is equal to the divergence of the fluxes, see eq. 4.1. For the second order derivative, one may write:

$$\frac{\partial^2 \overrightarrow{w}}{\partial t^2} = -\nabla \cdot \frac{\partial \overline{\overline{\mathcal{F}^i}}}{\partial t} = -\nabla \cdot \frac{\partial \overline{\overline{\mathcal{F}^i}}}{\partial \overrightarrow{w}} \frac{\partial \overrightarrow{w}}{\partial t} = \nabla \cdot \overline{\overline{\overline{\mathcal{A}}}} \nabla \cdot \overline{\overline{\mathcal{F}^i}} \tag{4.17}$$

with $\overline{\overline{\overline{\mathcal{A}}}}$ the Jacobian of the inviscid fluxes $\overline{\overline{\mathcal{F}^i}}$:

$$\overline{\overline{\overline{\mathcal{A}}}} = \frac{\partial \overline{\overline{\mathcal{F}^i}}}{\partial \overrightarrow{w}} \tag{4.18}$$

Inserting into eq. 4.16 yields:

$$\frac{\overrightarrow{w}^{n+1} - \overrightarrow{w}^{n}}{\Delta t} = -\nabla \cdot \left(\overline{\overline{\mathcal{F}^i}}\right)^n + \frac{1}{2} \left(\nabla \cdot \overline{\overline{\overline{\mathcal{A}}}} \nabla \cdot \overline{\overline{\mathcal{F}^i}}\right)^n \Delta t + \mathcal{O}(\Delta t^2) \tag{4.19}$$

This equation is integrated on the dual cell C_j:

$$\begin{aligned} V_j \frac{\overrightarrow{w}_j^{n+1} - \overrightarrow{w}_j^{n}}{\Delta t} &= -\int_{C_j} \nabla \cdot \left(\overline{\overline{\mathcal{F}^i}}\right)^n + \int_{C_j} \frac{1}{2} \nabla \cdot \left(\overline{\overline{\overline{\mathcal{A}}}} \nabla \cdot \overline{\overline{\mathcal{F}^i}}\right)^n \Delta t \\ = -\sum_{e \in D_j} \int_{C_j \cap K_e} \nabla \cdot \left(\overline{\overline{\mathcal{F}^i}}\right)^n &+ \frac{1}{2} \Delta t \sum_{e \in D_j} \int_{\partial(C_j \cap K_e)} \left(\overline{\overline{\overline{\mathcal{A}}}} \nabla \cdot \overline{\overline{\mathcal{F}^i}}\right)^n \overrightarrow{n} ds \\ &= -\sum_{e \in D_j} \left(\overrightarrow{r}_e\right)^n \frac{V_e}{n_e^v} + \frac{1}{2} \Delta t \sum_{e \in D_j} \left(\overline{\overline{\overline{\mathcal{A}}}}_e \overrightarrow{r}_e\right)^n \cdot \overrightarrow{s}_{j,e} \end{aligned} \tag{4.20}$$

The Jacobian matrix $\overline{\overline{\mathcal{A}}}$ of the inviscid fluxes is assumed constant inside each element. $\overrightarrow{s}_{j,e}$ denotes the normal vector of the dual cell j for the element K_e. The residual distribution matrix of the Lax-Wendroff scheme is deduced as:

$$D^{LW}_{j,e} = \left(-\overline{\overline{\mathcal{I}}} \frac{1}{n^v_e} + \frac{\Delta t}{2 n_d V_e} (\overline{\overline{\mathcal{A}}}_e \cdot \overrightarrow{s}_{j,e}) \right) \tag{4.21}$$

where $\overline{\overline{\mathcal{I}}}$ denotes the identity matrix. The Lax-Wendroff scheme is the only one step explicit scheme to achieve second order accuracy in both space and time. It has a compact stencil, which signifies that contributions for the nodal update only arise from the nearest neighbours ("2Δ stencil"). These properties make this scheme cheap in terms of computational cost. However, it is generally too dissipative at high wavenumbers for an accurate LES. Although often interpreted as an upwind term, the second order derivative appears only due to an improved approximation of the time derivative. As pointed out by Donea et al. [41], this term is added in the Taylor series to counterbalance the transient negative diffusion intrinsic to an explicit Euler time-stepping method. The previous derivation has only dealt with inviscid fluxes. However, the Lax-Wendroff scheme should be directly applied to the equation system that is to be numerically discretized and therefore also include viscous fluxes and source terms in the present case. When doing so, third- and fourth-order spatial derivatives arise from the diffusive fluxes in the second-order temporal derivative (eq. 4.17). In order to avoid the appearance of these terms, the Lax-Wendroff scheme is generally written as a two-step scheme when applied to the Navier-Stokes equations [87]. However, since convection dominated problems are to be solved in the present applications, the higher order contributions arising from the viscous fluxes are neglected in AVBP, allowing to keep the numerically efficient one-step formulation of the Lax-Wendroff scheme.

4.3.2 Taylor-Galerkin schemes

Taylor-Galerkin schemes are based on a Taylor expansion of the time solution vector similarly to the Lax-Wendroff scheme, but they rely on the finite element method for spatial discretization. In the finite element method, the solution vector and the fluxes at a given time t are approximated as a linear combination of local test functions defined for each mesh node:

$$\overrightarrow{w}(\overrightarrow{x}, t) = \sum_{k\in N_h} \overrightarrow{w}_k(t)\phi_k(\overrightarrow{x}) \tag{4.22}$$

and:

$$\overline{\overline{\mathcal{F}^i}}(\overrightarrow{x}, t) = \sum_{k\in N_h} \overline{\overline{\mathcal{F}^i_k}}(t)\phi_k(\overrightarrow{x}) \tag{4.23}$$

According to eq. 4.1, the flux vector $\overline{\overline{\mathcal{F}^i}}$ is a nonlinear combination of the solution vector $\overrightarrow{w}$. Therefore, eq. 4.23 is inconsistent with respect to eq. 4.22. Fletcher [56] demonstrated that this inconsistency does not result in a significant loss of accuracy on standard test cases while allowing substantial gains of computational time. For this reason, this approximation is adopted in AVBP.

In the following, test functions with compact support are chosen, which means that they are unity on one node and zero everywhere else. This implies that the test functions are only defined on the elements surrounding one node. Eqs. 4.22 and 4.23 must now be inserted into eq. 4.16. In order to shorten derivations, the second-order term in eq. 4.16 is neglected, a complete derivation is given by Lamarque [107]. Multiplying eq. 4.16 by a trial function $\omega(\overrightarrow{x})$ with compact support and integrating over the entire domain yields:

$$\int_\Omega \sum_{k\in N_h} \frac{\overrightarrow{w}^{n+1}_k - \overrightarrow{w}^{n}_k}{\partial t} \phi_k(\overrightarrow{x})\omega_j(\overrightarrow{x}) d\nu + \int_\Omega \sum_{k\in N_h} \overline{\overline{\mathcal{F}^i_k}}(t) \cdot \nabla\phi_k(\overrightarrow{x})\omega_j(\overrightarrow{x}) d\nu = 0 \quad \text{with} \quad j \in N_h \tag{4.24}$$

which can be simplified to:

$$\begin{aligned}
&\sum_{e\in T_h}\sum_{k\in K_e}\frac{\partial\overrightarrow{w}_k(t)}{\partial t}\int_{K_e}\phi_k(\overrightarrow{x})\omega_j(\overrightarrow{x})d\nu+\\
&\sum_{e\in T_h}\sum_{k\in K_e}\overline{\overline{\mathcal{F}_k^i}}(t)\cdot\int_{K_e}\nabla\phi_k(\overrightarrow{x})\omega_j(\overrightarrow{x})d\nu=0\qquad\text{with}\qquad j\in N_h
\end{aligned}\tag{4.25}$$

On linear elements, i.e. triangles in two dimensions and tetraedras in three dimensions, the following fundamental relation holds:

$$\nabla\phi_k=-\frac{\overrightarrow{s}_k}{n_d V_e}\qquad\text{for}\qquad k\in K_e\tag{4.26}$$

with the normal vector definition adopted in eq. 4.10. Eq. 4.26 implies that equal normal vectors with opposite signs are found on both sides of an element boundary. Since the flux vector is equal on both sides of the element due to continuity, all interior fluxes in the computational domain cancel out, a property referred to as conservativity. Therefore, eq. 4.26 implies the conservativity of linear finite element methods. Note that conservativity is not restricted to linear finite element methods and that one may similarly introduce flux formulations at boundaries for higher-order elements [48]. Moreover, it can be shown that:

$$\int_{K_e}\phi_j(\overrightarrow{x})d\nu=\frac{V_e}{n_v^e}\tag{4.27}$$

Equating trial and test functions ($\omega(\overrightarrow{x})=\phi(\overrightarrow{x})$) yields:

$$\begin{aligned}
&\sum_{e\in T_h}\sum_{k\in K_e}\frac{\overrightarrow{w}_k^{n+1}-\overrightarrow{w}_k^n}{\Delta t}\int_{K_e}\phi_k(\overrightarrow{x})\phi_j(\overrightarrow{x})d\nu+\\
&\sum_{e\in T_h}\sum_{k\in K_e}\left(\overline{\overline{\mathcal{F}_k^i}}\right)^n\cdot\int_{K_e}\nabla\phi_k(\overrightarrow{x})\phi_j(\overrightarrow{x})d\nu=0\qquad\text{with}\qquad j\in N_h
\end{aligned}\tag{4.28}$$

Inserting eqs. 4.26 and 4.27 into eq. 4.28 yields:

$$\overline{\overline{\mathcal{M}}}_j\frac{\overrightarrow{w}_j^{n+1}-\overrightarrow{w}_j^n}{\Delta t}-\sum_{e\in D_j}\frac{V_e}{n_v^e}\left(\overrightarrow{r}_e\right)^n=0\qquad\text{with}\qquad j\in N_h\tag{4.29}$$

$\overline{\overline{\mathcal{M}}}_j$ is called the mass matrix and defined as:

$$\overline{\overline{\mathcal{M}}}_j=\sum_{e\in T_h}\sum_{k\in K_e}\int_{K_e}\phi_k(\overrightarrow{x})\phi_j(\overrightarrow{x})d\nu\tag{4.30}$$

Neglecting the second-order term in eq. 4.20, it appears that the finite volume formulation of the Lax-Wendroff scheme (eq. 4.20) and the finite element formulation of the Lax-Wendroff scheme (eq. 4.29) are equal except for the presence of the mass matrix $\overline{\overline{\mathcal{M}}}_j$ (eq. 4.30) instead of the nodal volume V_j. The mass matrix makes the finite element formulation of the Lax-Wendroff scheme implicit in space compared to its finite volume counterpart. The additional numerical cost related to the inversion of the mass matrix is moderate as it may be approximated within two steps of a Jacobi algorithm with sufficient accuracy [34]. Moreover, the additional computational cost is compensated by two important advantages. First, the mass matrix allows more accurate solutions on deformed elements or elements with different size ratios. Indeed, it relates the average value in the control volume with the values at the vertices. This average value corresponds to the value at the barycenter of the dual cell, which does not always coincide with its geometric center. Second, the presence of the mass matrix allows

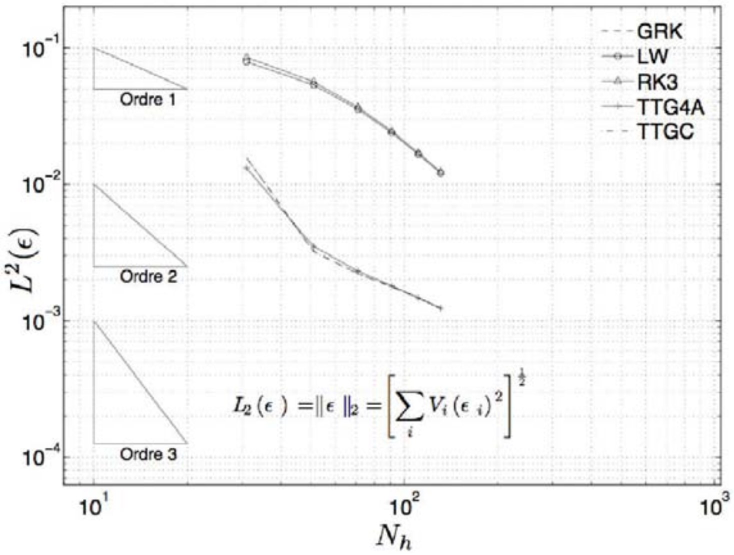

Figure 4.2 : *From Lamarque [107]: Mesh convergence for the different numerical schemes of AVBP for the advection of a Gaussian pulse with constant velocity* $\mathbf{c} = (1, 0)$ *on a two dimensional mesh composed of squares. The superconvergence phenomenon may be observed for the Taylor-Galerkin schemes (TTGC, TTG4A) as spatial accuracy drops from third to second order with mesh refinement*

the semi-discrete scheme (assuming perfect time discretization) to achieve up to fourth order spatial accuracy with linear finite elements [220]. This property is called superconvergence. It describes the fact that nodal errors may converge faster than those of the integrated scalar in finite elements. This phenomenon is only observed for high wavenumbers since the phase error at these wavenumbers is much lower in finite elements than in finite differences, as pointed out by Donea et. al [41]. However, the superconvergence property is rapidly lost if the spatial discretization is coupled with a low order time integration since the phase error does not decrease uniformly at all wavelengths. This results from the strong link between spatial and temporal discretizations for Taylor-Galerkin schemes. The superconvergence phenomenon is illustrated by the mesh convergence curves of the Taylor-Galerkin schemes TTGC and TTG4A for the advection of a Gaussian pulse in fig. 4.2 taken from Lamarque [107]. In this figure, the spatial accuracy of the Taylor-Galerkin schemes is seen to drop from third to second-order for finer mesh resolutions.

For bilinear elements such quadrilaterals or tetrahedra, the gradient of the shape functions is no longer constant inside each element and relation 4.26 may not be used. In AVBP, the shape function is split into a linear part and a bilinear correction term:

$$\phi_j^{bil}(\overrightarrow{x}) = \phi_j^{lin}(\overrightarrow{x}) + (\phi_j^{bil}(\overrightarrow{x}) - \phi_j^{lin}(\overrightarrow{x})) \tag{4.31}$$

The treatment of the linear part follows previous derivations while the bilinear correction term is determined analytically through transformation on canonical elements. More details on this aspect may be found in Colin and Rudgyard [34].

Now that the spatial discretization in the finite-element framework has been discussed, the temporal discretization is adressed. The Taylor-Galerkin schemes of AVBP combine two steps of the Taylor expansion of the time solution vector in order to increase temporal accuracy while maintaining a compact stencil for the spatial discretization:

$$\overrightarrow{\tilde{w}}^{\,n} = \overrightarrow{w}^{\,n} + \alpha \frac{\partial \overrightarrow{w}}{\partial t}\bigg|^n \Delta t + \beta \frac{\partial^2 \overrightarrow{w}}{\partial t^2}\bigg|^n \Delta t^2 \tag{4.32}$$

$$\overrightarrow{w}^{\,n+1} = \overrightarrow{w}^{\,n} + \frac{\partial \overrightarrow{\tilde{w}}}{\partial t}\bigg|^n \Delta t + \gamma \frac{\partial^2 \overrightarrow{\tilde{w}}}{\partial t^2}\bigg|^n \Delta t^2 \tag{4.33}$$

Inserting eq. 4.32 into eq. 4.33, it appears that fourth-order temporal accuracy may be achieved with two different sets of the coefficients $[\alpha, \beta, \gamma]$. The resulting schemes are called TTG4A and TTG4B [42]. Achieving only third-order temporal accuracy yields a degree of freedom on one of these coefficients. Colin and Rudgyard [34] use this degree of freedom to minimize the numerical dissipation of their TTGC scheme. Furthermore, restricting temporal accuracy to third-order allows for one single evaluation of the second-order temporal derivative in the two subiterations:

$$\overrightarrow{\tilde{w}}^{\,n} = \overrightarrow{w}^{\,n} + \alpha \frac{\partial \overrightarrow{w}}{\partial t}\bigg|^n \Delta t + \beta \frac{\partial^2 \overrightarrow{w}}{\partial t^2}\bigg|^n \Delta t^2 \tag{4.34}$$

$$\overrightarrow{w}^{\,n+1} = \overrightarrow{w}^{\,n} + \frac{\partial \overrightarrow{\tilde{w}}}{\partial t}\bigg|^n \Delta t + \gamma \frac{\partial^2 \overrightarrow{w}}{\partial t^2}\bigg|^n \Delta t^2 \tag{4.35}$$

Table 4.1 summarizes the different coefficients of the mentioned Taylor-Galerkin schemes.

Coefficient values	TTG4A	TTG4B	TTGC
α	1/3	0.141	0.49
β	1/12	0.116	1/6
γ	1/2	0.359	0.01

Table 4.1 : *Coefficient sets for certain two step Taylor-Galerkin schemes*

4.4 Viscous and artificial diffusion operators

This section presents the discretization of the diffusive fluxes and the artificial diffusion operators. Two different diffusion operators are found in AVBP. The first uses the cell-vertex framework combined to a finite volume spatial discretization. The latter yields a 4Δ stencil and implies that this diffusion operator does not dissipate scales smaller than 4Δ. Therefore, it favors the appearence of high wavenumber oscillations and yields unphysical energy accumulations of the smallest resolved scales in turbulence simulations. To correct this drawback, a new diffusion operator with a 2Δ stencil was designed [32]. This operator relies on a vertex-centered formulation combined with a finite element discretization. This operator predicts correct dissipation levels at the smallest resolved scales and dampens high wavenumber oscillations. For this reason, the 2Δ diffusion operator is used for all simulations in the present work. In order to stabilize the numerical simulations, artificial viscosities must be applied to the nodal updates. They are briefly presented in the following.

4.4.1 2Δ diffusion operator (vertex-centered)

The 2Δ diffusion operator was implemented in AVBP by Colin [32]. It follows the vertex-centered formalism. Therefore, the control volume associated with the spatial integration of this operator is the duall cell C_j instead of the primary cell K_e. Furthermore, the operator is derived in the finite element framework:

$$\begin{aligned}\nabla \cdot \overline{\overline{\mathcal{F}^v_j}} = \nabla \cdot \overline{\overline{\mathcal{F}^v}}(\overrightarrow{w}_j, \nabla \overrightarrow{w}_j) = \frac{1}{V_j}\int_{C_j} \nabla \cdot \overline{\overline{\mathcal{F}^v}}(\overrightarrow{w}, \nabla \overrightarrow{w}) d\nu = \\ -\frac{1}{V_j}\sum_{e \in D_j}\int_{C_j} \overline{\overline{\mathcal{F}^v}}(\overrightarrow{w}, \nabla \overrightarrow{w}) \cdot \nabla \phi_j(\overrightarrow{x}) d\nu = \\ \frac{1}{n_d V_j}\sum_{e \in D_j} \overline{\overline{\mathcal{F}^v_e}} \cdot \overrightarrow{s}_{j,e}\end{aligned} \tag{4.36}$$

The numerical evaluation of eq. 4.36 is based on a 2Δ stencil since it only involves contributions from the direct neighbours. Contrary to the 4Δ operator, this operator predicts correct dissipation levels at the smallest resolved scales.

4.4.2 Artificial viscosity

In AVBP, the numerical schemes for the convection of the gaseous phase are centered in space. These schemes display undesirable numerical oscillations which must be removed as they are unphysical and as they may alter the stability of simulations. Therefore, a second-order artificial viscosity which smooths steep gradients and a fourth-order hyperviscosity which suppresses node-to node oscillations are added to the spatial operator in eq. 4.15:

$$\frac{d\overrightarrow{w}_j}{dt} = -\mathcal{L}_j + \overrightarrow{d}_j^2 + \overrightarrow{d}_j^4 \tag{4.37}$$

The second-order artificial viscosity relies on a Pseudo-Laplacian written as:

$$\overrightarrow{d}_j^2 = \frac{1}{V_j}\sum_{e \in D_j} \frac{\epsilon^2 \zeta V_e}{n_v^e \Delta t}(\overrightarrow{w}_j - \overrightarrow{w}_e) \tag{4.38}$$

ζ is a sensor which tries to detect where to apply artificial viscosity. The sensor used in all presented simulations was implemented by Colin [33]. It attempts to limit the application of second-order artificial viscosity in zones of under-resolved vorticity, i.e. small turbulent eddies on a few grid cells. It is based on two different evaluations of a scalar gradient in a cell which allows to distinguish between physical and numerical oscillations [94]. The fourth-order hyperviscosity operator writes:

$$\overrightarrow{d}_j^4 = \frac{1}{V_j}\sum_{e \in D_j} \frac{\epsilon^4 V_e}{n_v^e \Delta t}\left[\left(\frac{1}{n_v^e}\sum_{k \in K_e} \nabla \overrightarrow{w}_k\right) \cdot (\overrightarrow{x}_j - \overrightarrow{x}_e) + (\overrightarrow{w}_e - \overrightarrow{w}_j)\right] \tag{4.39}$$

There is no sensor for the fourth-order viscosity which is applied in the entire comptuational domain. In the present formulation, no fourth-order viscosity is applied in the momentum equations in order not to dissipate small scale turbulent structures. Furthermore, the parameter ϵ^4 prevents the application of fourth-order viscosity in zones where second-order viscosity is applied:

$$\epsilon^4 = \max(0, \epsilon^4 - \zeta \epsilon^2) \tag{4.40}$$

4.5 Source terms

There exist two different spatial discretizations for the source terms. The first uses a vertex-centered approach and is used for the finite-volume schemes of AVBP such as Lax-Wendroff. The second discretization relies on the finite-element method and is employed for the Taylor-Galerkin schemes.

4.5.1 Vertex-centered source term

In this approach, the source term vector $\overrightarrow{s}$ is integrated at the element nodes where the variables are stored. The control volume chosen for the spatial discretization of the source term is the dual cell C_j:

$$\int_{C_j} \overrightarrow{s}\, dV = \overrightarrow{s}_j V_j \tag{4.41}$$

where $\overrightarrow{s}_j = \overrightarrow{s}(\overrightarrow{w}_j)$ is directly evaluated from the nodal values.

4.5.2 Finite-element source term

In the finite-element based evaluation of the source term vector, the spatial integration is performed on the primary cell and a scatter operation is performed to obtain the nodal contribution:

$$\sum_{e \in D_j} \int_{C_j \cap K_e} \overrightarrow{s} \phi\, dV = \sum_{e \in D_j} \frac{\overrightarrow{s}_e V_e}{n_v^e} \tag{4.42}$$

where $\overrightarrow{s}_e = \overrightarrow{s}(\overrightarrow{w}_e)$ is evaluated from the nodal average on the cell K_e:

$$\overrightarrow{w}_e = \sum_{k \in K_e} \frac{\overrightarrow{w}_k}{n_v^e} \tag{4.43}$$

It seems that the differences on results arising from both source term discretizations are only minor but the distinction is still kept in the solver for consistency reasons.

4.6 Time advancement

The Lax-Wendroff and TTG schemes combine temporal and spatial discretizations. The fully discretized Lax-Wendroff scheme is therefore readily obtained from eq. 4.20 as:

$$\overrightarrow{w}_j^{n+1} = \overrightarrow{w}_j^{n} - \frac{1}{V_j} \sum_{e \in D_j} \overline{\overline{D}}_{j,e} \overrightarrow{r}_e^{\,n} V_e \Delta t \tag{4.44}$$

with Δt the characteristic timestep. The notation is very similar for the TTG schemes, except that two successive steps need to be considered. In the TTG schemes, the update predicted in the first step has no physical signification and is only required to achieve the desired temporal accuracy in the second step which corrects the update from the first step. Thus, the TTG schemes are of predictor-corrector type. Combining eqs. 4.29, 4.32 and 4.33 yields:

$$\overrightarrow{\widetilde{w}}_j^{n} = \overrightarrow{w}_j^{n} - \left(\overline{\overline{\mathcal{M}}}_j\right)^{-1} \sum_{e \in D_j} \overline{\overline{D}}_{j,e} \overrightarrow{r}_e^{\,n} V_e\, \alpha \Delta t \qquad \text{(predictor step)} \tag{4.45}$$

$$\overrightarrow{w}_j^{n+1} = \overrightarrow{\widetilde{w}}_j^{n} - \left(\overline{\overline{\mathcal{M}}}_j\right)^{-1} \sum_{e \in D_j} \overline{\overline{D}}_{j,e} \overrightarrow{\widetilde{r}}_e^{\,n} V_e \Delta t \qquad \text{(corrector step)} \tag{4.46}$$

Other schemes of AVBP consider spatial and temporal discretizations separately, for instance a finite-volume/finite-element spatial discretization combined to a Runge-Kutta temporal advancement [88]. However, these schemes are not used in the present work and therefore not further discussed.

The numerical time step Δt is limited by stability conditions for the convective, diffusive and source term operators. In general, the time step is limited by the convective part and determined from the Courant-Friedrichs-Lewy (CFL) condition. In a one-dimensional framework, this condition may be written as:

$$\Delta t = \nu_{cfl} \frac{\min(\Delta x)}{\max|u + c|} \tag{4.47}$$

with c the speed of sound and ν_{cfl} the CFL constant which is of order unity for explicit numerical schemes. In two or three dimensions, the convective time step is limited by the spectral radius of the Jacobian of inviscid fluxes [107] but the underlying principle of the method remains identical. In particular, the global convective time step is limited by the smallest element size of the computational mesh and the computational cost is therefore highly dependent on this quantity.

4.7 Numerics in the Lagrangian solver

Since the Lagrangian solver tracks particles in their own frame of reference, the only numerical topics to be adressed in this section are the time advancement, the interpolation of fluid properties from the computational nodes to the particles and the interpolation of particle source terms on the grid nodes. For details on the particle search algorithm, the reader is referred to the thesis of García [63].

4.7.1 Time advancement

The time advancement of the Lagrangian solver relies on a first-order explicit Euler method:

$$f_p^{n+1} = f_p^n + H(f_p^n, f_{f@p}^n) \tag{4.48}$$

$H(\cdot)$ denotes a function depending on both properties of the particle f_p^n and properties of the fluid interpolated at the particle position $f_{f@p}^n$. Since the Taylor-Galerkin schemes are of predictor-corrector type (section 4.6), their intermediate step may not be used for the temporal advancement of the particles since it does not represent a physical state. Therefore, the temporal coupling between phases only occurs at full iterations of the gaseous solver. Using a first-order explicit Euler advancement for the particles allows a straightforward coupling between phases as the coupling terms are added at the end of the full iteration of the gaseous solver. The time advancement of both phases and the coupling between them are shown in fig. 4.3.

4.7.2 Interpolation methods

The evaluation of particle dynamics requires the interpolation of gaseous properties from the Eulerian grid to the particle position $x_{p,i}$. The expression for an arbitrary quantity f at the particle location $x_{p,i}$ is obtained as:

$$f_{f@p,i} = \sum_{j \in K_e} w(x_{p,i}, x_{n,i}) f \tag{4.49}$$

The term $w(x_{p,i}, x_{n,i})$ describes a generic interpolation function which defines the weights associated with the nodal coordinates $x_{n,i}$ of the cell K_e inside which the particle is located. Three different interpolation methods are available:

- an interpolation based on first-order Taylor expansion of the quantity to interpolate:

$$f(x_i) = f(x_{n,i}) + f'(x_{n,i})(x_i - x_{n,i}) \tag{4.50}$$

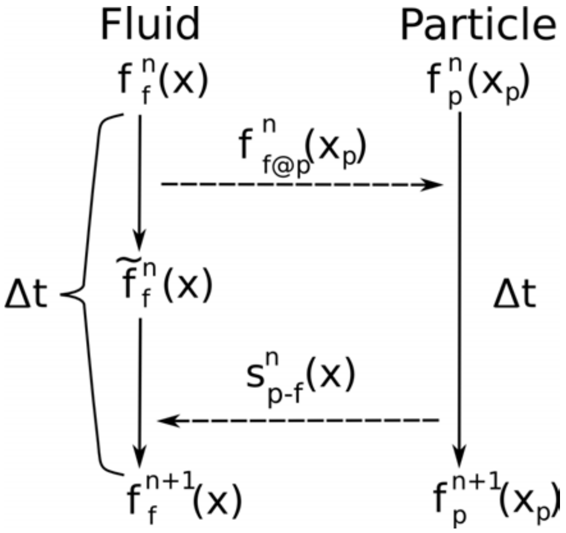

Figure 4.3 : *Sketch of the time advancement of both phases. For the fluid phase, a two-step temporal advancement of predictor-corrector type is assumed. At the beginning of the iteration, fluid properties are interpolated at the particle location. This allows to advance particle properties in time. After advancing the particle properties in time, the coupling terms between phases are calculated, interpolated on the Eulerian grid and added to the fluid residual in the second step.*

$x_{n,i}$ denotes the coordinates of the node n and $f'(x_{n,i})$ the first derivative of f at the node n. As pointed out by García [63], this interpolation method reduces the computational overhead to a strict minimum as the first derivatives of gaseous quantities at the nodes are directly available in the solver. On the contrary, chosing a second-order interpolation would require the computation and storage of second derivatives at the nodes.

- a linear-least squares method which recontructs linear polynomials for the interpolation of properties to the droplets. This leads to an overdetermined system and the coefficients of the linear polynomials are minimized in a least-squares sense:

  $$\min \left\| Ax - b \right\| = 0 \tag{4.51}$$

  The matrix A contains the nodal coordinates, the vector x the unknown coefficients of the linear polynomials and the vector b the nodal values of the scalars to interpolate.

- an interpolation based on Lagrangian polynomials. A Lagrange polynomial $P(x_i)$ is constructed as the function of degree (n-1) passing through the N nodal values $f(x_{n,i})$ of the quantity f in the computational cell K_e:

  $$P(x_i) = \sum_{j=1}^{N} \prod_{i=1}^{n_d} P_j^i(x_i) \qquad \text{with} \qquad P_j^i(x_i) = f(x_{j,i}) \prod_{\substack{k=1 \\ k\neq j}}^{N} \left(\frac{x_i - x_{k,i}}{x_{j,i} - x_{k,i}} \right) \tag{4.52}$$

García [63] observed very similar accuracies for all three methods for the simulation of a homogeneous isotropic turbulence laden with particles. This result indicates that these interpolation methods have similar leading truncation errors. However, García noted important differences in computational costs between these methods as the Taylor and Lagrange interpolation methods were computationally much faster than the Linear Least Squares method. For this reason, the Taylor interpolation method is used in the present work.

4.7.3 Coupling between phases

For coupling terms between phases, quantities obtained at the particle location need to be interpolated to the Eulerian grid of the gaseous phase. The distribution scheme for a nodal source term s_j consists of contributions from all particles located in one of the cells sharing the node j and denoted $\mathcal{D}_j$. It is obtained as:

$$s_j = \frac{1}{V_j} \sum_{k \in \mathcal{D}_j} \omega_{j,e}^{(k)} s_p^{(k)} \tag{4.53}$$

s_p^k denotes the source term of the particle k. $\omega_{j,e}^k$ denotes the interpolation weight for the source terms of the particle k to the node j. The source terms are obtained as quantities per unit volume and thus require division by the nodal volume V_j. Finally, the conservative weights $\omega_{j,e}^k$ are calculated as follows:

$$\omega_{j,e}^k = \frac{\prod_{j \neq n} \left\| \overrightarrow{x_p}^{(k)} - \overrightarrow{x_j} \right\|}{\sum_{k \in K_e} \prod_{l \neq k} \left\| \overrightarrow{x_p}^{(k)} - \overrightarrow{x_l} \right\|} \tag{4.54}$$

with $x_{n,i}$ the nodal coordinates and $\left\| . \right\|$ the norm operator.

4.7.4 Particle-wall interaction

At solid boundaries of a simulation, conditions reproducing the interaction of particles with walls need to be applied. In absence of numerical treatment, particles simply cross the domain boundaries and are no longer found by the particle search algorithm. The physics involved in droplet-wall interaction involve a variety of phenomena such as rebound, splashing and film formation. These phenomena should be included in the Lagrangian solver and a detailed numerical model was recently proposed by Garcia-Rosa et al. [183]. However, in the present work it is assumed that all particles rebound elastically at solid boundaries. At least, this allows to conserve liquid mass in the simulations but a more accurate modeling of droplet-wall interactions may be necessary for future simulations.

The numerical approach to handle elastic rebound at walls was developed by Jaegle [93], it is sketched in fig. 4.4. It consists in flagging all cells adjacent to a solid boundary of the computational domain. In addition, the normal vector of the solid boundary is stored for each flagged cell. As soon as a droplet is found in the flagged cell layer, its velocity normal to the boundary is reverted:

$$u'_{p,i} = u_{p,i} + 2(u_{p,j} \cdot n_{w,j}) n_{w,i} \tag{4.55}$$

$u_{p,i}$ and $u'_{p,i}$ respectively denote the droplet velocities before and after rebound, $n_{w,j}$ denotes the wall normal vector.

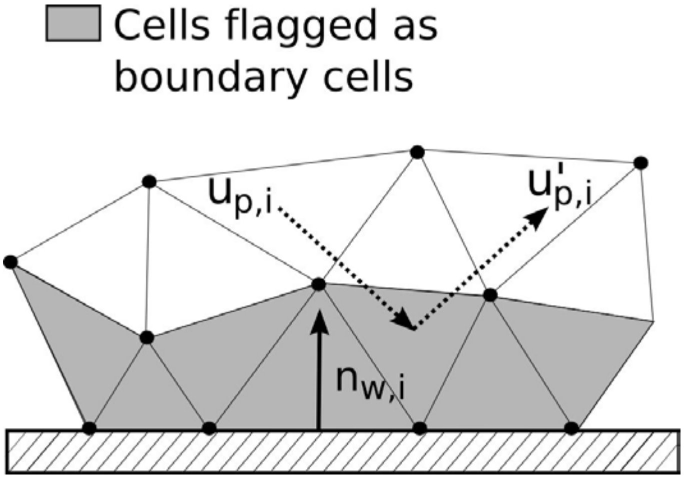

Figure 4.4 : *Sketch of the wall treatment for particles in the Lagrangian solver*

Part III

Spray modeling

Chapter 5

Liquid injection

Modeling of liquid injection is an important aspect in the numerical simulation of two-phase flows. However, the destabilization mechanisms occuring after liquid flow ejection and subsequently leading to the disintegration of the liquid into a dilute spray are physically complex. Furthermore, the accurate numerical representation of the liquid destabilization mechanisms requires the use of specific numerical techniques. These methods are not considered in the present work. Instead, two complementary approaches attempting to model liquid injection for pressure swirl-atomizers using different degrees of simplification are presented. In a first step, the impact of the atomization process on spray dynamics is neglected and the developed spray is directly injected at the atomizer orifice. The particle injection velocity profiles are then deduced from the flow field inside the atomizer. Information on the particle diameter distribution is reconstructed from experimental data. The main focus of this method lies in the reproduction of similar injection conditions for both Euler-Lagrange and Euler-Euler approaches in the view of a direct comparison between them in simulations of realistic geometries. Neglecting the impact of the liquid disintegration process on spray dynamics is however a drastic simplification. Therefore, complexity is added to the particle injection procedure by combining it with a secondary breakup model in a second step.

5.1 Liquid disintegration mechanisms

The present section briefly summarizes the physical mechanisms leading to the disintegration of liquid streams and the subsequent formation of a spray. It is organized as follows. The first part introduces fundamental numbers characterizing the disintegration of liquid streams and then discusses primary atomization mechanisms for liquid jets and liquid sheets. The second part presents a classification of secondary breakup mechanisms. The third part presents numerical tools for the simulation of primary atomization.

5.1.1 Primary atomization

Primary atomization covers the steps from liquid injection to the formation of the first liquid fragments. It is controlled by the presence of initial disturbances on the liquid-gas interface. Some of these disturbances grow in time and space due to a variety of physical mechanisms, leading to the ejection of liquid fragments. Primary atomization mechanisms differ notably for the considered liquid stream, for instance a liquid jet or a liquid sheet. The presence of a stream of coflowing air along the liquid surface has a strong influence on the development of instabilities [45]. Despite the dependency of primary atomization on the considered configuration, the destabilization regimes of liquid streams may be characterized by nondimensional numbers. The most important among these is the Weber number We, whose definition may be either based on gaseous or liquid densities:

$$We = \frac{\rho u_{l,i}^2 D_0}{\sigma_l} \qquad \text{and} \qquad We_l = \frac{\rho_l u_{l,i}^2 D_0}{\sigma_l} \tag{5.1}$$

where D_0 and σ_l respectively represent the nozzle diameter and the liquid surface tension. The Weber number represents a ratio between destabilizing aerodynamic forces and stabilizing surface tension forces acting upon a liquid stream of fragment. The Reynolds number represents a ratio of liquid inertial to viscous forces:

$$Re_l = \frac{\rho_l u_l D_0}{\mu_l} \tag{5.2}$$

It may be seen as an ability of the liquid flow to damp the development of instabilities. The Ohnesorge number Oh relates the liquid viscous forces to surface tension:

$$Oh = \frac{\mu_l}{(\rho_l D_0 \sigma_l)^{1/2}} = \frac{\sqrt{We_l}}{Re_l} \tag{5.3}$$

The Ohnesorge number is an additional indicator of liquid senstivity to instabilities at the liquid-gas interface.

5.1.1.a) Liquid jets

The disruption of liquid jets is of particular interest for Diesel engine applications and has been widely studied in the literature, see Lin and Reitz [123] and references therein. It may theoretically be described by linear stability analysis, whose principles are described for liquid jets following the description given by Lebas [111].

Consider an incompressible, round liquid jet of infinite length. The jet has a characteristic radius R and velocity $U_{z,l}$ while the gas moves with velocity U_z. It is assumed that there is no mass transfer between phases. The problem is described in a cylindrical coordinate system (r,ϕ,z) which moves with the characteristic velocity of the liquid jet $U_{z,l}$. Because of axissymmetry, there are no dependencies on the angular coordinate ϕ. Finally, the conservation equations are linearized around a mean state. For the liquid phase, this yields:

$$\frac{\partial u_{l,z}}{\partial z} + \frac{1}{r}\frac{\partial r u_{l,r}}{\partial r} = 0 \tag{5.4}$$

$$\frac{\partial u_{l,z}}{\partial t} + U_{l,z}\frac{\partial u_{l,z}}{\partial z} + u_{l,r}\frac{\partial U_{l,z}}{\partial r} = -\frac{1}{\rho_l}\frac{\partial p_l}{\partial z} + \nu_l\left(\frac{\partial^2 u_{l,z}}{\partial z^2} + \frac{1}{r}\frac{\partial}{\partial r}\left(r\frac{\partial u_{l,z}}{\partial r}\right)\right) \tag{5.5}$$

$$\frac{\partial u_{l,r}}{\partial t} + U_{l,z}\frac{\partial u_{l,r}}{\partial z} + u_{l,r}\frac{\partial U_{l,z}}{\partial r} = -\frac{1}{\rho_l}\frac{\partial p_l}{\partial r} + \nu_l\left(\frac{\partial^2 u_{l,r}}{\partial z^2} + \frac{1}{r}\frac{\partial}{\partial r}\left(r\frac{\partial u_{l,r}}{\partial r}\right)\right) \tag{5.6}$$

$$\tag{5.7}$$

where capital letters denote mean quantities and minuscules linearized quantities. The same equation system holds for the gas phase and is not rewritten. It is assumed that the interface $r = R$ between liquid and gas is perturbed by an infinitesimal axissymmetric wave of the form:

$$\eta = \eta(z,t) = \eta_0 \exp(-ikz + \omega t) \tag{5.8}$$

where $\eta(z,t)$ describes the displacement of the liquid surface and η_0 an initial disturbance level. k and ω respectively denote the wavenumber of the disturbance and its complex frequency, the real part ω_r of which characterizes the temporal growth of the disturbance. It is assumed that the tangential and normal components of the stress tensor are continuous at the interface. The linearized continuity conditions on the interface write:

$$\frac{\partial u_{l,z}}{\partial r} = -\frac{\partial u_{l,r}}{\partial z} \tag{5.9}$$

$$-p_l + 2\mu_l\frac{\partial u_{r,l}}{\partial r} - \frac{\sigma_l}{R^2}\left(\eta + R^2\frac{\partial^2 \eta}{\partial z^2} + p\right) = 0 \tag{5.10}$$

Finally, the kinematic condition on the interface writes:

$$u_{l,r} = \frac{\partial \eta}{\partial t} + U_{l,z}(r)\frac{\partial \eta}{\partial z} \tag{5.11}$$

Eqs. 5.4, 5.5 and 5.6 may be analytically solved by introducing a velocity potential ϕ_l and two stream functions ψ_l and ψ_g (one for each phase):

$$\begin{aligned} \phi_l &= \Phi_l(r)\exp(-ikz+\omega t) && (5.12)\\ \psi_l &= \Psi_l(r)\exp(-ikz+\omega t) && (5.13)\\ \psi_g &= \left(U_z(r) - i\frac{\omega}{k}\right)\eta f(r) && (5.14) \end{aligned}$$

where $f(r)$ is a function of the radius. Inserting eqs. 5.12-5.14 into eqs. 5.4-5.6 and using the continuity conditions at the interface, the following dispersion relation is obtained:

$$\omega^2 + \frac{2\nu_l k^2 \omega}{I_0(kR)}\left(I_1'(kR) - \frac{2kl}{k^2+l^2}\frac{I_1'(lR)}{I_1(lR)}I_1(kR)\right) = \frac{\sigma_l k}{R^2\rho_l}(1-R^2k^2)\frac{l^2-k^2}{l^2+k^2}\frac{I_1(kR)}{I_0(kR)} + \frac{\rho}{\rho_l}\left(U_{z,l}(r) - \frac{i\omega}{k}\right)^2 k^2\frac{l^2-k^2}{l^2+k^2}\frac{I_1(kR)}{I_0(kR)}\frac{K_1(kR)}{K_0(kR)} \tag{5.15}$$

where I_n and K_n respectively denote modified Bessel functions of the first and second kinds to order n. l is defined as:

$$l = \sqrt{k^2 + \frac{\omega}{\nu_l}} \tag{5.16}$$

The study of this dispersion relation allows to distinguish between four fundamental disintegration modes. These modes have been experimentally delimited in terms of the nondimensional numbers described in section 5.1.1 [45].

Rayleigh regime **(**$We_l > 8$**)**

This regime describes the evolution of a liquid jet injected at low velocity in a gaseous environment of low density compared to that of the liquid. Neglecting viscous effects of the liquid, the dispersion relation 5.15 reduces to:

$$\omega^2 = \frac{\sigma_l k}{R^2\rho_l}(1-R^2k^2)\frac{I_1(kR)}{I_0(kR)} \tag{5.17}$$

The necessary condition for the development of an instability writes:

$$kR < 1 \tag{5.18}$$

This result implies that the wavelength of the instability must be larger than the radius of the jet. Thus, the Rayleigh regime is characterized by axissymetric perturbations of large wavelengths which shed large fragments from the liquid. The size of the fragments is similar to the jet diameter. It is interesting to note that surface tension appears as the root cause of the instability in this regime (eq. 5.17).

First wind-induced regime ($1.2 + 3.41Oh^{0.9} < We < 13$)

In the first wind-induced regime, the liquid velocity is increased compared to the Rayleigh regime and becomes too large to neglect aerodynamic effects in the destabilization of the liquid jet. Under these conditions, eq. 5.15 writes:

$$\omega^2 + 3\nu_l k^2\omega = \frac{\sigma_l k}{2\rho_l R^3}(1-k^2R^2) + \frac{\rho}{\rho_l}\frac{U_{l,z}k^3R^3}{2R^2}\frac{K_0(kR)}{K_1(kR)} \tag{5.19}$$

Since the gas phase amplifies the growth rate of perturbations, a faster disruption of the jet is observed compared to the Rayleigh regime. The wavelengths of the developing surface instabilities are still larger than the jet radius and the particles shed from the liquid remain comparable to the jet diameter in size.

Second wind-induced regime ($13 < We < 40.3$)

The increase of the injection velocity in the first wind-induced regime reduces the wavelengths of the instabilities on the jet's surface and leads to the so-called second wind-induced regime. Further neglecting viscous effects in the liquid jet, the dispersion relation becomes:

$$\omega^2 = \frac{\rho U_{l,z} k^2 - \sigma_l k^3}{\rho_l} \tag{5.20}$$

Thus, the growth rate of perturbations is directly linked to the relative velocity between phase while surface tension forces stabilize the liquid jet.

Atomization regime ($We > 40.3$)

The atomization regime is typical of high pressure Diesel sprays. It is characterized by the formation of particles whose characteristic radiuses are much smaller than those of the liquid jet. This implies that the triggered instabilities are of very short wavelengths, i.e. $kR \gg 1$. Thus, the Bessel functions may be replaced by their asymptotic values at infinity in eq. 5.15, yielding:

$$(\omega^2 + 2\nu_l k^2)^2 + \frac{\sigma_l k^3}{\rho_l} - 4\nu_l k^3 \left(k^2 + \frac{\omega}{\nu_l}\right)^2 + (\omega + iU_{l,z}k)^2 \frac{\rho}{\rho_l} = 0 \tag{5.21}$$

It is important to note that the growth rate of perturbations no longer depends on the initial radius of the jet but only on its initial velocity and material properties: densities of both phases as well as liquid viscosity. However, the linearization of the conservation equations appears questionable in this regime because of large instability amplitudes.

Fig. 5.1a provides an illustration of the identified primary atomization regimes of liquid jets while fig. 5.1b displays jet lengths at disruption over the injection velocity at the nozzle. The jet length first increases linearly with injection velocity from the Rayleigh regime (A) to the first wind-induced regime (B), reaches a maximum and then decreases. The jet length still decreases from the first to the second wind-induced regime (C). Contradictory measurements of both increasing and decreasing jet breakup lengths have been reported in literature for the atomization regime (D) [123, 45]. These results seem to originate from the very high sensitivity of this regime to the flow field inside the nozzle. More particularly, the onset of breakup seems greatly influenced by the degree of flow development, the presence of turbulence in the jet at the nozzle exit and liquid cavitation phenomena in the nozzle. Fig. 5.2 displays the shadowgraph of a liquid jet under Diesel injection conditions. It illustrates the difficulties in the experimental characterization of the near-injector zone in the atomization regime: because of the high density and high unsteadiness of the liquid spray, optical access to the near-injector zone is very tedious. Therefore, experimental studies rely on specific techniques such as laser sources pulsed at extremely high frequencies.

5.1.1.b) Liquid sheets

Aeronautical atomizers generally form conical liquid sheets (see section 5.2.2). However, the literature on the latter is relatively scarce. Therefore, flat liquid sheets are discussed in the following as they share important properties with conical sheets.

Fraser and Eisenklam [58] characterized three fundamental modes of sheet desintegration.

When the liquid sheet is injected at low velocities, forces generated by surface tension cause the liquid sheet to contract into a thick rim, which then behaves and destabilizes similarly to a free jet. This disintegration regime is called the rim mode, an illustration of which is provided in fig. 5.3a.

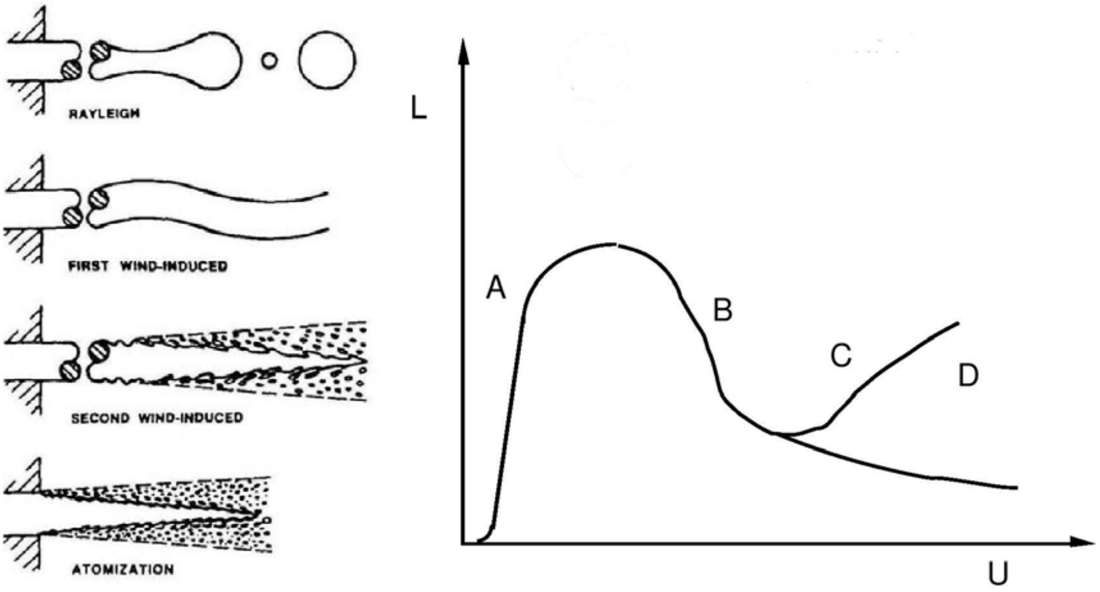

(a) (b)

Figure 5.1 : *(a) Schematic of the different atomization regimes of liquid jets, from Reitz [172]. (b) Schematic diagram of liquid jet breakup length curve as a function of liquid injection velocity, from Lin and Reitz [123]. A : Rayleigh regime. B: first wind-induced regime. C: second wind-induced regime. D: atomization regime*

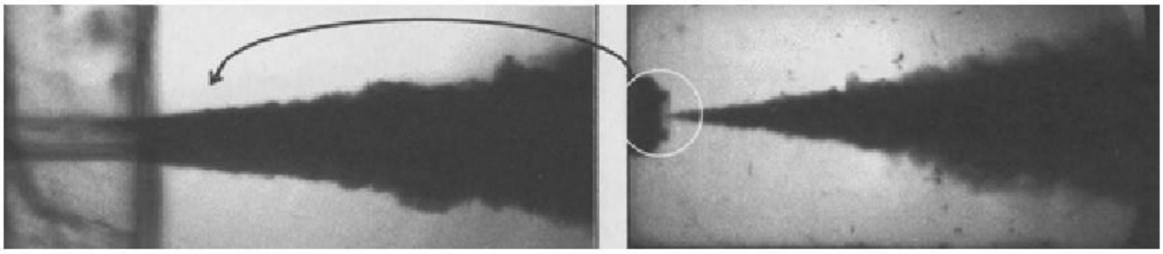

Figure 5.2 : *Visualization of a Diesel jet injection case for the whole jet and a close-up view close to the nozzle ($P_{inj} = 100$ MPa, $P = 6$ MPa, $D_0 = 200\,\mu m$) from Moreau [139]*

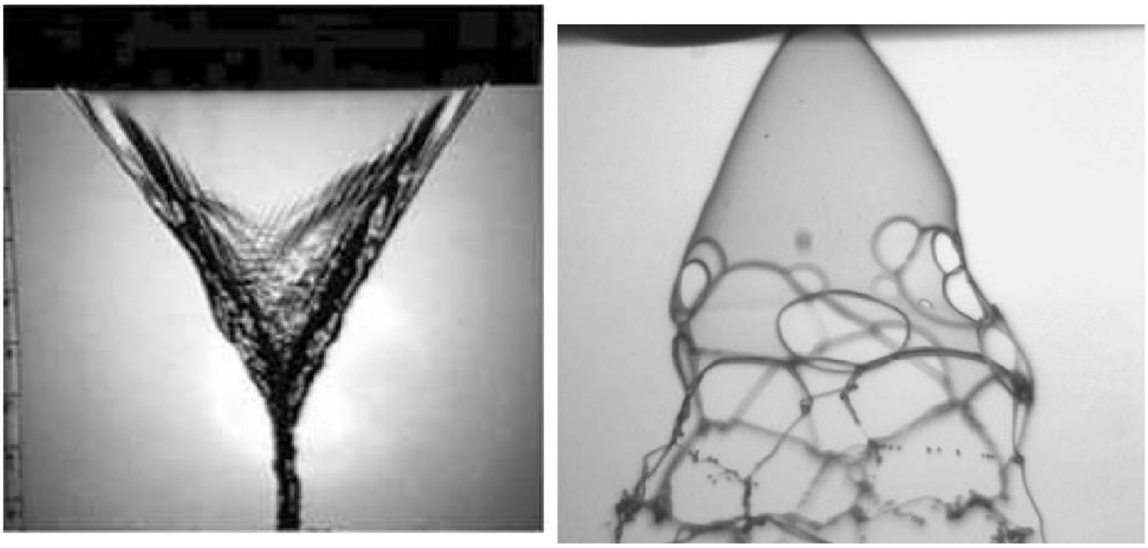

(a) (b)

Figure 5.3 : *(a) Visualization of the rim desintegration mode from Carvalho et al. [26]. (b) Visualization of the perforation mode for a viscous conical sheet. From Sindayihebura and Dumouchel [207]*

In perforated-sheet disintegration, holes appear in the sheet and are delimited by rims which contain the liquid initially included inside the holes. These holes grow in size until the rims of adjacent holes coalesce to produce liquid ligaments. These ligaments finally break into particles of varying size. An illustration of sheet perforation for a conical sheet is displayed in fig. 5.3b.

In the wave mode, the disintegration of the liquid sheet arises from undulating waves. From linear stability analysis (see section 5.1.1.a)), it appears that only two types of waves may develop on the sheet's surface [81]: either the two surfaces of the sheet oscillate in phase to produce the so called sinusoidal mode, or they oscillate out of phase to produce the dilatational mode. The dispersion relation of the sinusoidal mode writes [24]:

$$\omega = -\frac{u_l k \tanh(kh)}{\tanh(kh)(\rho/\rho_l) + 1} \pm \frac{[\sigma_l k^3(\tanh(kh) + \rho) - \rho_l \rho u_l^2 k^2 \tanh(kh)]^{1/2}}{\rho_l \tanh(kh)\rho} \tag{5.22}$$

The dispersion relation of the dilatational mode may be directly obtained from this relation by replacing the hyperbolic tangent function $\tanh(\cdot)$ by the hyperbolic cotangent function $\coth(\cdot)$. For large liquid to gas densitiy ratios, it appears from eq. 5.22 that the grow rate of the sinusoidal mode is greater than that of the dilatational mode for any wavelength. Thus, the liquid sheet desintegration is mainly influenced by the sinusoidal mode. However, two submodes of disintegration may be distinguished based on liquid injection velocity [131]:

- In the streamwise ligament breakup regime, the liquid injection velocity is too low for the dilatational mode to develop and the sheet disintegration is mainly dictated by the sinusoidal mode. The sheet disintegrates in the vicinity of the injector, leading to the formation of streamwise ligaments, as may be see in fig. 5.4a.
- For higher liquid injection velocities, the longitudinal mode may sufficiently develop and the sheet disintegrates through the combined action of dilatational and sinusoidal modes, leading to the formation of cells. This disintegration mode is called cellular breakup regime and leads to the formation of spanwise ligaments, see fig. 5.4b.

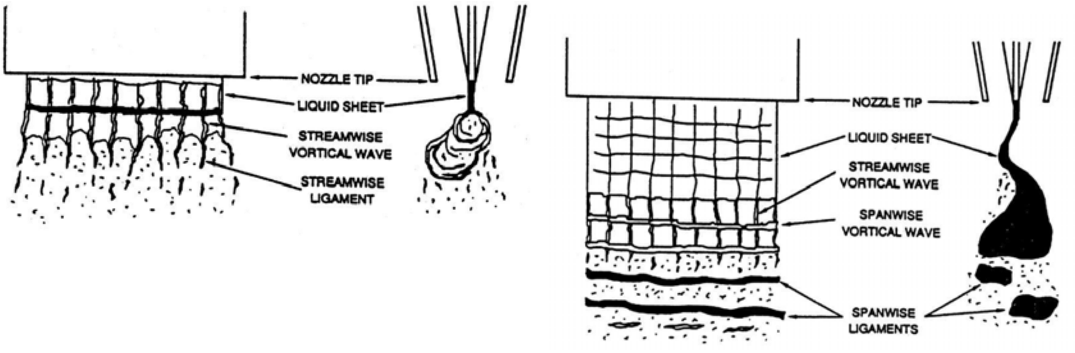

(a) (b)

Figure 5.4 : *Illustration of the streamwise ligament breakup regime (left) and the cellular breakup regime (right) for a flat liquid sheet. The sheet disintegration is mainly dictated by the sinusoidal mode in the streamwise ligament breakup regime while a combination of sinusoidal and dilatational mode governs the disintegration in the cellular breakup regime. From Stapper and Samuelsen [212]*

5.1.2 Secondary breakup

Primary atomization leads to the ejection of fragments from the liquid. When the aerodynamic forces acting upon these fragments are larger than the surface tension forces stabilizing them, they may undergo deformation and desintegrate into smaller fragments or particles. This process is called secondary breakup, it is characterized by the droplet Weber number:

$$We = \frac{\rho(u_{p,i} - u_i)^2 d_p}{\sigma_l} \tag{5.23}$$

d_p denotes an equivalent diameter of the liquid fragment or particle. Similarly, an Ohnesorge number based on the particle or fragment diameter may be defined:

$$Oh = \frac{\mu_l}{(\rho_l d_p \sigma_l)^{1/2}} \tag{5.24}$$

The Ohnesorge number characterizes the resistance of a liquid fragment or particle to deformations through viscous dissipation of kinetic energy.

Krzeczkowski [103] as well as Pilch and Erdmann [156] conducted analysis on secondary breakup mechanisms and classified them in five distinct regimes:

- vibrational breakup ($We < 12$), where the particle oscillates with the characteristic frequency of the vortex tail forming in the wake of the particle.
- bag breakup ($12 < We < 50$), which is identified by a hollow bag-shaped membrane surrounded by a ring torus, analogous to soap bubbles blown from a ring.
- bag-stamen breakup, also called multimode breakup ($50 < We < 100$), which is similar to bag breakup but with the presence of a stamen in the middle of the bag.
- particle stripping ($100 < We < 350$), which is characterized by the stripping of small fragments from the liquid boundary layer at the particle surface.
- catastrophic breakup ($We > 350$), where the particle is disintegrated by long wavelength amplitudes, creating several large fragments which generally undergo stripping.

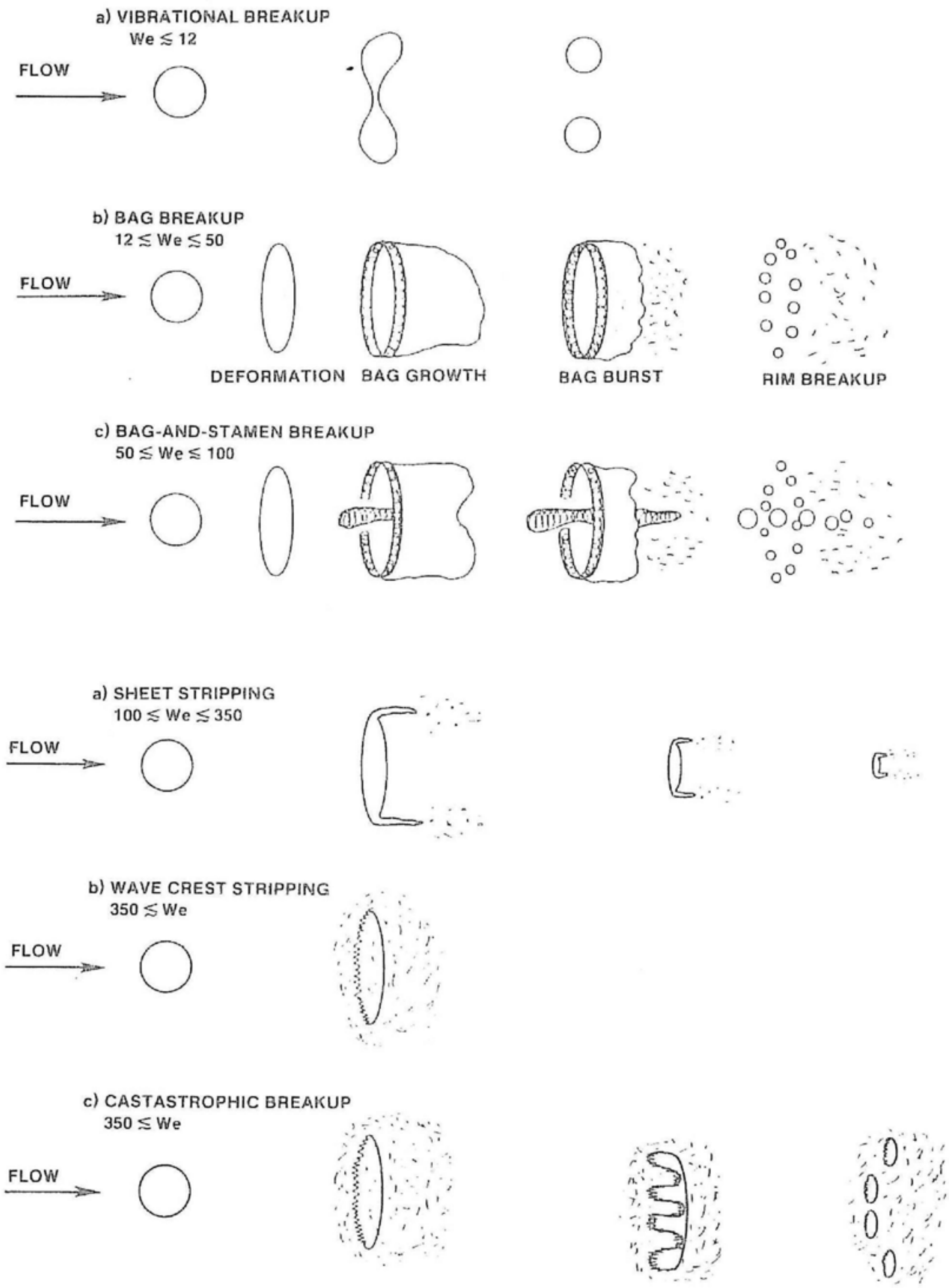

Figure 5.5 : *Classification of different secondary breakup regimes from Pilch and Erdmann [156]*

Fig. 5.5 presents a sketch of the enumerated breakup mechanisms.

Ranger and Nicholls [169] found that secondary breakup processes could be described by a characteristic time scale t_{bu} defined as:

$$t_{bu} = C_{bu}\sqrt{\frac{\rho_l}{\rho}}\frac{d_p}{|u_{p,i} - u_i|} \tag{5.25}$$

with $C_{bu} \approx 5$ varying only weakly with the Weber number, a result which was confirmed by the experimental study of Hsiang and Faeth [90]. Due to the difficulty to precisely observe particles after secondary breakup, there is only little experimental information available about the outcome of the breakup process, in particular the characteristic sizes and size distributions resulting from the different breakup regimes. Simmons [206] made the useful observation that sprays produced by a wide range of nozzle designs have similar particle size distributions when these are compared in a root/ normal graph, i.e. a $(d_p/d_{p,m})^{1/2}$ abscissa (with $d_{p,m}$ the mean droplet diameter) and an ordinate with a normal distribution scale. Hsiang and Faeth [90] found that the Simmons distribution was able to reproduce the size distribution resulting from all breakup regimes except for the stripping regime which exhibited a clear bimodal character due to the shedding of small liquid fragments from the boundary layer at the particle surface. In their study, Hsiang and Faeth [90] also provide a relationship for the Sauter mean diameter d_{32} (see section 3.6) after bag, bag-stamen and stripping breakup:

$$d_{32} = 6.2\left(\frac{\rho_l}{\rho}\right)^{1/4}\left(\frac{\mu_l a_p}{\rho_l\|\overrightarrow{u_p} - \overrightarrow{u}\|}\right)^{1/2} \tag{5.26}$$

with a_p the diameter of the parent particle and d_{32} the average Sauter mean diameter of the particles resulting from the breakup process.

5.1.3 Numerical tools for the simulation of primary atomization

This section presents two different approaches for the modeling of primary atomization. Direct Numerical Simulation of primary atomization explicitly resolves all time and length scales governing liquid disintegration. This approach is computationally intensive but has lately become affordable due to the continuous increase in computational resources. However, the Direct Numerical Simulation of primary atomization remains extremely challenging and the main numerical difficulties of this approach are outlined below in a first part. Reynolds Averaged methods for primary atomization represent a much cheaper alternative compared to Direct Numerical Simulation and are of major interest for industrial applications. They are briefly discssued in a second part.

5.1.3.a) Direct Numerical Simulation

Because most primary atomization applications occur at low Mach numbers and the two involved fluids are immiscible, liquid and gas flows may both be described by the incompressible Navier-Stokes equations. Since the equation sets of both phases are strictly identical, only those for the gas are given:

$$\frac{\partial u_j}{\partial x_j} = 0 \tag{5.27}$$

$$\frac{\partial \rho u_i}{\partial t} + u_j\frac{\partial}{\partial x_j}\rho u_i = -\frac{\partial p}{\partial x_i} + \frac{\partial \tau_{ij}}{\partial x_j} + \rho g_i + \sigma\kappa\delta(x_i - x_{f,i})n_{f,i} \tag{5.28}$$

The last term on the right-hand side of eq. 5.28 describes the surface-tension force, which is nonzero only at the location of the interface $x_{f,i}$. It is composed of the surface tension σ, the mean curvature $\kappa = (1/r_1 + 1/r_2)$ and its normal vector $n_{f,i}$.

The numerical resolution of eqs. 5.27 and 5.28 requires the precise knowledge of the interface location to evaluate the surface tension force. Numerically, the evolution of the phase interface may be either captured

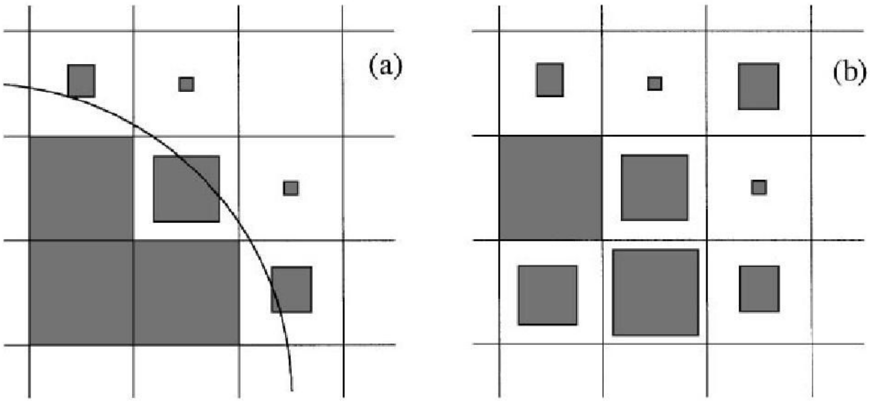

Figure 5.6 : *Visualization of the interface reconstruction problem in volume of fluid methods. The liquid volume fraction is represented as shaded squares proportional to the cell area. Right: Straightforward reconstruction of the interface. Left: More intricate reconstruction. From Scardovelli and Zaleski [195]*

by Volume of Fluid (VOF) or Level-Set approaches [195, 203, 74], which are both briefly described in the following.

The Volume of Fluid approach defines a marker function ψ which represents the liquid volume fraction inside each control volume V_c :

$$\psi(\overrightarrow{x}) = \frac{1}{V_c}\int_{V_c} H(\|\overrightarrow{x} - \overrightarrow{x_f}\|)dV \tag{5.29}$$

$H(\cdot)$ denotes the Heaviside function:

$$H(x) = \begin{cases} 0 & \text{if} \quad x < 0 \\ 1 & \text{if} \quad x > 0 \end{cases}$$

From mass conservation at the interface in absence of phase change, it follows that the interface motion is described by an advection equation of the marker function:

$$\frac{\partial \psi}{\partial t} + u_{f,i}\frac{\partial \psi}{\partial x_i} = 0 \tag{5.30}$$

where $u_{f,i}$ represents the velocity vector of the interface. Using adequate discrete representations of eq. 5.30, mass conservation may be ensured in a natural manner in Volume of Fluid approaches. However, the numerical resolution of eq. 5.30 requires knowledge of the interface location, which is not readily available when transporting the liquid volume fraction. Thus, the location of the interface must be reconstructed from the field of the marker function ψ in a first step. This involves estimating the normal vector orientation from the gradient of the marker function:

$$n_{f,i} = \frac{\partial \psi}{\partial x_i} \tag{5.31}$$

Then, a linear interface which divides the computational cell in two parts containing the proper amount of fluid in each part must be found [195]. This reconstruction step may become intricate (see fig. 5.6) and relies on complex geometrical algorithms. Once the interface has been reconstructed, its motion on the computational grid must be modeled with a numerically robust and precise advection algorithm. Since this aspect is common to both Volume of Fluid and Level Set methods, it is discussed after the presentation of the Level Set approach.

In Level Set methods, the interface is identified by a constant value ϕ_0 of a scalar function ϕ. Since the interface is identified by a single level of the scalar function ϕ, there is considerable freedom in the definition of

ϕ away from the interface. From a numerical point of view, ϕ should be a smooth function and it is commonly initialized as a signed distance function d to the interface:

$$\phi(x_i, t = 0) = \pm d \tag{5.32}$$

The interface motion is again described by a scalar advection equation:

$$\frac{\partial \phi}{\partial t} + u_{f,i} \frac{\partial \phi}{\partial x_i} = 0 \tag{5.33}$$

with $u_{f,i}$ the velocity vector of the interface. Contrary to Volume of Fluid methods, Level Set methods are not inherently mass conservative. To improve mass conservation properties of Level Set methods, Olsson and Kreiss [146] propose to define ϕ as a smeared out version of the liquid volume fraction:

$$\phi = \frac{1}{2} \left(\tanh \left(\frac{d}{2\epsilon} \right) + 1 \right) \tag{5.34}$$

where d is the minimum distance to the interface and ϵ corresponds to half the thickness of the interface. This defintion of ϕ combined with the use of a conservative numerical scheme for the resolution of eq. 5.33 shows good volume conservation properties in practice [146]. Level Set methods avoid the reconstruction of the interface and give direct access to its geometrical information, in particular the curvature κ which is required for the evaluation of surface tension forces:

$$\kappa = -\frac{\partial n_{f,i}}{\partial x_i} \tag{5.35}$$

This aspect is their main advantage compared to Volume of Fluid methods. However, this method has certain practical difficulties. Since the Level Set function is advected on the entire computational domain, an extension velocity of the interface velocity $u_{f,i}^{ext}$ needs to be defined for the numerical resolution of eq. 5.33. Zhao et al. [233] propose to use a divergence-free extension velocity, which allows to conserve the signed distance function properties of ϕ:

$$\frac{\partial u_{f,i}^{ext}}{\partial x_i} = 0 \tag{5.36}$$

During numerical simulations, the Level Set function may become stretched and spread through high velocity gradients. Under these conditions, ϕ may not necessarily remain a signed distance function. Thus, at later times in the computation, it may become necessary to reinitialize ϕ. The reinitialization step is numerically expensive and it is not completely clear how often it should be performed during a simulation [203].

The numerical resolution of the interface advection equation requires the use of specific numerical algorithms since it represents a sharp discontinuity. Adaptive grid refinement at the interface location may be used to ensure a sufficient numerical discretization of the gradients. When using fixed grid methods, upwind schemes are generally employed to limit spurious oscillations arising from the sharp gradients at the interface. The basic idea of upwinding methods consists in reconstructing the propagation of information from characteristic theory [88]. Although numerically stable, upwind methods may diffuse the interface through numerical dissipation, which is clearly undesirable. To compensate this effect, the truncation order of these methods needs to be decreased by using more accurate evaluations of spatial gradients (or numerical fluxes in a finite volume context). In this context, Non-linear Total Variation Diminishing (TVD) methods have been found to yield sufficient numerical precision while guaranteeing bounded numerical solutions [146]. Precision gains may also be achieved by applying upwinding procedures only in regions where it is strictly necessary while using less dissipative centered schemes in smoother regions of the flow field. This is the fundamental principle of Essentially Non-Oscillatory (ENO) schemes, which have found widespread use for both Volume of Fluid and Level Set approaches [135].

An additional difficulty in the simulation of primary atomization arises from the numerical treatment of the discontinuity in material properties at the interface and the evaluation of surface tension forces, which are only acting at the interface location. Generally, the interface jump is solved in an approximate manner by smoothing it over a few grid points. Considering a liquid-gas interface, density shows a strong discontinuity, which may be formally written as:

$$\rho(\overrightarrow{x}) = \rho_l + H(\|\overrightarrow{x} - \overrightarrow{x_f}\|)(\rho - \rho_l) \tag{5.37}$$

In the finite volume context, smoothing may be achieved by defining material properties as average values over the control volumes V_{cv}:

$$\bar{\rho} = \frac{1}{V_{cv}} \int_{V_{cv}} \rho \, dx_i = \rho_l + \psi(\rho - \rho_l) \tag{5.38}$$

It is apparent that this approach is ideally suited for volume of fluid methods and conservative level set methods. If using finite difference methods for the convection of the interface, material properties may be obtained from a nodal evaluation. In the volume of fluid context, this yields:

$$\rho(x_i) = \rho_l(x_i) + \psi(\rho(x_i) - \rho_l(x_i)) \tag{5.39}$$

The equivalent evaluation in the level set context writes:

$$\rho(x_i) = \rho_l(x_i) + H_\epsilon(\phi(x_i) - \phi_0(x_i))(\rho(x_i) - \rho_l(x_i)) \tag{5.40}$$

where H_ϵ is a smeared out version of the Heaviside function of characteristic thickness ϵ:

$$H_\epsilon(x) = \begin{cases} 0 & \text{if} \quad x > -\epsilon \\ \frac{1}{2}\left[1 + \frac{\phi}{\epsilon} + \frac{1}{\pi}\sin(\pi\phi\epsilon)\right] & \text{if} \quad -\epsilon < x < \epsilon \\ 1 & \text{if} \quad x > \epsilon \end{cases}$$

Despite these difficulties, considerable progress has been recently achieved in interface capturing techniques and these methods have enjoyed widespread interest in the scientific community over the last years [195, 203]. Fig. 5.7 from Ménard et al. [135], illustrates the capabilities of interface capturing techniques for the Direct Numerical Simulation of primary atomization in a turbulent liquid jet. Given the experimental difficulties in the characterization of primary atomization, Direct Numerical Simulation may offer a promising alternative to gain more physical insight into this phenomenon.

5.1.4 Reynolds Averaged Navier Stokes methods

Direct Numerical Simulation of primary atomization remains extremly costly because of the large range of time and length scales involved in this phenomenon. Therefore, simplifying approaches are necessary when considering the simulation of realistic configurations. Vallet and Borghi [222] have proposed a Reynolds Averaged Navier-Stokes approach for the simulation of primary atomization. In their method, the spray is treated in an Eulerian manner as strong interactions between the liquid-gas interface and the high density of the spray make the use of Lagrangian approaches impractical. The approach treats liquid-gas mixing using a two-phase medium of density ρ_{g-l}:

$$\frac{1}{\rho_{g-l}} = \frac{Y_l}{\rho_l} + \frac{1 - Y_l}{\rho} \tag{5.41}$$

where Y_l is the liquid mass fraction. Because of the strong density variations of the mixture, a Favre-weighted ensemble average is defined for quantities of the liquid-gas mixture:

$$\langle \rho_{g-l} Y_l \rangle = \langle \rho_{g-l} \rangle \widehat{Y_l} \tag{5.42}$$

The conservation equations for the liquid-gas mixture are now presented.

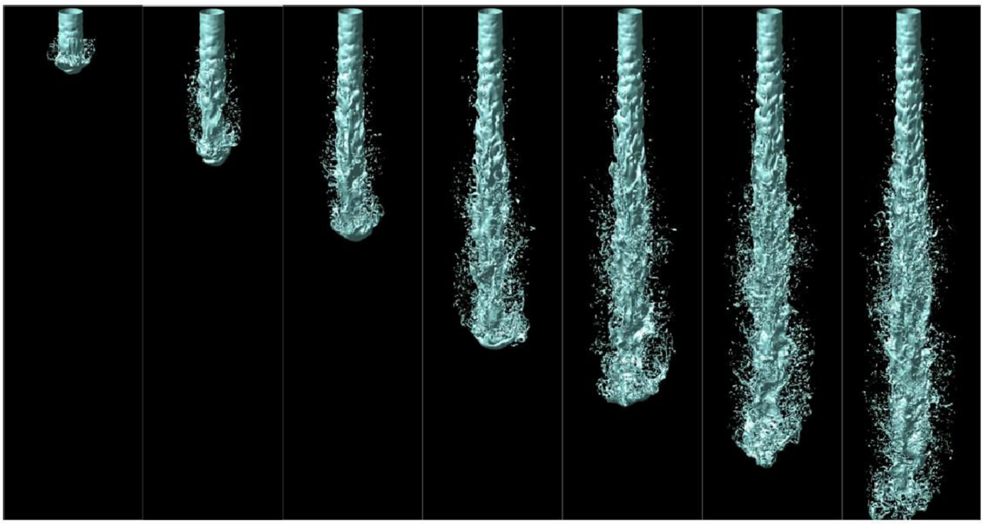

Figure 5.7 : *Snapshots of the direct numerical simulation of the primary atomization of a turbulent liquid jet (time step is* $2.5\mu s$*). From Ménard et al. [135]*

5.1.4.a) Conservation equations for the liquid-gas mixture

The evolution of the liquid-gas mixture is described by a set of transport equations to characterize the two-phase medium. The ensemble averaged conservation equation for liquid mass fraction in absence of evaporation writes:

$$\frac{\langle \rho_{g-l} \rangle \widehat{Y_l}}{\partial t} + \frac{\langle \rho_{g-l} \rangle \widehat{u_{g-l,i}} \widehat{Y_l}}{\partial x_j} = -\frac{\partial \langle \rho \rangle \widehat{u''_{g-l,i} Y_l''}}{\partial x_j} \tag{5.43}$$

where $\widehat{u_{g-l,i}}$ is the averaged mass-weighted velocity of the liquid gas mixture. The term on the right-hand side of eq. 5.43 describes the turbulent dispersion of the liquid. For details on the modeling of this term, the reader is referred to the thesis of Beau [13].

For the momentum equation of the two-phase mixture, it is assumed that the Reynolds number is sufficiently large to neglect viscous laminar effects. Therefore, the momentum equation of the two-phase mixture writes:

$$\frac{\langle \rho \rangle \widehat{u_{g-l,i}}}{\partial t} + \frac{\langle \rho \rangle \widehat{u_{g-l,i}} \widehat{u_{g-l,j}}}{\partial x_j} = -\frac{\partial \langle p \rangle}{\partial x_i} - \frac{\partial \langle \rho \rangle \widehat{u''_{g-l,i} u''_{g-l,j}}}{\partial x_j} \tag{5.44}$$

In the context of a two-phase mixture with strong density variations, the closure of the turbulent Reynolds stress tensor may require specific attention [13]. Finally, a transport equation is solved for the turbulent kinetic energy of the mixture, which is defined as:

$$\widehat{k_{g-l}} = \frac{1}{2} \widehat{u''_{gl,i} u''_{gl,i}} \tag{5.45}$$

It may be shown [13] that this quantity is related to the the turbulent kinetic energies of the gas and the liquid according to the relation:

$$\widehat{k_{g-l}} = \widehat{Y}_l \frac{1}{2} \langle u''_{l,i} u''_{l,i} \rangle + (1 - \widehat{Y}_l) \frac{1}{2} \langle u''_i u''_i \rangle + \frac{\left(u''_{l,i} Y_l'' \right)^2}{2} \left(\frac{1}{\widehat{Y}_l} + \frac{1}{1 - \widehat{Y}_l} \right) \tag{5.46}$$

The transport equation for the turbulent kinetic energy of the mixture then writes:

$$\begin{aligned}\frac{\partial\langle\rho\rangle\widehat{k_{g-l}}}{\partial t}+\frac{\partial\langle\rho\rangle\widehat{k_{g-l}}\widehat{u_{l,i}}}{\partial x_j} \quad = \quad & \frac{\partial}{\partial x_i}\left(\frac{\mu_t}{Sc_{t,k}}\frac{\partial\widehat{k_{g-l}}}{\partial x_i}\right)+\mu_t\left(\frac{\partial\widehat{u_{g-l,i}}}{\partial x_j}+\frac{\partial\widehat{u_{g-l,j}}}{\partial x_i}-\frac{2}{3}\frac{\partial\widehat{u_{g-l,k}}}{\partial x_k}\delta_{ij}\right)\frac{\partial\widehat{u_{g-l,i}}}{\partial x_j}+ \\ & \frac{2}{3}\langle\rho\rangle\widehat{k_{g-l}}\frac{\partial\widehat{u_{g-l,k}}}{\partial x_k} \quad - \quad \langle\rho\rangle 2\nu_{g-l}\widehat{\frac{\partial u''_{g-l,i}}{\partial x_j}\frac{\partial u''_{g-l,i}}{\partial x_j}}\end{aligned} \tag{5.47}$$

where a unitary Schmidt number Sc has been tacitly assumed. The last term on the right-hand side of eq. 5.47 represents the turbulent dissipation rate of kinetic energy of the mixture. Closures for this term are presented in Beau [13].

5.1.4.b) Transport of the mean interface density

In order to model primary atomization, the size of the fragments ejected from the liquid must be determined. This is done by solving a transport equation for the liquid-gas interface per unit volume Σ. The modeling framework is adapted from flame surface density methods in turbulent combustion [83]. This method allows to handle the strong topology changes at the surface of the liquid-gas interface. Its averaged transport equation is defined as:

$$\frac{\partial\widehat{\Sigma}}{\partial t}+\frac{\partial\widehat{u_{g-l,j}}\widehat{\Sigma}}{\partial t}=-\frac{\partial\widehat{u''_{g-l,i}\Sigma}}{\partial x_i}+\dot{\widehat{\Sigma}} \tag{5.48}$$

The second term on the right-hand side gathers creation/ destruction terms of the liquid-gas interface. Several contributions arise for this source term:

- oscillations of the interface through the development of instabilities.
- wrinkling of the interface through turbulence.
- ejection of fragments from the liquid.
- collisions/ coalescence between particles.

Modeling terms for each of these contributions may be found in Beau [13] and Lebas [111]. Combining the transport equations for liquid-gas mixture and the mean interface density allows to describe primary atomization at high Reynolds and Weber numbers in a Reynolds averaged sense. In the case of Diesel spray atomization, the results of Beau et al. [14] show that this method matches well with results from Direct Numerical Simulations. Furthermore, this method may be coupled with a Lagrangian solver in dilute regions of the spray to simulate the entire spray evolution, yielding the so-called Euler Lagrange approach for Sprays and Atomization (ELSA) [13, 111].

5.2 The FIMUR approach

The previous section has shown the great complexity in the numerical simulation of primary atomization and the development of the numerical tools to simulate this process were considered out of reach of the present work. Instead, the attempt was made to develop simplifying approaches for liquid injection. This section discusses an injection method, called FIMUR (Fuel Injection Method by Upstream Reconstruction), which attempts to model particle injection by pressure swirl atomizers for both Euler-Lagrange and Euler-Euler approaches. The model was developed jointly with Sanjosé [191]. It neglects effects of liquid disintegration on spray dynamics and directly injects the developed spray at the atomizer orifice. The model requires the following entries for a

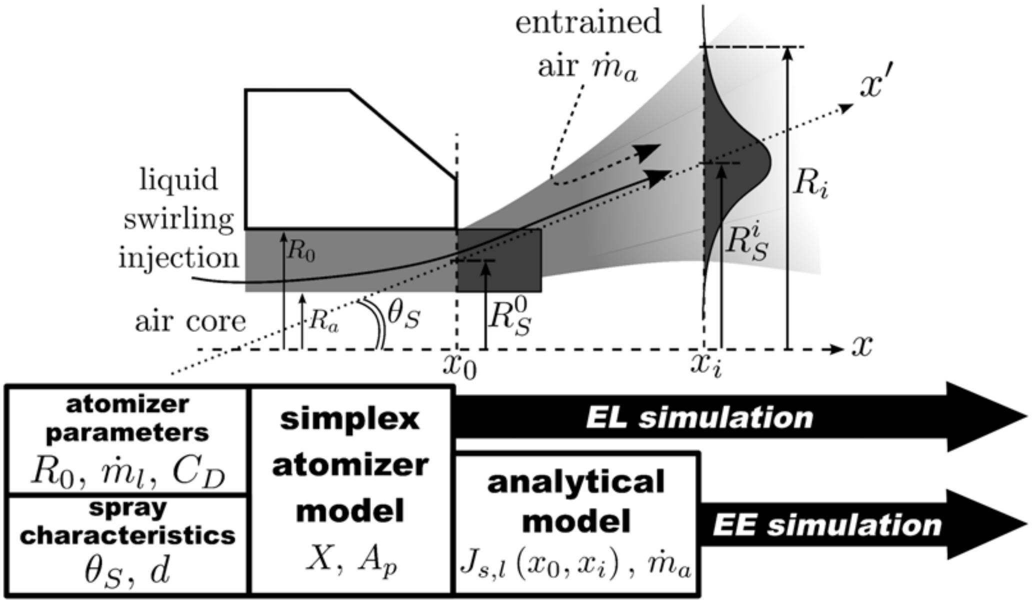

Figure 5.8 : *Sketch of the FIMUR methodolgy taken from Sanjosé [191]*

given pressure swirl atomizer: the liquid mass flow rate $\dot{m}_l$, the spray angle θ_s and the diameter of the atomizer orifice D_0, and the particle diameter distribution of the spray after primary and secondary atomization processes are completed. From these parameters, liquid velocity profiles at the atomizer orifice are reconstructed based on considerations on the flow field inside the atomizer and empirical correlations.

5.2.1 Methodolgy

Euler-Euler and Euler-Lagrange approaches differ considerably in their numerical frameworks and this directly affects the boundary conditions required for spray injection. In the Euler-Lagrange approach, particles may directly be injected at the atomizer orifice, defined by the axial plane $x = x_0$. This implies that the time scales of primary and secondary atomization processes are negligible compared to the characteristic time scales of the flow field so that their impact on spray dynamics in the dilute regime may be neglected. Although this hypothesis is a great simplification of real physics, there is no practical difficulty in injecting particles at the atomizer orifice in the Euler-Lagrange approach. On the contrary, the Euler-Euler approach may not directly inject particles at the atomizer orifice since the injection surface must be meshed with sufficient precision. Given the small orifice diameters encountered in practical applications (< 1 mm), this would imply very small cell sizes and degrade the global timestep of the simulation. A solution consists in artificially translating the injection boundary condition of the Euler-Euler approach further downstream to an axial position $x = x_i$ where the spray has sufficiently spread to be meshed with reasonable computational cost. Between the real atomizer orifice location $x = x_0$ and the Euler-Euler injection surface $x = x_i$, the spray evolution needs to be described. Fig. 5.8 summarizes the principles of the methodolgy.

The FIMUR methodology consists in three steps:

- First, the velocity profiles for particle injection at the atomizer orifice location $x = x_0$ are derived. The derivations are based on empirical correlations of Giffen and Muraszew [69], Rizk and Lefebvre [181] for pressure swirl atomizers of the simplex type.
- Second, the spray velocity components and the liquid volume fraction in the translated injection plane

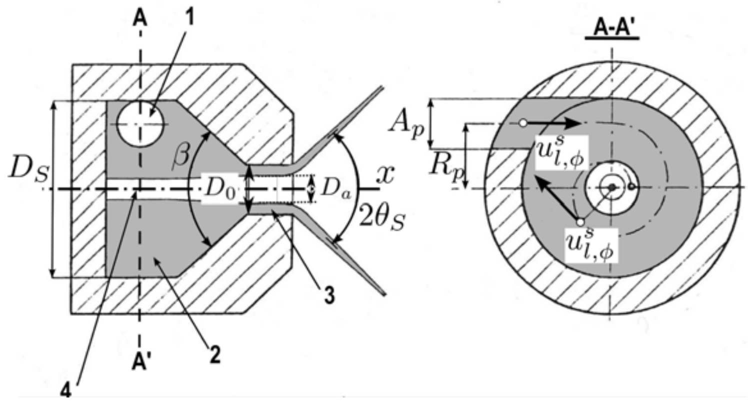

Figure 5.9 : *Schematics of a pressure swirl atomizer of the simplex type, adapted from Bayvel and Orzechowski [12]. A swirling motion (velocity $u^s_{l,\phi}$) is imposed to the fluid in the tangential inlet ports of cross section A_p. This motion generates an air core of diameter $D_a(=2R_a)$ at the atomizer orifice. The diameter of the atomizer orifice is denoted $D_0(=2R_0)$.*

$x = x_i$ are calculated by writing integral conservation laws for the spray evolution between the planes $x = x_0$ and $x = x_i$.

- Third, the air entrainement by the spray $\dot{m}_a$ and the momentum exchange between gas and spray $J_{s,l}$ from the plane $x = x_0$ to the plane $x = x_i$ are accounted for through an extension of Cossali's [36] model.

The Euler-Lagrange approach is only concerned with the first step of the FIMUR methodology. For this reason, the second and third steps are only briefly summarized and the reader is referred to Sanjosé [191] for more details on them.

5.2.2 Flow field inside pressure swirl atomizers

The FIMUR methodology focuses on pressure swirl atomizers. In this type of nozzle, the liquid is injected through tangential or helical passages to generate a swirling motion. The internal geometry of a pressure swirl atomizer of the simplex type is displayed in fig. 5.9. The liquid is injected through a tangential inlet port 1 into the swirl chamber 2 of diameter D_s $(=2R_s)$. The injection surface A_p of the swirl chamber is defined by $A_p = (\pi D_p^2)/4$. Due to the swirling motion, an air core is generated at the center of the orifice. The liquid leaves the atomizer orifice of diameter R_0 as a thin conical sheet which rapidly destabilizes, disintegrating into ligaments and then particles. The air core radius at the atomizer orifice is denoted R_a.

The following analysis is based on simplex atomizers, but the obtained results may be extended to other types of pressure-swirl atomizers according to Lefebvre [117]. In the following derivations, a cylindrical coordinate system (r, ϕ, x) is used. The spray formed at the atomizer orifice is assumed to be axissymetric so that there is no dependency on the angular coordinate ϕ. In addition, the liquid axial velocity at the atomizer orifice is assumed constant over the radial coordinate:

$$u_{l,x}(x = x_0, r) = u^0_{l,x} = \text{constant} \tag{5.49}$$

Under these assumptions, the liquid axial velocity at the atomizer orifice is directly obtained from mass conservation:

$$\dot{m}_l = u^0_{l,x}\rho_l A_0(1-X) \tag{5.50}$$

where A_0 is the area of the injection orifice. X represents the area ratio of the air core to the atomizer orifice:

$$X = \frac{A_a}{A_0} \tag{5.51}$$

where A_a is the surface of the air core section. For the liquid tangential velocity, conservation of angular momentum between the swirl chamber and the atomizer orifice is assumed:

$$u^0_{l,\phi} r = u^s_{l,\phi} R_s = \text{constant} \tag{5.52}$$

Mass conservation in the swirl chamber combined with eq. 5.52 then yields:

$$\dot{m}_l = u^s_{l,\phi} \rho_l A_p = u^0_{l,\phi} \frac{r}{R_s} \rho_l A_p \tag{5.53}$$

It is assumed that the liquid flow pattern inside the atomizer may be completely described by the imposition of a rotational motion to the axial flow [117]. Thus, liquid radial velocity vanishes at the atomizer orifice:

$$u^0_{l,r} = 0 \tag{5.54}$$

In summary, the velocity profiles at the orifice ($x = x_0$) write:

$$u^0_{l,x} = \frac{\dot{m}_l}{\rho_l \pi R_0^2 (1 - X)} \tag{5.55}$$

$$u^0_{l,r} = 0 \tag{5.56}$$

$$u^0_{l,\phi}(r) = \frac{\dot{m}_l}{\rho_l A_p} \frac{R^0_s}{r} \tag{5.57}$$

$$\alpha^0_l(r) = \begin{cases} 0 & \text{if } r \in [0, R_a] \\ 1 & \text{if } r \in [R_a, R_0] \end{cases} \tag{5.58}$$

where $R^0_s = (R_0 + R_a)/2$ denotes the center position of the liquid sheet.

Two unknowns remain in eqs. 5.55-5.57, namely the area ratio X of the air core to the atomizer orifice and the area of the tangential inlet ports A_p. These are internal parameters of the atomizer and must be evaluated through empirical correlations. From inviscid theory, Giffen and Muraszew [69] derive a relation between the spray angle θ_s and the area ratio X for simplex atomizers:

$$\sin \theta_s = \frac{2\sqrt{2}X}{(1 + \sqrt{X})\sqrt{1 + X}} \tag{5.59}$$

Rizk and Lefebvre [181] generalize this formula by accounting for friction losses inside the nozzle to obtain:

$$\cos \theta_s = \sqrt{\left(\frac{1 - X}{1 + X}\right)} \tag{5.60}$$

Jeng et al. [95] and Sakman et al. [188] performed numerical simulations of the flow field inside a simplex atomizer and compared their results with experimental data. They found eq. 5.60 in better agreement with their results compared to eq. 5.59. Therefore, eq. 5.60 is used in the follwing to determine the area ratio X from the spray angle θ_s. For the estimation of the tangential-injection surface A_p, a formula by Taylor [218], accommodated to the experimental data of Carlisle [25, 117] may be used:

$$A_p = 20.73\, C_D^2\, A_0 \tag{5.61}$$

C_D is the discharge coefficient and characterizes the pressure drop over the atomizer nozzle. It may be related to the area ratio X from inviscid theory:

$$C_D = 1.17 \sqrt{\frac{(1-X)^3}{(1+X)}} \tag{5.62}$$

The constant value 1.17 in eq. (5.62) has been adjusted to experimental results of Giffen [69].

5.2.3 FIMUR in the Euler-Euler approach

Eqs. 5.55-5.57 specify the velocity profiles of the spray at $x = x_0$. In the Euler-Euler approach, the injection plane is shifted further downstream for reasons of numerical resolution. Therefore, simplified equations characterising the spray evolution between the planes $x = x_0$ and $x = x_i$ need to be derived. Two main assumpations are made:

- The momentum exchange between the liquid and the gas phases is restricted to the drag force, responsible for air entrainment by the spray.
- The liquid fuel between planes $x = x_0$ and $x = x_i$ is considered a monodisperse spray. Evaporation is not taken into account and the particle diameter d_p remains constant.

In the shifted spray injection plane ($x = x_i$), the following assumptions are used for the particle and gas velocity distributions:

1. The liquid spray keeps its axissymmetrical shape around the (Ox) axis.
2. The particle axial velocity is constant over the radial coordinate.
3. A Gaussian profile is assumed for the liquid volume fraction.

Under these hypotheses, the expressions of the liquid volume fraction and velocity components in the injection plane $x = x_i$ simplify to:

$$u^i_{l,r}(\phi, r) = u^i_{l,r}(r) \tag{5.63}$$

$$u^i_{l,\phi}(\phi, r) = u^i_{l,\phi}(r) \tag{5.64}$$

$$u^i_{l,x}(\phi, r) = u^i_{l,x}|_{mean} \tag{5.65}$$

$$\alpha^i_l(\phi, r) = \alpha^i_l|_{max} \cdot e^{\frac{-(r-\mu)^2}{\sigma^2}} \tag{5.66}$$

This leads to the evaluation of 4 parameters ($u^i_{l,x}|_{mean}$, $\alpha^i_l|_{max}$, μ and σ) and 2 functions ($u^i_{l,r}(r)$ and $u^i_{l,\phi}(r)$). These quantities are determined by writing conservation equations for the spray between $x = x_0$ and $x = x_i$.

L1 Conservation of the injected-liquid mass.
The liquid mass flow rate through the disk $r \in [0, R_i]$ at $x = x_i$ is equal to the total injected liquid mass flow rate $\dot{m}_l$.

L2 Conservation of the spray angle.
The maximum of the liquid volume fraction is located along the main spray direction line (fig. 5.8). Its radial location R^i_s is then defined as:

$$R^i_s = R^0_s + (x_i - x_0)\tan(\theta_s) \tag{5.67}$$

L3 Non-evaporating monodisperse spray.
The injected spray does not evaporate in the near field $x \in [x_0, x_i]$. The drag force is the only considered force for the liquid phase. It can be evaluated as if the spray contained only spherical particles of diameter d_p.

L4 Conservation of axial momentum.
The momentum exchange between the injected liquid and the ambient fluid (air) is most prominent in the (Ox) injection direction and will be neglected in the perpendicular directions.

L5 Conservation of kinetic momentum.
As a consequence of the previous hypothesis, the particle trajectory projected in a plane perpendicular to the (Ox) injection direction follows a ballistic trajectory.

From the derivations of Sanjosé [191], it appears that the radial dependency of tangential velocity in eq. 5.57 (proportional to the inverse of the radius $1/r$) does not allow to analytically derive the velocity profiles in the translated injection plane $x = x_i$. However, the shape of the profile is not very important as it is distributed on a very narrow region. What is important is the range of velocities to recover the correct conical shape of the spray. Therefore, the inverse linear dependency is replaced by a linear dependency which ensures the same tangential velocity interval. The velocity profiles in the injection plane $x = x_0$ modify to:

$$u_{l,x}^0 = \frac{\dot{m}_l}{\rho_l \pi r_0^2 (1 - X)} \tag{5.68}$$

$$u_{l,r}^0 = 0 \tag{5.69}$$

$$u_{l,\phi}^0(r) = \frac{\dot{m}_l}{\rho_l A_p}(ar + b) \tag{5.70}$$

$$\alpha_l^0(r) = \begin{cases} 0 & \text{if } r \in [0, R_a] \\ 1 & \text{if } r \in [R_a, R_0] \end{cases} \tag{5.71}$$

The coefficients a and b of the linear profile are adjusted so that the minimum and maximum tangential velocities are identical for eqs. 5.57 and 5.70. The coefficients a and b are then obtained as:

$$a = \frac{R_0^S}{R_0^2} - \frac{R_0^S(1+\sqrt{X})}{\sqrt{X} R_0^2} \tag{5.72}$$

$$b = \frac{R_0^S(1+\sqrt{X})}{\sqrt{X} R_0} \tag{5.73}$$

The effect of this modification on the spray velocity profiles downstream injection is remarkably moderate, as will be shown in section 5.3.3. The velocity profiles defined for the spray at the location $x = x_0$ through eqs. 5.68-5.70 may now be used to derive profiles at the shifted injection plane $x = x_i$ from the conservation laws stated above. The derivation of these profiles may be found in Sanjosé [191].

5.3 Particle injection in the Lagrangian solver

Before presenting a test of the FIMUR injection methodology described above for the Lagrangian solver, a few details on the numerical injection procedure are provided. Then, the reconstruction of particle size distributions from experimental data is discussed.

5.3.1 Numerical injection procedure in the Lagrangian solver

The Lagrangian particle injection procedure is described from a global point of view in the following. It consists in the following steps:

- The specified mass flow rate yields a mass of particles to inject per timestep:

$$m_p^{\Delta t} = \dot{m}_p \Delta t \tag{5.74}$$

- Particle diameters are generated according to the input size distribution and associated particles are injected as long as their total mass remains below the mass to inject per timestep:

$$\sum_i \left[\frac{4}{3} \pi \left(\frac{d_{p,i}}{2} \right)^3 \rho_p \right] - m_p^{\Delta t} > 0 \tag{5.75}$$

  Since particles of finite mass are injected, the mass to inject per timestep is never matched exactly and the remainder is reported to the next timestep.

- Coordinates are assigned to each particle according to the location of the injection point and the injection pattern. For the FIMUR model, the particles are randomly placed on a ring defined by the air core on the inner side and the orifice of the atomizer on the outer side: $r \in [R_a, R_0]$.
- Velocities are imposed for each particle according to its radial position from the relations given in eqs. 5.68-5.70.

The particle diameter distributions used in the simulations are reconstructed from experimental data. The following sections detail the procedures to randomly generate particle diameters following continuous lognormal and Rosin-Rammler laws. These distributions are found to reasonably approximate particle diameter distributions encountered in practical applications, as demonstrated by an illustrative example.

5.3.2 Reconstruction of particle size distributions

5.3.2.a) Lognormal distributions

In order to approximate a particle size distribution by a lognormal law, the mean particle diameter $d_{p,m}$ and the standard deviation σ_p of the size distribution must be known. A lognormal distribution is defined as:

$$f(d_p; d_{p,m}^{ln}; \sigma_p^{ln}) = \frac{1}{\sqrt{2\pi} d_p \sigma_{ln}} \exp \left(- \frac{[\ln(d_p) - d_{p,m}^{ln}]^2}{2(\sigma_p^{ln})^2} \right) \tag{5.76}$$

where $d_{p,m}^{ln}$ and σ_p^{ln} are the mean and the variance of the diameter's logarithm. These variables may be deduced from the mean diameter $d_{p,m}$ and the standard deviation σ_p using the following relations:

$$d_{p,m}^{ln} = \ln(d_{p,m}) - \frac{1}{2} \ln \left(1 + \left(\frac{\sigma_p}{d_{p,m}} \right)^2 \right) \tag{5.77}$$

$$\sigma_p^{ln} = \ln \left(1 + \left(\frac{\sigma_p}{d_{p,m}} \right)^2 \right) \tag{5.78}$$

The numerical generation of particle diameters following a lognormal law is based on the random number generator of Leva [121], which generates normally distributed random numbers according to a given mean and standard deviation. For a lognormal distribution, it is not the variable itself but its logarithm which is normally distributed. Thus, taking the exponential of a normally distributed function $N(d_{p,m}^{ln}, \sigma_p^{ln})$ yields a lognormally distributed function $N\ln(d_{p,m}^{ln}, \sigma_p^{ln})$:

$$X \sim N(d_{p,m}^{ln}, \sigma_p^{ln}) \Rightarrow Y = exp(X) \sim N\ln(d_{p,m}^{ln}, \sigma_p^{ln}) \tag{5.79}$$

Therefore, one needs to take the exponential of the normal random number generated according to the mean $d_{p,m}^{ln}$ and the standard deviation σ_p^{ln} to obtain a random number following the desired lognormal law.

5.3.2.b) Rosin-Rammler distribution

The Rosin-Rammler distribution is given by:

$$f(d_p) = q\,(d_{p,m})^{-q}\, d_p^{q-1} \exp\left[-\left(\frac{d_p}{d_{p,m}}\right)^q\right] \tag{5.80}$$

$d_{p,m}$ is the mean diameter of the distribution while the parameter q pilots the width of the distribution [8]. In the present work, q is determined through an algorithm which minimizes the error between the target distribution and the Rosin-Rammler approximation in a least-squares sense.

The numerical generation of a particle diameter following a Rosin-Rammler distribution with given parameters $d_{p,m}$ and q is based on a rejection method [166]. In a rejection method, an envelope function $g(d_p)$ of the target distribution $f(d_p)$ is constructed. The envelope function must lie above the target function at any point:

$$f(d_p) < g(d_p) \tag{5.81}$$

Once the envelope function is constructed, a random number u in the range [0;1] and a random diameter x_d in the range $[d_{p,min}, d_{p,max}]$ are generated. Two cases are now distinguished:

$$\begin{cases} u < f(x_d)/g(x_d) & : \text{the random diameter } x_d \text{ is accepted} \\ u > f(x_d)/g(x_d) & : \text{the random diameter } x_d \text{ is rejected} \end{cases}$$

The sampling is repeated until a random diameter x_d fulfilling the condition is found. It may be shown that the sampling resulting from this procedure yields a function following the distribution $f(d_p)$.

Fig. 5.10 displays an example of the numerical approximations of an experimental size distribution using the lognormal and the Rosin-Rammler laws. The experimental data corresponds to the size distribution of a spray resulting from a pressure-swirl atomizer in a swirled combustor (see chapter 7). The numerical fits are the best approximations obtained for both lognormal and Rosin-Rammler distributions. Both are obtained from a very large sample number of particle diameters ($> 3.10^5$ particles). The parameters of the numerical fits are provided in table 5.1. The results of fig. 5.10 indicate that both distributions provides a reasonable approximation to experimental data. The lognormal distribution appears slightly superior to the Rosin-Rammler distribution for the present example.

5.3.3 Test of the FIMUR injection procedure

The numerical implementation of the FIMUR model in the Lagrangian solver is tested in a cubic geometry with an inlet, an outlet and lateral sidewalls. The atomsphere in the domain is at rest. Particles are injected at the inlet according to the velocity profiles defined by eqs. 5.55-5.57 (tangential velocity proportional to the inverse

Rosin-Rammler	Lognormal
Mean diameter $d_{p,m}$: 53 μm	Mean diameter $d_{p,m}$: 52.89 μm
Width parameter q: 1.55	Standard deviation σ_p: 40.89 μm

Table 5.1 : *Parameters of the particle distribution functions to approximate an experimental size distribution resulting from a pressure swirl atomizer*

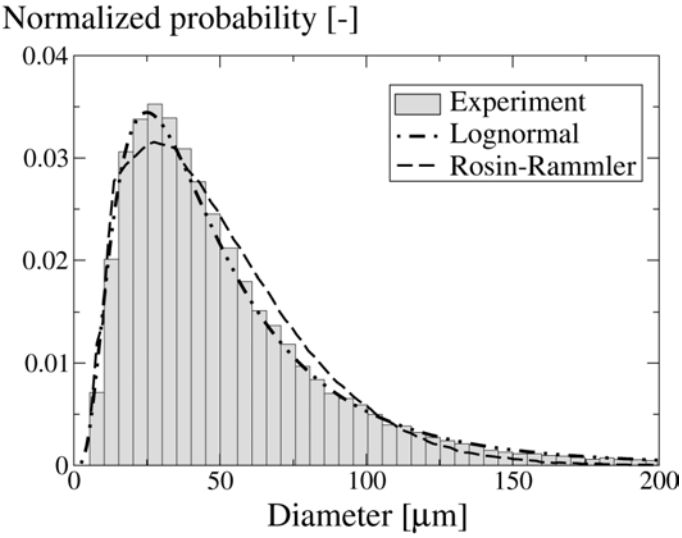

Figure 5.10 : *Normalized experimental diameter distribution of a swirled combustor (see chapter 7) averaged over the first measurement plane ($z = 6$ mm) compared to the best fits obtained with Lognormal and Rosin-Rammler distributions.*

of the radius: case A) and eqs. 5.68-5.70 (tangential velocity proportional to the radius: case B) respectively. A midplane cut of the geometry presenting the injection pattern is shown in fig. 5.11. The parameters chosen for injection are those of the pressure swirl atomizer employed in the swirled combustor simulated in the next chapter and are summarized in table 5.2.

In order to allow for an analytical integration of the particle trajectories, the drag law is modified to obtain a particle relaxation time which is independent of the particle Reynolds number Re_p:

$$\tau_p' = \frac{18\mu}{\rho_p d_p^2} \tag{5.82}$$

Furthermore, coupling between both phases is disabled so that the velocity of the gaseous phase remains constant. Under these assumptions, the temporal evolution of the particle velocity is simply:

$$u_{p,i}(t) = u_{p,i}^0 \exp(-\tau_p'/t) \tag{5.83}$$

where $u_{p,i}^0$ denotes the particle velocity at injection. The particle position as a function of time is obtained as:

$$x_{p,i}(t) = u_{p,i}(t)\tau_p'(1 - \exp(-t/\tau_p')) \tag{5.84}$$

The plane chosen for the comparison between the analytical profiles and the simulated profiles is located 9 mm downstream the injection position, see fig. 5.11. The results for case A are displayed in fig. 5.12 whereas the results for case B are shown in fig. 5.13.

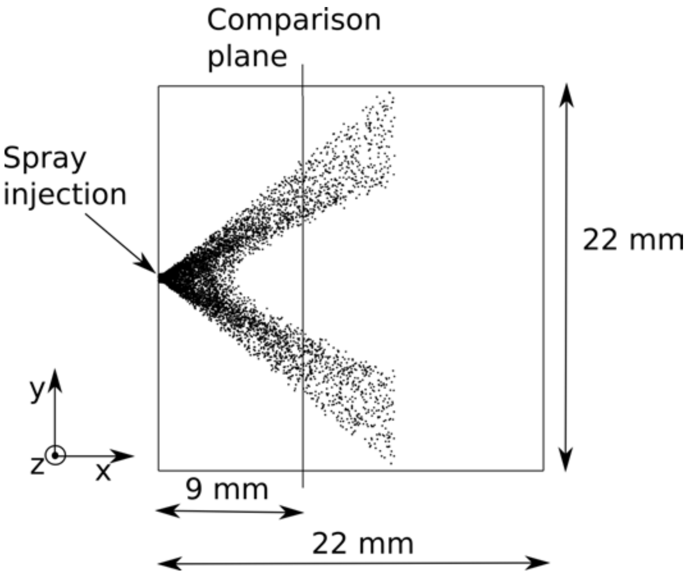

Figure 5.11 : *Sketch of the geometry for FIMUR testing. Cut through the midplane of the domain, particles are displayed in 2 mm slice. The comparison plane is located 9 mm downstream injection.*

Parameter	Values
Mass flow rate	$\dot{m}_l = 1$ g/s
Atomizer orifice diameter	$D_0 = 0.5$ mm
Spray angle	$\theta_S = 40°$
Particle diameter d_p	55 μm (monodisperse)
Area ratio X (eq. 5.60)	0.260
Liquid axial velocity $u_{x,l}$ (eq. 5.50)	8.81 m/s
Area of tangential inlet ports A_p (eq. 5.61)	$3.5 \cdot 10^{-7}\text{m}^2$

Table 5.2 : *Parameters of liquid injection*

For both cases, the agreement between the simulation data and the analytical solution is good, showing that the injection velocity profiles are implemented correctly. The magnitudes of axial velocity are identical in both cases as expected, only a slight shift in the radial spread of the spray is observed. The magnitude of the tangential velocity component appears very diminished in both cases because most of the initial tangential velocity turns into a radial component through a trigonometric effect, see fig. 5.14a. The different radial dependencies of the tangential velocity appear clearly in both cases, inversely linear in fig. 5.12 and linear in fig. 5.13, but the radial velocity profiles are not sensitive to them. This results from a balistic sorting effect. Particles exiting the atomizer orifice with the greatest tangential velocity are located along the outer envelope of the spray independently of their initial radial location due to the effect illustrated on fig. 5.14b. Similarly, particles with the lowest tangential velocities are located at the inner envelope. Therefore, the radial velocity increases with the radial coordinate in both cases. Since the range of tangential velocity are identical in both cases, the resulting spray envelopes are very similar. It would have been very interesting to directly compare Euler-Lagrange and Euler-Euler velocity profiles on such configuration, but the resulting velocity and liquid volume fraction profiles led to numerical difficulties in the Euler-Euler simulations. Therefore, the only comparison between Euler-Lagrange and Euler-Euler injections for this methodology will be performed for the simulation of an

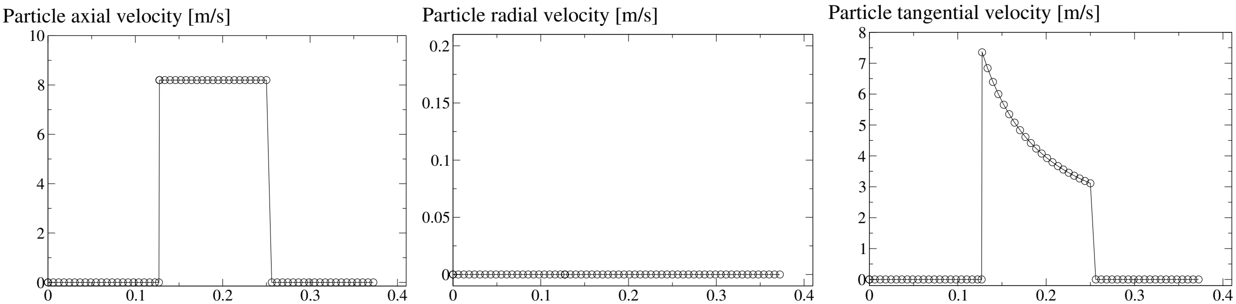

(a) Axial velocity (b) Radial velocity (c) Tangential velocity

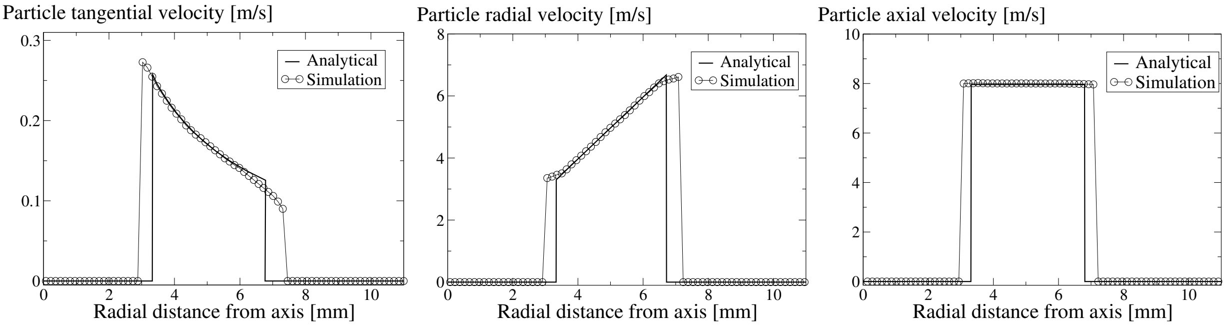

(d) Axial velocity (e) Radial velocity (f) Tangential velocity

Figure 5.12 : *Velocity profiles for case A (eqs. 5.55-5.57). Top: velocity profiles at injection. Botton: velocity profiles in the comparison plane located 9 mm downstream injection*

aeronautical combustor (see chapter 7).

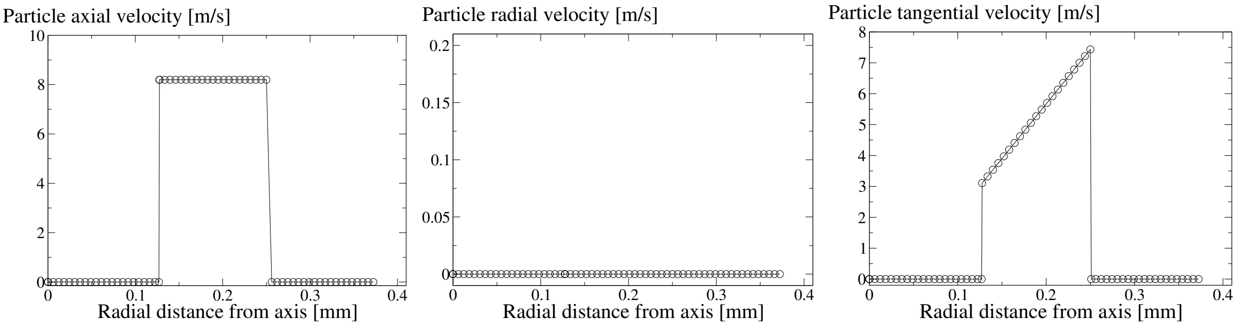

(a) Axial velocity (b) Radial velocity (c) Tangential velocity

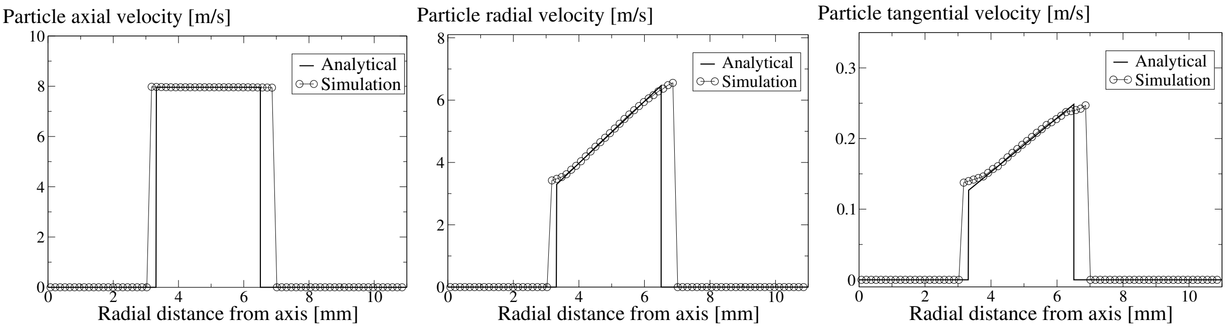

(d) Axial velocity (e) Radial velocity (f) Tangential velocity

Figure 5.13 : *Velocity profiles for case B (eqs. 5.68-5.70). Top: velocity profiles at injection. Botton: velocity profiles in the comparison plane located 9 mm downstream injection*

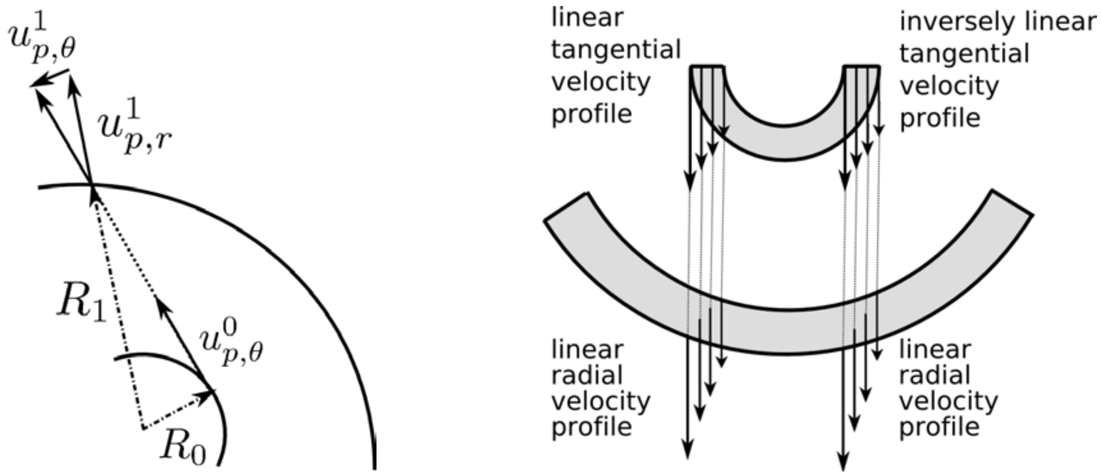

(a) (b)

Figure 5.14 : *a: Conversion of tangential velocity into radial velocity through trigonometry. b: linear radial velocity profile obtained for both cases due to the conversion of tangential to radial velocity components*

5.4 Secondary breakup model

The FIMUR methodology for pressure-swirl atomizers described in the previous section neglects the effects of primary and secondary atomization on spray dynamics by directly injecting the developed spray at the atomizer orifice. The velocity profiles of the injected spray are thus set identical to those of the liquid sheet leaving the atomizer orifice. This is a great simplification of real physics and may induce erroneous predictions since the dynamics of a liquid sheet and a developed spray differ considerably. Furthermore, the drag properties of the liquid fragments issued from primary atomization and disintegrating into smaller elements through secondary breakup are also notably different from those of the smaller particles present in the developed spray. The errors associated with this simplification may become important if there is a large velocity difference between liquid and gas at injection, which is expected to be the case in aeronautical applications. These limitations may be partly compensated through the implementation of a secondary breakup model in the Lagrangian solver. This implementation is directly complementary to the FIMUR approach: instead of directly injecting the developed spray at the atomizer orifice, the injection model may be improved by injecting large blobs at the atomizer orifice which are expected to yield a better representation of the liquid/ spray dynamics in the vicinity of the injector. The secondary breakup model will then ensure the stepwise disintegration of these blobs into the developed spray. The present section is organized as follows. First, a brief review of particle breakup models in the Lagrangian framework is presented. Second, the chosen secondary breakup model is described in more detail. Validation cases of this secondary breakup model are provided in the next chapter.

5.4.1 Bibliography

The Lagrangian approach tracks individual particles and may therefore not accurately reproduce the dynamics of a destabilizing liquid/ gas interface after injection. Therefore, the disintegration of a liquid stream is represented by a train of particles with the same characteristic diameter. Depending on the predominance of either primary or secondary atomization on spray dynamics, Lagrangian breakup models attempt to either reproduce primary atomization or secondary atomization mechanisms. The most popular breakup models in the literature are the Wave/ Kelvin-Helmholtz model of Reitz [173] and the TAB (Taylor-Analogy Breakup) model of O'Rourke and Amsden [148]. Both models are briefly described in the following.

The Wave/ Kelvin-Helmholtz Model [173] considers the primary atomization of a stationary, round, liquid jet injected into an inviscid, incompressible gas. Under these conditions, a dispersion relation between the disturbance frequency ω and the wavelength $\lambda = 2\pi/k$ of the fastest growing wave may be determined through linear stability theory (see section 5.1.1.a)). Curve fits of the numerical solutions to these quantities yield the following relations:

$$\omega = \sqrt{\frac{\sigma_l}{\rho_l a_p}} \frac{0.34 + 0.385 We_l^{0.15}}{(1+Oh)(1+1.4T^{0.6})} \tag{5.85}$$

$$\lambda = 9.02 a_p \frac{(1+0.45\sqrt{Oh})(1+0.4T^{0.7})}{(1+0.87We^{1.67})^{0.6}} \tag{5.86}$$

where Oh denotes the Ohnesorge number, σ_l the liquid surface tension, We and We_l the numbers based respectively on the density of the liquid and the gas (see section 5.1.1). Since the liquid jet is represented by a train of particles of the same characteristic radius, the jet radius has been replaced by the radius a_p of a parent particle undergoing disintegration in eqs. 5.85 and 5.86. The characteristic number T is defined as:

$$T = Oh\sqrt{We} \tag{5.87}$$

The size of the child particles resulting from the disintegration of a parent particle are determined from the wavelength of the fastest growing disturbance wave in the liquid jet. This disturbance defines a characteristic breakup time scale defined as:

$$t_{bu}^{KH} = 3.726 B_1 \frac{a_p}{\lambda\omega} \tag{5.88}$$

where the constant B_1 depends on nozzle characteristics. The breakup time scale is combined with a simple rate equation for the evolution of the parent particle size a_p, yielding:

$$\frac{da_p}{dt} = -\frac{(a_p - r_p)}{t_{bu}^{KH}} \qquad \text{with} \tag{5.89}$$

The radius of the child particle is defined as:

$$r_p = \begin{cases} B_0\lambda & \text{if } B_0\lambda \leq a_p \\ \text{min}\left[\left(\frac{3\pi a_p^2 u_l}{2\lambda}\right)^{1/3} ; \left(\frac{3a_p^2\lambda}{4}\right)^{1/3}\right] & \text{if } B_0\lambda > a_p \text{ (only once)} \end{cases}$$

where $B_0 = 0.61$ according to Reitz [173]. With this method, small child particles are created while large parent particles continually decrease in size. In addition to the parent particle velocity, the newborn particles inherit a normal velocity $u_{p,i}^{bu}$ accounting for rim expansion in a plane normal to the relative velocity between parent particle and gas, see fig 5.15.

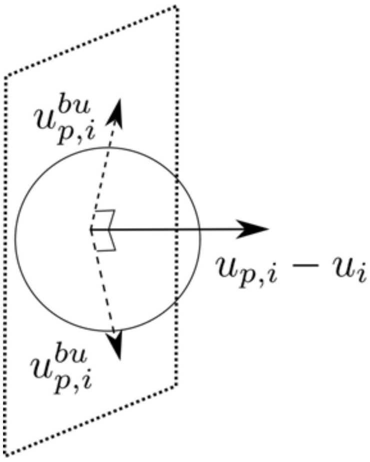

Figure 5.15 : *Sketch of the expansion velocity $u_{p,i}^{bu}$ added to the newborn particles after breakup. This velocity is randomly located in a plane normal to the relative velocity between particle and gas.*

Consider the injection of a train of particles in a quiescent atmosphere. In absence of breakup, the gaseous phase is simply accelerated in the direction of particle velocity. Thus, the velocity vectors of gas and particles remain aligned at all times and so do the particles. In the presence of breakup, this reasoning remains unchanged except for the velocity component $u_{p,i}^{bu}$ inherited by the newborn particles after breakup. Therefore, this velocity is responsible for the radial expansion of the spray and is directly linked to the spray angle θ_S when simulating the atomization of a liquid jet in a quiescent atmosphere. The Wave model uses this consideration to estimate the norm of $u_{p,i}^{bu}$ as:

$$u_{p,i}^{bu} = u_{l,0} \tan(\theta) \tag{5.90}$$

where $u_{l,0}$ is the liquid injection velocity. The angle θ is randomly sampled in the range $[0; \theta_s]$. The spray angle θ_s is estimated as:

$$\tan(\theta_s) = A_1 \lambda \frac{\omega}{u_{l,0}} \tag{5.91}$$

where A_1 represents a constant depending on nozzle design.

The TAB model [148] is a secondary breakup model based on the analogy, suggested by Taylor, between an oscillating, distorting particle and a spring-mass system. The surface tension forces are analogous to the restoring force of the spring while the external forces on the mass are similar to the aerodynamic forces extered upon the particle. Damping forces due to liquid viscosity are also included in the analogy. Therefore, breakup is mathematically written as a damped, forced oscillator:

$$m\frac{d^2x}{dt^2} = F - kx - d\frac{dx}{dt} \tag{5.92}$$

where x is the displacement of the particle equator from its spherical undisturbed position. The coefficients of this equation are obtained from Taylor's analogy:

$$\frac{F}{m} = C_F\frac{\rho|u_{p,i} - u_i|}{\rho_l r_p} \tag{5.93}$$

$$\frac{k}{m} = C_k\frac{\sigma_l}{\rho_l r_p^3} \tag{5.94}$$

$$\frac{F}{m} = C_d\frac{\mu_l}{\rho_l r_p^2} \tag{5.95}$$

C_F, C_k and C_d are constants of the model. The particles are assumed to break when their distortion exceeds a critical value proportional to the particle radius:

$$x > C_b r_p \tag{5.96}$$

with C_b a constant of the model. Eq. 5.92 may be solved analytically and the fulfillment of the breakup criterion (eq. 5.96) is then checked for each particle. The size of the child particles issued from breakup is determined by equating the energy of the parent particle to that of the child particles, while their number is deduced from mass conservation. In addition to the parent particle velocity, the child particle inherits a velocity in a plane normal to the relative velocity between particle and gas (see fig. 5.15). The magnitude of the normal velocity component is deduced from the outward velocity at the equator of the parent particle at the moment of breakup. Tanner [217] proposed an extension of this model called ETAB (Enhanced Taylor-Analogy Breakup). Instead of the energy considerations of O'Rourke and Amsden [148], the ETAB model assumes time exponential decay of the parent particle radius to determine the child particle sizes. On the contrary, the magnitude of the normal velocity component of the child particles is deduced from an energy balance between parent and child particle.

Many other breakup models exist in the literature which focus on more specific applications such as air assisted liquid sheets, air assisted liquid jets (airblast atomizers) etc... A review of a variety of breakup models is given by Raju [167]. Other approaches are based on a combination of primary and secondary atomization models such as the Wave-FIPA model of Habchi et al. [80], which combines the Wave model of Reitz [173] to a secondary breakup model based on the experimental data collection of Pilch and Erdman [156]. More recently, Gorokhovski and co-workers [73, 75, 4] proposed an original secondary breakup model based on ideas by Kolmogorov [101]. The main assumption of the model is that the number of fragments generated by a breakup event is independent of the parent particle size. Kolmogorov demonstrated that under this assumption and for a constant breakup frequency, the long-time limit of particle size distribution follows a lognormal law. According to Gorokhovski and Saveliev [75], this assumption is in agreement with experimental observations of secondary breakup processes at high relative velocities between phases. It seems furthermore confirmed by the observed good agreement between the experimental size distribution of a pressure swirl atomizer in a swirled combustor and the numerical lognormal law approximation in fig. 5.10. On the contrary, the TAB and Wave models are deterministic and produce a single size particle diameter at each breakup process. The final distribution obtained with these models is therefore not expected to match the broad size range encountered in practical applications. For this reason, the breakup model of Gorokhovski and co-workers [73, 75, 4] is preferred here. This model is referred to as the Fast Atomization Stochastic Treatment (FAST) secondary breakup model in the following.

5.4.2 Formulation of the FAST secondary breakup model

In this section, details on the Fast Atomization Stochastic Treatment (FAST) secondary breakup model implemented in AVBP are provided. In a first part, theoretical aspects are presented while the second part treats numerical aspects related to the implementation of the model.

5.4.2.a) Derivation of the breakup distribution function

Consider a parent particle of radius a_p which disintegrates with a breakup frequency f_{bu} (representing the number of breakup events per time unit). In the mean, the disintegration of the parent particle leads to the formation of n_p child particles, each one characterized by its radius r_p. The size reduction of the parent particle through a breakup event may be formally written as:

$$a_p \Rightarrow r_p = \alpha a_p \tag{5.97}$$

where α is a random number in the interval $[0;1]$. Let $q(\alpha)$ denote the disintegration spectrum, which represents the normalized probability to find a child particle radius r_p in the interval $[\alpha a_p; (\alpha + d\alpha)a_p]$:

$$\int_\alpha q(\alpha) d\alpha = 1 \tag{5.98}$$

Then $n_p q(\alpha) d\alpha$ represents the number of particles produced after a breakup event and lying in the interval $[\alpha a_p; (\alpha + d\alpha)a_p]$.

Consider $F(a_p)$ the non-normalized size distribution of parent particles. Then, $f_{bu} F(a_p) da_p$ gives the number of parent particles in the interval $[a_p; a_p + da_p]$ disintegrating per unit time. The present model assumes that the number of child particles resulting from the breakup of a parent particle a_p is independent of the latter's size. Therefore, the number of child particles produced by parent particles lying in the interval $[\alpha a_p; (\alpha + d\alpha)a_p]$ writes $n_p q(\alpha) d\alpha f_{bu} F(a_p) da_p$. Only the child particles lying in the range $[r_p; r_p + dr_p]$ are selected in the following. This is achieved by the characteristic function of a small interval dr_p:

$$dr_p \delta(r_p - \alpha a_p) = \begin{cases} 0 & \text{if} \quad \alpha \notin [\alpha a_p; (\alpha + d\alpha) a_p] \\ 1 & \text{if} \quad \alpha \in [\alpha a_p; (\alpha + d\alpha) a_p] \end{cases} \tag{5.99}$$

where $\delta(\cdot)$ denotes the Dirac delta function. The total number of child particles in the interval $[r_p, r_p + dr_p]$ is then obtained as:

$$\begin{aligned} dr_p f_{bu} \int_\alpha \int_{a_p} n_p q(\alpha) \delta(r_p - \alpha a_p) F(a_p) da_p d\alpha &= \\ dr_p f_{bu} n_p \int_\alpha \int_{a_p} q(\alpha) \delta\left(a_p - \frac{r_p}{\alpha}\right) F(a_p) da_p \frac{d\alpha}{\alpha} &= \\ f_{bu} n_p \int_\alpha F\left(\frac{r_p}{\alpha}\right) q(\alpha) \frac{d\alpha}{\alpha} da_p & \end{aligned} \tag{5.100}$$

The variation of the particle number in the interval $[r_p, r_p + dr_p]$ arises from the disintegration of parent particles and the appearance of newborn particles through breakup, yielding the balance:

$$\frac{\partial F(r_p)}{\partial t} = f_{bu} n_p \int_\alpha F\left(\frac{r_p}{\alpha}\right) q(\alpha) \frac{d\alpha}{\alpha} da_p - f_{bu} F(r_p) \tag{5.101}$$

This equation may be normalized by the particle number density per unit volume $n = \int_{r_p} F(r_p) dr_p$ according to the relation:

$$\int_\alpha \int_{r_p} F(r_p) \left(\frac{r_p}{\alpha}\right) q(\alpha) \frac{d\alpha}{\alpha} dr_p = \int_{r_p} F(r_p) dr_p' \int_\alpha q(\alpha) d\alpha = n \tag{5.102}$$

where $r'_p = r_p/\alpha$. Then, the evolution of the particle number density per unit volume follows as:

$$\frac{\partial n}{\partial t} = (n_p - 1) f_{bu} n \tag{5.103}$$

Combining eqs. 5.101 and 5.103, the evolution equation for the normalized particle radius distribution through breakup is obtained as:

$$\frac{\partial f(r_p)}{\partial t} = \int_\alpha f\left(\frac{r_p}{\alpha}\right) q(\alpha) \frac{d\alpha}{\alpha} - f_{bu} n_p f \tag{5.104}$$

with:

$$\int_\alpha f\left(\frac{r_p}{\alpha}\right) q(\alpha) \frac{d\alpha}{\alpha} := I_+ F \tag{5.105}$$

the so-called breakup operator. Noting that this operator is invariant under the scaling symmetry $\alpha \rightarrow \alpha r$, Gorokhovski and Saveliev [75] show that the asymptotic solution of eq. 5.104 in the long-time limit writes:

$$\begin{aligned} f(r_p, t) = \frac{1}{a_{p,0}} \frac{1}{\sqrt{2\pi \langle \ln^2 \rangle \nu t}} \exp\left(-\frac{\langle \ln(\alpha)\rangle^2}{2\langle \ln^2 \alpha\rangle} \nu t\right) \times \\ \exp\left(-\frac{\ln^2(r_p/a_{p,0})}{2\langle \ln^2 \alpha\rangle \nu t}\right) \left(\frac{a_{p,0}}{r_p}\right)^{1-\langle \ln^2 \alpha\rangle} \qquad t \rightarrow \infty \end{aligned} \tag{5.106}$$

where $a_{p,0}$ is the initial diameter of the parent particle and $\nu = f_{bu} n_p$. This relation shows that moments $\langle \ln^k \alpha \rangle$ of the disintegration spectrum $q(\alpha)$ higher than two have no influence on the normalized distribution of particle radius in the long-time limit. Thus, the factor $1/\alpha f(r/\alpha)$ of the breakup operator (eq. 5.105) is expanded into a logarithmic series [73]:

$$\frac{1}{\alpha} f\left(\frac{r_p}{\alpha}\right) = \sum_{n=0}^{\infty} (-1)^n \frac{1}{n!} \left(\frac{\partial}{\partial r_p} r_p\right)^n f(r_p) \ln^n \alpha \tag{5.107}$$

This expansion may now be inserted into eq. 5.103 neglecting all moments higher than two. Eq. 5.103 then takes the form of a Fokker-Planck differential equation:

$$\frac{\partial f(r_p)}{\partial t} = \left[-\frac{\partial}{\partial r_p} r_p \langle \ln \alpha \rangle + \frac{1}{2} \frac{\partial}{\partial r_p} r_p \frac{\partial}{\partial r_p} r_p \langle \ln^2 \alpha \rangle\right] \nu f(r_p) \tag{5.108}$$

Introducing the initial particle radius distribution $f_0(r_{p,0})$, the final solution to eq. 5.108 writes:

$$f(r_p, t) = \frac{1}{r_p} \int_0^\infty \frac{1}{\sqrt{2\pi \langle \ln^2 \alpha \rangle \nu t}} \exp\left[\frac{-(\ln(r_{p,0}/r_p) + \langle \ln \alpha \rangle \nu t)^2}{2\langle \ln^2 \alpha \rangle}\right] f_0(r_{p,0}) dr_{p,0} \tag{5.109}$$

Therefore, the evolution of the initial particle radius distribution $f_0(r_{p,0})$ through breakup is governed by a lognormal law. Knowing the initial radius distribution, eq. 5.109 allows to sample child particle radiuses for the breakup of a parent particle.

5.4.2.b) Computational aspects of the FAST secondary breakup model

The present section provides details on the numerical implementation of the FAST secondary breakup model. From a global perspective, a secondary breakup model consists in the following steps:

- At each time step of the simulation, it is checked whether a particle remains stable or undergoes secondary breakup.
- If a particle undergoes secondary breakup, the size of the child particles resulting from the disintegration of the parent particle must be determined.
- In addition to the radius, all other physical properties of the child particles must be defined.

These steps are now successively described in more detail for the FAST model. Two physical criteria are used to distinguish between breaking and stable particles. Particles are considered unstable if their Weber number exceeds a critical value:

$$We = \frac{\rho d_p (u_i - u_{p,i})^2}{\sigma_l} > We_{cr} \tag{5.110}$$

This relation may be reexpressed to define a critical particle radius $r_{p,cr}$ above which particles are considered unstable:

$$r_{p,cr} = \frac{We_{cr}\sigma_l}{2\rho(u_i - u_{p,i})^2} \tag{5.111}$$

The critical Weber number We_{cr} based on particle radius is defined following Pilch and Erdman [156]:

$$We_{cr} = 6(1 + 1.077 Oh^{1.6}) \tag{5.112}$$

For highly turbulent flows, Gorokhovski [73] proposes to modifiy the evaluation of the relative particle to gas velocity to account for the fact that the entire turbulence spectrum may contribute to the disintegration of the particle. Following Gorokhosvki [73], the root-mean square relative velocity between gas and particles is written as:

$$\langle (u_i - u_{p,i})^2 \rangle = \epsilon \tau_p \tag{5.113}$$

where ϵ and τ_p respectively denote the turbulent dissipation rate and the particle relaxation time scale. In Large-Eddy Simulations, the turbulent dissipation rate may be evaluated from:

$$\epsilon = 2\overline{s}_{ij}\overline{s}_{ij}\nu_t \tag{5.114}$$

Combining eq. 5.111 and eq. 5.113 yields a critical particle radius above which breakup occurs:

$$r_{p,cr} = \left(\frac{9}{2} \frac{We_{cr}\sigma_l \nu}{\epsilon \rho_l} \right)^{1/3} \tag{5.115}$$

This relation is only valid in sufficiently turbulent flows. Therefore, eq. 5.115 must be used in combination with a criterion distinguishing whether to use eq. 5.115 or 5.111 as the particle stability criterion. In the present work, this distinction is based on the Reynolds number evaluated at the particle location: if the latter lies above 5000, eq. 5.115 is used. Otherwise, the critical radius is defined through eqs. 5.111.

In addition to the particle stability criterion, a characteristic breakup time scale must be determined. This is because a particle does not undergo breakup immediately once it becomes unstable: it is either deformed by aerodynamic forces or oscillates through individual particle instability mechanisms. Gorokhovski [73] associates the characteristic particle breakup time scale with the fastest growth rate of Rayleigh-Taylor waves in the high-speed limit:

$$t_{bu}^{RT} = B \frac{r_p}{|u_i - u_{p,i}|} \sqrt{\frac{\rho_l}{\rho}} \tag{5.116}$$

with $B = \sqrt{3}$ according to the TAB model [148]. Thus, it is checked at each computational time step if the particle lifetime exceeds the breakup time scale t_{bu}^{RT} given by eq. 5.116 and if its Weber number lies above the critical value We_{cr} provided by eq. 5.112. If both criteria are fulfilled for the considered particle, it undergoes secondary breakup. Note that the particle lifetime is initialized to zero for newly injected particles and newborn child particles. It is incremented by the timestep of the gaseous solver at each iteration.

For each breaking particle, the size of its child particles must be determined. In section 5.4.2.a), it has been shown that the evolution of the particle radius distribution under breakup is governed by:

$$f(r_p,t) = \frac{1}{r_p}\int_0^{\infty} \frac{1}{\sqrt{2\pi\langle \ln^2\alpha\rangle \nu t}} \exp\left[\frac{-(\ln(r_{p,0}/r_p) + \langle \ln\alpha\rangle \nu t)^2}{2\langle \ln^2\alpha\rangle}\right] f_0(r_{p,0})dr_{p,0} \tag{5.117}$$

with $f_0(r_{p,0})$ initial particle radius distribution. This distribution is written as a dirac delta function for each breaking parent particle:

$$f_0(r_{p,0}) = \delta(\ln(a_p - r_{p,0})) \tag{5.118}$$

where a_p denotes the radius of the parent particle. From a computational point of view, it is more straightforward to determine samples of the child particle radiuses from the cumulative distribution function:

$$T(r_p,t) = \int_{-\infty}^{r_p} f(r_p,t)dr_p \tag{5.119}$$

Inserting eqs. 5.118 and 5.117 into eq. 5.119 yields:

$$T(r_p,t) = \left[\frac{1}{2} + \frac{1}{2}\text{erf}\left(\frac{\ln(r_p) - \ln(a_p) + \langle\ln(\alpha)\rangle}{\sqrt{2\langle\ln^2(\alpha)\rangle}}\right)\right] \tag{5.120}$$

where erf denotes the error function. This relation yields the cumulative particle distribution after the breakup of a parent particle of radius a_p. Since the breakup of each particle is considered separately according to eq. 5.118, this procedure is called “deterministic” although the generation of the particle sizes after breakup is random. A “stochastic” version of the breakup algorithm may be formulated by applying eq. 5.120 to the normalized particle size distribution inside a given control volume, typically the computational cell [73]:

$$f_0(r_{p,0}) = \sum_{n=1}^{N} \delta(\ln(a_p - (r_{p,0})_n)) \tag{5.121}$$

where N denotes the number of particles inside the control volume. This approach is adopted by Gorokhovski and co-workers [73, 75, 4], but a brief comparison between stochastic and deterministic algorithms performed in the present work showed that both approaches yielded similar results in practice with a clear advantage in terms of compuational expense for the deterministic approach. For this reason, the deterministic formulation of the secondary breakup model has been used in the present work.

In order to fully describe the cumulative distribution function $T(r_p,t)$, the first two moments $\langle\ln\alpha\rangle$ and $\langle\ln^2\alpha\rangle$ of the disintegration spectrum $q(\alpha)$ (see section 5.4.2.a)) need to be defined. Apte et. al [4] propose:

$$\langle\ln\alpha\rangle = k_1 \ln\left(\frac{We_{cr}}{We}\right) \tag{5.122}$$

$$-\frac{\langle\ln\alpha\rangle}{\langle\ln^2\alpha\rangle} = k_2 \ln\left(\frac{r_{p,0}}{r_{p,cr}}\right) \tag{5.123}$$

with We_{cr} defined by eq. 5.112. The critical particle radius is either evaluated according to eq. 5.111 in laminar regions or eq. 5.115 in turbulent regions. k_1 and k_2 denote free constants of the model. The constant k_1 controls the mean of the distribution used to generate the particle sizes after breakup while k_2 controls the deviation from this mean.

The cumulative distribution function of particle radius after breakup is now entirely defined for each breaking particle. Generating random numbers $x_r \in [0;1]$ and finding the abscissa for which:

$$T(r_p, t) = x_r \tag{5.124}$$

yields a statistical particle radius r_p after breakup.

At this point, child particle radiuses are randomly generated as long as their mass remains below the mass of the parent particle:

$$\sum_i r_{p,i}^3 < a_p^3 \tag{5.125}$$

When the sum of the child particle masses exceeds the parent particle mass, the last generated particle radius is rejected. Instead, a final child particle radius is deduced from the mass difference between parent and the sum of the child particles to ensure mass conservation during breakup. Apart from the radius, the child particles inherit all physical properties of the parent particle such as temperature, position, etc... In order to reproduce the physical picture of particles being torn apart by aerodynamic forces, the velocity of the child particles is composed of two contributions: the velocity the parent particle and a velocity factor $u_{p,bu}$, whose norm is defined as:

$$|u_{p,i}^{bu}| = \frac{a_p}{t_{bu}^{RT}} \tag{5.126}$$

with t_{bu} defined by eq. 5.116. The direction of this additional velocity is randomly chosen in a plane normal to the relative velocity between particle and gas $(u_i - u_{p,i})$ (see fig. 5.15). To finalize the breakup process, the parent particle is removed from the simulation at the end of the timestep.

5.4.3 Conclusions

This chapter dealt with the modeling of liquid injection. In a first part, theoretical and numerical aspects of the disintegration of liquid streams were presented. First, primary atomization mechanisms of liquid jets and flat liquid sheets were described. Nondimensional numbers and stability theory appeared as important tools to characterize primary atomization regimes of liquid streams. Then, secondary breakup regimes were briefly discussed. Finally, numerical tools for the simulation of primary atomization were presented. Direct Numerical Simulations of primary atomization explicitly tracking the interface location as well as Reynolds Averaged methods describing primary atomization through a single-phase density were briefly discussed.

Since the implementation of interface capturing techniques in the AVBP solver was considered out of reach for the present work, very simplified injection methods were used instead. The FIMUR (Fuel Injection Method by Upstream Reconstruction) injection methodology focused on pressure swirl atomizers and attempted to reproduce similar injection conditions for both Euler-Lagrange and Euler-Euler methods. It neglected the atomization process and directly injected the developed spray at the atomizer orifice. Liquid injection velocity profiles were then derived from considerations on the flow field inside the atomizer while informations on the particle size distribution were reconstructed from experimental data. As the injection surface needed to be sufficiently discretized in Euler-Euler simulations, the injection boundary condition was artificially translated further downstream in the latter to reduce compuational expense. Using the injection velocity profiles derived at the atomizer orifice, evolution equations were then analytically solved to characterize spray dynamics between the atomizer orifice and the translated injection plane. This step imposed additional constraints on the injection velocity profiles at the atomizer orifice, which needed to be further simplified. Tests performed for spray injection in a quiescent atmosphere revealed that the modifications on the velocity profiles at the atomizer orifice had only little impact on spray velocity profiles further downstream due to a balistic sorting effect. In addition, these tests allowed to validate the correct implementation of the injection velocity profiles in the Euler-Lagrange solver. Direct comparisons of Euler-Lagrange and Euler-Euler injections on a simplified test case as presented in this chapter could not be performed due to numerical difficulties encountered in the Euler-Euler simulations. Therefore, the only comparison between Euler-Lagrange and Euler-Euler injections for this methodology will be performed for the simulation of an aeronautical combustor (see chapter 7).

In order to add more physical detail to the FIMUR injection model, it was chosen to partly account for the liquid disintegration process in the Lagrangian solver through the implementation of a secondary breakup model. The choice was made for the Fast Atomizing STochastic (FAST) secondary breakup model, whose particle size distribution after breakup is governed by a lognormal law. This property motivated the choice for this model as it seemed a good approximation to particle size distributions encountered in practical applications. Theoretical aspects of the model were presented in a first step before adressing details of numerical implementation. In particular, relations characterizing the breakup criterion, the breakup time scale, the mean and standard deviation of the particle distribution function after breakup were detailed. Validation cases for this breakup model will be presented in the next chapter.

Chapter 6

Validation of the secondary breakup model

This chapter presents two different validation cases for the FAST secondary breakup model implemented in the AVBP solver. The first test case consists in the injection of liquid through a single hole nozzle in a closed cylindrical chamber at various gas pressures. It was used by Apte et al. [4] to validate their implementation of the FAST secondary breakup model in the LES solver CDP. Therefore, this test case offers the possibility to compare present results with both experimental data and results of Apte et. al [4].

The second test case simulates the injection of a liquid jet perpendicularly to a turbulent gaseous crossflow. This configuration is of practical interest for aeronautical engines using multipoint injection systems. Experimental data is available for this test case from the studies of Becker et al. [15]. This geometry was previously simulated by Jaegle [93], who derived an injection model to account for the presence of the liquid column but neglected secondary breakup. The present work proposes to combine Jaegle's liquid column model [93] and the implemented secondary breakup model. Therefore, the impact of secondary breakup modeling may be directly assessed by comparison of the present results with those of Jaegle [93].

6.1 Diesel injection experiment

The present section discusses the simulation of spray atomization in a closed cylindrical chamber at conditions representative of Diesel engine applications. The first part focuses on the validation of the model by comparison with experimental data and results of Apte et al. [4]. The second part briefly discusses the impact of grid resolution on results.

6.1.1 Experimental conditions

The experiment of Hiroyasu and Kadota [86] is a standard validation case for secondary breakup models [174, 148] and was also used by Apte et al. [4] to validate their implementation of the FAST secondary breakup model. It consists in the injection of Diesel fuel through a single hole nozzle in a closed cylindrical chamber at various gas pressures. The closed cylindrical chamber has a length of 13.6 cm and a diameter of 5.6 cm while the nozzle diameter equals 300 μm. A sketch of the geometry is provided in fig. 6.1. The experiment is simulated for three different gas pressures, the operating conditions are detailed in table 6.1. The large Weber numbers at injection indicate that the disintegration of the liquid takes place in the atomizaton regime (see section 5.1.1.a)). Characteristic properties of the Diesel fuel are summarized in table 6.2.

Parameters	Case I	Case II	Case III
Gas pressure p [MPa]	1.1	3.0	5.0
Gas temperature T [K]	300	300	300
Injection time [ms]	2.5	4.0	5.0
Injection velocity [m/s]	102	90.3	86.4
Deduced mass flow rate [g/s]	6.05	5.36	5.13
Injection Weber number We [-]	1450	4000	6600

Table 6.1 : *Test conditions for the experiments of Hiroyasu and Kadota [86]*

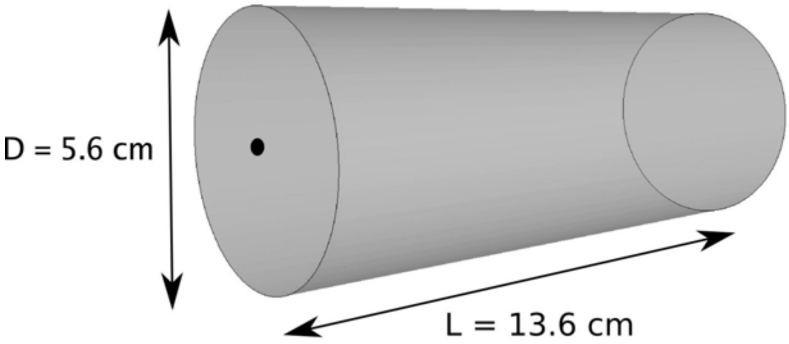

Figure 6.1 : *View of the geometry. The circle denotes the location of the injection point.*

Liquid parameters	Values
Surface tension σ_l [N/m]	0.0261
Density ρ_l [kg/m^3]	840
Kinematic viscosity ν_l [Pa·s]	$2.1 \cdot 10^{-3}$

Table 6.2 : *Physical properties of the Diesel fuel*

6.1.2 Numerical parameters

Fig. 6.2 displays a front view of the computational mesh. It is composed of (100 x 65 x 65) hexaedric cells and reproduces the mesh used by Apte et al. [4] in their simulations in terms of cell number and grid refinement at the axis.

As in the experiments, the cylinder is completely closed and a noslip condition is applied at the walls. Due to the high density of the spray and the high liquid injection velocities, the coupling between both phases is strong and induces a substantial acceleration of the gas in the spray region. As a consequence, important gradients are generated in the simulations between the gas at rest and the gas accelerated within the spray boundaries. In order to handle these gradients, the TTG4A scheme is used for convection because of its improved dispersive

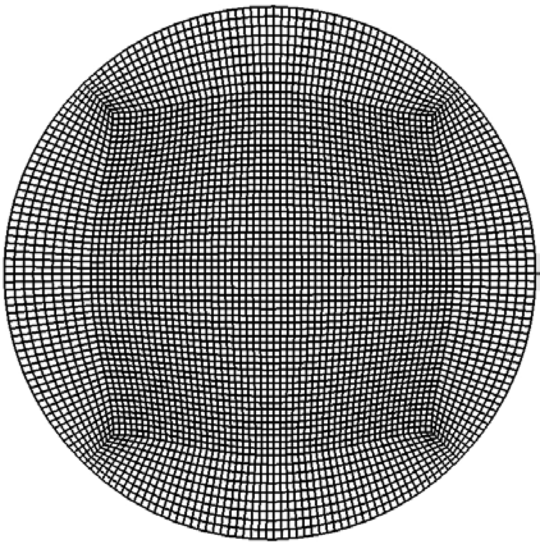

Figure 6.2 : *Front view of the computational mesh*

properties compared to the TTGC scheme [107]. Due to the good dispersive properties and the higher numerical dissipation of the TTG4A scheme, no artificial viscosity needs to be applied for stabilization. The simulation time is 2.5 ms for the three cases, which has been judged sufficient for comparisons with experiments by Apte et al. [4]. No parcel approach is used in the present work and coalescence effects are not taken into account. The size of the particles injected in the simulation corresponds to the diameter of the nozzle orifice, $d_p = 300\,\mu$m.

The breakup model presented in section 5.4.2 is used with the same constants in the three cases: $k_1 = 0.1$ and $k_2 = 0.8$. These values are in good agreement with those used by Baricault [10] ($k_1 = 0.1$ and $k_2 = 1$) for simulations of spray atomization in a closed cylindrical chamber at gas pressures of respectively 1.0 and 2.0 MPa. The values $k_1 = 0.6$ and $k_2 = 1$ recently recommended by Apte et al. [5] were also tested but did not yield satisfactory results. Table 6.3 provides a summary of the numerical parameters used in the present simulations. These parameters remain identical for the three simulated cases.

Numerical Parameters			
Gas	Values	Liquid (all cases)	Values
Convection	TTG4A	Breakup constant k_1	0.1
Diffusion	2Δ operator	Breakup constant k_2	0.8
Subgrid-scale model	Wale	Parcel approach	No
Second order AV	$\epsilon^2 = 0.0$	Two-way coupling	Yes
Fourth order AV	$\epsilon^4 = 0.0$	Evaporation	No
		Interpolation	Taylor

Table 6.3 : *Numerical parameters for the simulation of spray atomization in a closed cylinder*

6.1.3 Results

Figs. 6.3-6.5 display the spray pattern in a 2 mm slab of the mid-plane for cases I-III at three different moments of the simulation, respectively $t = 0.5$ ms, $t = 1.25$ ms and $t = 2.0$ ms. The disintegration of the injected

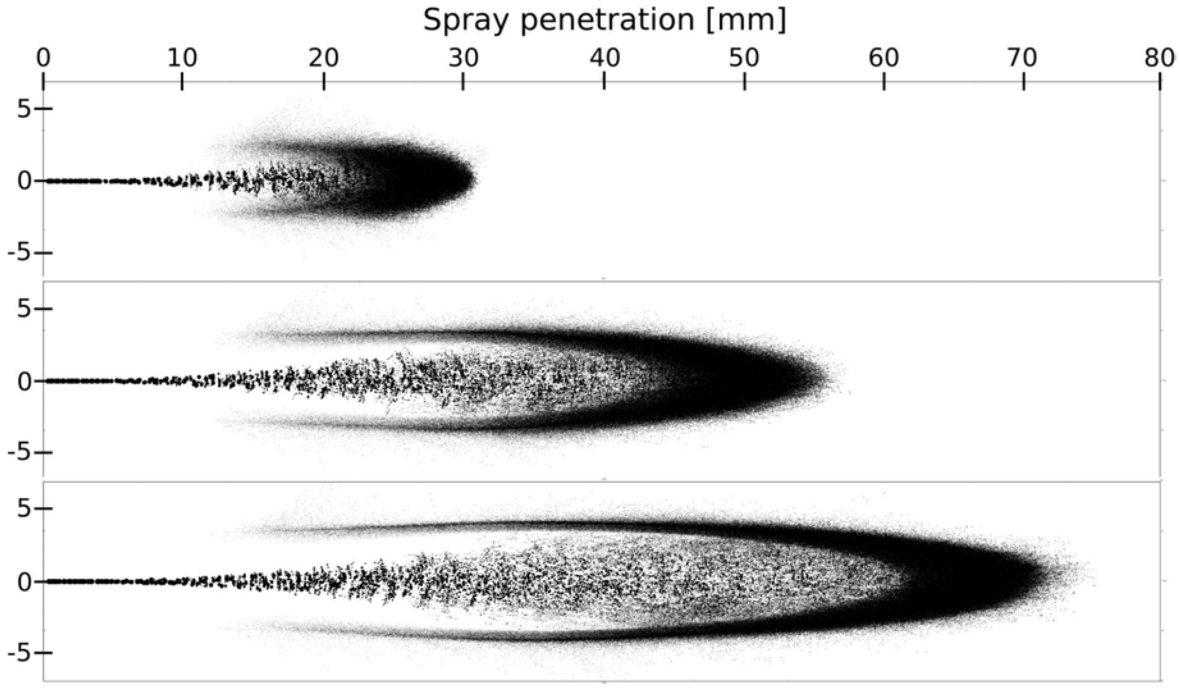

Figure 6.3 : *Spray pattern in a 2 mm slab from the mid-plane for case I (1.1 MPa chamber pressure) at three different moments of the simulation: t= 0.5 ms, 1.25 ms, 2.0 ms. Size of the symbols scales with particle diameter.*

"blobs" into smaller particles along the axis is clearly visible. The spray penetration length decreases at higher chamber pressures, which is due to enhanced damping of liquid momentum by the gas. The visual spray angle increases with gas pressure as a consequence of the higher aerodynamic forces exerted upon the particles. Long side branches appear in the wake of the spray, which is an unphysical behavior. The amount of particles contained in these side branches seems to increase with gas pressure. A close observation of the time evolution of the spray indicates that these wake particles originate from the atomization of the spray into very fine particles at the spray tip. In this zone, the gas has not yet been accelerated by the spray, leading to high relative velocities between particles and gas. This leads to the disintegration of the spray into a very fine mist since the size of the generated child particles decreases with increasing Weber number in the secondary breakup model (see eq. 5.122). The issued child particles travel radially outwards as they inherit a velocity component normal to the relative velocity between gas and particles. They are then gradually decelerated through momentum exchange with the gaseous phase. The child particles which come to rest at the radial extremities of the spray remain there since both the gas and the particles keep vanishing velocities in this zone as time proceeds. It is believed that the explicit account for coalescence phenomena at the tip of the spray would limit the occurence of this effect.

Fig. 6.6 displays the penetration lengths of the tip of the spray compared to experiments. The spray tip is defined as the axial distance including more than 99% of the liquid mass [153]. The spray penetration curves flatten as time proceeds because the spray momentum in axial direction is progressively reduced through the increasing radial expansion of the spray. Present results are in reasonable agreement with experiments for case I and case II although the slope of the penetration curves is underestimated at the latest times. Resonable agreement is also observed between present results and those of Apte et al. [6] for cases I and II. On the contrary, the penetration length is underestimated from an early moment of the present simulation compared to experiments. Results of Apte et al. [6] compare better with experiments for this case although penetration lengths are still underestimated. Since the spray penetration length is assumed to mainly depend on the local particle diameter and the radial spread of the spray, quantitative comparisons of these quantities are necessary

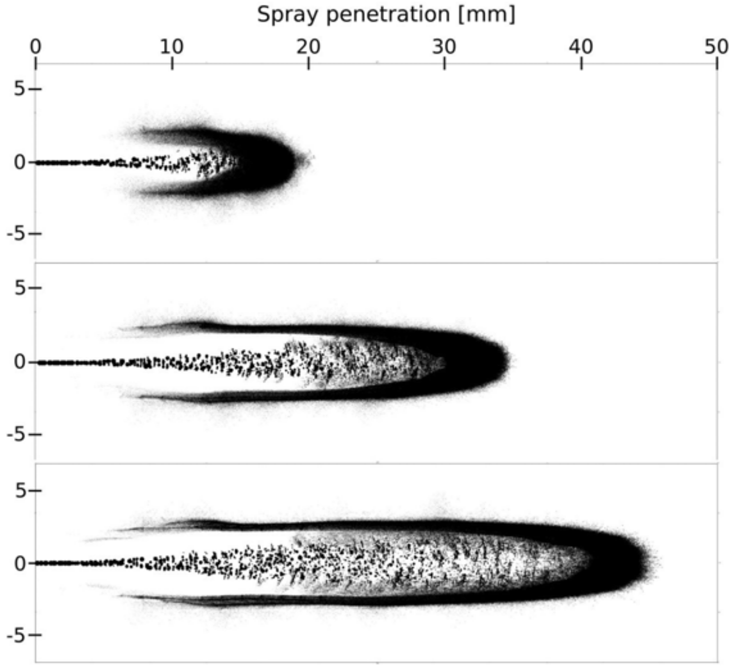

Figure 6.4 : *Spray pattern in a 2 mm slab from the mid-plane for case II (3.0 MPa chamber pressure) at three different moments of the simulation: t= 0.5 ms, 1.25 ms, 2.0 ms. Size of the sybols scales with particle diameter.*

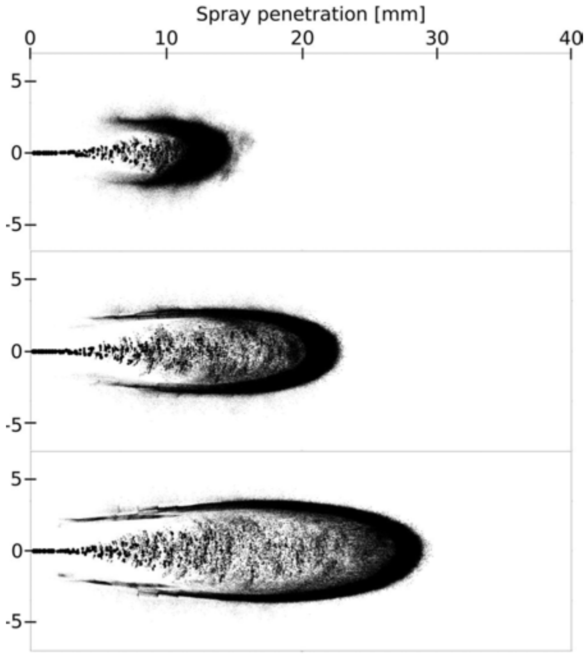

Figure 6.5 : *Spray pattern in a 2 mm slab from the mid-plane for case III (5.0 MPa chamber pressure) at three different moments of the simulation: t= 0.5 ms, 1.25 ms, 2.0 ms. Size of the symbols scales with particle diameter.*

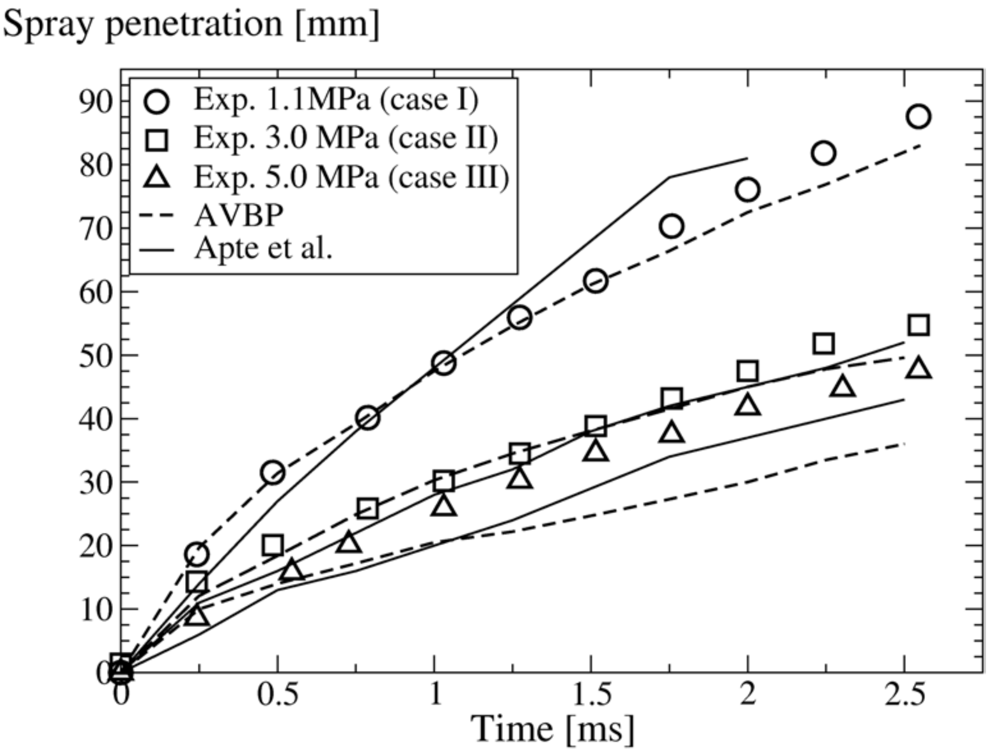

Figure 6.6 : *Spray penetration lengths for the three cases. Symbols: Experiments. Continuous lines: AVBP simulations. Dashed lines: simulations of Apte et al. [6]*

to asses the origin of the differences between present results and those of Apte et al. [6] for case III.

The spray angle is an important characteristic linked to atomization since it directly depends on the generated particle sizes and their momentum in radial direction. Two different measures of the spray angle are reported in the literature.

In the experiments of Hiroyasu and Kadota [86], the spray angle was measured visually with a high-speed camera of the backlighted spray. Results according to a visual measurement method from the injector to the tip of the spray (see fig. 6.7) are shown in fig. 6.8. To compensate the lack of precision inherent to this method, measurements of the spray angle were performed each 0.25 ms of the simulation and averaged over time. The observed agreement with experiments is good.

Apte et al. [6] performed their simulations with a parcel approach which is not adapted to this measurement method because the spray envelopes are not clearly distinguishable. Therefore, they used the spray angle measurement method of Tanner [217], who defines the spray angle as the tangent to the radial spread of the spray drawn from the nozzle to the spray tip which includes at least 99% of the spray mass (see fig. 6.9). The results obtained with this method are displayed in fig. 6.10. In the present work, the increase of the spray angle with chamber pressure is overpredicted. However, the maximal error is of order 14% for case I, which remains acceptable. The results of Apte et al. [6] show better qualitative agreement with experiments as they correctly predict the increase in spray angle with chamber pressure. Furthermore, their values are closer to experimental data compared to the present work. It appears that spray angle obtained for case III in the present work lies above the value reported by Apte et al. [6]. This implies that the spray loses more momentum through radial expansion in the present work for case III compared to the simulations of Apte et al. [6]. This effect might explain the differences in spray penetration lengths observed for this case in fig. 6.6.

Fig. 6.11 displays the evolution of the Sauter mean diameter (SMD or d_{32}, see eq. 3.97) along the spray axis

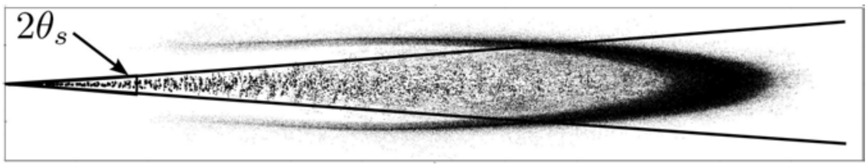

Figure 6.7 : *Spray angle measurement based on visual method [86]*

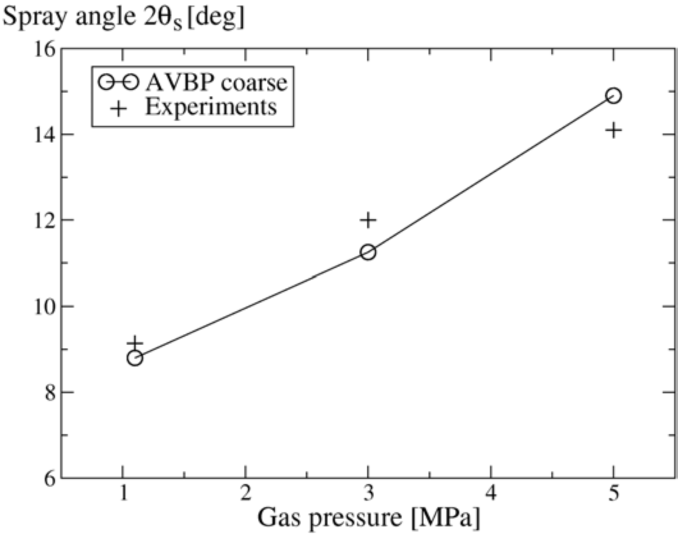

Figure 6.8 : *Measures of spray angle based on visual method and comparison with experiments*

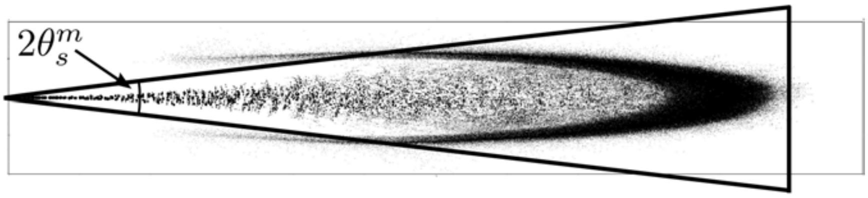

Figure 6.9 : *Spray angle measurement based on inclusion of 99% mass of liquid within the tangents [217]*

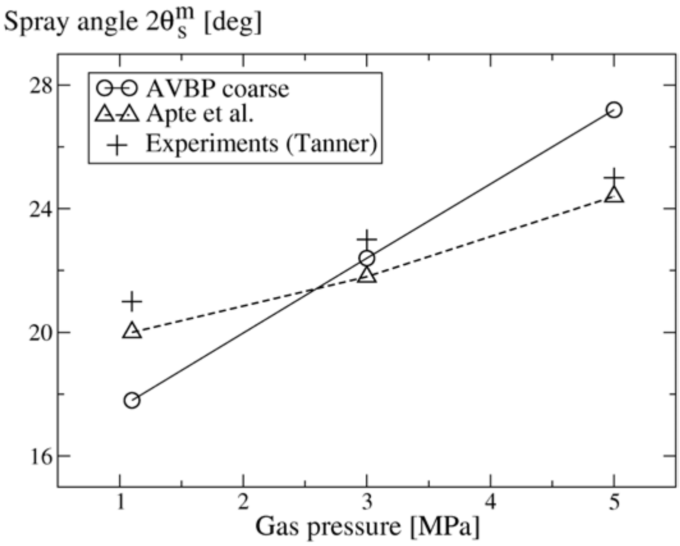

Figure 6.10 : *Measures of spray angle based on inclusion of 99% mass of liquid within the tangents*

x. The axial origin represents the location of the nozzle. The SMD is obtained from an average of the particle diameters in axial slices of 2 mm thickness. Only one experimental point is available for comparison at the axial location $x = 65$ mm. All curves show a strong decrease in the SMD close to injection before reaching more or less constant levels. For case I, the decrease of the SMD is more pronounced in the simulation of Apte et al. [6] and reaches a constant level at $x = 20$ mm whereas in the present work, this level is reached at $x = 35$ mm. The SMD level obtained for case I in the present work is closer to the experimental value at $x = 65$ mm compared to Apte et al. [6] who find less than 20μm. This result is surprising since the present work predicts larger particle diameters at all axial locations and a smaller spray angle for case I, from which one could expect higher penetration lengths. However, penetration lengths of the present work lie below those of Apte et al. [6] for $t > 1$ ms in fig. 6.6. This behavior may arise from the different numerical schemes used for convection or slight differences in the grid resolution between both studies [1] (see section 6.1.4). Apte et al. [6] do not provide the curves of their Sauter mean diameter profiles for cases II and III so that no comparison can be made for them. In the present work, the SMD levels downstream injection are greatly mispredicted for cases II and III. The experimental value of the SMD is even seen to increase at $x = 65$ mm with pressure, which is not at all captured in the present work. Particle coalescence effects, which are presently not taken into account, are expected to be responsible for this behavior [174, 148]. At the tip of the spray, an increase of the SMD is observed for all present simulations. This effect is probably due to the acceleration of the gaseous phase by the spray which reduces the relative velocity between the gas and the following particles. This allows larger unbroken particles to penetrate further into the chamber, until they reach more quiescent regions of the gas at the tip of the spray, where they atomize because of the larger relative velocity between gas and particles in this region.

Fig. 6.12 displays the particle mass distribution at the axial location $x = 65$ mm for case I. For discrete particle diameter classes, the particle mass distribution writes:

$$f_{3,i} = \frac{n_i(\pi d_p^3)/6}{\sum_{i=1}^{k} n_i(\pi d_p^3)/6} \tag{6.1}$$

where n_i represents the number of particles in the class i and k denotes the total number of classes. Results obtained by Apte et al. [4] are also represented for comparison. The first observation is that both distributions

---

[1] the exact resolution used by Apte et al. is not known

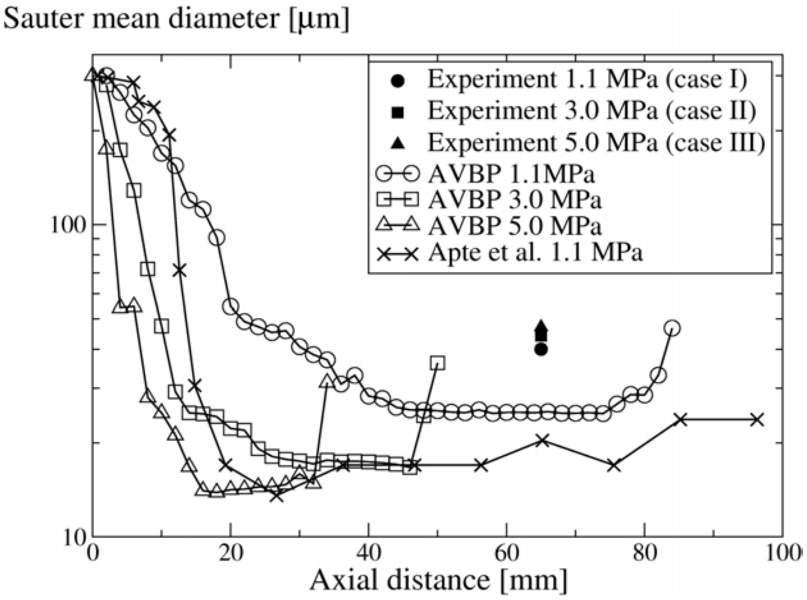

Figure 6.11 : *Evolution of the Sauter mean diameter (log scale) along the spray axis for the three cases on the coarse mesh. Results from Apte et. al [4] for case I are also displayed.*

follow a lognormal law, which is a key feature of the present secondary breakup model and validates the implementation of the algorithm used to randomly sample child particle sizes. However, the distribution obtained in the present work appears more narrow than the mass distribution reported by Apte et al [6]. Note that these results are not in contradiction with the SMD measurements provided in fig. 6.11 as the abscissa of the SMD is located below the peak value of the particle mass distribution [117].

Finally, it is important to check mass conservation during simulations modeling spray atomization. To this purpose, a series of post-processing tools have been implemented in AVBP. Their description is given in appendix B. Figs. 6.13-6.15 respectively show particle mass balances, source terms of particle mass and particle mass evolution over time for case I. Similar results were obtained for cases II and III but are not shown. The particle mass balance is closed to a very good relative accuracy. The source terms of particle mass are displayed in fig. 6.14. Only a short portion of the injection curve is shown to evidence the discrete mass injection. It appears from fig. 6.14 that a few particles are lost during the simulation, which still seems acceptable since approximately 600 particles are lost for a total number of more than 3.5 million particles at the end of the simulation. The relative error in total particle mass at the end of the simulation is approximately $2 \cdot 10^{-5}$. Lost particles are those located on the face of a hexaedric element whose four points are not coplanar. The losses originate from deficiencies of the particle search algorithm and possible improvements are currently being investigated by García [63].

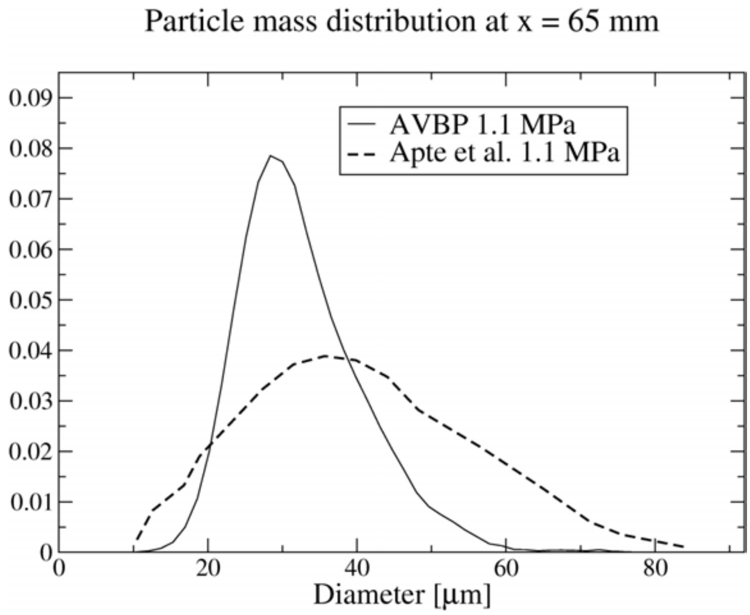

Figure 6.12 : *Particle mass distribution at the axial location* $x = 65$ *mm for case I. The distribution obtained by Apte et al. [4] is also displayed for comparison*

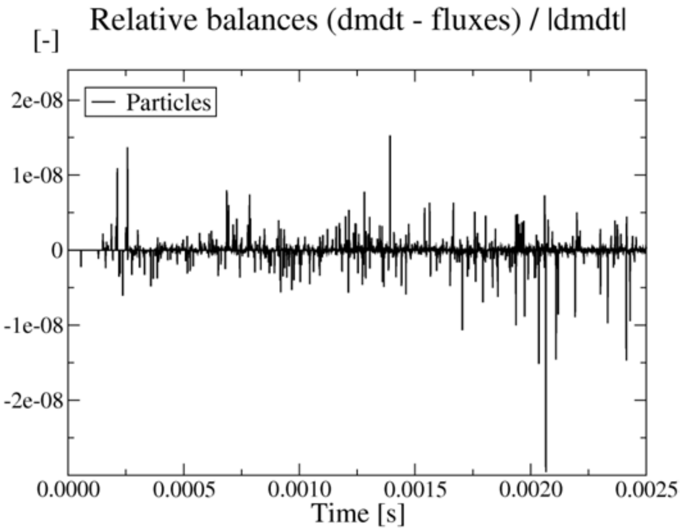

Figure 6.13 : *Particle mass balance for case I*

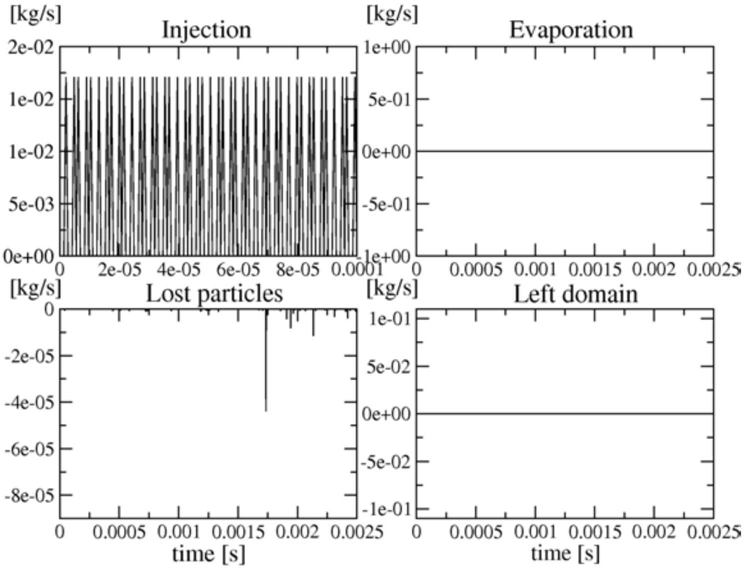

Figure 6.14 : *Source terms of particle mass for case I*

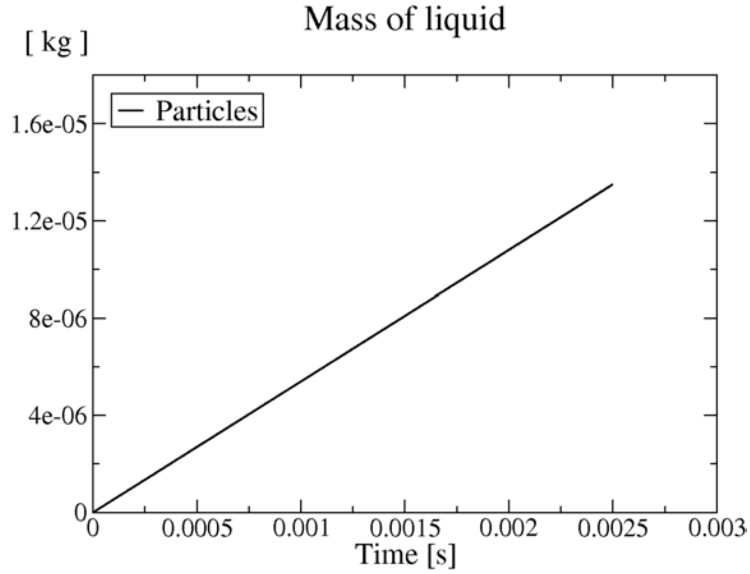

Figure 6.15 : *Particle mass evolution for case I*

6.1.4 Mesh dependency of results

This section proposes to assess effects of mesh dependency on simulation results. This investigation is motivated by several studies reporting grid dependent results of Lagrangian spray atomization simulations [76, 2, 73]. Therefore, a brief comparison of results obtained for two different mesh resolutions is performed before discussing possible reasons of this behavior. To this purpose, the simulations results presented in the previous section with a resolution of (100 x 65 x 65) hexaedral cells are compared to simulations performed on a mesh composed of (200 x 130 x 130) hexaedral elements. The meshes are respectively referred to as coarse (100 x 65 x 65) and fine (200 x 130 x 130) in the following.

The impact of grid resolution on spray penetration lengths is displayed in fig. 6.16. It appears that the spray penetration length is greatly overpredicted on the fine mesh for case I compared to experiments. Differences between both mesh resolutions decrease for higher pressures, which is probably due to the increased damping of spray momentum by the gas, making results less sensitive to variations in spray momentum.

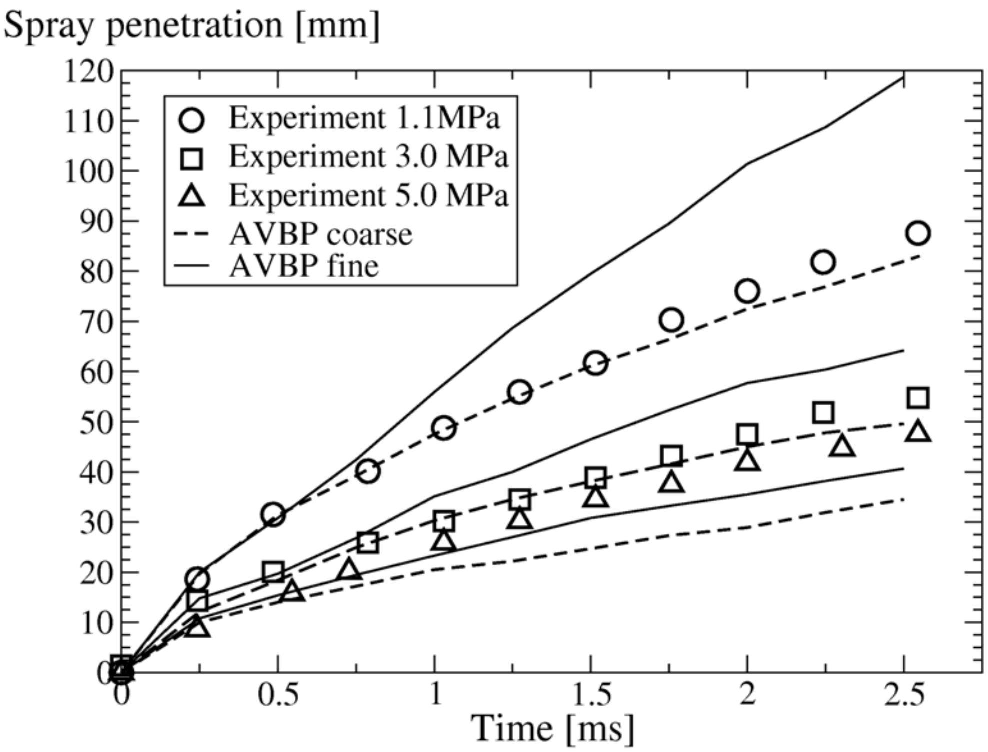

Figure 6.16 : *Comparison of spray penetration lengths for two different mesh resolutions: coarse (100 x 65 x 65) and fine (200 x 130 x 130). Symbols: Experiments. Lines: Simulations.*

The comparison of spray angles for both mesh resolutions based on the visual method [86] is displayed in fig. 6.17. It appears that spray angles are considerably reduced for the fine mesh and discrepancies compared to experiments are large. These reduced spray angles imply that less spray momentum is lost to the gas by radial expansion, which is consistent with the increased spray penetration lengths reported for the fine mesh.

In order to further understand the important differences in spray penetration lengths and spray angles, profiles of gaseous axial velocity along the axis are displayed in fig. 6.18 at the instants $t = 0.5$ and $t = 1.0$ for both meshes. It appears that the acceleration of the gaseous phase is enhanced on the fine mesh. This behavior may explain the increase in the spray penetration lengths: as the relative velocity between particles and gas is reduced on the fine mesh, particle breakup is delayed and unbroken particles with higher inertia may penetrate

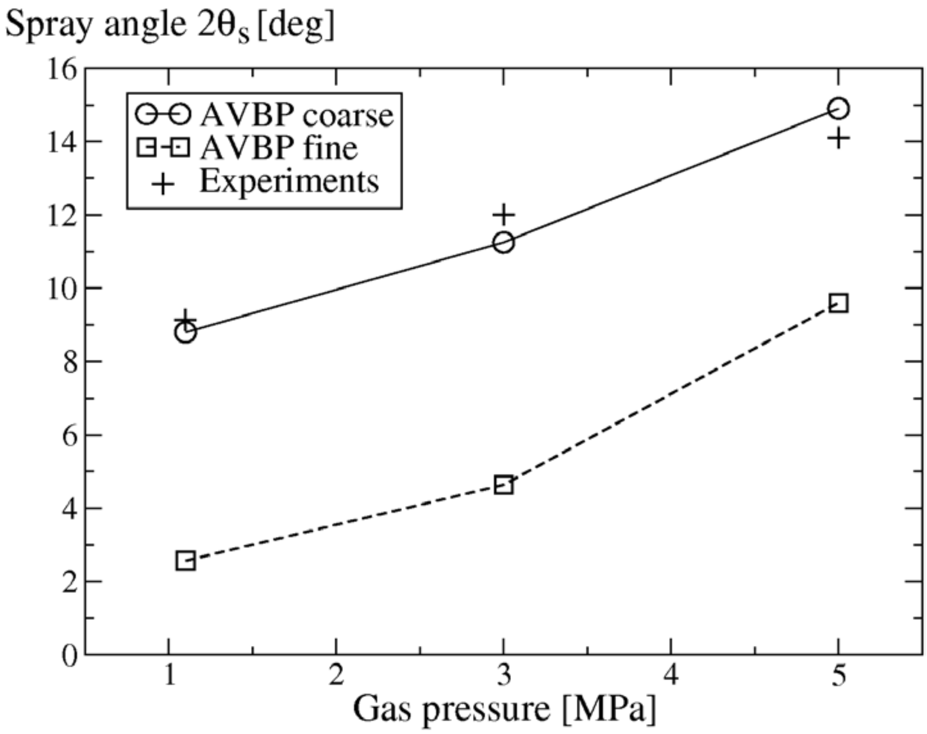

Figure 6.17 : *Measures of spray angle based on visual method [86] and comparison with experiments for coarse (100 x 65 x 65) and fine mesh resolutions (200 x 130 x 130)*

further along the axis. This hypothesis seems confirmed by the comparison of the particle mass distributions at $x = 65$ mm displayed in fig. 6.19, which shows a broadening of the particle mass distribution towards larger diameters for the fine mesh.

Since the acceleration of the gas is only dictated by the coupling terms of the spray, it is believed that these discrepancies originate from a different spatial distribution of these coupling terms. In order to illustrate this effect, fig. 6.20 displays the interpolation of a particle coupling term denoted s^{p-f} on two equistant one-dimensional meshes. Grid resolution is doubled for the mesh on the right compared to the mesh on the left. Consider the coupling terms arising from three particles located at the same position on both grids. It is assumed that all particles have the same source term, which takes the arbitrary value one. On the coarse mesh, the particles are respectively located at distances of 1/4 Δx, 1/2 Δx and 3/4 Δx from the grid node i. Linear interpolation of the particle source terms weighted with the nodal distance yields a weight of 1/4 + 1/2 + 3/4 = 1.5 on nodes i and i+1. On the fine mesh, the central particle location coincides with node j while the other particles are located in the middle of the adjacent cells. Thus, the source term interpolated to the central node writes 1/2 + 1 + 1/2 = 2 while a source term of 1/2 is applied at the adjacent nodes. This example illustrates that source term profiles may vary with grid resolution and that higher source term values may be locally observed on finer meshes. It also suggests that the numerical resolution of source terms may be improved with grid refinement: while the source term gradient is resolved on two nodes for the coarse grid on the left of fig. 6.20, it is resolved on three nodes for the fine mesh. This effect may have an impact on the numerical diffusion of these gradients, especially in the present simulations where large velocity gradients may be expected between the gas accelerated within the spray and the surrounding quiescent gas.

In addition, the interpolation of gaseous properties to the particle location is subject to numerical errors which decrease with grid refinement. This effect is sketched on fig. 6.21, which displays a particle located on two one-dimensional meshes of different resolutions. Consider the interpolation of the sketched gaseous

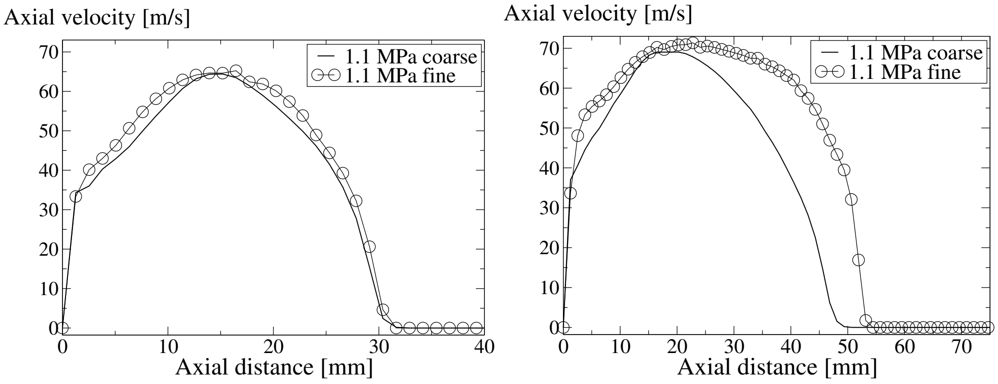

(a) Time $t = 0.5$ ms

(b) Time $t = 1.0$ ms

Figure 6.18 : *Evolution of axial velocity at the axis over axial distance at different instants of the simulation. Comparison between coarse and fine mesh resolutions*

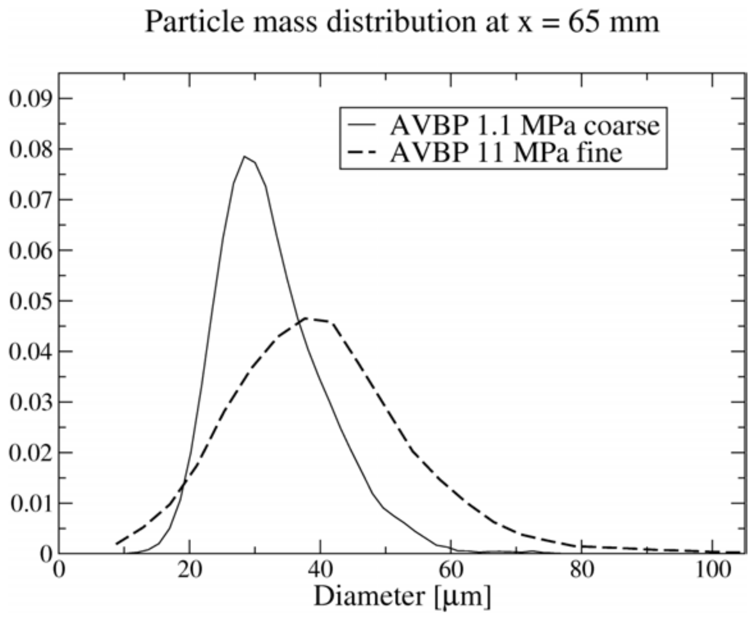

Figure 6.19 : *Influence of grid resolution on the particle mass distribution function at $x = 65$ mm.*

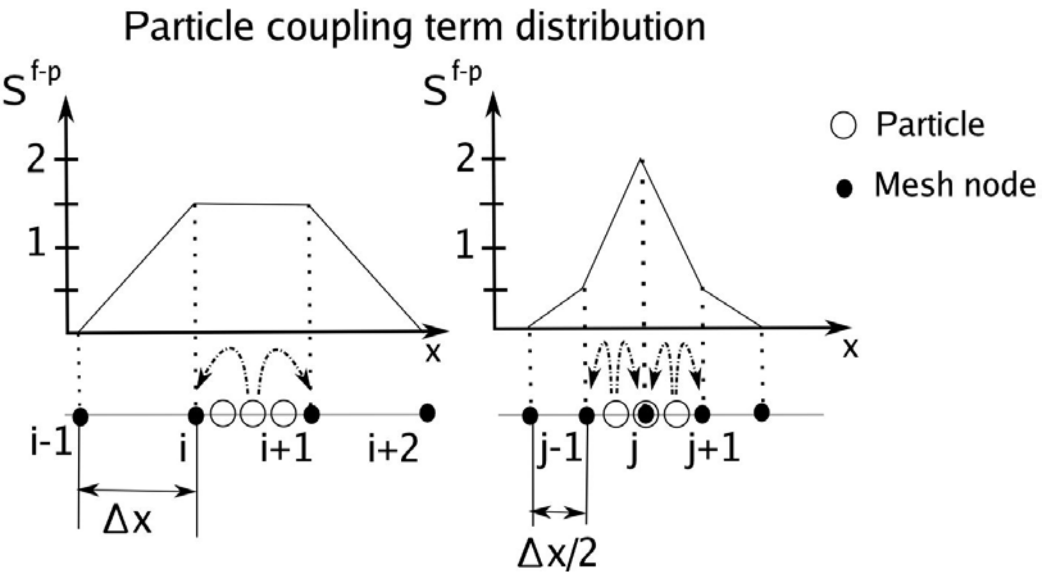

Figure 6.20 : *Sketch of the particle coupling term distributions for two one-dimensional equidistant meshes of different resolution*

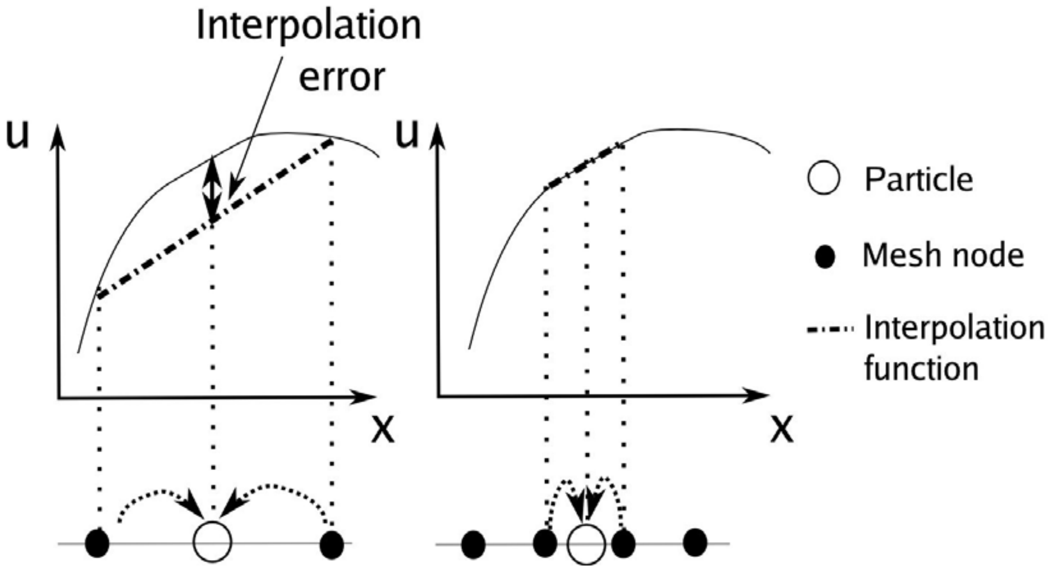

Figure 6.21 : *Sketch of the errors associated with the interpolation of gaseous properties (in this example the velocity u) at the particle location for two one-dimensional equidistant meshes of different resolution*

velocity profile at the particle location for both grid resolutions. The linear interpolation of the gas velocity at the particle location yields an error proportional to the distance between particle and grid node if the function to interpolate is itself not linear. Therefore, interpolation errors on the gaseous velocity at the particle location may lead to the prediction of different particle accelerations/ decelerations on both meshes. It is believed that the observed mesh sensitivity of present results arises from a combination of these two effects: a different spatial source term distribution and different error levels in the interpolation of gas velocities at the particle location. Both effects show the clear limitations of Lagrangian simulations for atomizing sprays at conditions representative of Diesel engines. Conclusions of the present section will be given after the discussion of the second validation case.

6.2 Simulation of a liquid jet in a turbulent gaseous crossflow

The implemented secondary breakup model is now tested in the case of a liquid jet injected perpendicularly to a turbulent gaseous crossflow. Such configuration is of great interest for new aeronautical combustor designs involving multipoint injection systems, where a series of liquid jets are injected perpendicularly to the airflow, resulting in a quick mixing and a homogeneous vapor distribution. Thus, such injection is expected to yield stable lean combustion regimes required for low NO_x emissions. Predicting the particle size distributions, liquid jet penetration heights and subsequent interactions with the airflow is a necessary step to further optimize the combustion process.

The considered geometry reproduces an experiment performed by Becker et al. [15] at pressure conditions typical for aeronautical engines. Three different mass flow rates of liquid were examined at constant gaseous crossflow conditions. In the following, simulations of these three cases with different levels of simplification are compared:

- simulations with a liquid column model based on empirical correlations to inject the developed spray, performed by Jaegle [93].
- simulations combining the liquid column model of Jaegle [93] and the secondary breakup model developed in the present work.

The objective of this comparison is to determine whether the use of a secondary breakup model may result in better predictions of the resulting spray field.

6.2.1 Physical mechanisms

Recent experimental findings on liquid jets in gaseous crossflows were recently reviewed by Wu et al [231]. Earlier works [196, 142] mainly focused on determining penetration lengths of the liquid jets and trajectories of the liquid column. The recent use of pulsed shadowgraphy by Wu et al. [231], Sallam et al. [190] and Lee et al. [116] also allowed to retrieve physical properties in the dense spray zone such as wavelengths of liquid surface waves, ligament sizes ejected from the column and their velocities as well as characteristic breakup times of the column.

Two main primary breakup mechanisms have been evidenced in previous studies of liquid jets in gaseous crossflows [231]. The first is called column breakup and describes the amplification of wavelike disturbances on the column surface, leading to the ejection of ligaments with subsequent disintegration into a spray. The second mechanism is called surface breakup and describes the stripping of small particles from the liquid phase boundary layer which forms near the colum surface. The predominance of the respective mechanism mainly depends on two characteristic numbers. The first is the aerodynamic Weber number:

$$We_{ae} = \rho D_0 u_\infty^2 / \sigma_l \tag{6.2}$$

where D_0 denotes the diameter of the injection orifice and u_∞ is the bulk velocity of the gaseous crossflow. The second fundamental quantity is the momentum flux ratio:

$$q = \rho_l w_{l,0}^2 / \rho u_\infty^2 \tag{6.3}$$

where $w_{l,0}$ is the injection velocity of the liquid jet. Note that these relations are expressed in the coordinate system that will be used throughout this section: the gaseous freestream is parallel to the x-axis, the liquid crossflow is injected along the z-axis while the transverse direction coincides with the y-axis (see fig. 6.25). A classification based on the aerodynamic Weber number and the momentum flux ratio was proposed by Wu et al. [231] and is displayed in fig. 6.22, where the three momentum flux ratios of the experiment of Becker et al. [15] are also placed: $q = 2$, $q = 6$, $q = 18$. While the case $q = 2$ appears dominated by column breakup,

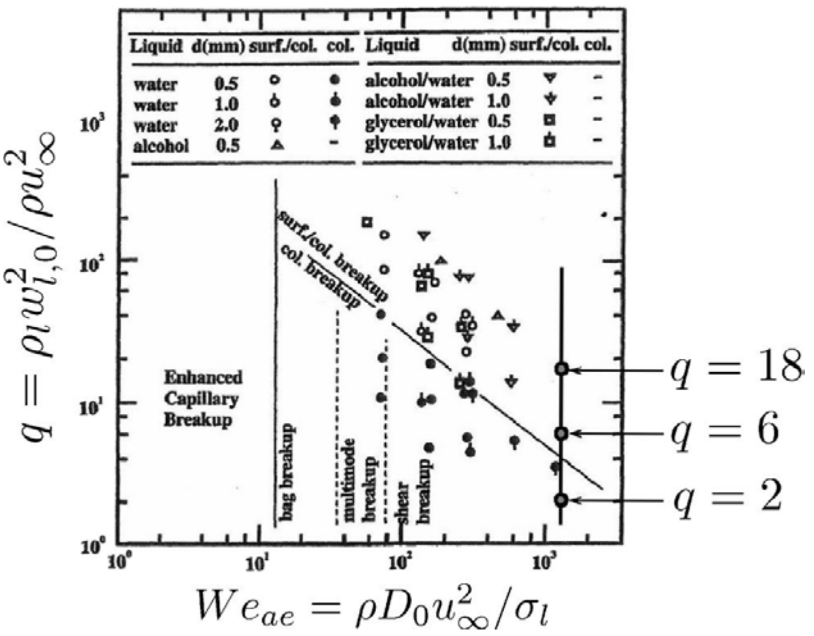

Figure 6.22 : *Classification of the different breakup regimes for the liquid jet in a gaseous crossflow, taken from Wu et al. [231]. The different mass flux ratios investigated in the experiment of Becker et al. [15] are also marked.*

the cases $q = 6$ and $q = 18$ lie in the region of combined surface and column breakup. In this regime, surface breakup only removes a certain amount of the liquid mass before column breakup takes places. An illustration of both breakup regimes is provided in fig. 6.23, which displays pulsed shadowgraphs from Freitag and Hassa [59] with a schematic from Jaegle [93].

6.2.2 Column model

The far-field penetration of a liquid jet injected in a turbulent gaseous crossflow is greatly influenced by the presence of a liquid column. The trajectory of this column differs considerably from that of spherical particles. Furthermore, the disintegration of the large ligaments ejected from the liquid column into small particles leads to a significant change in drag properties which is expected to affect the spray trajectory. Jaegle [93] proposed a model to account for the presence of the liquid column, it is based on the following principles:

- the liquid directly “turns” into the developed spray at the column breakup point: secondary breakup is neglected.
- in the region between liquid injection and column breakup point, a modified drag law is applied to the particles to account for the presence of the liquid column. After this point, particles recover their normal drag properties.
- if surface breakup is present, the mass flow rate of liquid stripped from the liquid column and the characteristic size of resulting particles are determined. These particles inherit the liquid column velocity and an additional velocity to account for their stripping from the column.

Since in the present work secondary breakup is explicitly taken into account, the first aspect of the model must be modified: the liquid no longer turns into the developed spray at the column breakup point. Instead, large

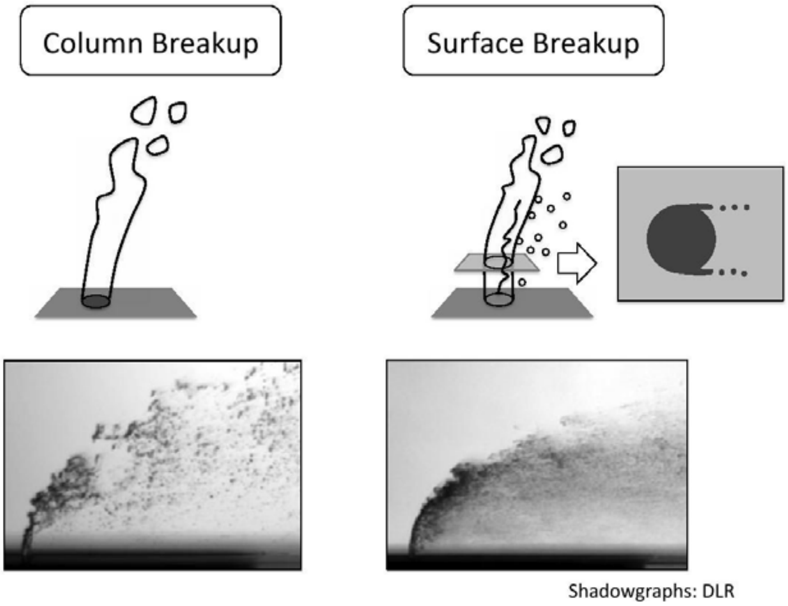

Figure 6.23 : *Illustration of the column breakup regime (left) and the surface breakup regime (right). Sketches from Jaegle [93]. Shadowgraphs: Freitag and Hassa [59].*

“blobs” representative of the liquid fragments ejected from the column are injected at the nozzle orifice. The size of these blobs is a new entry of the model and must be determined. The remaining aspects of the model are left unchanged: a modified drag law is applied to the blobs until they reach the column breakup point, after which they recover their normal drag properties. A sketch of the present modeling procedure as compared to the physical phenomena involved in the desintegration of the liquid jet in a gaseous crossflow is shown in fig. 6.24. Although mostly relying on empirical correlations, the present approach allows to account for all important processes governing the column disintegration and its impact on spray dynamics.

The first entry of the model is the column breakup point. Its location may be obtained from the work of Fuller et al. [61], who consider a liquid column subjet to a drag force. The column is assumed to be oriented perpendicularly to the gaseous crossflow along the z-axis and the drag force is assumed to be parallel to the freestream direction x over the entire column length. y is the transverse coordinate, see fig. 6.25. By introducing an average drag coefficient C_d for the liquid column, the authors derive the following momentum balance:

$$\frac{\pi}{4}\rho_l D_0 \frac{du_l}{dt} = \frac{1}{2}\rho C_d u \sqrt{[u^2 + (w - w_l)^2]} \tag{6.4}$$

where D_0 is the liquid column diameter. From their experimental studies, Fuller et al. [61] report an average drag coefficient $C_d = 4.39$, which will be used to modify particle drag along the column trajectory. In order to further simplify this relation, Fuller et al. [61] assume $(w - w_l)^2 \ll u^2$. The authors also consider that the gaseous quantities remain constant at their freestream values, i.e. $\rho = \rho_\infty$, $u = u_\infty$. Using these hypotheses, eq. 6.4 simplifies to:

$$\frac{du_l}{dt} = \frac{2C_d}{D_0\pi}\frac{\rho_\infty}{\rho_l}u_\infty^2 \tag{6.5}$$

Integrating this relation twice gives the streamwise deflection of the column as a function of time:

$$x_l(t) - x_0 = \frac{C_d}{D_0\pi}\frac{\rho_\infty}{\rho_l}u_\infty^2 t^2 \tag{6.6}$$

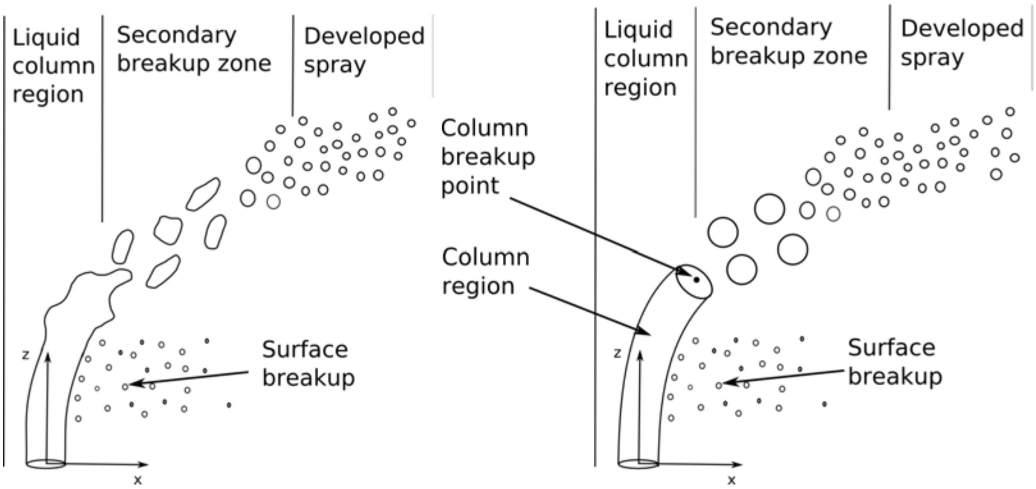

Figure 6.24 : *Left: classification of different regions of the liquid atomization. Right: schematic of the employed modeling strategy*

where x_0 is the streamwise coordinate of the injection point (see fig. 6.25). Fuller et al. [61] also provide an estimate for the characteristic column breakup time scale:

$$t_{bu}^{col} = C_{bu}^{col} \frac{D_0}{u_\infty - w_{l,0}} \sqrt{\frac{\rho_l}{\rho_\infty}} \tag{6.7}$$

with $C_{bu}^{col} \approx 2.58$ for the presently considered range of aerodynamic Weber numbers. Combining eqs. 6.7 and 6.6, the streamwise location of the column breakup point is then obtained as:

$$\frac{x_{bu}^{col} - x_0}{D_0} = \frac{C_d (C_{bu}^{col})^2}{\pi} \frac{u_\infty^2}{(u_\infty - w_{l,0})^2} \tag{6.8}$$

The height of the column breakup point is obtained by assuming that the liquid injection velocity $w_{l,\infty}$ remains unchanged along the column trajectory. The column height is then directly determined from eq. 6.7 as:

$$\frac{z_{bu}^{col} - z_0}{D_0} = C_{bu}^{col} \frac{w_{l,0}}{u_\infty - w_{l,0}} \sqrt{\frac{\rho_l}{\rho_\infty}} \tag{6.9}$$

Finally, deflections of the column along the transverse coordinate are neglected:

$$y_{bu}^{col} = y_0 \tag{6.10}$$

The location of the breakup point is then defined by eqs. 6.8, 6.10 and 6.9 for the $x-$, $y-$ and $z-$ coordinates respectively.

For the momentum flux ratios $q = 6$ and $q = 18$, the developed spray is not only produced by secondary breakup of the liquid fragments ejected from the column but also by surface breakup, which occurs due to lateral stripping of the liquid boundary layer from the column surface. A basic model accounting for this phenomenon needs to specify at least two quantities: the mass of liquid removed from the liquid boundary layer and a characteristic particle diameter.

The mass of liquid removed from the column is obtained by adapting a model developed for the stripping of a liquid boundary layer from a spherical particle [169] to the liquid column. The equation for the liquid mass flow rate stripped per unit column length l_{col} is obtained as:

$$\frac{d\dot{m}_l^{strip}}{dt} = \frac{3}{2} l_{col} \rho_l \sqrt{\pi D_0 A a_l u_\infty} \tag{6.11}$$

The reader is referred to Ranger and Nichols [169] for a detailed derivation of this relation. The constants a_l and A are respectively defined as:

$$a_l = \sqrt{\left(\frac{8}{3}\frac{\mu_l}{\mu}\right) / A u_\infty} \tag{6.12}$$

$$A = \left(\frac{\rho_l}{\rho_\infty}\frac{\mu}{\mu_l}\right)^{1/3} \tag{6.13}$$

The characteristic size of the stripped particles can be determined from the work of Chou et al. [29], who determined the quantity of liquid removed from a particle undergoing surface/ stripping breakup. It is assumed that their results can be transposed to the case of a liquid column. Chou et al. [29] distinguish between two regimes: the transient shear breakup regime and the quasi-steady regime. In the quasi-steady regime, the size of the fully developed liquid boundary layer has a surface proportional to the column diameter, i.e. $\delta \sim D_{col}$. It is assumed that the column breakup time scale is large enough to ensure a fully developed boundary layer. If the mass removed from the liquid column is further assumed is small, the boundary layer thickness δ may be replaced by the injection nozzle diameter D_0 in the correlation of Chou et al. [29], yielding:

$$d_{32}^{strip} = 0.09 D_0 \tag{6.14}$$

Note that this correlation is also in very good agreement with more recent experimental results of Sallam et al. [189]. The stripped particles inherit the velocity of the liquid column plus a velocity contribution in streamwise direction arising from the stripping process. From experimental measurements, Chou et al. [29] give the following relation for the streamwise velocity of the stripped fragments:

$$u_l^{strip} = u_{l,s} + 0.37(u_\infty - u_{l,s}) \tag{6.15}$$

where $u_{l,s}$ is the streamwise velocity of liquid column at the location of surface breakup.

When accounting for secondary breakup, large “blobs” representing liquid fragments issued from column breakup are injected at the nozzle. A characteristic diameter may be estimated for these blobs using an experimental correlation provided by Sallam et al. [189]. The authors provide an estimate for the wavelength of the column surface instabilities λ_s as a function of the aerodynamic Weber number. Assuming that each wave leads to the ejection of a single fragment and that column deformation effects are small, the equivalent diameter of the ejected fragments may be estimated from mass conservation as:

$$d_p^{eq} = \left(\frac{3}{2} D_0^2 \lambda_s\right)^{1/3} \tag{6.16}$$

with $\lambda_s \approx 0.15 D_0$ for the present range of aerodynamic Weber numbers [189].

6.2.3 Geometry

The computational domain represents a short stretch of the measurement duct of the experiment of Becker et al. [15] (fig. 6.25) The coordinate system is centered on the injection point. x denotes the gaseous streamwise coordinate while z points in the direction of the liquid injection. The air inlet is located 55 mm upstream the liquid injection point. The outlet is located 150 mm downstream the liquid injection. All lateral surfaces represent walls. The air is injected with 100 m/s, yielding a Reynolds number based on the channel width of $Re = 1 \cdot 10^6$. Bulk pressure and temperature of the airflow are respectively p = 6 bar and T = 290 K. Becker et al. [15] performed experiments for three different mass flow rates of liquid at constant injection orifice diameter, leading to three different mass flux ratios: q = 2, 6, 18. For the three cases, the gaseous parameters are kept constant. The resulting operating conditions for the three different momentum flux ratios are summarized in table 6.4.

Momentum flux ratio	$q = 2$	$q = 6$	$q = 18$
Gas temperature T [K]		290	
Gas pressure p [bar]		6	
Gas bulk velocity u_∞ [m/s]		100	
Liquid mass flow rate $\dot{m}_l$ [g/s]	1.7	2.95	5.11
Injection velocity $w_{l,0}$ [m/s]	13.46	23.31	40.38
Liquid temperature T_l [K]		275	
Liquid density ρ_l [kg/m^3]		795	
Injection orifice diameter D_0 [mm]		0.45	

Table 6.4 : *Liquid injection conditions for the three different momentum flux ratios*

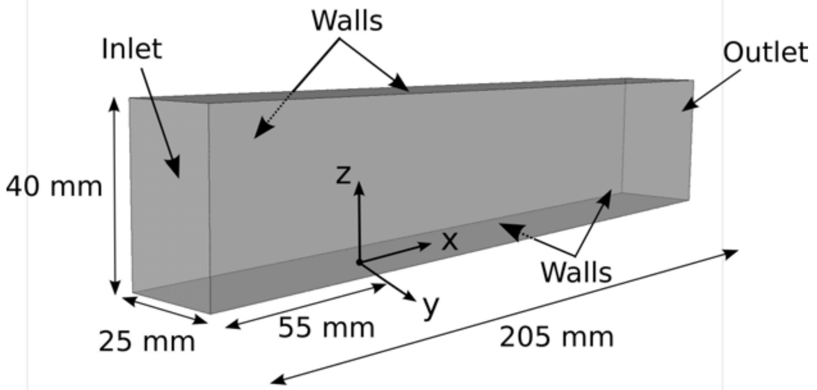

Figure 6.25 : *Computational domain of the jet-in crossflow configuration. The injection point coincides with the origin of the coordinate system*

6.2.4 Computational details

The unstructured mesh contains approximately 1,5 million tetrahedric cells, a midplane cross section through the computational domain is shown in fig. 6.26. Due to the relatively long stretch of the experimental duct upstream the liquid injection, it is assumed that the flow field is fully turbulent at the simulation inlet. Therefore, synthetic turbulence is injected at the inlet. The fluctuation field is generated according to the methods of Klein et al. [99] and Kraichnan [102]. The statistics of the injected turbulent flow field are obtained by simulating a periodic stretch of duct with same cross-section and physical properties. Furthermore, the periodic duct displays the same mesh resolution so that statistics (mean and rms velocity field) are obtained at the same filter level, minimizing the noise generated by the turbulence injection. More details on this aspect may be found in Jaegle [93]. The lateral walls and the outlet are respectively modeled with adiabatic wall laws and a non-reflective pressure outflow condition. The first grid point in wall normal direction is roughly located at 500 wall units, which is consistent with the use of wall laws.

For the gaseous phase, the second-order Lax-Wendroff scheme is used for convection and the standard Smagorinsky model is used for subgrid scale modeling. The 2Δ operator is used for diffusion. The application

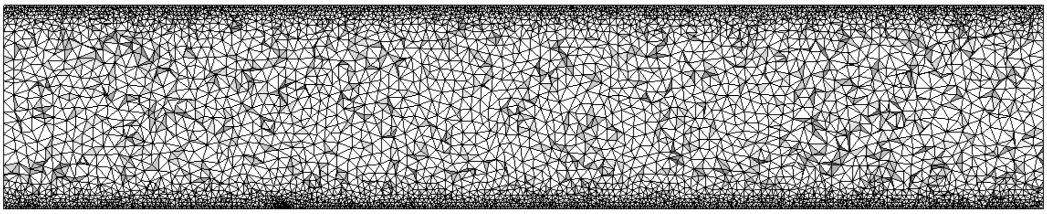

Figure 6.26 : *View of the computational mesh in a mid-plane cut*

of artificial viscosity relies on the Colin sensor [33]. For the liquid phase, three different types of particles are injected:

- First, large blobs modeling the liquid fragments resulting from column breakup and which subsequently undergo secondary breakup are injected. Their diameter is given by eq. 6.16. Note that Jaegle [93] injects a developed spray whose size distribution fits the experimental measurements of Becker et al.[15] at $x = 80$ mm for the case $q = 6$. The particle mass flow rate is equal to the total liquid mass flow rate minus the mass flow rate of liquid removed from the column through surface breakup.
- Second, particles equal to the characteristic stripping diameter, eq. 6.14, are injected, their mass flow rate being given by eq. 6.11.
- Finally, ghost blobs modeling the coupling between both phases are injected. Their diameter is equal to the injector diameter. Once they reach the liquid column breakup point, they are removed from the simulation.

The modified drag law for the liquid column is applied to all particles inside the liquid column region. The large blobs regain their normal drag properties as soon as they reach the column breakup point. The stripped particles regain their normal drag properties at a random column height. The probability to release a stripped particle from the column increases with the column height. The stripped particles inherit an additional velocity in streamwise direction given by eq. 6.15.

Evaporation is explicitly taken into account in the simulations but its effects are negligible due to the low difference between gas and particle temperature. Due to the moderate liquid mass flow rates, no parcel approach is used in the simulations. Two-way coupling is enabled and interpolation of gaseous properties to the particles is based on a first-order Taylor method. Particle wall interaction is modeled through elastic rebound for all particles. A summary of the numerical parameters used in the present simulations is given in table 6.5.

In the present work, the secondary breakup constants k_1 and k_2 are adjusted to reproduce the experimental size distribution of the developed spray for case $q = 6$ at $x = 80$ mm (see fig. 6.30). These parameters are kept constant for the three simulations. The resulting values $k_1 = 0.02$ and $k_2 = 0.16$ are significantly lower than for the Diesel injection case. It is believed that this effect results from the underestimation of child particles sizes at large Weber numbers. The effects of this underestimation are more pronounced in this configuration because the gaseous freestream velocity is less affected by coupling between phases. Therefore, a large velocity difference between particles and gas is maintained over long times in this configuration contrary to the spray atomization simulations of section 6.1, where the gas is strongly accelerated by the particles. In order to understand why child particle sizes are underestimated at large Weber numbers, the relation providing the mean of the particle size distribution after breakup is rewritten:

$$\langle \ln \alpha \rangle = k_1 \ln \left(\frac{We_{cr}}{We} \right) \tag{6.17}$$

where $\alpha = r_p/a_p$ is the ratio of the child particle radius to the parent particle radius. This relation indicates that the radius of the child particles decreases in the mean with increasing Weber number. Although this relation may reasonably hold for moderate Weber numbers, it is believed that it is no longer appropriate at large Weber numbers. These are characterized by catastrophic breakup, which leads to the formation of a few large liquid fragments which generally undergo stripping (see section 5.1.2). Stripping breakup is characterized by the removal of small liquid fragments from the liquid boundary layer at the surface of the particle. Therefore, secondary breakup at large Weber numbers seems to lead to the formation of a few large and many small child particles [90]. In the present model, such bimodal distribution can only be enforced by setting the mean of the particle size distribution after breakup close to the diameter of the parent particle, i.e. by setting the constant k_1 to small values. This is because no restriction is made on the number of child particles in the FAST secondary breakup model. Therefore, a parent particle may disintegrate into a large number of small particles for small values of α. In a model limiting the number the number of child particles (typically two or three in other secondary breakup models), mass conservation would still ensure the presence of a large child particle. This drawback of the model could either be alleviated by modifying eq. 6.17 for large Weber numbers or limiting the number of child particles in general. Note that the negligence of coalescence phenomena and particle deformations prior to breakup may also induce an underprediction of the particle sizes of the developed spray. These effects would then have to be compensated by modifications of the breakup constants k_1 and k_2.

Numerical Parameters			
Gas	Values	Liquid (all cases)	Values
Convection	Lax-Wendroff	Breakup constant k_1	0.02
Diffusion	2Δ operator	Breakup constant k_2	0.16
Subgrid-scale model	Smagorinsky	Parcel approach	No
Artificial viscosity sensor	Colin	Two-way coupling	Yes
Second order AV	$\epsilon^2 = 0.07$	Evaporation	Yes
Fourth order AV	$\epsilon^4 = 0.04$	Interpolation	Taylor
		Wall interaction	Elastic rebound

Table 6.5 : *Numerical parameters of the liquid jet in gaseous crossflow*

6.2.5 Results

Fig. 6.27 displays the instantaneous axial velocity field in the midplane superimposed with particles contained in a 1 mm slab. The size of the symbols scales with the diameter of the particles. The black line denotes the location of the experimental measurement plane, $x = 80$ mm.

The effect of increasing momentum flux ratio is correctly reproduced as the spray plume remains close to the wall for the case $q = 2$ while it is clearly detached for $q = 18$. The particles issued from surface breakup and the particles issued from column breakup are clearly distinguishable for the cases $q = 6$ and $q = 18$. Their different trajectories lead to a gap between the respective sprays in the vicinity of injection because there is no smooth transition between surface and column breakup in the liquid column model. The interaction with turbulence is clearly visible as particles are entrained in the resolved vortical structures of the LES further downstream injection. It appears that the higher penetration of the liquid column for increasing momentum flux ratios considerably broadens the spray plume. This effect originates from the stripping of liquid over the increasing liquid column length. Furthermore, the increase in momentum flux ratio probably induces a delay in the balistic sorting mechanism which separates particles according to their size. Fig. 6.28 displays a closeup view of the liquid column region for the three momentum flux ratios. The deflection of the liquid column by the gaseous crossflow is seen to decrease for higher momentum flux ratios. This has the important consequence that the relative velocity between gas and particles is reduced for lower momentum flux ratios. Since the size of the particles resulting from secondary breakup globally increases with decreasing relative velocity between gas

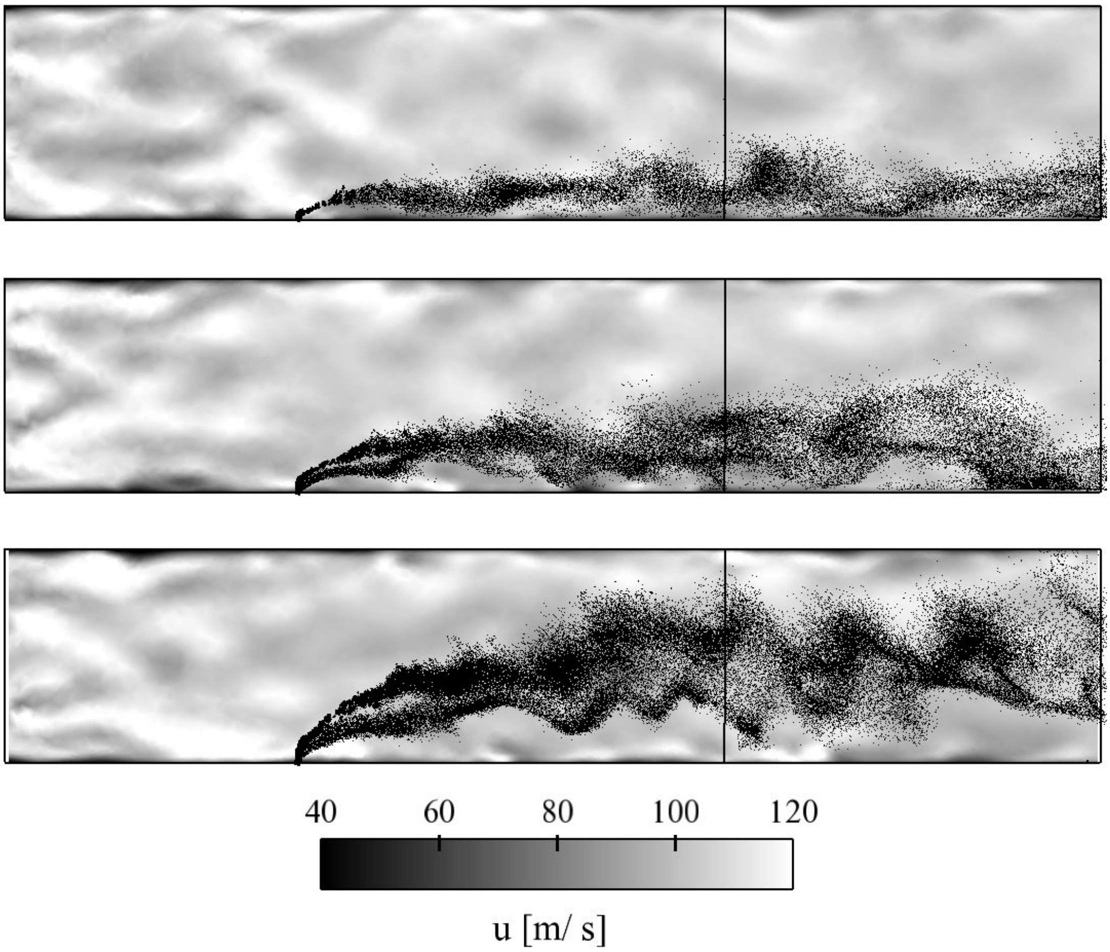

Figure 6.27 : *Instantaneous field of axial velocity in the midplane* $y = 0$ *superimposed with particles. Cases from top to bottom:* $q = 2, q = 6, q = 18$*. The vertical black line denotes the experimental measurement plane (*$x = 80$ *mm)*

and particles, the characteristic mean diameter of the spray is expected to decrease with momentum flux ratio.

Fig. 6.29 displays averaged iso-contours of liquid volume flux ϕ_l in a transverse cross-section at the experimental measurement location $x = 80$ mm. The average is performed from 30 decorrelated instantaneous solutions. The liquid volume flux is defined as:

$$\phi_l = \alpha_l \sqrt{u_l^2 + v_l^2 + w_l^2} \tag{6.18}$$

The liquid velocities are obtained through interpolation of the particle velocities on the computational grid and summation of all particle contributions inside a computational cell. For the case $q = 6$, a graph of liquid volume flux is available from the experiments of Becker et al [15]. The broadening of the spray plume in wall normal direction for higher momentum flux ratios visible in fig. 6.27 is confirmed by the iso-contours of liquid volume flux. On the contrary, the spray plume does not broaden much in the transverse direction, leading to a more elongated shape of the liquid volume flux towards higher momentum flux ratios. It seems that this effect is overestimated in the simulations, as the liquid volume flux contour is too elongated in the simulation for the case $q = 6$ compared to the experimental contour for which a circular shape is observed.

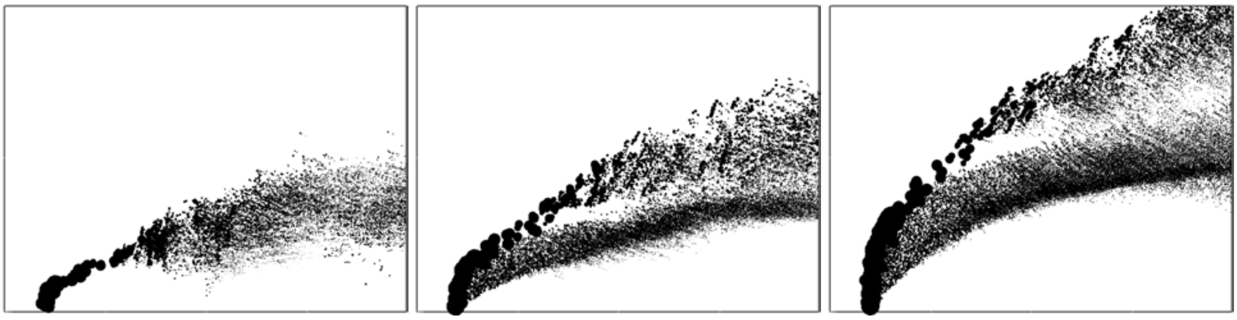

Figure 6.28 : *Closeup view of the column and of the atomizing spray. From left to right:* $q = 2, q = 6, q = 18$

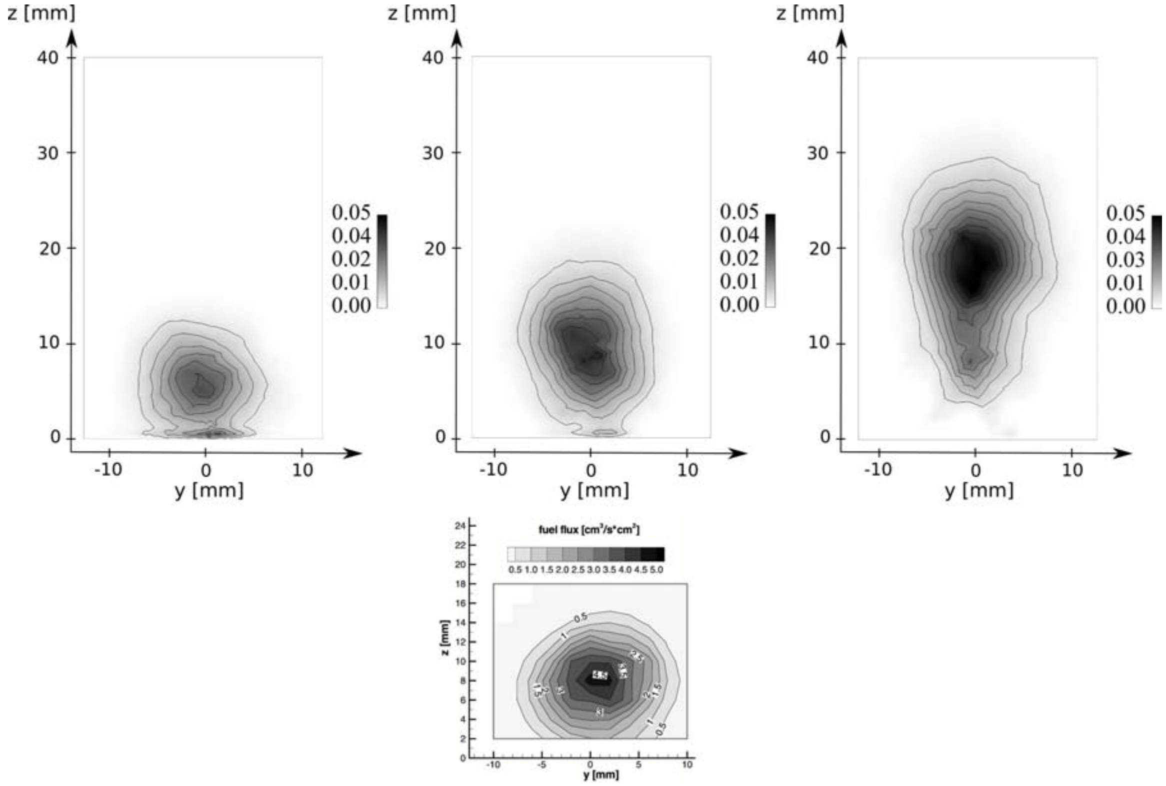

Figure 6.29 : *Isocontours of averaged liquid volume flux* ϕ_l $[m^3/sm^2]$ *in a transverse plane at* $x = 80$ *mm. The average is performed with 30 decorrelated instantaneous solutions. Top row: simulation results. From left to right:* $q = 2, q = 6, q = 18$*. Bottom: experimental result for the case* $q = 6$ *from Becker et al. [15]*

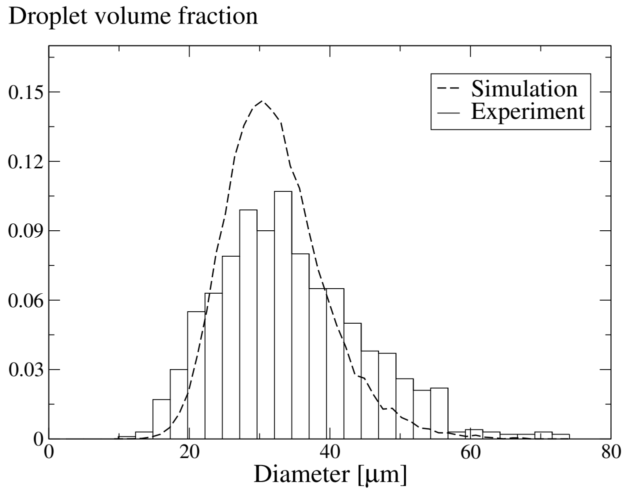

Figure 6.30 : *Particle volume fraction for $q = 6$ at $x = 80$ mm, $y = 0$ mm, $z = 8$ mm. Comparison between simulation and experiments from Becker et al. [15]*

Fig. 6.30 displays the particle volume fraction at $x = 80$ mm, $y = 0$, mm $z = 8$ mm for the case $q = 6$. It is defined as the sum of the particle volumes for a given diameter class divided by the sum of the particle volumes over all classes. The experimental distribution is reasonably well reproduced by the secondary breakup model, which gives an additional illustration of the fact that many particle size distributions encountered in practical applications may be approximated with a lognormal law. Recall however that these results were obtained by adjusting the breakup constants k_1 and k_2 to this case. These paremeters were then kept constant for cases $q = 2$ and $q = 18$ to asses their sensitivity to variations in the momentum flux ratio. Unfortunately, there is no experimental data on particle size distributions for cases $q = 2$ and $q = 18$.

Fig. 6.32 displays the time averaged liquid volume flux for the three momentum flux ratios over the wall normal distance at the location $x = 80$ mm. Time-averaged data is obtained at different wall distances z and additionally averaged over the transverse direction y as done in the experiments (fig. 6.31). Spatial averaging along the y-axis is performed in an integral manner:

$$\langle \phi_l(x, \bar{y}, z) \rangle = \frac{1}{l_y} \int_0^{l_y} \langle \phi_l(x, y, z) \rangle dy \tag{6.19}$$

where l_y represents the length of the geometry in transverse direction and $\langle \cdot \rangle$ denotes a time averaging operator. The results obtained by Jaegle [93] are also reported in fig. 6.32 to assess the effect of secondary breakup in the simulations. The differences between the results of Jaegle [93] and the present work appear very limited for the case $q = 2$. For both, the location of maximum volume flux is located above the experiment and the curves appear too broad in wall normal direction. Differences between the simulations with and without breakup increase with momentum flux ratio. For cases $q = 6$ and $q = 18$, secondary breakup shifts the location of the maximum volume flux towards higher wall normal locations for the cases $q = 6$ and $q = 18$. For these values, the simulations without breakup show closer agreement with experiments. The differences probably originate from the different spray properties after the column breakup point. Three major differences are expected between simulations with and without breakup in the column breakup region:

- In the simulations with secondary breakup, large blobs gradually disintegrating into the developed spray are found after the column breakup point whereas the developed spray is directly present in the simulations without breakup. The large particles present in the simulations with breakup display higher inertia and will therefore penetrate further into the gaseous crossflow.

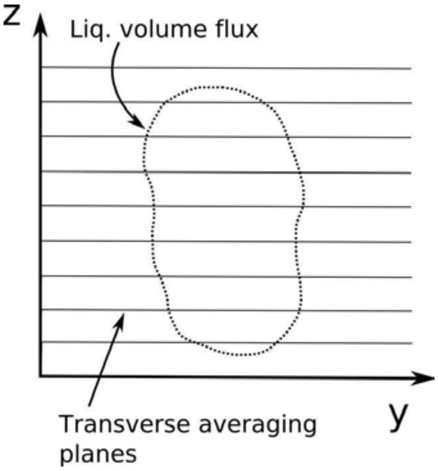

Figure 6.31 : *Sketch of the averaging procedure in transverse direction (y-axis) at $x = 80$ mm, which consists in weighted integral of a given quantity f over this direction (eq. 6.19)*

- The inclusion of secondary breakup is expected to induce a denser spray after the column breakup point, which will in turn enhance the coupling between phases. In particular, more air entrainment is expected in this region compared to the simulations without breakup, lowering the relative velocity between phases and enhancing the column penetration heights. A brief quantitative analysis shows that this effect may be sigificant. From the mean profiles of liquid volume fraction and liquid streamwise velocity (not shown) for case $q = 6$, the values $\alpha_{l,bu}^{col} \approx 1 \cdot 10^{-2}$ and $u_{l,bu}^{col} \approx 50$ m/s are obtained at the location of the column breakup point. A similar procedure for the gas shows that its density and velocity are approximately equal to the freestream values, i.e. $\rho_b u^{col} \approx \rho_\infty \approx 7.2$ kg/m^3 and $u_{bu}^{col} \approx u_\infty = 100$ m/s. The momentum flux ratio at the column breakup point is then obtained as $q_{bu}^{col} = \rho_{l,bu}^{col} \alpha_{l,bu}^{col} (u_{l,bu}^{col})^2 / \rho_b u^{col} (1 - \alpha_{l,bu}^{col})(u_{l,bu}^{col})^2 \approx 0.28$. This value indicates that coupling between phases at the column breakup point may impact the spray penetration height as the momentum of gas and spray are comparable there. However, note that the dense spray zone is also characterized by coalescence phenomena, which are neglected in the present work. Furthermore, particle deformation effects prior to breakup are not taken into account. These deformations are expected to induce significant changes in particle drag properties and thus influence the coupling between phases. For these reasons, coupling effects between phases in the dense zone are probably not well reproduced in the present simulations either.

- The last difference concerns the velocity of the child particles issued from secondary breakup: in addition to the velocity of the parent particle, they inherit a velocity normal to the relative velocity between gas and parent particle. This normal velocity accounts for the strong deformation of particles during the breakup process through aerodynamic forces or individual particle instability mechanisms.

The first and third effect are expected to yield increased penetration heights and a broadening of the spray plume, resulting in peak values of liquid volume flux located at higher wall normal distances and broader spatial distributions of liquid volume flux. Such effects are indeed observed in fig. 6.32 and are best visible for case $q = 18$. However, since the results of Jaegle [93] appear to already overestimate both the peak location and the spread of liquid volume flux, present results are in even worse agreement with experiments. The results of Jaegle [93] hint on an overestimation of the height of the column breakup point in the liquid column model. This effect could arise from an underestimation of the column deflection by the empirical drag coefficient C_d (eq. 6.4) or the negligence of the liquid injection velocity attenuation along the column trajectory. Furthermore, droplet deformation effects during secondary breakup, which are presently not taken into account, may also be a source of discrepancies for the liquid volume flux.

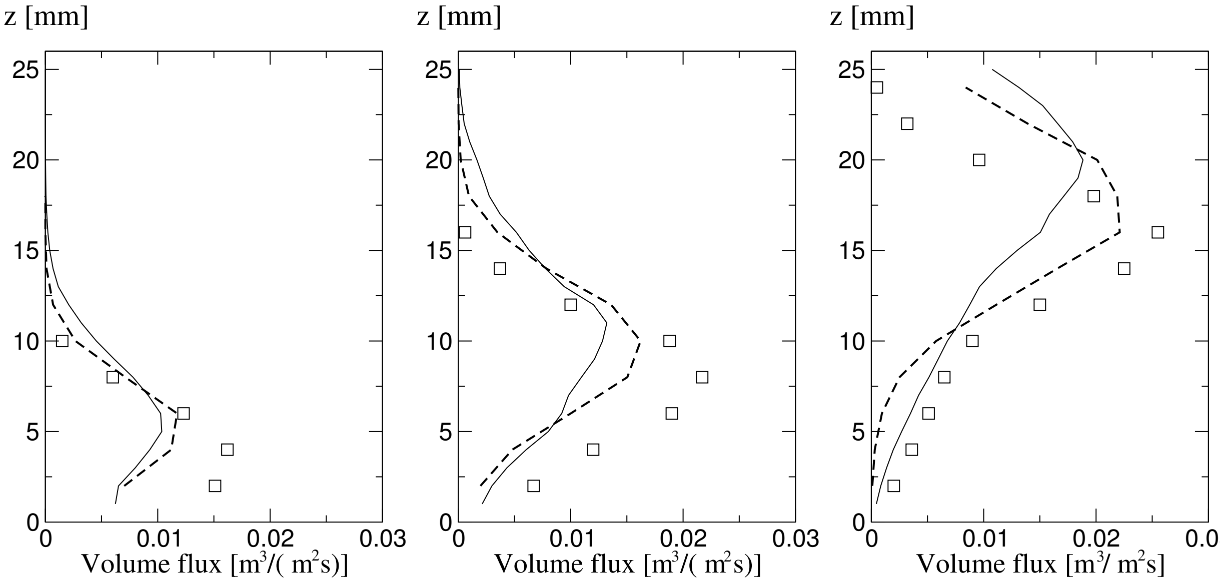

Figure 6.32 : *Liquid volume flux at the location $x = 80$ mm over the wall normal distance. Results are averaged over the transverse direction as done in the experiments. – present work, - - results by Jaegle, (column model without secondary breakup) □ experiments from Becker et al. [15]*

Fig. 6.33 displays the Sauter mean diameter (SMD) for the three momentum flux ratios over the wall normal distance at the location $x = 80$ mm. Data is obtained at different wall distances z and averaged over the transverse direction y as done in the experiments (fig. 6.31). The data is furthermore locally weighted by the liquid volume flux to follow the methodology of Becker et al. [15]. Particles are sorted according to their inertia when penetrating into the gaseous crossflow so that the particle SMD increases in positive wall normal direction. An exception to this behavior is observed in the vicinity of the wall for the case $q = 2$. Here, the SMD increases towards the wall. Becker et al. [15] suggest that this effect may originate from the influence of the boundary layer. The authors argue that when particles encounter the reduced gaseous velocities in this region, particle breakup is delayed due to the diminished relative velocity between gas and particles and the resulting SMD is larger. This effect is not reproduced by the secondary breakup model, although the decrease of the SMD towards the wall becomes smoother in its vicinity. Note that the increase of the SMD towards the wall for the case $q = 2$ may also originate from particle-wall interaction effects, which can not be reproduced in the simulations since elastic rebound is assumed for all particles. The inclusion of secondary breakup lowers the increase of the SMD in positive wall normal direction and the SMD profiles are in far better agreement with experiments for case $q = 2$ and $q = 6$ compared to simulations without secondary breakup. The reasons for the reduced slopes of the SMD curves in wall normal direction are the attenuation of balistic sorting due to the presence of larger particles after the column breakup point, the enhanced coupling between phases in this region compared to simulations without breakup and the expansion of the dense spray in a region normal to the relative velocity between phases due to breakup. Effects of different spray size distributions between the simulations with and without breakup are expected to be negligible as the SMD range remains relatively narrow for the three momentum flux ratios. For $q = 18$, the simulations with and without breakup yield similar agreement with experiments. This result indicates that the impact of secondary breakup on balistic sorting effects of particles according to their size becomes negligible for higher momentum flux ratios. This effect is due to increasing liquid column heights, which induce a more important deflection of the column by the gaseous crossflow, thus reducing the relative velocities between gas and liquid fragments in the secondary atomization zone.

Fig. 6.34 displays gas-particle velocity correlations in the plane $x = 80$ mm for the case $q = 6$. Very similar results are obtained for the cases $q = 2$ and $q = 18$ and are not shown. The particle velocities

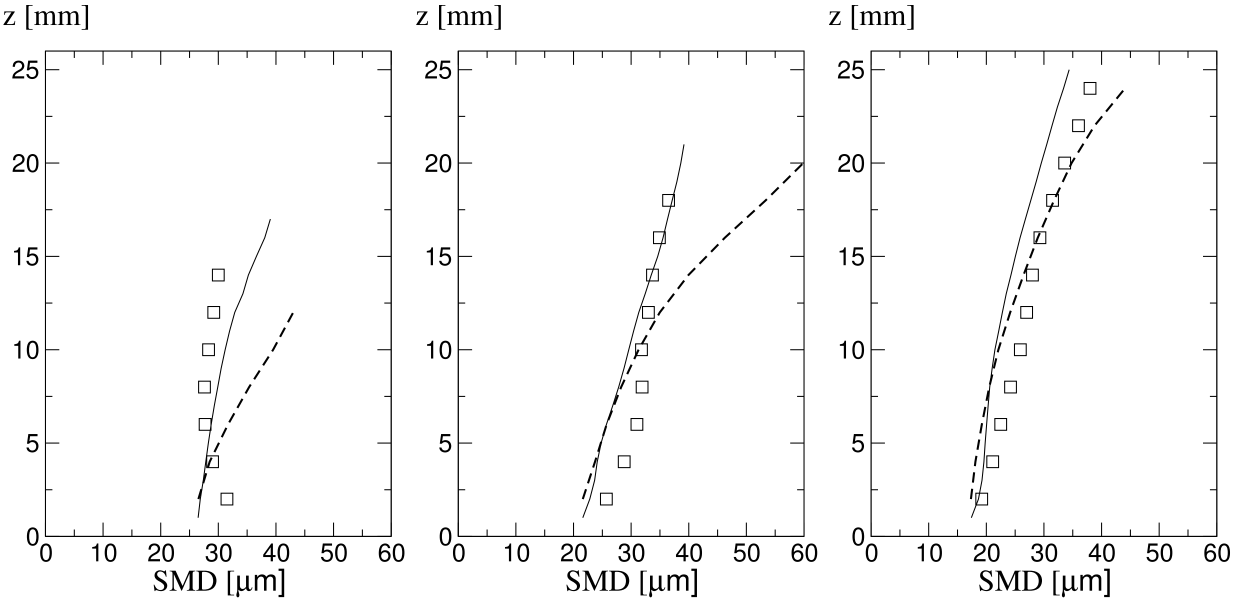

Figure 6.33 : *Sauter mean diameter (SMD) at the location $x = 80$ mm over the wall normal distance. Results are averaged over the transverse direction as done in the experiments. — present work, - - results by Jaegle (column model without secondary breakup) □ experiments from Becker et al. [15]*

are concentrated in the vicinity of the equilibrium line for both axial and transverse velocities. Deviations from equilibrium between gas and particles are probably due to the interaction of particles with the vortical strucutures of the gaseous flow. These results indicate that more accurate injection modeling for the liquid jet in crossflow does not only improve the spatial diameter distribution in the vicinity of injection but also in dilute regions at conditions close to equilibrium.

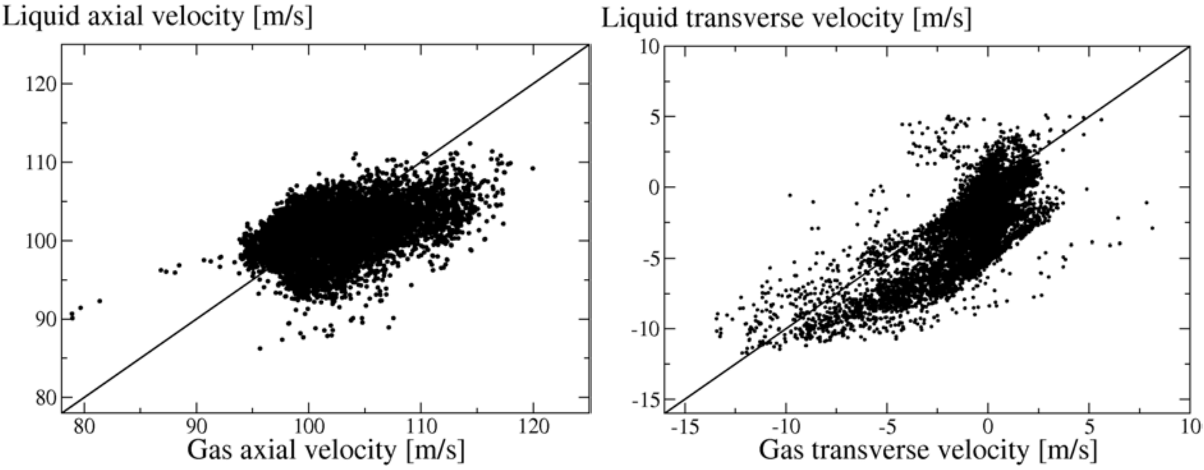

Figure 6.34 : *Gas-particle velocity correlations at the location $x = 80$ mm for the case $q = 6$. Left: axial velocity. Right: transverse (in wall normal direction) velocity*

6.2.6 Conclusions

This chapter presented the application of the FAST secondary breakup model to two different test cases. The first case reproduced the injection of liquid through a single hole nozzle into a closed cylindrical chamber at various gas pressures. Simulations were performed with the grid resolution used by Apte et al. [4] in their validation of the FAST secondary breakup model. Simulation results showed good agreement with both experimental data and results of Apte et al. [4] for gas pressures of 1.1 and 3.0 MPa. For a gas pressure of 5.0 MPa, the spray penetration length was largely underestimated compared to experiments. This behavior was found to originate from an overestimation of the spray angle and an underestimation of the Sauter mean diameter compared to experimental data. The latter effect was assumed to originate from the negligence of coalescence phenomena in the simulation. The implementation of the FAST secondary breakup model was further validated by considering particle mass distributions (which followed a log-normal law as dictated by the model) and mass conservation. After the validation step, effects of grid resolution on simulation results were assessed. Results were found highly sensitive to this parameter, with a strong increase in spray penetration lengths and a strong decrease in spray angles for higher grid refinements. This effect may originate from a different spatial distribution of coupling terms between phases on the grids. Furthermore, varying interpolation errors of gaseous properties at the particle location, especially velocity for the evaluation of drag, may also lead to differences for varying grid resolutions. Both effects show the important limitations of Lagrangian approaches in the prediction of spray atomization phenomena at conditions representative of Diesel engines.

The second test case simulated the injection of a liquid jet perpendicularly to a turbulent gaseous crossflow. Simulation results were compared to experimental data and results of Jaegle [93], who developed an injection model to account for the presence of the liquid column but neglected secondary breakup. Present simulations combined Jaegle's [93] liquid column model with the FAST secondary breakup model. The explicit account for secondary breakup yielded a considerable improvement of time-averaged Sauter mean diameter profiles in the direction of the liquid jet compared to experimental data. This effect probably resulted from a more accurate reproduction of balistic sorting mechanisms when accounting for the disintegration of the liquid fragments ejected from the liquid column. These improvements were obtained at a location where gas and particles were already at equilibrium, indicating that improved injection modeling was also beneficial to the prediction of spray properties in dilute regions for this case. For the profiles of liquid volume flux, secondary breakup shifted the peak value of liquid volume flux to higher column heights. This behavior was expected due to the presence of particles with higher inertia after the column breakup compared to the developed spray in the simulations of Jaegle [93]. However, since Jaegle's results already overestimated the peak location of liquid volume flux, present results were in even worse agreement with experimental data for this quantity.

The breakup constants of the FAST secondary breakup model were found to vary significantly for both validation cases. This effect probably results from an underestimation of the size of child particles issued from breakup at large Weber numbers. This underestimation seems more pronounced for the liquid jet in gaseous crossflow due to higher relative velocities between gas and particles compared to the Diesel injection simulation, where the gas is strongly accelerated by the spray. The negligence of coalescence phenomena and particle deformation effects prior to breakup may be additional causes of discrepancies. Both effects are expected to have a significant impact on the particle size distribution of the developed spray, but are presently not taken into account. These aspects require further investigation to improve the predictivity of the FAST secondary breakup model.

Lire
la seconde partie
de la thèse